

Engineering hybrid nanostructures for the photocatalytic activation of Pt(IV) prodrugs

Laura Filomena Mazzei

eman ta zabal zazu



Universidad
del País Vasco

Euskal Herriko
Unibertsitatea

Donostia, 2023

ENGINEERING HYBRID NANOSTRUCTURES FOR THE PHOTOCATALYTIC ACTIVATION OF PT(IV) PRODRUGS

Ph. D. Thesis presented by

Laura Filomena Mazzei

For the degree of Doctor in Applied Chemistry and Polymeric Materials
by Universidad del País Vasco-Euskal Herriko Unibertsitatea

Thesis Supervisors:

Prof. Aitziber L. Cortajarena

Prof. Luca Salassa

Donostia – San Sebastian, April 2023



DISEÑO DE NANOESTRUCTURAS HÍBRIDA PARA LA ACTIVACIÓN FOTOCATALITICA DE PROFÁRMACOS DE PT(IV)

Tesis doctoral presentada por

Laura Filomena Mazzei

Para optar al grado de Doctor en Química Aplicada y de los Materiales
Poliméricos por la Universidad del País Vasco-Euskadi Herriko
Unibertsitatea

Tesis dirigida por:
Prof. Aitziber L. Cortajarena
Prof. Luca Salassa

Donostia – San Sebastian, April 2023



Table of Contents

<i>List of figures</i>	i
<i>Resumen</i>	ix
<i>Summary</i>	xv
<i>Chapter 1: Hybrid systems for the activation and delivery of metal-based anticancer drugs: an overview on their components</i>	1
1.1. Platinum complexes	3
1.1.1 Introduction	3
1.1.2 Pt(IV) complexes photoactivation	8
1.1.3 Strategies for the delivery of Pt(IV) photoactivable prodrugs	16
1.2. Flavins	19
1.3. Inorganic and biological scaffolds for delivery	26
1.3.1. Gold nanoparticles	26
1.3.2. Protein structure: the four hierarchical levels of organisation	33
1.3.3. Repeat proteins	35
1.3.4. Proteins as scaffold for multifunctional assembly systems	39
<i>Chapter 2: Bioorthogonal catalysis: the dual role of transition-metal complexes</i>	45
2.1. Introduction	47
2.1.1. Bioorthogonal chemistry and catalysis reactions combined together	48
2.2. Bioorthogonal catalysis with metal complex as catalyst	50
2.3. Bioorthogonal photocatalysis with metal complex as substrate	63
2.4. General objectives	71
<i>Chapter 3: Synthesis and characterisation of flavins and Pt(IV) complexes</i>	73
3.1. Introduction	75

3.1.1.	Flavins	75
3.1.2.	Platinum complexes	78
3.1.3.	Cysteines chemistry of CTPR scaffold functionalisation	82
3.2.	Results and Discussion	83
3.2.1	Synthesis of iodoacetamide-functionalised riboflavin	84
3.2.2	Synthesis of maleimide-functionalised riboflavin	93
3.2.3	Synthesis of <i>cis,cis,trans</i> -[Pt(NH ₃) ₂ (Cl) ₂ (O ₂ CCH ₂ CH ₂ CO ₂ H) ₂]	95
3.2.4	Synthesis of <i>cis,cis,trans</i> -[Pt(NH ₃) ₂ (Cl) ₂ (OCOCH ₃)(O ₂ CCH ₂ CH ₂ CO ₂ H)] and its NHS-activated derivative	100
3.3.	Conclusions	105
3.4.	Experimental Section	106
<i>Chapter 4: Au-based nanozymes for the activation of Pt(IV) anticancer prodrugs</i>		109
4.1.	Introduction	111
4.2.	Results and Discussion	112
4.2.1	Synthesis and characterisation of nanozyme	113
4.2.2	Interactions studies of nanozyme scaffolds with Pt complexes and FMN	122
4.2.3	Pt(IV) prodrugs photoactivation studies	130
4.3.	Conclusion	136
4.4.	Experimental section	137
<i>Chapter 5: Hybrid protein-based constructs for platinum prodrug photoactivation</i>		139
5.1.	Introduction	141
5.2.	Results and Discussion	145
5.2.1	Bioconjugation procedure and characterization of hybrid protein-based constructs	145
5.2.2	Photostability and photoactivation studies	153
5.2.3	Incubation experiments with glutathione (GSH)	158

5.2.4	<i>In vitro</i> studies	160
5.3.	Conclusions	165
5.4.	Experimental section	166
<i>Chapter 6: General conclusions and future perspective</i>		175
<i>References</i>		181
<i>Acknowledgement</i>		201
<i>List of publications</i>		203

List of figures

Figure 1.1 Structure of platinum(II) anticancer complexes.	3
Figure 1.2 Schematic diagram of the cytotoxic pathway of cisplatin.	4
Figure 1.3 Structures of platinum(IV) prodrugs complexes tested in clinical trials.	6
Figure 1.4 Simplified orbital and excited-state diagram for a d^6 metal complex with octahedral coordination (strong crystal field is assumed).	10
Figure 1.5 Jablonski energy diagram for an excited molecule.	11
Figure 1.6 First generation of Pt(IV) complexes with iodide as leaving ligands..	13
Figure 1.7 Second generation of Pt(IV) complexes.	15
Figure 1.8 Azido-Pt(IV) anticancer agents functionalised with targeting ligands.	16
Figure 1.9 Schematic representation of the self-assembly of Pt-DA complex functionalised with G_4K^+ borate hydrogels.	17
Figure 1.10 Chemical structures of riboflavin (Rf), flavin mononucleotide (FMN) and flavin adenine dinucleotide (FAD).	20
Figure 1.11 Redox and acid-base equilibria of flavins.	21
Figure 1.12 Photodegradation products of riboflavin in presence of light.	23
Figure 1.13 Visible light-mediated cyclisation of thiobenzanilides.	24
Figure 1.14 Direct cyclisation photocatalytic synthesis of benzocoumarins via (-)-riboflavin-mediated electron transfer.	24
Figure 1.15 Decarboxylative cyanation of carboxylic acids.	25
Figure 1.16 ERED-catalysed stereoselective cyclisation of α -chloroamide.	26
Figure 1.17 Illustration of nanoparticles scale of different objects.	26
Figure 1.18 Construction of Pt-DNA-Au NPs developed by dhar et al.	30
Figure 1.19 Schematic drawing of the chemical structure of AuNP-BBN-Pt nanoparticles design by Paulo and co-workers.	32
Figure 1.20 Primary, secondary, tertiary, and quaternary structure of a protein.	33
Figure 1.21 Structures of the 20 amino acids, classified by the charge of their side chains.	34
Figure 1.22 Representation of repeat protein scaffold.	36

Figure 1.23 Ribbon representation of a single consensus tetratricopeptide repeat (CTPR) unit, in which the a helix is colored in green and the b helix in orange.	38
Figure 2.1 (a) Copper-catalysed alkyne azide cycloaddition (CuAAC) from sharpless and meldal work. (b) Ruthenium-catalysed deallyloxylation from meggers and collaborators work.	51
Figure 2.2 Ruthenium catalyst structure employed by Meggers and co-workers.	52
Figure 2.3 Catalytic deprotection of dialloc protected DAPI catalysed by RuCp*(COD)Cl complex.	53
Figure 2.4 Bioorthogonal deprotection of Ayba group via Au-catalysed cyclisation and release of a secondary amine containing a drug developed by Tanaka group.	55
Figure 2.5 Ruthenium-catalysed deallyloxylation reaction and palladium-catalysed prodrug activation developed by Rotello's group.	57
Figure 2.6 Molecular structures of pH switchable and control ligands on gold nanoparticles (AuNPs) for the nanozyme developed by Rotello's group.	58
Figure 2.7 Scheme for the synthesis and nanoencapsulation of PdCl ₂ (TFP) ₂ into PLGA-PEG nanoparticles.	59
Figure 2.8 Chemical structures of caged MMAE (Alloc-SIL-C16-MMAE) and DOX (Alloc-SIL-C16-DOX).	60
Figure 2.9 Intracellular Pd-exomes-mediated conversion of the prodrug to the clinically approved HDAC inhibitor, panabinstat.	62
Figure 2.10 5-fluorouracil and O-alkyl panobinostat prodrugs employed in Unciti-Broceta works reported in 2022 and 2021.	63
Figure 2.11 Photocatalytic activation of cisplatin from Pt(IV) prodrug under blue light irradiation (460 nm).	65
Figure 2.12 Chemical structures of: Rf, FMN, and FAD. Flavoproteins structures of: minisog (pbd id: 6gpu), nox (pdb id: 1nox), gox (pdb id: 1cf3) and gr (pdb id: 2hqm).	65
Figure 2.13 Structures of flavin derivatives and flavoprotein (catalysts) and of Pt(IV) prodrugs (substrates) used in Gurruchaga work.	66

- Figure 2.14** Photocatalytic reaction for the Pt(IV) prodrug activation promoted by miniSOG, under blue light irradiation and in presence of nadh as electron donor. 67
- Figure 2.15** Flavin-catalysed generation of cisplatin (Pt(II) complex) from a Pt(IV) prodrug precursor inside diethylaminoethyl agarose microbeads (AGM). 68
- Figure 2.16** Mechanism of the photocatalytic activation of Pt(IV) prodrugs by flavins (*r* = ribityl; *r'* = adenine dinucleotide) and the two Pt(IV) prodrug complexes studied. 69
- Figure 2.17** Representation of the photocatalytic conversion of Pt(IV) prodrugs to their active Pt(II) drug (oxaliplatin) by a Ru(II) photocatalyst with simultaneous $^1\text{O}_2$ generation. 70
- Figure 2.18** Schematic representations of: mechanism of the photoactivation of Pt(IV) prodrug used for the experiments performed in this thesis; supramolecular nanozyme developed in Chapter 4 and multifunctional hybrid constructed reported in Chapter 5. 72
- Figure 3.1** The three most common oxidation states of the isoalloxazine heterocycle. 75
- Figure 3.2** Structures of isoalloxazine moiety with the five positions for flavin modifications. 76
- Figure 3.3** Oxidation reactions of Pt(II) complex in presence of chlorine and hydrogen peroxide in water. 79
- Figure 3.4** Oxidation reaction of Pt(II) complex in presence of hydrogen peroxide in alcohol. 79
- Figure 3.5** Oxidation reactions of Pt(II)(cbdc)(dpda) (cbdc=1,1-cyclobutanedicarboxylate, dpda = 2,2-dimethyl-1,3-propanediamine) in presence of hydrogen peroxide and acetic acid with *cis*-[Pt(IV)(O₂CCH₃)₂(cbdc)(dpda)] as product and in presence of hydron peroxide and acetic anhydride (with a small amount of acetic acid) with *trans*-[Pt(IV)(O₂CCH₃)₂(cbdc)(dpda)] as product. 80
- Figure 3.6** Oxidation reactions of Pt(II) complex in presence of anhydrides in organic solvents. 82

Figure 3.7 Complete synthesis scheme for the iodoacetamide-functionalised riboflavin (Rf-IA).	85
Figure 3.8 Chemical structure of the intermediate I for the synthesis of Rf-IA (step 1), with the letter code used for the assignment in the $^1\text{H-NMR}$.	86
Figure 3.9 $^1\text{H-NMR}$ spectrum of I (Figure 3.8) in CDCl_3 .	87
Figure 3.10 Chemical structure of the intermediate II for the synthesis of Rf-IA (step 2), with the letter code used for the assignment in the $^1\text{H-NMR}$.	87
Figure 3.11 $^1\text{H-NMR}$ spectrum of II (Figure 3.10) in CDCl_3 .	88
Figure 3.12 Chemical structure of the intermediate III for the synthesis of Rf-IA (step 3), with the letter code used for the assignment in the $^1\text{H-NMR}$.	89
Figure 3.13 $^1\text{H-NMR}$ spectrum of III (Figure 3.12) in CD_3OD .	90
Figure 3.14 ESI-MS spectrum of III (Figure 3.12).	90
Figure 3.15 Chemical structure of the final product Rf-IA (step 4), with the letter code used for the assignment in the $^1\text{H-NMR}$ and $^{13}\text{C-NMR}$.	91
Figure 3.16 $^1\text{H-NMR}$ spectrum of Rf-IA (Figure 3.15) in CD_3OD .	92
Figure 3.17 $^{13}\text{C-NMR}$ spectrum Rf-IA (Figure 3.15) in CD_3OD .	92
Figure 3.18 ESI-MS spectrum of Rf-IA (Figure 3.15).	93
Figure 3.19 UV-Vis of Rf-IA in water.	93
Figure 3.20 Complete synthesis scheme for the maleimide-functionalised riboflavin (Rf-mal).	94
Figure 3.21 Chemical structure of the final product Rf-mal (step 4), with the letter code used for the assignment in the $^1\text{H-NMR}$ and $^{13}\text{C-NMR}$.	94
Figure 3.22 $^1\text{H-NMR}$ spectrum of Rf-mal (Figure 3.21) in CD_3OD .	95
Figure 3.23 Synthetic procedure for the preparation of Pt1 .	96
Figure 3.24 Reaction steps of the synthesis of cisplatin for the final product Pt1 (step 1).	96
Figure 3.25 Chemical structure of the intermediate IV for the synthesis of Pt1 (step 2).	97
Figure 3.26 $^1\text{H-NMR}$ spectrum of IV (Figure 3.25) in $(\text{CD}_3)_2\text{SO}$.	98
Figure 3.27 Chemical structure of the final product Pt1 (step 3), with the letter code used for the assignment in the $^1\text{H-NMR}$.	98

Figure 3.28 $^1\text{H-NMR}$ spectrum of Pt1 (Figure 3.27) in D_2O .	99
Figure 3.29 ESI-MS spectrum of Pt1 (Figure 3.27).	99
Figure 3.30 Synthetic procedure for the preparation of Pt2 and Pt2-NHS .	100
Figure 3.31 Chemical structure of the intermediate V (step 2), with the letter code used for the assignation in the $^1\text{H-NMR}$.	100
Figure 3.32 $^1\text{H-NMR}$ spectrum of V (Figure 3.31) in $(\text{CD}_3)_2\text{SO}$.	101
Figure 3.33 Chemical structure of the final product Pt2 (step 3), with the letter code used for the assignation in the $^1\text{h-nmr}$.	102
Figure 3.34 $^1\text{H-NMR}$ spectrum of Pt2 (Figure 3.33) in $(\text{CD}_3)_2\text{SO}$.	103
Figure 3.35 ESI-MS spectrum of Pt2 (Figure 3.33).	103
Figure 3.36 Chemical structure of the final activated product Pt2-NHS (step 3), with the letter code used for the assignation in the $^1\text{H-NMR}$.	104
Figure 3.37 $^1\text{H-NMR}$ spectrum of Pt2-NHS (Figure 3.36) in $(\text{CD}_3)_2\text{SO}$.	105
Figure 3.38 ESI-MS spectrum of Pt2-NHS (Figure 3.36).	105
Figure 4.1 Flavin-mediated photocatalytic activation of Pt(IV) prodrugs under blue light irradiation.	112
Figure 4.2 Complete synthesis scheme for the thiol ligands, TACN-C11-SH .	114
Figure 4.3 Chemical structure of the intermediate VI for the synthesis of TACN-C11-SH (step 1), with the letter code used for the assignation in the $^1\text{H-NMR}$.	114
Figure 4.4 $^1\text{H-NMR}$ spectrum of VI (figure 4.3) in CDCl_3 .	115
Figure 4.5 Chemical structure of the intermediate VII for the synthesis of TACN-C11-SH (step 2), with the letter code used for the assignation in the $^1\text{H-NMR}$.	116
Figure 4.6 $^1\text{H-NMR}$ spectrum of VII (figure 4.5) in CD_3OD .	117
Figure 4.7 Chemical structure of the intermediate VIII for the synthesis of TACN-C11-SH (step 3), with the letter code used for the assignation in the $^1\text{H-NMR}$.	117
Figure 4.8 $^1\text{H-NMR}$ spectrum of VIII (Figure 4.7) in CDCl_3 .	118
Figure 4.9 Chemical structure of the final product TACN-C11-SH (step 4), with the letter code used for the assignation in the $^1\text{H-NMR}$ and $^{13}\text{C-NMR}$.	118
Figure 4.10 $^1\text{H-NMR}$ spectrum of TACN-C11-SH (Figure 4.9) in CD_3OD .	119
Figure 4.11 $^{13}\text{C-NMR}$ spectrum of TACN-C11-SH (Figure 4.9) in CD_3OD .	120

Figure 4.12 Schematic representation of the synthesis procedure for gold nanoparticles.	120
Figure 4.13 Characterisation of TACN AuNPs: (a) ¹ H-NMR in CD ₃ OD; (b) UV-Vis in CH ₃ OH (0.2 mm); (d) TEM micrograph; (e) Size distribution histogram (number of particles > 250); (f) TGA thermal curve.	122
Figure 4.14 Type of interactions between TACN AuNPs and FMN, and TACN AuNPs and Pt1.	123
Figure 4.15 (a) Detail of ¹ H-NMR spectrum of Pt1 (500 μm) in the absence and presence of TACN AuNPs 100 μm and FMN 25 μm. (b) Detail of ¹ H-NMR spectrum of Pt1 (3 mm) in the presence of TACN AuNPs (1 mm) and of NOE pumping spectrum recorded in the same conditions.	125
Figure 4.16 DOSY spectra of Pt1 (500 μm) in D ₂ O in the absence (a) or in the presence of 100 μm TACN AuNPs and 25 μm FMN (b) or AuNPs 1 mm.	126
Figure 4.17 Absorption and fluorescence spectra of riboflavin in water.	128
Figure 4.18 FMN fluorescence titrations (a) before and (b-d) after inner filter effect corrections for the FMN alone and in the presence of TACN AuNPs (100 μm), with or without addition of 1 equivalent of Zn(NO ₃) ₂ .	129
Figure 4.19 Photoreduction scheme under blue light irradiation (460 nm, 5.30 mw/cm ²) for Pt1. The products of the reaction are cisplatin and two molecules of succinate.	130
Figure 4.20 (a) Photocatalytic activation of Pt1 by FMN (grey dashed line), FMN@TACN AuNPs (green solid line) and FMN@Zn-TACN AuNPs (blue solid line). (b) photocatalytic activation of Pt1 by tacn AuNPs (green solid line) and Zn-TACN AuNPs (blue solid line).	132
Figure 4.21 Photocatalytic activation of Pt1 by free FMN in MES buffer (10% D ₂ O).	132
Figure 4.22 Photocatalytic activation of Pt1 by FMN@TACN AuNPs without (a) or with (b) Zn(NO ₃) ₂ in MES buffer (10% D ₂ O).	133
Figure 4.23 Photocatalytic activation of Pt1 by TACN AuNPs without (a) or with (b) Zn(NO ₃) ₂ in MES buffer (10% D ₂ O).	133
Figure 4.24 Photobleaching of FMN@TACN AuNPs and free FMN.	134

Figure 4.25 Dark stability of Pt2 in the presence of FMN@TACN AuNPs (a) without or (b) with $Zn(NO_3)_2$, and in presence of TACN AuNPs (c) without or (d) with $Zn(NO_3)_2$ in MES buffer (10% D_2O).	134
Figure 4.26 (a) TOF values (min^{-1}) and (b) TON values reached after 32 minutes of irradiation for FMN@TACN AuNPs , FMN@Zn-TACN AuNPs , FMN , TACN AuNPs and Zn-TACN AuNPs in MES buffer (calculated in the range of 15-45% conversion).	135
Figure 5.1 Platinum prodrug structure.	143
Figure 5.2 Activation pathways from prodrug form, in red (inactive), to the drug one, in green (active). Cisplatin was chosen as reference drug structure.	144
Figure 5.3 Consensus tetratricopeptide repeat (CTPR) protein single modules.	146
Figure 5.4 Bioconjugation scheme for the hybrids studied in this chapter.	147
Figure 5.5 UV-Vis spectra of Rf-IA molecule in PBS buffer (140 mM NaCl, 50 mM phosphate buffer pH 8.5), over 24 hours.	148
Figure 5.6 Characterization of the CTPR_n-Rf conjugate.	149
Figure 5.7 Characterization of the CTPR_n-Rf-Pt2 hybrid.	152
Figure 5.8 Photostability of Rf , FMN , Rf-IA and CTPR_n-Rf in (a-f) PBS (140 mM NaCl, 50 mm phosphate buffer pH 7.4) and (g-n) MES buffer (18 mM, pH 6.4) under blue light irradiation (460 nm, 3.5 mw/cm^2).	154
Figure 5.9 Photoreduction scheme under blue light irradiation (460 nm, 3.5 mw/cm^2) for Pt1 . The products of the reaction are cisplatin and two molecules of succinate.	155
Figure 5.10 Photocatalytic activation of free Pt1 by FMn (grey dashed), CTPR4-Rf (green), CTPR6-Rf (blue) and CTPR8-Rf (purple).	156
Figure 5.11 Photocatalytic activation under blue light (460 nm) of Pt1 by (a) free FMN , (b) CTPR4-Rf , (c) CTPR6-Rf , (d) CTPR8-Rf in MES buffer (10% D_2O).	156
Figure 5.12 Dark stability of Pt1 in the presence of FMN and the protein-catalyst bioconjugate systems in MES buffer (10% D_2O): (a) FMN , (b) CTPR4-Rf , (c) CTPR6-Rf , (d) CTPR8-Rf .	157
Figure 5.13 Photocatalytic activation under blue light (460 nm) of Pt1 in MES buffer (10% D_2O).	157

Figure 5.14 Photostability of **CTPR6-Rf-Pt2**. 158

Figure 5.15 (a) Dark stability of cisplatin (50 μM) co-incubated with GSH (500 μM) in water, monitored at 0, 6 h and 24 h; (b) dark stability of **Pt2** (50 μM) co-incubated with GSH (500 μM), monitored at 0, 6 h and 24 h; (c) UPLC chromatograms for **CTPR6-Rf-Pt2** (50 μM) co-incubated with gsh (500 μM) at 0, 6 h and 24 h did not show any major MS peak corresponding to free pt species. 160

Figure 5.16 (a) Dose response curve of cisplatin and **Pt2** complex in PANC-1 cancer cell line. (b) Cell viability percentage in PANC-1 cancer cells following treatment with **CTPR6** in dark condition. (c) Fluorescence resorufin (reduced form of resazurin) intensity of non-treated PANC-1 cancer cells in dark condition (dark grey) and under light on/off (light gray). The cells were irradiated for 45 min total, with blue light (3.5 mW/cm^2). (d) Fluorescence resorufin (reduced form of resazurin) intensity of non-treated PANC-1 cancer cells with light on/off (light grey) and with light on (medium grey). 162

Figure 5.17 Procedure scheme for cell viability experiments. 163

Figure 5.18 (a) Percentage cell viability in PANC-1 cancer cells following treatment with cisplatin (grey dashed line), **CTPR6-Rf-Pt2** (solid red line) and **CTPR6-Rf** + free **Pt2** (solid light blue line) under light irradiation (45 min, light on/off regime, 460 nm, 3.5 mW/cm^2). (b) Percentage cell viability in PANC-1 cancer cells following treatment with cisplatin (grey dashed line), **CTPR6-Rf-Pt2** (solid red line) and **CTPR6-Rf** + free **Pt2** (solid light blue line) in the dark. 163

Figure 5.19 (a) Percentage cell viability in PANC-1 cancer cells following treatment with cisplatin (dashed line), **CTPR6-Pt2** (violet) and **CTPR6-Rf** (green) systems under light irradiation (45 min, on/off regime 460 nm, 3.5 mW/cm^2). (b) Percentage cell viability in PANC-1 cancer cells following treatment with cisplatin (dashed line), **CTPR6-Pt2** (violet) and **CTPR6-Rf** (green) systems in dark conditions. The concentrations reported refer to drug/prodrug. 164

Figure 5.20 UV-Vis spectra of conjugated systems: (a) **CTPR4-Rf**, (b) **CTPR6-Rf** and (c) **ctpr8-Rf** in PBS buffer (140 mM NaCl, 50 mM phosphate buffer pH 8.5) after the elimination of free functionalized riboflavin. 172

Resumen

Los avances en catálisis bio-ortogonal están generando nuevas oportunidades para llevar a cabo reacciones quimio-selectivas en entornos biológicos complejos, con aplicaciones en biomedicina y bio-imagen. Estas transformaciones pueden ocurrir sin interferir con las funciones biológicas. La amplificación de señales químicas y la selectividad son características intrínsecas de la catálisis, y se pueden aprovechar para controlar los efectos de los medicamentos en los sistemas biológicos.

Sin embargo, la selectividad no es el único problema relacionado con el uso de los medicamentos, ya que su uso puede causar efectos secundarios durante los tratamientos. Las reacciones secundarias de los medicamentos pueden dar lugar a efectos inespecíficos, los cuales pueden reducir su eficacia. La combinación de bio-ortogonalidad y catálisis puede ofrecer ventajas para el diseño de nuevas estrategias de activación de profármacos, evitando así los efectos secundarios de los fármacos. Un ejemplo para el cual es particularmente importante es para los fármacos derivados de Pt(II), como cisplatino o carboplatino, que pueden causar disfunción renal, neurotoxicidad, náuseas y vómitos. Por lo tanto, en el área de la química inorgánica medicinal, los investigadores están realizando esfuerzos en el diseñar profármacos de Pt(IV) para superar estas desventajas. Los profármacos de platino son las formas inactivas de los medicamentos y se caracterizan por ser compuestos inertes que pueden activarse dentro de las células cancerosas, reduciendo de esta manera la exposición de las células sanas al fármaco.

Además, en los últimos años, se ha investigado el estudio de reacciones bio-ortogonales con moléculas que pueden imitar el comportamiento de las enzimas para la activación de sustratos en entornos biológicos. Las transformaciones bio-ortogonales se realizan en presencia de complejos de metales como catalizadores. Sin embargo, se han desarrollado nuevos métodos que utilizan los agentes metálicos como sustratos, mientras moléculas orgánicas y otros complejos de metales actúan como catalizadores. Un ejemplo interesante de una molécula orgánica utilizada en estos procesos foto-catalítico, son las flavinas.

Los profármacos se pueden combinar con moléculas inorgánicas o biológicas, como por ejemplo nanomateriales como nanopartículas, o biomoléculas como proteínas, para obtener sistemas híbridos para aplicaciones biomédicas. De esta manera, es posible lograr un sistema más controlado donde los profármacos se inmovilizan en los nanomateriales.

En las últimas décadas, el uso de estos nanomateriales para aplicaciones biomédicas ha sido ampliamente investigado. En particular, las nanopartículas de oro (AuNPs) han sido utilizadas para fines biomédicos debido a su excelente biocompatibilidad, mínima toxicidad y baja inmunogenicidad.

Diferentes grupos han producido nanoenzimas para la activación de fármacos anticancerígenos atrapando los catalizadores basados en metales de transición en AuNPs. Incorporando estos fármacos en las NP, es posible resolver limitaciones para su aplicación en terapia relacionadas con la biocompatibilidad, la estabilidad y la baja solubilidad en agua de estos complejos metálicos. Además, las nanoenzimas pueden aumentar la solubilidad en agua y proteger los catalizadores de metales de los entornos biológicos.

Adicionalmente, no solo el agente anticancerígeno puede ser integrado en estas plataformas inorgánicas o biológicas, sino que también una variedad de elementos funcionales puede ser incorporados según la aplicación. Por ejemplo, en el campo de la foto-activación, la adición del catalizador a estas plataformas podría aumentar la velocidad de reacción de la conversión del profármaco a su forma activa. Con ambos, el profármaco de metal y el catalizador, integrados en una plataforma seleccionada, se consigue localizar a los elementos individuales espacialmente cerca, lo que podría mejorar la eficiencia del sistema multicomponente.

Las proteínas son moléculas complejas compuestas de cadenas de aminoácidos que se pliegan en estructuras tridimensionales. Estas realizan una amplia gama de funciones dentro de los organismos vivos, como catalizar reacciones bioquímicas, transmitir señales entre células y proporcionar soporte estructural. Las proteínas son biomoléculas versátiles, en las cuales la estructura y función están estrechamente relacionadas. Se consideran candidatas óptimas para construir medicamentos biológicos y herramientas de diagnóstico, debido a su

naturaleza adaptable, y pueden ser usadas en construcciones híbridas multifuncionales. Las proteínas sirven como elemento central en estos híbridos, y su ingeniería ha demostrado un potencial excepcional para crear nuevos sistemas funcionales aplicables en diversos campos como la imagen biomédica, la biodetección, la bioelectrónica y la catálisis, entre otros. En particular, las proteínas de repetición, con su estructura modular, son plataformas ideales para la ingeniería de proteínas. Entre ellas, las proteínas CTPR (del inglés *Consensus Tetratricopeptide Repeat*), compuestas por repeticiones de un módulo hélice-giro-hélice de 34 aminoácidos, se han utilizado con éxito en el diseño de híbridos proteína-nanomaterial para diversas aplicaciones. Solo ocho residuos conservados desempeñan un papel clave en el plegamiento de la CTPR, dando la posibilidad de introducir mutaciones en el resto de las posiciones. Además, las CTPR han demostrado ser plataformas robustas para generar sistemas complejos a través de la organización de otros elementos funcionales, como nanopartículas de oro, nanoclusters metálicos, nanoclusters con actividad redox (NCs), nanotubos de carbono, porfirinas, complejos metálicos y otros.

En esta tesis, los dos primeros capítulos presentan una descripción general del estado del arte de este proyecto de investigación basado en el diseño de estructuras híbridas para la foto-activación bio-ortogonal y la catálisis de agentes anticancerígenos. Los tres capítulos siguientes detallan la metodología y los resultados del trabajo experimental.

El **primer capítulo** ofrece una visión general de los principales elementos estudiados en esta tesis. El capítulo comienza con una introducción a los agentes anticancerígenos a base de platino y el uso de estos compuestos metálicos en medicina, describiendo los conceptos de medicamentos y profármacos, así como los métodos de foto-activación. La sección sobre complejos de platino concluye con una discusión sobre las posibles estrategias para la vehiculización de profármacos foto-activables de Pt(IV). Posteriormente, el capítulo incluye una sección sobre flavinas, describiendo sus propiedades fotoquímicas, térmicas y químicas, con especial énfasis en los procesos foto-catalíticos. La última sección del Capítulo 1 está dedicada a las plataformas inorgánicas y biológicas empleadas para la vehiculización de fármacos, centrándose principalmente en los utilizados en esta tesis: nanopartículas de oro y proteínas

de repetición. Para cada sección, se ilustran algunos de los ejemplos más interesantes descritos en la literatura.

El **segundo capítulo** ilustra las reacciones de catálisis bio-ortogonales que implican complejos de metales. El enfoque principal de este capítulo es resaltar la doble función de los complejos de metales de transición en este tipo de reacciones. La discusión se estructura en dos secciones: la catálisis bio-ortogonal con complejos metálicos como catalizadores, y la fotocatálisis bio-ortogonal con complejos metálicos como sustratos. En particular, la segunda parte del Capítulo 2 se centra en los pro-fármacos de platino en forma de complejos metálicos. Los pro-fármacos de platino pueden activarse mediante varios mecanismos, incluida la activación enzimática, los cambios de pH, el potencial redox o por factores externos como la luz. En este capítulo, se reporta la activación de los pro-fármacos de Pt(IV) por un factor externo, luz azul. De hecho, nuestro grupo ha reportado recientemente diferentes estudios sobre la combinación de la química bio-ortogonal y las reacciones de catálisis. El método innovador en estos estudios está centrado en el uso del complejo de platino como sustrato de la reacción, mientras que el fotocatalizador está asociado con las moléculas de flavinas.

En el **tercer capítulo** se presentan los procedimientos de las reacciones orgánicas e inorgánicas, utilizados para la preparación de los compuestos y estructuras empleadas en la tesis. Se reporta en detalle cada paso de las síntesis y la caracterización del fotocatalizador y de los sustratos empleados en los estudios de esta tesis. Para el fotocatalizador, se desarrollaron dos riboflavinas modificadas con la introducción de dos grupos funcionales. El propósito de la incorporación de estos grupos era obtener una molécula que pudiera unirse covalentemente a la plataforma de proteínas (CTPR) a través de una reacción con los aminoácidos del CTPR y el grupo funcional de la riboflavina. Para los sustratos metálicos, se sintetizaron dos complejos de platino. Estos compuestos son ambos una forma de profármaco de cisplatino (fármaco) y difieren en sus ligandos axiales.

El **cuarto capítulo**, investiga la conversión foto-catalítica, bajo irradiación de luz azul, del profármaco de Pt en su forma activa en un modelo de nanozima. El flavín mononucleótido, las nanopartículas de oro decoradas con un C11-tiol que

lleva un grupo de cabeza de 1,4,7-triazaciclononano, y el complejo de platino fueron seleccionados respectivamente como fotocatalizadores, nanozima y sustrato. Se realizaron experimentos de fluorescencia y estudios de RMN (DOSY y NOE-*pumping*) para investigar la interacción entre la plataforma de nanozima con el fotocatalizador y el sustrato, respectivamente. Luego, se investigó el comportamiento catalítico de las nanozimas a través de experimentos de ^1H -RMN. Los resultados obtenidos mostraron un aumento en la velocidad de conversión del sustrato debido a la presencia de las nanopartículas de oro.

En el **quinto capítulo** se discute el uso de híbridos basados en proteínas para controlar el transporte y la foto-activación de los pro-fármacos de platino, mediados por riboflavina. Aquí se describe el diseño de proteínas CTPR para unir covalentemente tanto el fotocatalizador de flavina como el complejo de Pt(IV), empleando diferentes CTPRs. Los resultados obtenidos muestran que uno de los tres híbridos analizados fue el mejor para la activación de pro-fármacos de platino bajo irradiación de luz azul, con una eficiencia comparable al sistema de referencia (sin proteína). Posteriormente, se realizaron estudios de viabilidad celular *in vitro* en células cancerosas de páncreas PANC-1 para este constructo. Los resultados muestran que nuestro sistema tiene una capacidad de eliminación casi análoga a la del cisplatino (control positivo).

Los estudios realizados en esta tesis aportan evidencia del uso potencial de nanopartículas de oro y proteínas repetitivas diseñadas como plataformas efectivas para regular la biodistribución de agentes anticancerígenos de platino y controlar su activación. Además, los resultados obtenidos demuestran que la presencia de estas estructuras no obstaculiza la activación fotoquímica de los pro-fármacos metálicos tanto en entornos simples como en células cancerosas.

Summary

Advances in biorthogonal catalysis are creating new opportunities to perform chemoselective transformations in complex biological environments, with applications in biomedicine and bioimaging. These transformations can occur without interfering with normal biological functions. Amplification of chemical signals and selectivity are intrinsic features of catalysis, and they can be exploited to control the effects of drugs in biological systems.

However, selectivity is not the only problem related to the use of drugs, as their use in treatments can cause side effects. Side reactions of drugs can lead to off-target effects, which could reduce their efficacy. Combining bioorthogonal and catalysis concepts can offer advantages for the design of new prodrug activation strategies that can overcome the drug side effects. For example, this is particularly important for Pt(II) drugs, such as cisplatin or carboplatin, which can cause renal dysfunction, neurotoxicity, nausea, and vomiting. Hence, in the area of medicinal inorganic chemistry, researchers are putting efforts in designing Pt(IV) prodrugs to overcome these drawbacks. Platinum prodrugs are the inactive forms of the drugs and are characterised by being a more inert compounds that can be activated within cancer cells, reducing, in this way, the exposure of healthy cells to the drug.

Furthermore, in recent years, the study of biorthogonal reactions with molecules that can mimic the behavior of the enzymes has been investigated for substrate activation in biological environments. Usually, biorthogonal transformations are conducted in the presence of metal complexes as catalyst. However, new approaches have been developed that employ metal-based agents as substrates, while the role of the catalyst is attributed to organic molecules or other metal complex. An interesting example of an organic molecule used in photocatalytic process is flavins.

The prodrugs can be combined with inorganic or biological scaffolds, such as nanomaterials like nanoparticles or biomolecules like proteins to obtain hybrid systems for biomedical application. In this way, it is possible to achieve a more controlled system where the prodrugs are localized on the scaffold.

In recent decades, the use of nanomaterials for biomedical applications has been extensively investigated. In particular, gold nanoparticles (AuNPs) have been widely utilized for biomedical purposes due to their excellent biocompatibility, minimal toxicity, and low immunogenicity.

Furthermore, different groups have demonstrated the realization of nanozymes for the activation of anticancer drugs by entrapping transition metal catalysts on a AuNPs scaffold. By incorporating them on the NP scaffold, limitations related to biocompatibility, stability, and low water solubility of the metal complexes can potentially be solved. In addition, nanozymes can increase water solubility as well as protect the metal catalysts from biological environments.

Moreover, not only the anticancer agent can be loaded onto these inorganic or biological platforms, but a variety of functional elements can be incorporated depending on the intended application. For example, in the photoactivation field, the addition of the catalyst to these scaffolds could increase the reaction rate of the prodrug conversion to its active form. With both metal prodrug and catalyst loaded onto the desired template, the single elements are kept closer, which could enhance the efficiency of the structure.

Proteins are complex molecules made up of chains of amino acids that fold into intricate three-dimensional structures. They perform a wide range of functions within living organisms, such as catalysing biochemical reactions, transmitting signals between cells, and providing structural support. Thus, proteins are versatile biomolecules and their structures and functions are closely connected. They are considered optimal contenders for constructing biological medicines and diagnostic tools, due to their adaptable nature, and can be employed in multifunctional hybrid constructs. Proteins serve as the central element in these hybrids, and their design and engineering have shown exceptional potential for creating new functional systems for diverse fields like imaging, sensing, conductive materials, and catalysis. In particular, repeat proteins, with their repeated modular structure, are ideal scaffolds for engineering. Among repeat proteins, consensus tetratricopeptide repeat proteins (CTPRs) are a helix-turn-helix motif of 34 amino acids that have been successfully employed in designing of protein-nanomaterial hybrids for various applications. Only eight residues play a key role in defining the CTPR fold, leaving ample room for introducing

mutations. Moreover, CTPRs have proven to be robust platforms for generating constructs that facilitate the templating of gold nanoparticles, metallic nanoclusters, redox-active nanoclusters (NCs), carbon nanotubes, porphyrins, metal complexes, and others.

In the thesis, the first two Chapters present an overview of the state of the art of this research project based on the design of hybrid structure for bioorthogonal photoactivation and catalysis of anticancer agents. The subsequent three Chapters detail the methodology and results of the experimental work.

The **first chapter** provides an overview of the main elements studied in this thesis. The Chapter begins an introduction to platinum anticancer agents and the use of these metal-based compounds in medicine, covering concepts of drug and prodrug and photoactivation approaches. The section on platinum complex concludes with a discussion of possible strategies for the delivery of the Pt(IV) photoactivatable prodrugs. The Chapter then proceeds to the flavins section, describing their photo, thermal and chemical properties, with a particular emphasis on the photocatalytic processes. The final section of Chapter 1 is dedicated to inorganic and biological scaffolds employed for delivery, with a focus on the ones used in the thesis: gold nanoparticles and repeat proteins. For each section, some of the most interesting examples reported in literature are described.

The **second Chapter** illustrates bioorthogonal catalysis reactions involving metal-based complexes. The main focus of this Chapter is to highlight the dual role of transition-metal complexes in this type of reaction. The discussion is structured into two sections: bioorthogonal catalysis with metal complexes as catalysts, and bioorthogonal photocatalysis with metal complexes as substrates. In particular, the second part of Chapter 2 focuses on platinum prodrugs in the form of the metal complexes. Platinum prodrugs can be activated through various mechanisms, including enzymatic activation, changes in pH, redox potential or by external factors such as light. In this Chapter, the activation of Pt(IV) prodrugs by external factor, blue light, is reported. Indeed, our group recently reported different studies about the combination of bioorthogonal chemistry and catalysis reactions. The innovation approach in these studies is

connected to the use of platinum complex as substrate of the reaction, while the photocatalyst is associated to flavins molecules.

In the **third Chapter**, organic and inorganic reactions procedures used for the preparations of the compounds and structure employed un the thesis, are presented. The synthesis steps and the characterization of the photocatalyst and of the substrates employed for the studies in this thesis are presented in this Chapter. For the photocatalyst, two modified riboflavins were developed with the introduction of two functional groups. The purpose of the incorporation of these groups was to obtain a molecule that could be covalently bound to the protein scaffold (CTPR) through a reaction with the amino acids of the CTPR and the functional group of the riboflavin. For the metal substrates, two platinum complexes were synthesised. These compounds are both a prodrug form of cisplatin (drug) and differed for their axial ligands.

The **fourth Chapter**, investigates the photocatalytic conversion, under blue light irradiation, of Pt prodrug into its active form in nanozymes model. Riboflavin phosphate, Au nanoparticles decorated with a C11-thiol bearing a 1,4,7-triazacyclononane headgroup, and the platinum complex were selected respectively as photocatalyst, nanozyme scaffold and substrate. Fluorescence titrations and NMR (DOSY and NOE-pumping) studies were conducted to investigate the interaction between the nanozyme scaffold with the photocatalyst and the substrate, respectively. Then, catalytic performances of the nanozymes were carried out through ^1H -NMR experiments. The results obtained showed an increase in the substrate conversion rate due to the presence of the interacting gold nanoparticles.

In the **fifth Chapter**, the use of protein-based hybrid for controlling the delivery and the photoactivation of platinum prodrugs, mediated by riboflavin, is discussed. Here, the design of CTPR proteins for linking covalently both a flavin photocatalyst and Pt(IV) complexes is described, employing different CTPRs. The results obtained show that one of the three hybrids analysed, was the best in terms of platinum prodrug activation under blue light irradiation, with an efficiency comparable to the reference system (no protein). Later, *in vitro* cell viability studies were conducted on pancreatic PANC-1 cancer cells for this

construct. The results show that our systems has a killing ability almost analogous to the one of cisplatin (positive control).

The studies conducted in this thesis provide evidence for the potential use of gold nanoparticles and engineered repeat proteins as effective templates for regulating the delivery of platinum anticancer agents and controlling their activation. Furthermore, the results obtained, demonstrate that the presence of these scaffolds does not hinder the photocatalytic activation of the metal-based prodrugs in both simple environments and cancer cells.

Chapter 1

Hybrid systems for the activation and delivery of metal-based anticancer drugs: an overview on their components

Chapter 1

1.1. Platinum complexes

1.1.1 Introduction

Metal-based compounds have long been used in the past for the treatment of disease. The ancient Chinese, Egyptians and Assyrians were aware of the importance of employing metal-based compounds in the treatment of illnesses, such as the usage of cinnabar (mercury sulphide) in the cure of ailments. Later, between the 5th and 4th century before Christ, the two Greek philosopher, Empedocles and Aristotle, strengthened the use of metal-based compounds as therapeutic agents. Their approach was supported by the knowledge of the Roman physicians, Pliny and Celsus, on the use of cinnabar for the treatments of trachoma and venereal diseases.¹ However, the limited understanding between therapeutic and toxic doses was the dominant problem.² The history of the use of metal-based compounds changed in 1965, when cisplatin (cis-diamminedichloridoplatinum), a Pt(II) complex, was accidentally discovered by Barnett Rosenberg. He observed that this platinum complex was able to block the cells division in *Escherichia coli*. In 1978, cisplatin was approved by the Food and Drug Administration (FDA) to be used for anticancer treatments.³ During the years, different Pt(II) complexes have been developed aiming at solving the drug resistance and sides effects related to cisplatin. Nowadays, the use of other two platinum complexes, carboplatin and oxaliplatin, have been clinically approved around the world, while other three derivatives just in selected countries (nedaplatin, lobaplatin and heptaplatin) (**Figure 1.1**).⁴

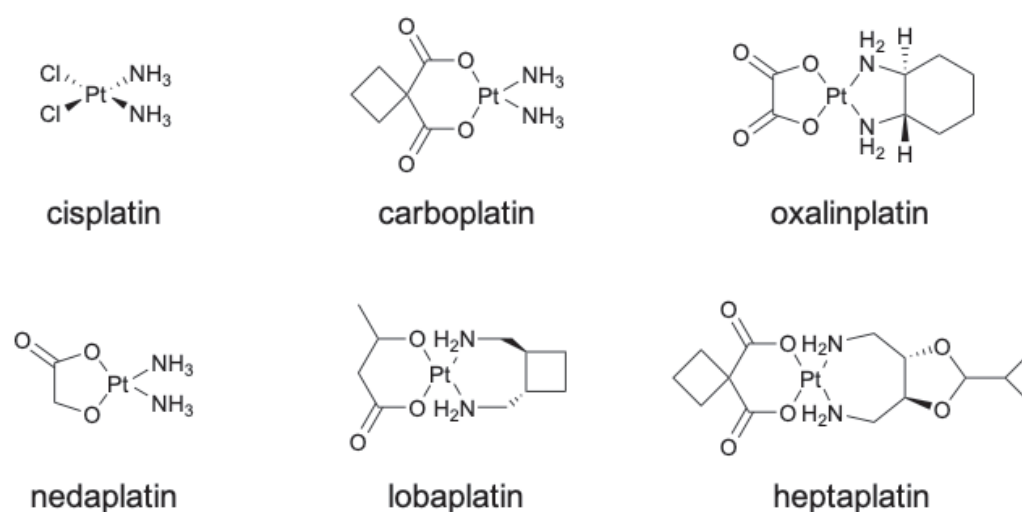


Figure 1.1 Structure of platinum(II) anticancer complexes.

The mechanism of action of cisplatin has been studied extensively.^{5,6,7} Its cytotoxicity has been associated to the binding with the DNA, followed by single-stranded DNA breakage.⁷ When this platinum complex enters into the cytoplasm, its two chloride ligands are replaced by water molecules creating first the mono aquo and then the bis-aquo species of cisplatin.⁷ Both of these complexes are good electrophiles, since H₂O is a better leaving group than Cl⁻, with affinity for sulfhydryl groups on proteins and nitrogen donor atoms on nucleic acids.^{7,8,9} The N7 positions of the imidazole ring of two adjacent guanines is the most common position for the binding of cisplatin in the DNA. A stop in cell division and cell apoptosis are the consequence observed for the formation of the Pt-DNA adducts.^{8,9} It has been found that the prevailing adducts formed by cisplatin with the DNA are 1,2-d(GpG) intrastrand cross-link (G = guanine) and, in a less percentage, 1,2-d(ApG) intrastrand cross-link (A = adenine). Other adducts such as 1,3-intrastrand cross-links and interstrand cross-link are instead minor adducts (**Figure 1.2**).⁶

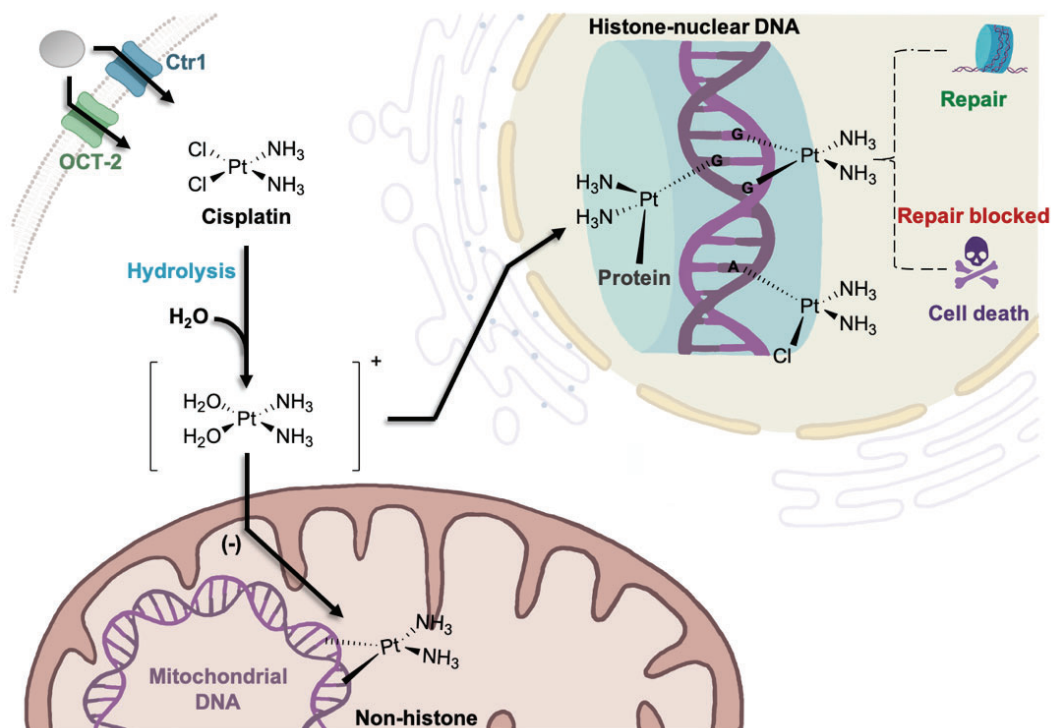


Figure 1.2 Schematic diagram of the cytotoxic pathway of cisplatin. After entering the cell by copper transferase receptor (CTR1) or passive diffusion, cisplatin is activated by the replacement of the two chloride ions with water molecules. The bis-aquo complex binds then the DNA, causing distortion of the double helices with the activation of the programmed cell death.¹⁰ Scheme adapted from ref. 10.

The Pt(II) complexes are characterised by a square planar geometry composed by two non-leaving ligands (L) and two leaving ones (X). For cisplatin, the L groups are nitrogen donors ($-\text{NH}_3$) and are maintained in the DNA-platinum adducts. The Pt-N bonds indeed are kinetically inert and stable thermodynamically. The X groups are characterised by the chloride ligands that are lost by the complex after the internalisation into the cytoplasm.¹¹

This drug is known to be very effective for testicular cancer, but presents some limitation like the lack of effectiveness against other types of cancers, the maximum amount that can be administrated and several toxic side effects.¹² It has been observed that cisplatin causes renal dysfunction, neurotoxicity, nausea and vomiting. To circumvent these problems, changes in the design of the metal complex have been developed during the years working with Pt(IV) complexes that present two additional ligands, called axial ligands. The oxidation state of these complexes is +4 (Pt(IV) complexes) which involves a change in the structure, from a square planar in the case of the drugs (Pt(II) complex) to a six-coordinate octahedral geometry in the second one. Compared to Pt(II), Pt(IV) complexes, so called prodrug, is a more inert complex and thanks to this characteristic some side reactions are avoided before the binding with the DNA and the circulation lifetime is higher.^{9,12,13} Moreover, Pt(IV) are stable enough to be administrated orally and thanks to the axial ligands it is possible to implement into the structure of the complex functional or targeting groups. These modifications can help in the improvement of the pharmacological properties of the prodrugs.¹¹

Since Pt(IV) complexes are mostly inert, they need to be activated to obtain the drug form (active specie). The activation of these complexes can be promoted by internal or external sources. In the first case, biological reductants like ascorbate or glutathione (GSH) are the common cellular reducing agents that reduce Pt(IV) prodrugs into Pt(II) drugs.¹¹ Ascorbate is commonly present in blood plasma with 50-150 μM concentration range, reaching 1 mM inside cells.^{11,14} The reduction of Pt(IV) complex (in the case of the prodrug form of cisplatin) by this reducing agent involves a reductive attack by the ascorbate on the chloride ligands with the formation of a bridge transition state. The transfer of the two electron from the ascorbate to the

Chapter 1

Pt(IV) complex, permits the release of the two chlorides.^{15,16} The typical concentration of glutathione instead, is around 900 μM in blood and above 2 mM inside cells.¹⁷ Differently from ascorbate, GSH reduces Pt(IV) prodrugs via halide bridge electron transfer without the formation of intermediates.^{11,18,19}

Alternatively, the activation of the prodrugs can be promoted by external stimuli such as light, temperature, magnetic field etc.²⁰ In the next section (1.1.2) the activation process of Pt(IV) compounds, promoted by light, is discussed in detail.

Among different Pt(IV) compounds developed along the years, ormaplatin, iproplatin and satraplatin are the most remarkable ones (**Figure 1.3**).

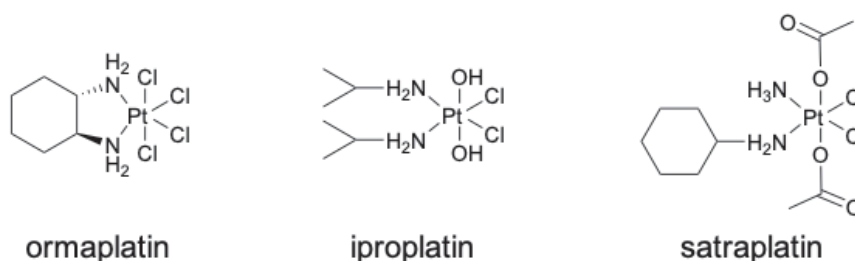


Figure 1.3 Structures of platinum(IV) prodrugs complexes tested in clinical trials.

Ormaplatin, also known as tetraplatin, was the first prodrug complex that reached clinical trials. It undergoes to a rapid reduction to dichloro(trans-1,2-diaminocyclohexane)platinum(II). Two administration approaches of ormaplatin (intravenous and intraperitoneal) and different dosages were tested in Phase I clinical trials showing behaviors similar to cisplatin.^{9,13} Moreover, it showed a significant anti-proliferative activity (the ability of a compound to stop the growth of cells) in models of cisplatin-resistant cancer.²¹ However, Phase II has not been yet announced.^{9,13} Iproplatin is another Pt(IV) complex developed, with two equatorial chloride groups that are cis to one another. As axial ligands instead, iproplatin owns two hydroxide groups. Iproplatin was tested in clinical trials reaching Phase III.¹³ For the Phase II trials, iproplatin was tested in different cancer types: ovarian carcinoma,²² testicular cancer,²³ colorectal carcinoma,²⁴ breast cancer,²⁵ and urothelial cancer.²⁶ Phase III trials were conducted in ovarian cancer patients²⁷ and those with metastatic epidermoid carcinoma of the head and neck.¹³ From these studies, it was concluded that this compound it was not able to achieve the same efficiency of cisplatin and no other trials were

conducted.¹³ Unlike ormaplatin, iproplatin is less prone to the reduction by biological reducing agents, probably due to the presence of the hydroxide axial ligands. This implies a slower deactivation of the complex, allowing an easy distribution throughout the body of the complex.^{9,13} Satraplatin was the first prodrug designed for an oral administration. Its chemical structure is composed by two acetate groups and a cyclohexyl group which increases lipophilicity and allows oral administration.²⁸ From preclinical studies it showed a better toxicity profile than cisplatin and activity in cisplatin-resistant human cancer cell lines. As iproplatin, it arrived to Phase III clinical trials where the treatments of satraplatin and prednisone (a glucocorticoid medication used to suppress the immune system and decrease inflammation) were compared against placebo and prednisone, as second-line therapy for patients who had received a cytotoxic agent, which in some cases was docetaxel.²⁹ Docetaxel is an antimicrotubular agent used in particular for treating breast cancer. This agent principally exerts its cytotoxic activity by promoting and stabilising microtubule assembly and, at the same time, preventing their disassembly. This results in inhibition of normal cell division.³⁰ The study on Phase III showed that the satraplatin/prednisone combinations led to a 36% decrease in pain progression and an improvement in progression-free survival rates. However, it did not receive the approbation by FAD since the overall survival of patients was not significantly improved and that more than one-half of the patients in the study had received prior docetaxel treatment.^{9,13,29}

Based on the nature of the axial ligands, Pt(IV) can be divided in three categories: complexes with targeting agents in the axial positions, complexes with bioactive axial ligands (like drugs, enzyme inhibitors etc.) and complexes having axial ligands free of any bioactivity such as hydroxides, chlorides or acetates. Some examples of Pt(IV) complexes with non-bioactive ligands are ormaplatin, iproplatin and satraplatin described before.¹¹ Furthermore, in 1992, Kelland *et al.* identified a relation between the number of carbon atoms in the axial ligands and the cytotoxicity of the complex. Increasing the number of the carbon atoms, the cytotoxicity of the compound is improved.³¹ To try to improve Pt(IV) complexes properties, during the years targeting group were implemented in the axial ligands. Keppler and Galanski analysed the effect of the lipophilicity and the

reduction potential of Pt(IV) cytotoxicity. They synthesised different prodrugs compound changing the lipophilicity of the axial ligands with esters of succinic anhydride. They prepared bis(carboxylato) dichlorido(ethane-1,2-diamine)platinum(IV) compounds, and some of them showed IC₅₀ values in the low nM range. They observed correlation between the lipophilicity and the cytotoxicity of Pt(IV) ester derivatives — the more lipophilic the complex, the higher cytotoxic effect. Moreover, they found that the ester derivatives of the Pt(IV) complex showed a significant effect on the antiproliferative potency on cancer cells.^{32,33} Lippard and Dhar tried to address the resistance of some cancer cells to apoptosis triggered by cisplatin, developing a new Pt(IV) prodrug called mitaplatin. Mitaplatin, bore two dichloroacetate (DCA) moieties in the axial positions. The choice to incorporate DCA was related to the fact that this molecule is an anticancer agent capable of inverting the metabolism of most solid tumours by inhibiting a key enzyme in cancer cells (pyruvate dehydrogenase kinase, PDK). Moreover, DCA does not seem to have any destructive effect on normal cells. Lippard and Dhar hypothesised that mitaplatin can have a dual killing mode in the cancer cells.³⁴ The platinum centre interacts with its own target, nuclear DNA, and DCA released inside the cells upon reduction, attacks mitochondria at the same time. Affecting the mitochondrial at the same time of the DNA, should increase the platination of nuclear DNA. A recent study demonstrate that cisplatin might have a direct impact in mitochondria in head and neck cancer.³⁵ The mitochondrial defects are associated with the cisplatin resistance phenotype.³⁶ It was proposed that a more negative membrane potential might promote translocation of the active and cationic form of cisplatin from the cytoplasm to mitochondria reducing the possibility of binding with the DNA. Hence, the combination between cisplatin with a mitochondrial targeting moiety should be an attractive therapeutic strategy for attacking cisplatin-resistant tumours. These results demonstrated the utility of targeting cancer cell-specific pathways and a possible way to generate selective anticancer agents.³⁴

1.1.2 Pt(IV) complexes photoactivation

The use of light for activating platinum anticancer prodrugs has been largely studied.³⁷ Light irradiation has the ability to alter the electronic structure of molecules changing both physical and chemical properties.^{37,38} The resulting

excited state has normally a short lifetime, but as the molecule returns to its ground state, the energy can be dispersed in different ways. The transfer of energy to other species, the production of light or heat and the chemical modification of the structure can be examples of the dissipation of this energy. Transition metal complexes with d^6 electronic configuration, such as Pt(IV) compounds undergo photochemical and photophysical processes regulated by different excited states. The corresponding transitions to the excited state are defined depend on the nature of the orbitals involved in the electronic transition, as **(Figure 1.4)**:

- Metal-centred (MC) transitions: are orbitally (Laporte)-forbidden and can be also spin-forbidden if the state of the spin changes. They are characterised by weak absorption and usually involve population of antibonding orbitals. MC excited states generated often lead to bond lengthening and favour ligand substitution.
- Charge-transfer (CT) transitions: are more intense than MC transitions. They could involve metal-to-ligand (MLCT), ligand-to-metal (LMCT) or to-solvent (TS) transitions. CT transitions can induce redox reaction with the generation of radicals.
- Ligand-centred (LC) transitions: are involved only ligand-centred orbitals and are generally observed in highly delocalised systems.³⁷

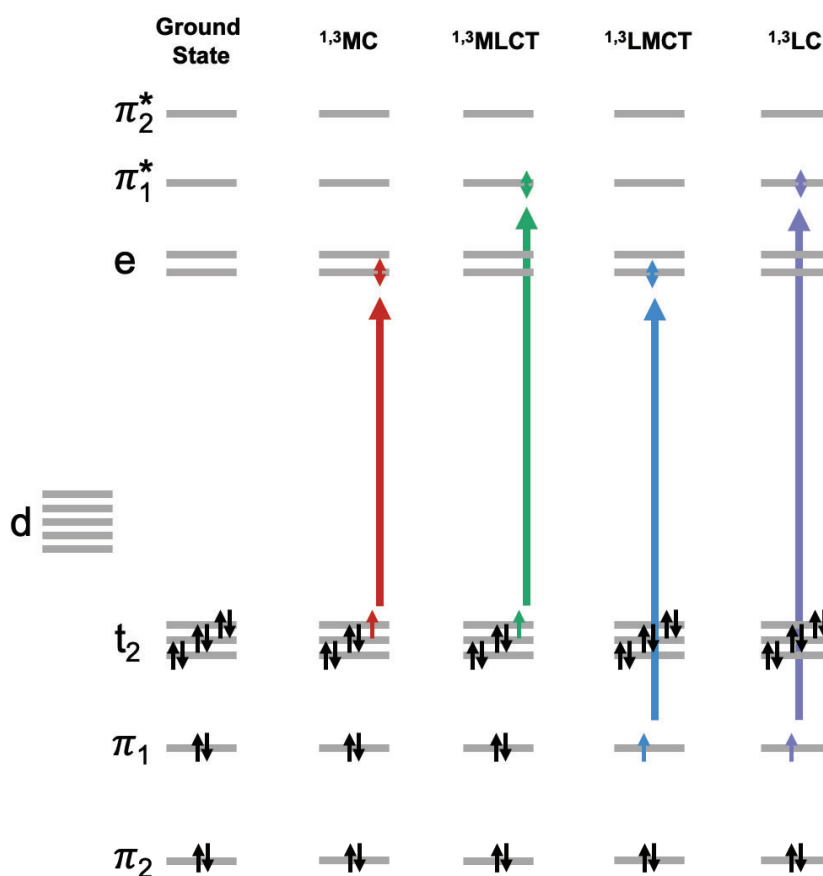


Figure 1.4 Simplified orbital and excited-state diagram for a d⁶ metal complex with octahedral coordination (strong crystal field is assumed). The double-colored arrows represent the electron involved in each electronic transition. Scheme adapted from ref. 37.

Once the excited states are generated, they evolve through different physical radiationless processes to return to the ground state such as: intersystem crossing (ISC), internal conversion (IC), vibrational relaxation, intramolecular vibrational redistribution and solvation dynamics. Radiative mechanism like fluorescence (singlet-singlet transition) and phosphorescence (triplet-singlet transition) take place with an emission of light with a longer wavelength than the one used for the excitation. All the possible process are reported in the Jablonski energy diagram in **Figure 1.5**.³⁷ In the decay from the excited states to the ground state, of the excited metal complexes, photochemical reactions (*i.e.* ligand dissociation, redox or substitution processes, etc.) can take place at any stage. Moreover, the study of the excited states involved in the photoactivation of the metal complex are usually analysed by time-resoled techniques and computation methods. These analyses showed that the photochemistry reactions can happened

when the electronic-state evolution is not complete, from both singlet and triplet states.³⁷

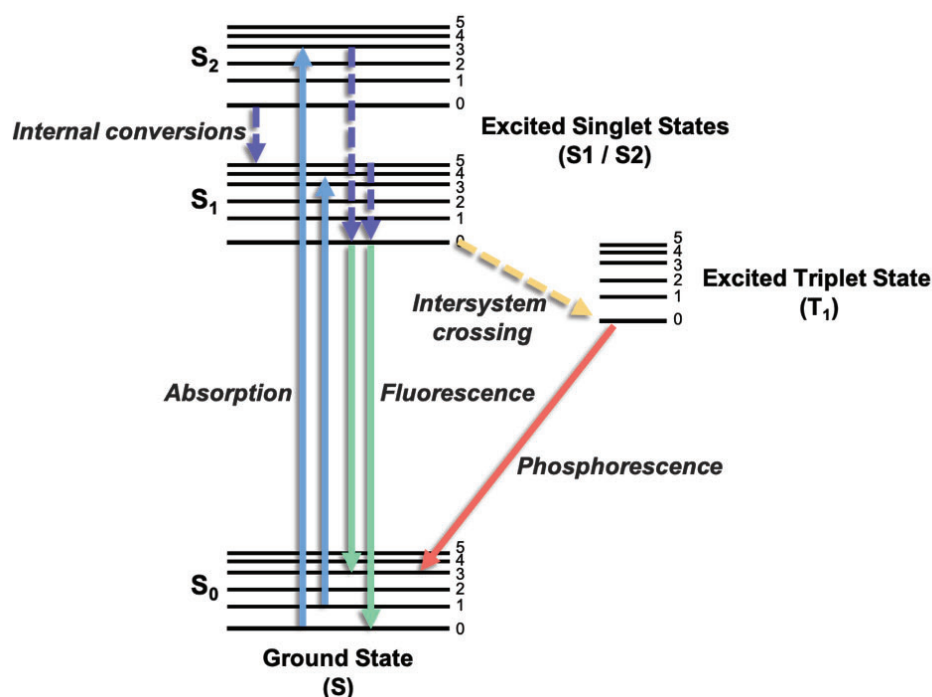


Figure 1.5 Jablonski energy diagram for an excited molecule. Scheme adapted from a contribution of Ian D. Johnson and Michael W. Davidson from the National High Magnetic Field Laboratory (The Florida State University).

The excited states are generally accessible by irradiations at different wavelengths. Once they reached the excited states, upon irradiations, the emission occurs from their triplet state (phosphorescence process). Thanks to the efficient intersystem crossing promoted by the metal ion, the lifetime of their triplet states is shorter (μs) than the one of the organic compounds (ms) and the emission quantum yield is comparably high. Moreover, additional characteristics that should be taken into account for good photoactivatable metal complexes as anticancer prodrugs, include: possible photoactivation in the red region for an higher depth penetration, no cytotoxicity in the dark (only after the activation) and efficiency in the photochemical process.³⁷

Over the years, there have been various applications of light with metal complexes. Rosenberg was the first also to use light to photoactivate Pt(IV) complexes. In 1967, he noticed that when a solution of $(\text{NH}_4)_2[\text{PtCl}_6]$ is

Chapter 1

irradiated, photochemical change in the platinum complex occurs. Under irradiation, the chloride ions are replaced by 1, 2, or 3 ammonia molecules with a resulting neutral species, $[\text{PtCl}_4(\text{NH}_3)_2]^0$ that inhibited cell division in *Escherichia coli*.³⁹

Later, Bednarski and his laboratory, reported the first studies related to the photochemistry, DNA-binding and antiproliferative properties of the photoproducts originated from iodide Pt(IV) diamine complexes. Metal complexes developed by his group were characterised by iodides as leaving ligands and ethylenediamine (en) as non-leaving group. The first derivative synthesised and studied was *trans,cis*- $[\text{PtCl}_2\text{I}_2(\text{en})]$ (**Figure 1.6**). It was observed that under irradiation (410 nm), this platinum complex was subjected to photodecomposition, generating $[\text{PtCl}_2\text{I}_2(\text{en})]$ which is capable to bind DNA. Unfortunately, its decomposition was not due to the light because it was observed also in dark conditions. No differences in toxicity in cancer cell were observed comparing the sample kept in dark to the ones irradiated with light.⁴⁰

To try to solve the problem of the low stability in dark, Bednarski *et al.* synthesised subsequently other two Pt(IV) complexes changing the axial chloride ligands. Acetates and hydroxides groups were used obtaining respectively: *trans,cis*- $[\text{Pt}(\text{OAc})_2\text{I}_2(\text{en})]$ and *trans,cis*- $[\text{Pt}(\text{OH})_2\text{I}_2(\text{en})]$ (**Figure 1.6**). In absence of light, no DNA-binding were observed for none of the compounds. On the contrary under 375 nm irradiation, 63% of the platinum was covalently bound to DNA after 6 h for *trans,cis*- $[\text{Pt}(\text{OAc})_2\text{I}_2(\text{en})]$ and only 10% for the *trans,cis*- $[\text{Pt}(\text{OH})_2\text{I}_2(\text{en})]$. DNA binding studies was confirmed the formation of Pt(II) as products of the photoreduction of Pt(IV). For the cytotoxicity in cancer cells (TCCSUP human bladder), both derivatives showed an increase after the irradiation, even if they could kill cancer cells in the low micromolar range also in the dark. Indeed, NMR studies showed displayed that both compounds were rapidly reduced via inner-sphere mechanism by biothiols such *N*-acetylcysteine and GSH.⁴¹

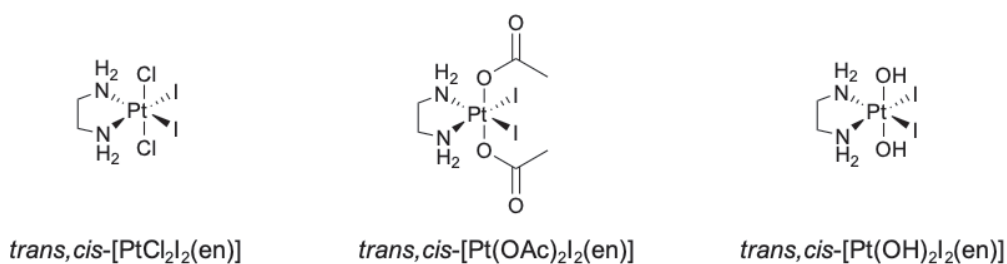


Figure 1.6 First generation of Pt(IV) complexes with iodide as leaving ligands. From the left: $trans,cis-[PtCl_2I_2(en)]$ prodrug, $trans,cis-[Pt(OAc)_2I_2(en)]$ prodrug and $trans,cis-[Pt(OH)_2I_2(en)]$ prodrug. (en = ethylenediamine, OAc = acetate).

As second generation of photoactivable Pt(IV) compounds, diazido-Pt(IV) complexes, were developed in a collaboration between the groups of Bednarski and Sadler. $Cis,trans-[Pt(en)(N_3)_2(OH)_2]$ and $cis,trans,cis-[Pt(N_3)_2(OH)_2(NH_3)_2]$ are two representative examples of this class of agents (**Figure 1.7**). Sadler and Bednarski observed that, compared to diiodo-Pt(IV) complexes (first generation), the diazido compounds are very stable toward hydrolysis (around 90 days) and no reaction with 5'-GMP and GSH occurred in dark. Both the diazido-Pt(IV) complexes were tested on human bladder cancer cells, comparing their behaviour with and without light.

In the dark, after 6 hours of incubation, the two complexes were able to produce a low inhibition in cell growth. Under irradiation (366 nm) instead, inhibition was observed with a decrease in the IC_{50} value from $>300 \mu M$ (dark) to $49 \mu M$ and $63 \mu M$ for $cis,trans,cis-[Pt(N_3)_2(OH)_2(NH_3)_2]$ and $cis,trans-[Pt(en)(N_3)_2(OH)_2]$ respectively. The photochemistry and the anticancer activity of the isomer $trans,trans,trans-[Pt(N_3)_2(OH)_2(NH_3)_2]$, was later studied by the Sadler group (**Figure 1.7**). In the dark, this compound was stable in the presence of 5'-GMP, but under 1 min irradiation it went through photoreduction forming the $trans-[Pt(NH_3)_2(5'-GMP-N_7)_2]$ adduct. Compared to the results obtained from the same photoreaction process for $cis,trans-[Pt(en)(N_3)_2(OH)_2]$ and $cis,trans,cis-[Pt(N_3)_2(OH)_2(NH_3)_2]$, the efficiency of the trans isomer was evidently much higher. The phototoxicity of this complex was studied in human HaCaT keratinocytes. Sadler and his collaborators observed that in absence of light, no toxic effects were developed ($IC_{50} > 288 \mu M$), but upon irradiation the same efficiency of cisplatin was reached ($IC_{50} = 156 \mu M$ for the trans isomer and $IC_{50} = 144 \mu M$ for cisplatin).

Hence, they demonstrated that this new class of photoactivatable Pt(IV) azide compounds are stable under biological conditions, but under

Chapter 1

irradiation are subjected to reduction and bind to nucleotides. Moreover, they showed phototoxic consequence in cancer cell lines and no effect in dark. These photoactivatable Pt(IV) azide compounds had the potential to avoid the side-effects associated with cisplatin and represented a promising area for new drug development.⁴²

Based on the results obtained with *trans,trans,trans*-[Pt(N₃)₂(OH)₂(NH₃)₂], Sadler and co-workers developed two *trans*-azido derivatives, *trans,trans,trans*-[Pt(N₃)₂(OH)₂(NH₃)(py)] and *trans,trans,trans*-[Pt(N₃)₂(OH)₂(py)₂] where py is a pyridine (**Figure 1.7**). *Trans,trans,trans*-[Pt(N₃)₂(OH)₂(NH₃)(py)] was tested first in different cancer cells line comparing its efficiency after activation with light (UV and visible, 5 J/cm²) with the one of cisplatin. This Pt(IV) complex showed a low selectivity in the cancer cell lines studied, in contrast with the cisplatin. It can be activated with UVA and visible light showing good efficiency in both cases. Later, Sadler and co-workers studied the antitumor activity of this platinum complex also *in vivo*, working with female mice bearing xenografted OE19 esophageal carcinoma tumours. The mice were treated with the drug, administrated intraperitoneally with a single injection, for 2 hours before the irradiation with 420 nm wavelength light (xenon lamp). Good results *in vitro* and *in vivo* studies were observed, being the first successful photoactivated metal-based prodrug showing an enhancement in the anticancer activity *in vivo* upon irradiation. The compound indeed did not show any toxic effect in mice, also with a dose 10 time more than the one used typically with cisplatin.⁴³

The *trans,trans,trans*-[Pt(N₃)₂(OH)₂(py)₂] was also studied by the Sadler group. They found that this complex was thermally more stable than the monoamine *trans,trans,trans*-[Pt(N₃)₂(OH)₂(NH₃)(py)] and the diamine *trans,trans,trans*-[Pt(N₃)₂(OH)₂(NH₃)₂] and the pyridine ligands remained bound to the platinum after the photoactivation. The phototoxicity of *trans,trans,trans*-[Pt(N₃)₂(OH)₂(py)₂] under 365 nm light irradiation was tested in different cancer cells lines: keratinocytes (HaCaT), parental (A2780) and cisplatin-resistant (A2780CIS) ovarian carcinoma, oesophageal adenocarcinoma (OE19) and hepatoma (HepG2). In HaCaT cells, the complex studied showed to be an order of magnitude more potent compared to cisplatin with low doses irradiation (420 nm, 5 J/cm²). Moreover, for

trans,trans,trans-[Pt(N₃)₂(OH)₂(NH₃)₂] was not observed any fragmentation or condensation of the nuclei in the photoactivation experiments, suggesting a different mechanism of action than cisplatin.⁴⁴

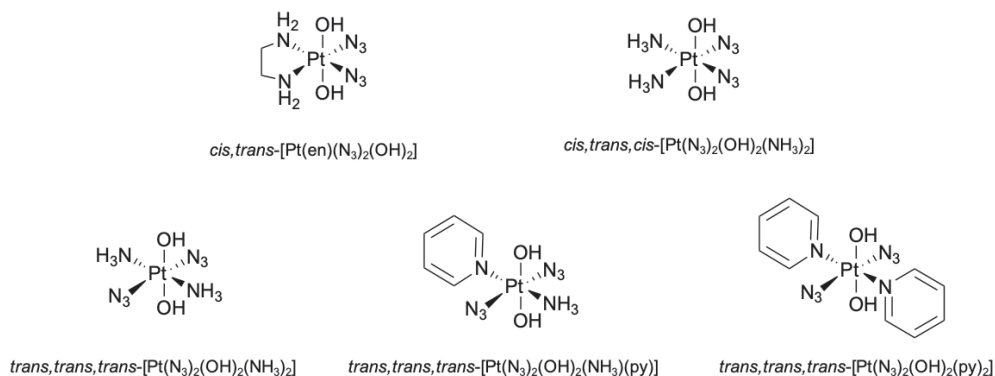


Figure 1.7 Second generation of Pt(IV) complexes. On the top: *cis,trans*-[Pt(en)(N₃)₂(OH)₂] (left) and *cis,trans,cis*-[Pt(N₃)₂(OH)₂(NH₃)₂] (right) prodrugs; on the bottom: *trans,trans,trans*-[Pt(N₃)₂(OH)₂(NH₃)₂] (left), *trans,trans,trans*-[Pt(N₃)₂(OH)₂(NH₃)(py)] (middle) and *trans,trans,trans*-[Pt(N₃)₂(OH)₂(py)₂] (right) prodrugs. (en = ethylenediamine, py = pyridine).

A step forward in the use of photoactivable Pt(IV) prodrugs was achieved by Marchán and Sadler. They designed new Pt anticancer agents implementing targeting properties to the *trans*-azido Pt derivatives. For obtaining these capabilities, *trans,trans,trans*-[Pt(N₃)₂(OH)₂(py)₂]⁴⁵ and *trans,trans,trans*-[Pt(N₃)₂(OH)(succ)(py)₂]⁴⁶ (succ = succinylate, py = pyridine) complexes were coupled respectively to a cyclic peptide containing the RGD sequence (-Arg-Gly-Aps) and to guanidinoneomycin (**Figure 1.8**). The RGD is selectively recognized by $\alpha_v\beta_3$ and $\alpha_v\beta_5$ transmembrane glycoproteins overexpress in cancer cells while guanidinoneomycin is known to be able to transport large bioactive cargos in cells. In both cases, the Pt-conjugated system, showed selectivity for the human malignant melanoma cells (SK-MEL-28) displaying an improvement in the intracellular accumulation. Moreover, under 420 nm irradiation (5 J/cm²), phototoxicity effects in SK-MEL-28 cells were identified due to the ability of the systems to bind the nucleobase model (5'-GMP) and RNA.

These compounds demonstrate the great potential of photoactivatable Pt(IV) complexes for platinum-conjugates anticancer treatments based on the ability of targeting molecules (thanks to the axial ligands) and on the generation of Pt(II) active species under light irradiation.

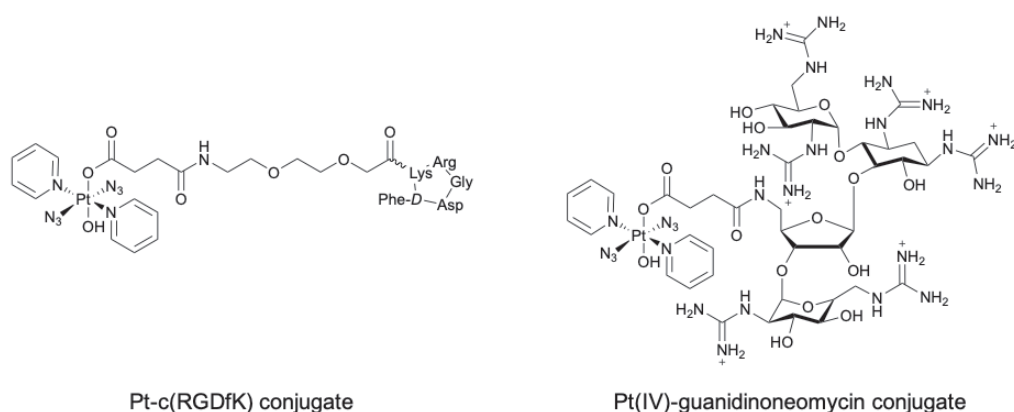


Figure 1.8 Azido-Pt(IV) anticancer agents functionalised with targeting ligands. Left panel: *trans,trans,trans*-[Pt(N₃)₂(OH)₂(py)₂] conjugated with a cyclic peptide containing the RGD sequence (–Arg–Gly–Asp–) (Pt-c(RGDfK) conjugate). Right panel: *trans,trans,trans*-[Pt(N₃)₂(OH)(succ)(py)₂] (succ = succinate, py = pyridine) conjugated to guanidinoneomycin (Pt(IV)-guanidinoneomycin conjugate). Structures adapted respectively from ref. 45 and ref. 46.

1.1.3 Strategies for the delivery of Pt(IV) photoactivable prodrugs

The use of Pt(IV) agents, thanks to the two axial ligands, provides tuneable biological properties such as lipophilicity, redox stability, cancer-cell targeting and improved cellular uptake.^{13,9} The need of more efficient systems that avoid the undesirable side reactions of Pt(II) complex with proteins or thiols has led researches to investigate the chemistry of these compounds.⁹ Encapsulation or conjugation with nanomaterials, such as amphiphilic micelles, emulsion, liposomes or nanoparticles, showed for example an increase in the tumor targeting and in the loading efficiency, an higher cytotoxicity and a decrease in the side reactions.²⁰ Moreover, also the delivery of platinum anticancer complexes can be improved with these strategy. Along the years, different systems have been developed. The group of Sadler developed supramolecular photoactivatable anticancer hydrogel coupling *trans,trans,trans*-[Pt(N₃)₂(Py)₂(OH)(succinate)] to dopamine (**Pt-DA**) and incorporated it in G-quadruplex-based hydrogel (**Pt-G₄K⁺B**) (**Figure 1.9**). The aim of their work was to exploit the hydrogel for the delivery of Pt prodrugs to cancer cells. Indeed, these two systems were tested in cisplatin-resistant cancer cells, A2780 (human ovarian cancer cells) and in noncancerous human fibroblast cells, MRC-5. They observed that, in A2780 cells, **Pt-G₄K⁺B** exhibited activity in the dark (IC₅₀ = 16 μM), but under blue light irradiation (1 h, 465 nm, 50 mW) was much more potent (IC₅₀ = 3 μM).

Furthermore, in noncancerous MRC-5 cells, no toxic effects were observed indicating a photocytotoxicity selectivity (selectivity factor > 18) of the hydrogel.⁴⁷

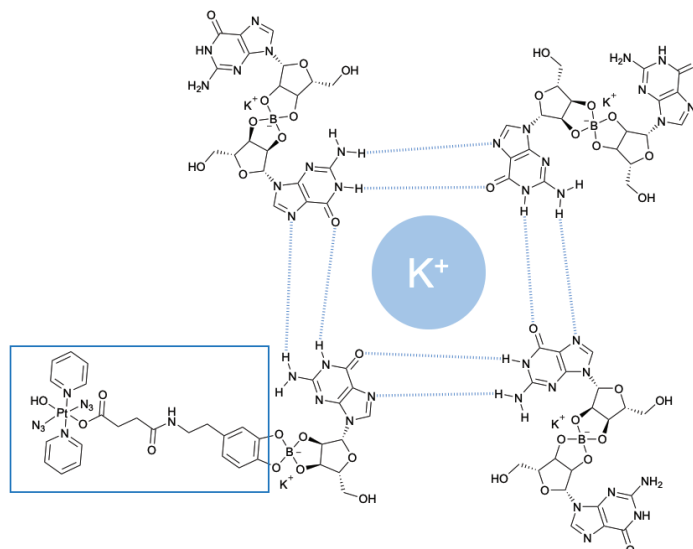


Figure 1.9 Schematic representation of the self-assembly of Pt-DA complex functionalised with G₄K⁺ borate hydrogels. Scheme adapted from ref. 47.

Different approaches have been developed by researcher for moving the light-irradiation wavelengths used for the photoactivation of Pt(IV) prodrugs, in the therapeutic windows (red and NIR region of the spectrum). For this purpose, various nanomaterials have been studied.

Mareque group's developed core-shell CdSe-ZnS quantum dots (QDs) loaded with [PtCl₄(bpy)] (bpy = 2,20-bipyridine). They demonstrated that irradiating this system with visible light for 1 hour, around 2000–2200 molecules of Pt(II) species per QD were generated. The results obtained demonstrate the opportunity to use QDs and Pt(IV) prodrugs for the photodynamic and platinum-based anticancer treatments. Furthermore, it was the first step for creating QDs capable of transporting Pt(IV) compound to the tumor helping their uptake by cancer cells and the release of the active species under irradiation.⁴⁸ Lately, the same group, developed a water-soluble QD-filled PEGylate micelles (MQDs), based on the core-shell CdSe-ZnS quantum dots,⁴⁸ for the generation of the anticancer drug cisplatin from a Pt(IV) prodrug after irradiation.⁴⁹ Mareque and collaborators demonstrated that they could generate cisplatin from the Pt(IV) complex ([Pt(NH₃)₂Cl₂(O₂CCH₂CH₂CO₂H)₂]) under visible light. They observed that the

Chapter 1

Pt(IV) complex was pharmacologically inactive in the dark and only after irradiation with visible light, and in the presence of MQDs, the active species was formed. Moreover, they investigated the release of the platinum drug also *in vitro*, working with a prostate cancer cells line (PC-3). In the absence of QDs, the platinum complex was inert and non-toxic under irradiations, but in presence of the MQDs they observed an increase in the cytotoxicity ($IC_{50} = 25 \mu M$).⁴⁹

Another example of the activation of Pt(IV) prodrugs was provided by upconverting nanoparticles (UCNPs). Their low toxicity *in vitro* and *in vivo*, their imaging capability make these systems interesting candidates to be investigated for these types of applications. These nanomaterials emerged for their characteristics as an attractive candidate to act as a NIR-induced mediator due to their intrinsic upconversion-luminescent properties.⁵⁰ UCNPs are able to absorb NIR photons and convert them to visible/UV light. UCNPs are commonly composed by an inorganic host lattice (NaYF₄, NaGdF₄, NaLuF₄, KYF₄), activator ions (Er³⁺, Tm³⁺, Ho³⁺) and sensitizer ions (Yb³⁺).⁵¹

For example, our group described the photoactivation of [Pt(NH₃)₂(Cl)₂(O₂CCH₂CH₂CO₂H)₂] (Pt(IV) complex) by NIR light (980 nm) using a core-shell UCNPs. The Pt(IV) complex was functionalised with the biocompatible PEGylate phospholipid DSPE-PEG(2000)-NH₂ for the decoration of the surface of these NaYF₄:Yb³⁺/Tm³⁺@NaYF₄ UCNPs. In 4 hours, this system was able to release the active species Pt(II) (cisplatin) under 980 nm light irradiation (4.9 W/cm²).⁵²

Pherfahl *et al.* studied the photoactivation of light-sensitive diiodido-Pt(IV) complexes, coupled to upconverting lanthanide-doped hexagonal NaGdF₄ nanocrystal. They developed two strategies for the coupling: covalent attachment of the metal compounds via amide bond formation and electrostatic interactions between Pt(IV) complex and the surface of UCNPs. In human leukemia cell (HL60), modified Pt(IV)-UCNPs systems were tested in the dark and under light irradiation. The cells were exposed to five repetitions of 30 min irradiation with 15 min dark intervals. The covalent conjugates showed a higher cytotoxicity under NIR light (980 nm, 1.2 W/cm²)

compared to the electrostatic one. Nevertheless, both systems produced a decrease in cell viability under NIR light compare to the dark.⁵³

1.2. Flavins

The term “flavin” came from Latin “flavus”, yellow. Flavin indeed is typically used to define a family of a water soluble, yellow-orange organic compounds containing the basic structure 7,8-dimethyl-10-alkyl isoalloxazine.^{54,55} The discovery and characterization of this molecule started in 1879 when Blyth isolated a bright yellow pigment from cow milk.⁵⁶ He called it *lactochrome*, “lacto” because of the milk and “chrome” for the yellow pigment, but during the years the name of this molecule passed through different ones. In 1933 György, Khun, and Jauregg named it *lactoflavin* and in 1937 the Council of Pharmacy and Chemistry of the American Medical Association changed the name in *riboflavin* when it was established that lactoflavin's structure resulted from isoalloxazine binding two methyl groups and a sugar radical.⁵⁷ The milestone in the discovery of this molecules are summarized in **Table 1.1**:

Table 1.1 Milestone in the discovery of riboflavin.⁵⁷

Date	Researcher	Comments
1897	Blyth	Isolation of <i>lactochrome</i>
1906	Hopkins	Reported that synthetic diets lacked an organic nutrient present in minute amounts in milk that stimulated appetite, food consumption and growth in rats and mice
1915	McCollum	Proposed two accessory factors in diet: a water-soluble B and a fat-soluble A.
1927	Goldberger	Proposed there was an anti-pellagra factor in eggs, milk, etc., and it was the same substance as water-soluble B identified by McCollum
1927	Chick and Roscoe	Proposed the water-soluble B identified by McCollum was composed by two factors: anti-beriberi B ₁ and the B ₂ factor
1932	György	Suggested that B ₂ factor comprised an anti-pellagra factor and growth-promoting factor

Chapter 1

1932	Warburg and Christian	Extracted a yellow enzyme from yeast and demonstrated the yellow colour was dialyzable and could be recoupled to the enzyme
1933	György, Khun, and Jauregg	Isolation of <i>lactoflavin</i> from milk
1934-1935	Kuhn and Karrer	Independently described the structure of riboflavin
1935	Birch, György and Harris	Differentiated the anti-pellagra factor from the growth-promoting vitamin B ₂ factor
1935	Theorell	Confirmed that the yellow cofactor of riboflavin was the FMN
1939	Sebrell and Harris	Demonstrated riboflavin was essential in man
1968	Glatzle	Proposed the use of the glutathione reductase test as a functional measurement of riboflavin status

Riboflavins (Rf) is also known as vitamin B₂ and is fundamental for living organism. It can be produced by plants and many microbes, but animals must consume foods like milk, green vegetables, whole grains, egg whites, cheese, and fresh meat to obtain this essential component.^{57,54} After the consumption, Rf is widely spread in tissues and very few amount is free. The majority of riboflavin indeed is contained inside cells in two coenzyme forms: flavin adenine dinucleotide (FAD) and as flavin mononucleotide (FMN) in lower quantity (**Figure 1.10**).⁵⁴

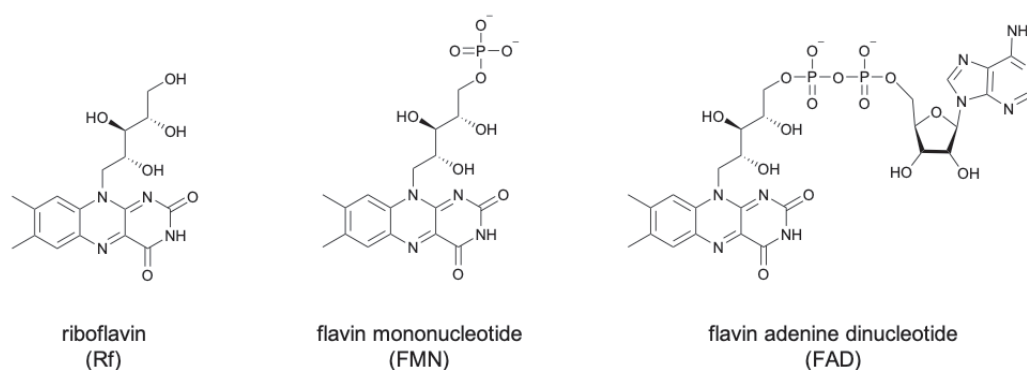


Figure 1.10 Chemical structures of riboflavin (Rf), flavin mononucleotide (FMN) and flavin adenine dinucleotide (FAD).

FAD and FMN have been known for their ability to participating in both one-electron and two-electron transfer processes. This implies that flavin molecules can be presented in three redox states: oxidized, one-electron reduced (semiquinone), and two-electron reduced (hydroquinone) (**Figure 1.11**). Hence, due to the ability of flavins to transfer single electrons, hydrogen atoms, and hydride ions, flavoenzymes are particularly adaptable in terms of substrate modifications and types of reactions. When FAD and FMN are free in solution, hence not bounded to an enzyme, the equilibrium of the different species is pH-dependent. At physiological pH (between pH 4.2 and 5.6), based on their pK_a , six of the nine possible structures are physiologically stable. At pH 7 instead, only a 5% of an equimolar mixture of reduced and oxidized flavin is stable as radical (highly reactive molecule with at least one unpaired electron).⁵⁴

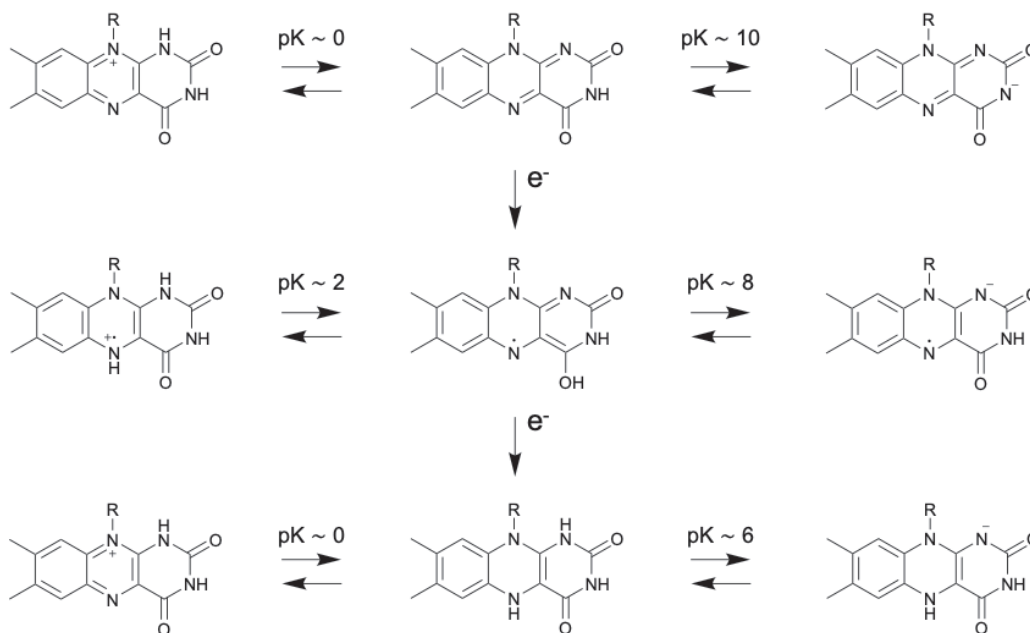


Figure 1.11 Redox and acid-base equilibria of flavins. Scheme adapted from ref. 54.

The redox potential at pH 7 of free flavin is around $E_m = -200\text{mV}$, a value that can change when flavin are bound to proteins in a range from -400 mV to $+60\text{ mV}$. This is due to the protein environment that influences the flavin properties. It is known that, in general, the closeness of a positive charge residue increases the redox potential, instead a negative charge residue or a hydrophobic environment decreases it.⁵⁴ Furthermore, the redox potential usually measured in aqueous solution is related to the hydroquinone state of flavins, since the semiquinone presents a low stability. Indeed, the first

Chapter 1

reduction is followed by the protonation and the reduction of neutral flavin semiquinone to the anionic hydroquinone.^{54,58} The redox equilibrium of flavins can then dramatically change by binding with proteins. Some enzymes exhibit no stabilisation of flavin semiquinone specie while others give almost 100%. In this case, with the stabilisation of the semiquinone thanks to the binding with the enzyme, both $E_{ox/sq}$ and $E_{sq/red}$ are achievable. In some cases, the pK_a is dramatically shifted up from 8.5 if the neutral radical species are stabilized by proteins across the whole range of pH levels at which the enzyme is stable. In other cases instead, the pK_a can be dramatically reduced if the semiquinone anion is stabilized.⁵⁴

In the ultraviolet and visible region of the absorption spectrum, all oxidized flavins display high absorption. Their spectra show the characteristic four peaks at 445, 375, 265, and 220 nm related to $\pi \rightarrow \pi^*$ transitions. The intersystem crossing from the singlet to the triplet state of flavins is typically effective when they are photoexcited. The quantum yields of Rf and FMN triplet formation were found to be 0.375 and 0.225, respectively. Conversely, the triplet quantum yield of FAD is very low compared to the one of Rf and FMN, because of the efficient radiationless decay to the ground state due to the stacking between the flavin and the adenine moieties. The neutral forms of flavins exhibit an intense yellow-green fluorescence at around 520 nm; however, their anions and cations are non-fluorescent. The fluorescence quantum yield of Rf is 0.28 in water at pH 7.^{54,59}

Even if flavins are thermostable molecules, they are especially sensible to light. Under irradiation (visible or UV) the isoalloxazine moiety undergoes photoreduction where the ribityl side chain acts as electron donor in the absence of an external one. The products obtained by the reduction maintain the same optical properties (absorbance and emission) of the flavin, except for lumichrome (LC). This molecule is the only one among the products that changes structure, losing the alkyl chain at the N10 position of the flavin ring. The other compounds obtained from the effect of the light are: formylmethylflavin (FMF), carboxymethylflavin (CMF), lumiflavin (LF) and cyclodehydroriboflavin (CDRF). FMF is an intermediate in the photodegradation of Rf, it is hydrolysed to LC and LF and is oxidized to CMF. In detail, the formation of these products is promoted by both the singlet

and triplet excited states of riboflavin. FMF, LC and LF are formed by the excited triplet state of Rf, instead the excited singlet state plays a role in the formation of LC and CDRF (**Figure 1.12**).^{60,54}

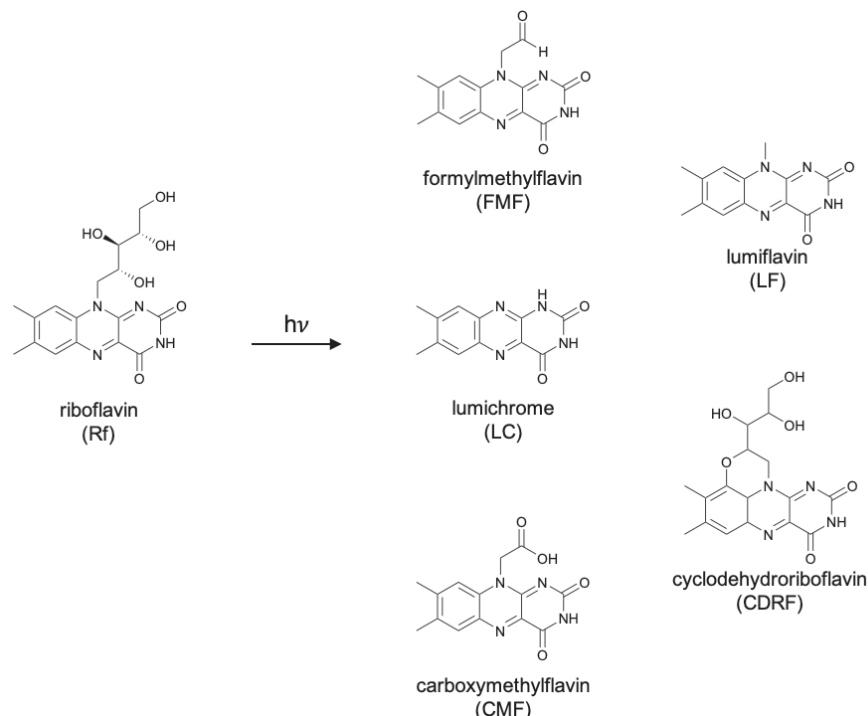


Figure 1.12 Photodegradation products of riboflavin in presence of light. Reaction scheme adapted from ref. 60.

Beside this type of reactions, flavins act as photocatalysts in different photocatalytic processes acting the role of the catalyst in different synthetic organic transformation. For example, Schmidt and his group reported a photochemical approach for the cyclisation of thiobenzanilides (**Figure 1.13**). The reaction was conducted under nitrogen atmosphere, using riboflavin 2',3',4',5'-tetraacetate (RFTA) as photocatalyst and potassium peroxydisulfate as a sacrificial oxidizing agent under blue light irradiation (3 W). Moreover, this reaction was a transition-organic photoredox catalysis that occurred in absence of transition-metal complexes catalysis under very mild conditions, useful for pharmaceutical uses.⁶¹

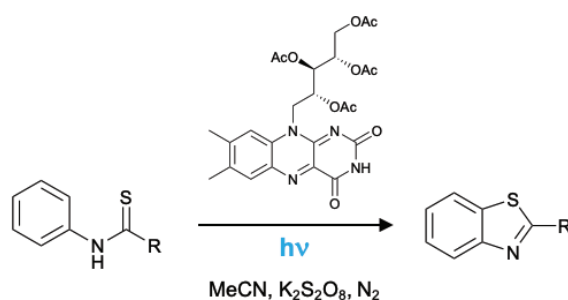


Figure 1.13 Visible light-mediated cyclisation of thiobenzanilides. Reaction scheme adapted from ref. 61.

Gilmour and collaborators investigated the generation of a heterocyclic core after a photoinduced single electron transfer mediated by riboflavin (**Figure 1.14**). In this process, riboflavin acted as photo organocatalysts, promoting the E \rightarrow Z isomerization of cinnamic acids in a first step. Subsequently, the activated photocatalyst subtracted an electron from the carboxylic acid, inducing a cyclisation with the adjacent aromatic ring.⁶²

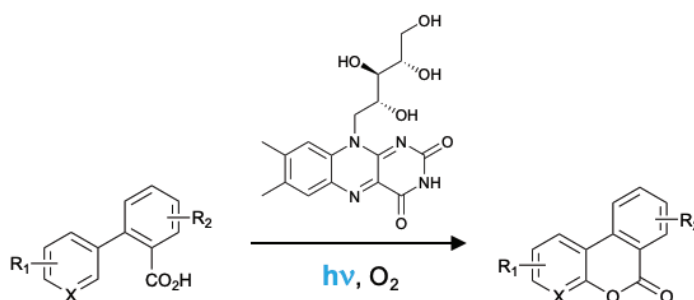


Figure 1.14 Direct cyclisation photocatalytic synthesis of benzocoumarins via riboflavin-mediated electron transfer. Reaction scheme adapted from ref. 62.

A modified riboflavin, in specific a riboflavin tetraacetate (RFTA), was used by Ramirez *et al.* for the oxidation of carboxylic acids supported by blue light irradiation (450 nm, 15 mW/cm²) (**Figure 1.15**). After decarboxylation, the generated radicals are trapped by tosyl cyanide (TsCN), yielding the desired nitriles without any further additive, in a redox-neutral process. Here, the dual role of RFTA, as a base and as the photocatalyst, allow performing the reaction in the absence of base or other additive.⁶³

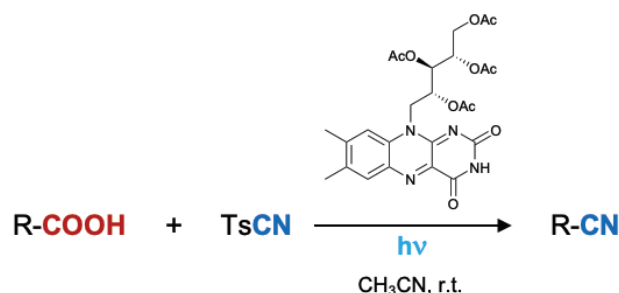


Figure 1.15 Decarboxylative cyanation of carboxylic acids. Reaction scheme adapted from ref. 63.

Since riboflavin is a stable photocatalyst, it has been studied also for cooperative catalysis. This type of catalysis is related to a collaboration between two catalysts in which their catalytic cycles work in agreement to generate a new single bond in organic transformations.⁶⁴ An example of the use of Rf in cooperative catalysis was given by Cibulka and collaborators, where they combine flavin photocatalyst and organocatalysts to catalyse the aerobic oxidation of toluene and benzyl alcohols under visible light irradiation. The system reported allowed the oxidation of challenging substrates with high oxidation potential. Moreover, this was the first cooperative enzyme model reported in which an ethylene-bridged flavinium salt worked in both oxidation reaction promoted by light and monooxygenation in dark.⁶⁵

Furthermore, flavoenzymes can catalyse different type of reactions, such as oxidation, reduction, monooxygenation and dehydrogenation.⁶⁶ An example in which flavoenzymes are commonly used is related to the biocatalytic reductive processes for the asymmetric reduction of C=C double bonds (ene-reductases processes).^{66,67} The Hyster group reported in 2019 a reductive cyclisation of α -chloroamides, catalysed by flavin-dependent ene-reductases (ERED) from a *Gluconobacter oxydans* (GluER) upon irradiation with cyan light (**Figure 1.16**). They found that a variety of chiral lactams can be obtained after the irradiation. Moreover, UV-Vis analysis showed the formation of a new absorption feature with a maximum peak of around 500 nm, corresponding to the formation of a charge-transfer complex between the substrate and the flavin hydroquinone. This species indeed was observed only in the presence of the ERED, indicating the important role of the protein

in the electron transfer. Overall, this transformation demonstrated the first example of a challenging catalytic asymmetric radical cyclisation.⁶⁸

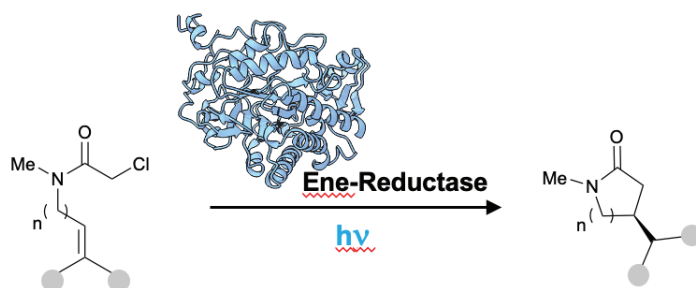


Figure 1.16 ERED-catalyzed stereoselective cyclisation of α -chloroamides. (OYE1 PDB ID: 1BWK). Reaction scheme adapted from ref. 68.

1.3. Inorganic and biological scaffolds for delivery

1.3.1. Gold nanoparticles

In the last few decades, the use of nanomaterials for biomedical applications has been investigated extensively. A nanomaterial (from the Greek “nanos”, dwarf) is a material with a single unit sized (in at least one dimension) between 1 and 100 nm (**Figure 1.17**).⁶⁹

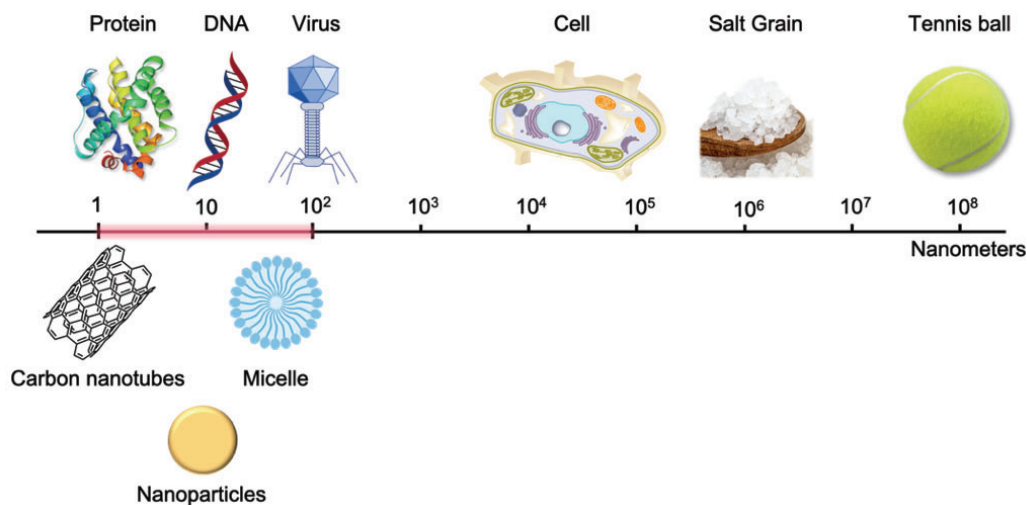


Figure 1.17 Illustration of nanoparticles scale of different objects. Scheme adapted from a work of the WICHLab (University of New South Wales, Australia).

These materials can be generally made of metal, carbon, polymer, or by composites (such as polymer-metal, silica-metal, graphene-metal), or in the core-shell form. Nanomaterials have remarkable properties, such as the possibility of surface functionalisation thanks to their high surface area to volume ratio, variable and tuneable porosity, chemical versatility and shape

and size control. For these features, nanomaterials are interesting candidates in the biomedical sector for the production of tissue-engineered scaffolds (e.g., blood vessels, bone), drug delivery systems (gene therapy, cancer treatments, drugs for chronic respiratory infections), chemical sensors or biosensors,⁷⁰ among others. Within the large family of nanomaterials, nanoparticles (NPs) are noteworthy for their properties for diagnostic and therapeutic applications.⁷¹ In particular, nanoparticles for drug delivery application shows key advantages such as: overcoming the stability and solubility issues of chemotherapeutic drugs; protecting the drug from modifications by enzymes (proteases and other metabolic enzymes) with a prolonged circulation time in the blood; enhancing drug targeting and the distribution; controlling the drug release kinetics; and reducing resistance to treatment by delivering multiple drugs.⁷² Nanoparticles indeed can deliver drugs to specific sites following a predesigned and, depending on the composition and engineering of the nanoparticles, it is possible to control the drug release.⁷⁰ The drugs can be loaded on the NPs through absorption or covalent linkage on the surface or can be incorporated during their synthesis.⁷³

Nanoparticles can be made of various metals, such as: gold, silver, titanium oxide and iron. Among these different inorganic NPs, gold nanoparticles (AuNPs) have been exploited for biomedical applications thanks to their good biocompatibility and low toxicity and immunogenicity. Moreover, AuNPs display interesting electronic and optical properties that are directly correlated to the average core size. A change in the size of the bulk metal causes a variation of their properties. For example, the surface plasmon band (520 nm) in the UV-Vis spectra is characteristic for AuNPs with a gold core bigger than 2 nm, but disappears in the case of smaller nanoparticles.^{74,75} The gold core, inert and nontoxic, can be obtained with different sizes, from 1.5 nm to 150 nm. This nanometric scale provides a large surface area for efficient drug targeting and ligand conjugation and protection.^{76,77,75} The surface of the gold nanoparticles can be modified with different functional group, such as polyethylene glycol (PEG), ssDNAs, antibodies, peptides, drugs, fluorescent markers, and siRNAs in order to confer multiple properties.^{75,78} This capability of tailored functionalisation allows to fabricate AuNPs that can act as molecular sensors, therapeutic

Chapter 1

agents, and vehicles for imaging agent and drug delivery.⁷⁹ The typical ligands used to cover the surface of gold nanoparticles and to incorporate additional functional moieties are generally characterised by thiols, phosphines and amines as gold-interacting group. These ligands indeed exhibit good affinity for gold surfaces and act as anchors for the ligands.^{78,80} In addition, the ligands bounded to the surface of the nanoparticles are also fundamental for to the colloidal stability. This is an important aspect for their application as therapeutic agents since they need to be stable also under harsh conditions such as the bloodstream or inside the cells.⁸¹

Gold nanoparticles synthesised for biological applications, are usually prepared using the colloidal synthesis method. This approach utilizes a metal precursor, a reducing agent, and a stabilizing agent, allowing the control on the size, shape, and optical properties of the nanostructures.⁸² Nanoparticles of different shapes including nanosphere, nanorods, and nano-cages are commonly obtained.^{82,75} Moreover, focusing on the drug delivery field, it is important to take into account the biocompatibility and the interaction with the biological system. For this purpose, spherical gold nanoparticles were found to be the most investigated. These gold nanoparticles can be prepared with different synthesis protocols according to the desired size. The first synthesis was proposed by Faraday in 1857 that described the reduction of tetrachloroauric(III) acid (HAuCl_4) to form colloidal gold suspensions.⁸³ This method was then developed by Turkevich in 1953. Turkevich's synthesis allows to make spherical gold nanoparticles with a size of about 20 nm, bringing to boiling point a solution of HAuCl_4 and then adding sodium citrate.⁸⁴ The procedure described by Turkevich has two main steps: nucleation and growth which occur at the same time. The initial step is the oxidation of citrate in dicarboxy acetone followed by the reduction of gold(III) chloride in gold(I) chloride. At the end, gold atoms are obtained from the disproportionation of three molecules of gold(III) chloride.⁸⁵ This synthesis has been adapted by different research groups and all the developed chemical methods employed a component which reduces gold and another one for the stabilisation of the formed gold nanoparticles, important also for the shape-control during the synthesis of AuNPs. In 1970, Frens optimized this method discovering that the ratio of gold salt to trisodium citrate is the factor that controls the size of gold nanoparticles in

the case of this specific synthesis. Thanks to these methods, gold nanoparticles with a size between 9 nm and 150 nm can be obtained.⁸⁶ In 1990 Brust and co-workers developed an alternative method to synthesize small spherical gold nanoparticles, with a diameter between 1 and 3 nm. Their strategy was based on a two-phase (water-toluene) reduction of a gold salt by sodium borohydride with an alkanethiol in the solution.⁸⁷ Subsequently, Brust's procedure was optimized by different research groups including Scrimin's group using dioctylamine as a stabilizing agent. This allowed an easier control on the size of the gold nanoparticles, an increase in their stability before the final passivation with the desired thiols and the possibility of adding the thiols in mild conditions and with a minimum excess.⁸⁸ This method was the one that we adopted for the synthesis of gold nanoparticles (Chapter 4).

As reported before, the surface of gold nanoparticles can be modified with a variety of functional groups, tuning the properties of the AuNPs for specific fields such as drug delivery.⁸⁹ Along the years indeed, AuNPs have been studied as nanocarriers for the delivery of drugs (such as paclitaxel, doxorubicin, gemcitabine) or Pt-based (pro)drugs.⁷¹ Here, we highlight the use of gold nanoparticles in relation with the delivery of Pt anticancer drugs.

The group of Lippard was one of the first to investigate the use of AuNPs for Pt-based prodrug delivery. They developed gold nanoparticles, functionalised with thiolate oligonucleotides for the coupling with Pt(IV) compounds through amide linkage (**Pt-DNA-Au NPs**) (**Figure 1.18**). This system was designed for the release of cytotoxic dose of cisplatin upon intracellular reduction. Cell internalisation was first analysed with fluorescence microscopy using functionalised mixed nanoparticles with Pt(IV) compound and a 5' dye (Cy5), finding a vesicles localisation after 6 hours and cytosol localisation after 12 hours. The ability of killing cells was tested in human lung carcinoma (A549), in human prostate cancer (PC3), in cervical cancer (HeLa) and in human osteosarcoma (U2OS) cells to investigate the efficacy of **Pt-DNA-Au NPs** in the release of toxic dose of cisplatin. The final construct showed higher antiproliferative activity in all the different cell lines. In A549 cells, cisplatin showed an IC_{50} of 11 μ M while for the **Pt-DNA-Au NPs** construct was 0.9 μ M, underlining the higher killing

ability of their system compare to cisplatin. For the U2OS cells, the IC_{50} for **Pt-DNA-Au NPs** and cisplatin were respectively 3.4 μM and 5.1 μM . Similarly, in HeLa and PC3 cells, **Pt-DNA-Au NP** (IC_{50} 6.0 and 2.5 μM , respectively) reflected a greater activity than that of cisplatin (IC_{50} 9.4 and 4.6 μM , respectively). The Pt(IV) prodrug alone did not show any significant killing of cancer cells under the same conditions. Lippard group then investigated the formation of 1,2-d(GpG) intrastrand cross-links on DNA with Pt(II) complex since is related to the anticancer activity of cisplatin. They followed the reduction of **Pt-DNA-Au NP** in HeLa cells, confirming the formation of Pt(II) 1,2 d(GpG) intrastrand cross-links. Their conjugate, in which the Pt(IV) is inactive, was internalized by cells and here reduced to release cisplatin, which enters the nucleus inducing cell death.⁹⁰

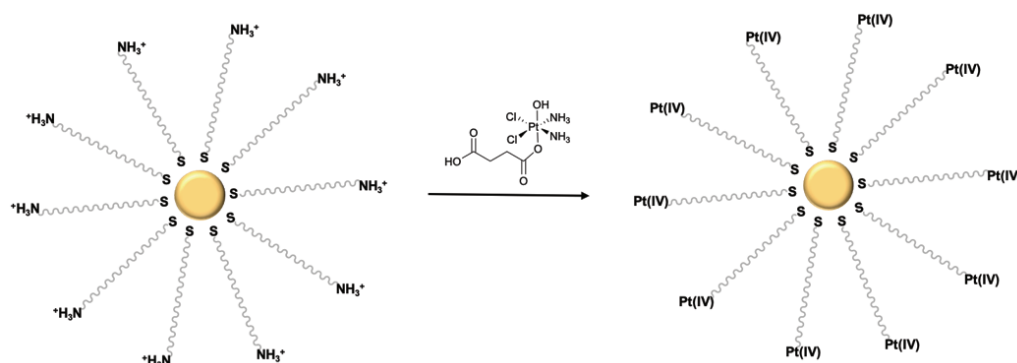


Figure 1.18 Construction of **Pt-DNA-Au NPs** developed by Dhar *et al.* Scheme adapted from ref. 90.

Similarly, one year later, Brown *et al.* functionalised AuNPs with a thiolate poly(ethylene glycol) (PEG) monolayer, capped with a carboxylate group for improving the delivery of platinum drugs. They used as drug model oxaliplatin loaded to the PEG monolayer surface of the NPs. *In vitro* experiments were conducted to study the uptake, the localisation and the cytotoxicity of their system.⁹¹ A549 human lung epithelial cells and HCT116, HCT15, HT29 and RKO human colon cancer cell lines were chosen since lung and colorectal cancers are the first and third most common cancer type in the world.^{91,92} They observed an IC_{50} of 0.495 nM in the A549 cell line for the platinum-tethered gold nanoparticles, which was almost 6-fold more active than oxaliplatin (IC_{50} 0.775 μM). Also, in colon cancer cell lines, their nanoparticles system showed a higher cytotoxic effect (5.6-fold) compared to the one of the drug alone. The internalisation of the platinum functionalised gold nanoparticles in A549 cells was studied as well, revealing

an unusual ability to penetrate the nucleus. Non-functionalised AuNPs, as well as the PEGylated ones, are known not to be able to penetrate cell nuclei. Brown *et al.* hypothesised that the internalisation of their system was due to a platinum-mediated transport mechanism, where the oxaliplatin is released into the nucleus and binds to the DNA.⁹¹

Recently Paulo and co-workers synthesised a small spherical gold nanoparticles (**AuNP**, 4 nm gold core) functionalised with thiolates DOTA derivative, a GRPR-targeting bombesin analogue (**BBN**) and Pt(IV) prodrugs with and without PEGylate linker, **AuNP-BBN-Pt** (**Figure 1.19**).⁷¹ The DOTA ligands avoided the aggregation in solution of the nanoparticles and can coordinate a variety of metals ions, such as Gd^{3+} and $^{67}Ga^{3+}$, used for diagnostic and therapeutic applications. These metal ions display great potential for magnetic resonance imaging (MRI) and single photon emission computed tomography (SPECT).⁹³ The bombesin derivatives (**BBN**) conferred a target ability⁷¹ to the AuNP as previously demonstrated by Paulo's and other groups.^{94,95,96,93} It can deliver imaging (*i.e.*, ^{67}Ga) and therapeutic radionuclides (*i.e.*, ^{198}Au and ^{177}Lu) to tumor cells overexpressing the gastrin releasing peptide receptor (GRPR).⁷¹ They studied the biological behaviour of these target-specific nanoplatforms in cancer (PC3 cell line) and non-cancer (RWPE-1 cell line), comparing their activity with cisplatin. The internalisation in PC3 cancer cells were first analysed, and the AuNPs system without any PEGylate linker showed a better internalisation. Moreover, they observed also a higher IC_{50} value for the non-PEGylate system ($IC_{50} = 9.3 \pm 2.3 \mu M$), similar to cisplatin, compared to the PEGylate ones ($IC_{50} = 100 \pm 30 \mu M$). Selected the no-PEGylate Pt in the AuNP-BNN-Pt conjugate, they analysed its cellular uptake through the quantification of gold and platinum by particle-induced X-ray emission (PIXE) analysis. A larger accumulation of Pt, compared to Au, was observed in the tumor cells. Moreover, the cytotoxic activity and the selectivity of **AuNP-BBN-Pt** and cisplatin were compared in normal prostate epithelial cell line (RWPE-1). The conjugate system showed an IC_{50} value of $97 \pm 18 \mu M$, while the drug $8.1 \pm 1.9 \mu M$ with a respectively selective index of 10 and 1.3. The highest selectivity of **AuNP-BBN-Pt** was due to the presence of the targeting BBN peptide that promoted a preferential uptake in the GRPR-positive cell line (PC3 cancer cell) compared to the RWPE-1 cell line. *In vivo* studies, in mice with PC3 tumor, were then

performed. They radiolabelled the **AuNPs-BBN-Pt** with ^{67}Ga ($^{67}\text{Ga-AuNP-BBN-Pt}$), for studying the biodistribution of the system by microSPECT-CT imaging. A long retention of $^{67}\text{Ga-AuNP-BBN-Pt}$ at the tumor site and a small distribution in surrounding organs and tissues, even after 72 h of injection, were observed. Hence, their work demonstrated the ability of GRPR-targeted AuNPs for the specific delivery of Pt(IV) prodrugs to prostate cancer PC3 cells, within an image-guided and theranostic approach.⁷¹

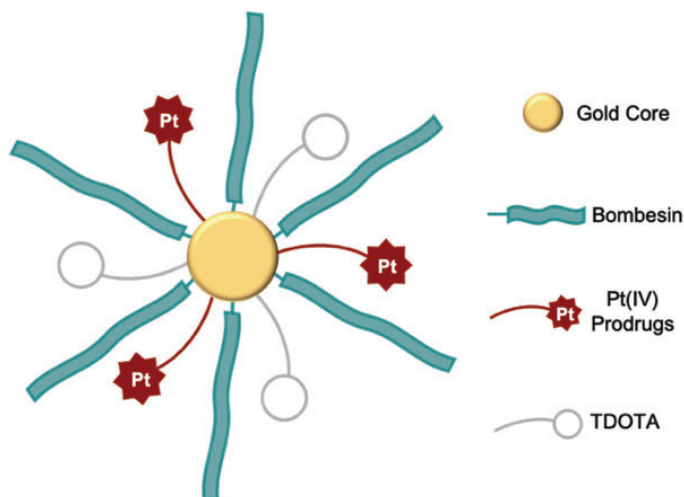


Figure 1.19 Schematic drawing of the chemical structure of **AuNP-BBN-Pt** nanoparticles design by Paulo and co-workers. Scheme adapted from ref. 71.

1.3.2. Protein structure: the four hierarchical levels of organisation

In 1838, Jöns Berzelius coined the word “protein”; from the Greek word *proteios* meaning “primary” or “of first rank”. Indeed, proteins are the most prevalent biological macromolecules, present in all cells and cell components.⁹⁷

Proteins are complex biomolecules that play essential roles in various biological processes. They have a four-level structural organisation, including primary, secondary, tertiary, and quaternary structures, which are formed by different interactions between amino acids (**Figure 1.20**).

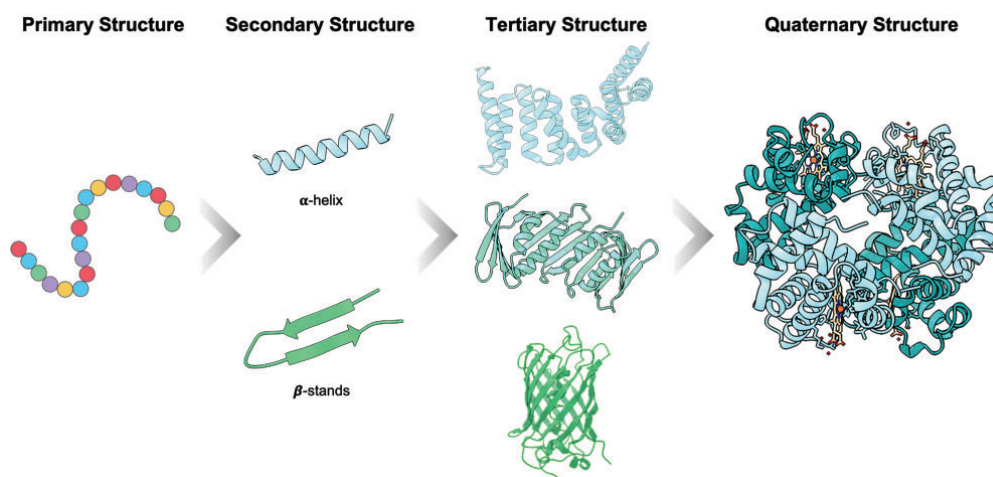


Figure 1.20 Primary, secondary, tertiary, and quaternary structure of a protein. In the primary structure, each circle represented an amino acid. The two main secondary structure elements, α -helix and β -strand are shown. For the tertiary structures are reported three examples: Tetratricopeptide repeat (TPR) protein helical structure composed by only α -helical motifs (PDB ID: 2aVp), Proliferating cell nuclear antigen (PCNA) protein composed by α -helical and β -sheets motifs (PDB ID: 1GE8), and the Green Fluorescence Protein (GFP) composed predominantly by β -sheets forming a β -barrel structure (PDB ID: 2B3Q). To illustrate the quaternary structure is reported the hemoglobin structure in which monomers of the tetrameric structure are colored differently (PDB ID: 1SHR).

The primary structure is the linear sequence of amino acids linked together by peptide bonds. This type of bond is a covalent bond between the carboxyl group of one amino acid and the amino group of another. Due to the chemical nature of the amide bond, the peptide link between the two amino acids acquires a nature of a partial double bond. The C-N distance (1.32 Å) is indeed shorter than a normal single bond and slightly longer than a double bond. This characteristic introduces rigidity to the structure making it unable to rotate freely and, as a consequence, all the peptide groups lie in the same plane. There are mainly 20 natural amino acids and all of them are α -amino acids with the common structure reported in **Figure 1.21**.^{97,98} Amino acids can exist in the L-amino acid and in D-amino acid forms, such as for the carbohydrates and nucleic acids. However, only the enantiomer L-amino acid and the D-ribose are present in nature for proteins and nucleic acids respectively. This homochirality in the single amino acid of proteins, confer homochirality as well for the higher-order structures, such as secondary and tertiary ones.^{99,98} Commonly to all these amino acids are the amino group, the carboxylic acid one and a hydrogen link to the α carbon. The fourth bond is represented by the R group, or side chain, that is different in each amino

Chapter 1

acid and varies in size, polarity, hydrophobicity, charge, volume etc (**Figure 1.21**). The linear sequence of amino acids, or primary structure, mainly determines the secondary and tertiary structure. Due to the planar nature of the peptide bond, the allowed secondary structures are α -helix and β -strands. The α -helix conformation is obtained through internal hydrogen bonding between nitrogen (donor) and oxygen (acceptor) atoms. On the contrary, β -strands structures are not able to form internal hydrogen bonds and are assembled with hydrogen bonds between the different strands. The assembly of two or more β -strands forms a structure called β -sheet. The tertiary structure is the assembly of the secondary structures in a stable, compact and biologically active conformation. The last structure, is the quaternary structure, in which several protein chains or subunits interact through non-covalent bonds form larger multimers.^{97,98}

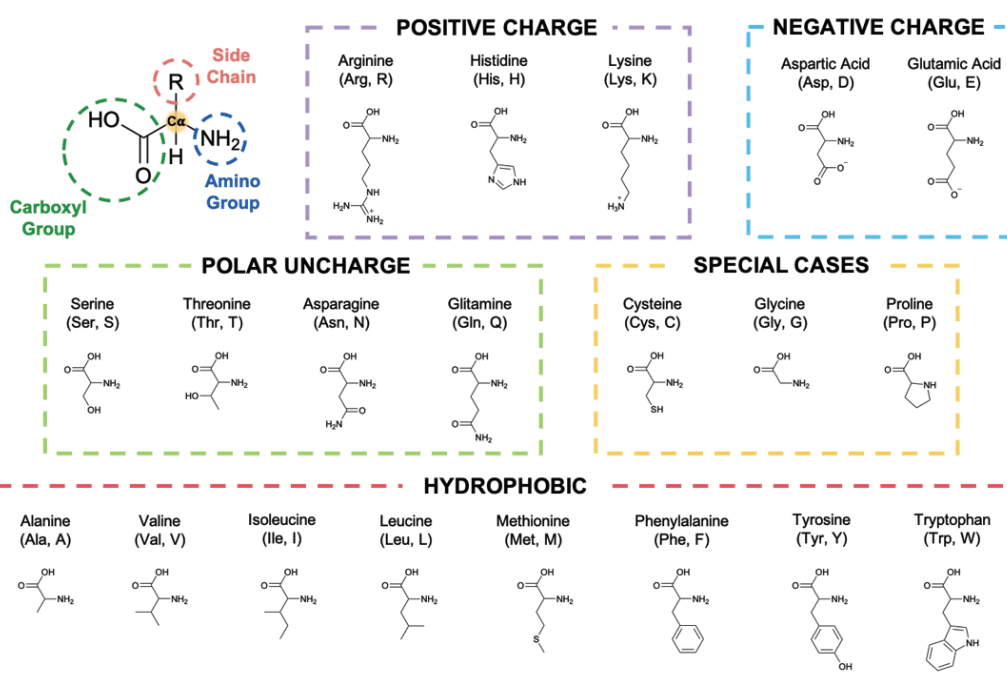


Figure 1.21 Structures of the 20 amino acids, classified by the charge of their side chains. On the top, from the left panel to the right one: the general structure of an amino acid with the amino group (dark blue dash circle), the carboxyl group (dark green dash circle) and the general side chain R (salmon dash circle) linked to the C_α . Amino acids with positive charge side chain (light purple rectangular) and amino acids with negative charge side chain (light blue rectangular). On the middle, on the left panel polar amino acids with uncharged side chain (light green rectangular) and on the right one, special cases amino acids (yellow rectangular). On the bottom, amino acids with hydrophobic side chain (red rectangular).

1.3.3. Repeat proteins

Repeat proteins were identified for the first time in 1990. These proteins are formed of tandem arrays of a small structural unit. The length of the repeat units can vary from 18 to 47 amino acids and can be composed by α -helix, β -strands, or a combination of the two secondary structure elements. A characteristic of repeat proteins is that each repeat interacts only with the two adjacent repeats resulting in linear, modular, and extended structures in contrast with the globular proteins. Globular proteins indeed present compact tertiary structures where residues far apart in the linear sequence interact to each other. The most abundant and well-known repeat proteins are: armadillo repeats (ARMs), leucine-rich repeats (LRRs), ankyrin repeats (ANKs), and tetratricopeptide repeats (TPRs).^{100,101}

Armadillo repeat proteins are composed by 42 amino acids that were first discovered in 1989 in the product of the *Drosophila melanogaster* segmentation polarity gene Armadillo. ARMs are quite abundant in eukaryotic proteins that take part in different cellular processes such as signalling, transport, and cytoskeletal regulation. Armadillo domain is a right-handed superhelix where each repeat is composed of three α -helices. Moreover, since these repeats are characterised by the conservation of the hydrophobic core residues, the superhelix structure with hydrophobic core is the structural basis present in all ARMs proteins (**Figure 1.22**).^{102,103}

Leucine-rich repeats are usually 20-30 amino acid long with a range between 2 and 42 number repeats. LRRs are present in a huge number of proteins, from virus to eukaryote and are involved in protein-protein interactions.¹⁰⁴ Furthermore, these repeat proteins present a high number of variations in the sequence and can be divided into two regions within the domain: a highly conserved segment, 11-residue stretch with the conserved sequence LxxLxLxx(N/C)xL (where L indicates leucine, N or C indicate asparagine or cysteine, respectively, and X is any amino acid)¹⁰⁵ and a variable segment.^{104,106} Arc or horseshoe shapes are adopted by LRR domains; a bowed tube on the inner face, with a parallel β -sheet and the outer face with a variety of secondary structures, such as α -helix, 3_{10} -helix, pII, and β -turn, specific to each LRR subfamily (**Figure 1.22**).^{104,106}

Chapter 1

Ankyrin repeats proteins consist typically of 33 amino acids with β -turn followed by two antiparallel helices and a loop reaching the β -turn of the next repeat. ANKs proteins are usually composed by 4 to 6 repeats, however it was observed that there is not a specific limitation on the motifs number. Like other repeat proteins, ANKs are involved in protein-protein interactions. Even if all of their surface can participate in these interactions, most ANK domains interact with their partners via the β -turns and then the α -helices (**Figure 1.22**).^{107,108}

The last repeat proteins reported are the tetratricopeptide repeat. This type of proteins was identified in 1990 and their name emerges from the 34 amino acid sequence that constitute the single repeat unit. Each repeat motif forms a helix turn helix motif and adjacent repeats stack together in a parallel way to create a superhelical structure. TPR proteins are usually composed by 3 to 16 repeats with some proteins displaying a larger number of repeats. It was observed that in natural proteins 3 is the most common number (**Figure 1.22**).^{109,110}


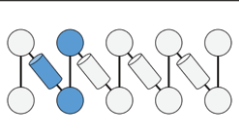
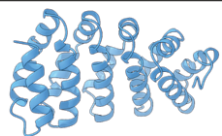

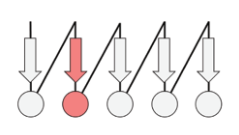
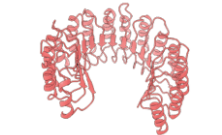

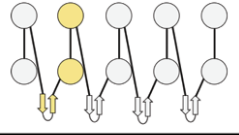
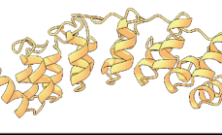

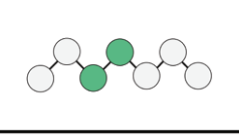
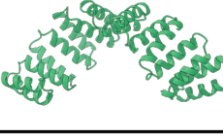
Repeat type	Residues per repeat	Structural motif	Topology	3D view
ARM	42			
LRR	23-28			
ANK	33			
TPR	34			

Figure 1.22 Representation of repeat protein scaffold. In order from the top to the bottom: ARM (PDB ID: 4DB9), LRR (PDB ID: 1a4y), ANK (PDB ID: 4o60) and TPR (PDB ID: 5xi8).

TPRs have been extensively used in protein engineering. From the alignment of natural TPR sequences, the CTPR (consensus tetratricopeptide repeat) sequence was obtained. The sequence of CTPR was designed by Regan's

group from a statistical analysis of natural TPRs.¹¹⁰ As the natural TPRs that are assembled in a tandem repeat arrays, CTPR proteins maintain the helix conformation forming a right-handed superhelical structure.¹¹¹ Only few amino acid positions in CTPR sequence are conserved and are responsible for maintaining the proteins fold. The amino acids in the other positions instead can be substituted, without compromising the TPR fold, for introducing new functionalities like different chemical reactivities or specific bonding activities (**Figure 1.23**).¹¹² Moreover, CTPR proteins are highly thermally stable when compare to the natural TPR and their stability increases with the number of repeats. For example, in 2011, Cortajarena *et al.* reported two studies related to CTPR stability.^{113,114} In the first example, they investigated the equilibrium stability of CTPR proteins, composed by different number of an identical consensus repeat motif, screening from 2 (CTPR2) to 20 (CTPR20) repeats. From calorimetric studies, they observed an increase in the stability, reflected by an increase in the melting temperature (T_m) with the number of CTPR repeats.¹¹² Cortajarena *et al.* investigated also the thermal stability of CTPR proteins by introducing different mutations into the basic repeating unit.¹¹⁴ They observed an increase in the stability of the mutated proteins compared to the original CTPR sequence through chemical and thermal denaturation experiments. Significant increase in the melting temperature (T_m) was obtained, with a T_m at around 80°C for the CTPR2 variants, when compared to natural TPRs with two repeats protein of about 40°C.¹¹⁴

Due to their high stability, CTPR proteins are more tolerant to the introduction of mutations in their sequence,¹¹⁵ thus being ideal scaffolds for engineering protein-based multifunctional systems.

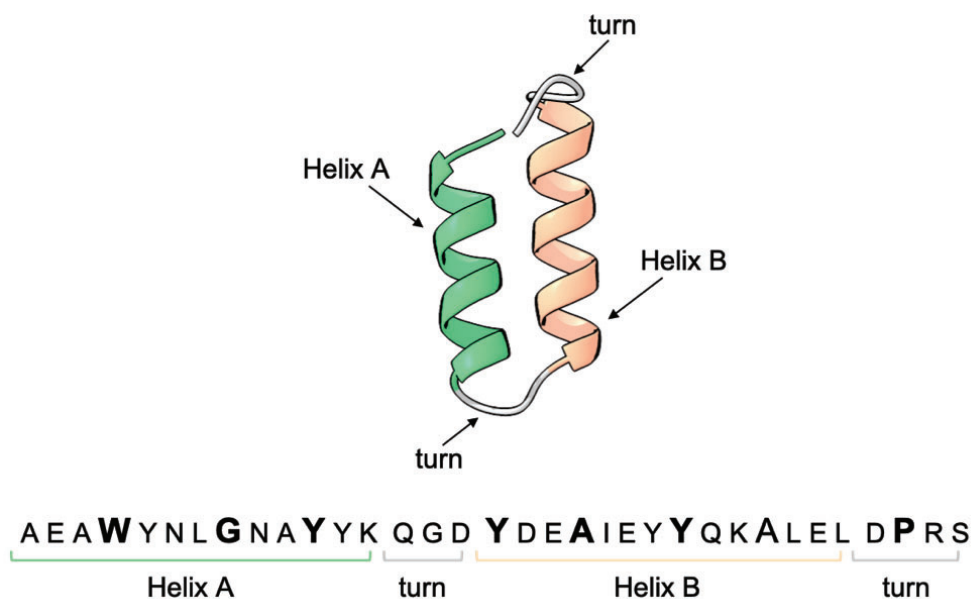


Figure 1.23 Ribbon representation of a single consensus tetratricopeptide repeat (CTPR) unit, in which the A helix is colored in green and the B helix in orange. Repeat extracted from the crystal structure of a CTPR8 (PDB ID: 2AVP). The amino acid sequence for the CTPR is shown related to the different secondary structural elements with the repeat and highlighting the conserved positions in bold.

1.3.4. Proteins as scaffold for multifunctional assembly systems

Despite recent major improvements in the diagnosis and management of common diseases, new technologies and strategies to reduce the limitations and the disadvantages of the common therapeutic and diagnostic approaches are still needed to be explored. Nature has been of inspiration for researchers for developing new tools for therapy and diagnostics. In particular proteins have been identify as good candidates to play as scaffolds in the development of multifunctional systems, hosting active components such as metal, organic molecule, or nanomaterials.¹¹⁶ Many biohybrid arrangements can be identified in nature, an example is given by the metalloprotein, hemoglobin. This protein contains a metal cofactor and is the principal human oxygen carrier. It consists of two α and two β subunits, where a binding pocket for the heme group (porphyrin structure with a ferrous ion in the centre) is present.¹¹⁷ Moreover, in recent years, new systems based in the used of repeat proteins as scaffold have been developed. Their modular structure indeed gives the possibility to introduce different elements at specific positions within the structure encoding precise

arrangements. Hence, the fusion of therapeutic engineered proteins with nanomaterials or organic molecules in protein-based hybrids results in cooperative entities that exhibit new functionalities. These hybrids are capable of overcoming the limitations of current applications and could lead to the development of new solutions. In this context, CTPR proteins represent an ideal template for anchoring different functional elements.¹¹⁶ The Cortajarena's group reported examples on the design of CTPRs to arrange porphyrins molecules,¹¹⁸ gold nanoparticles (AuNPs),¹¹⁹ and single-walled carbon nanotubes (SWCNTs),¹²⁰ in selective positions and orientations through the introduction of mutated residues along the CTPR superhelix.¹¹⁶ These works demonstrated that CTPR proteins can serve as templates for the development of multifunctional hybrids, with a precise control over the arrangement of the functional elements, enabling the combination of the properties of the protein and the ones of the arranged elements.¹¹⁶ In the porphyrins-CTPR hybrid, engineered cysteines mutations were used for the conjugation with a specific number of porphyrins derivatives at a defined distance and orientation.¹¹⁸ The same concept was then translated to the AuNPs system, where the nanoparticles were introduced by covalent bonds with the cys at selected positions of the proteins scaffold.¹¹⁹ Additionally, for binding SWCNTs, the presence of aromatic tyrosines and inserted histidines to the inner part of the superhelix were exploited to allow CTPR to wrap around the tubes.¹²⁰

Furthermore, these modifications give the possibility to combine the templating, biological activity, and biocompatibility of the protein scaffold with the potential diagnostic and therapeutic modalities of the elements bounded.^{121,116} Some examples are given by the use of CTPR proteins combined with metal nanocluster, quantum dots¹²² and magnetic nanoparticles.¹²³ For example, the used of quantum dots for biomedical applications is studied intensively nowadays since their high emission quantum yield, the excellent resistance to photo-bleaching, their photostability and the large Stokes shift.^{124,125,126,127} Our group reported a protein engineering approach for the synthesis and stabilisation of biocompatible metal nanoclusters (NCs)¹²⁸ and cadmium sulphide (CdS) quantum dots (QDs).¹²² We employed CTPR proteins with different number of modules to explore the effect of the size of the metal coordination

Chapter 1

obtained through the histidine and cysteines residues. The Prot-QDs and Prot-NC hybrids showed an improvement on the photoluminescence and photostability properties, as well as on the stability under physiological conditions. Moreover, both Prot-QDs and Prot-NC are able to enter into living cells, showing great cell labelling capacity without affecting cell viability, making them interesting candidates for biomedical applications.^{122,128} This approach could be translated also to other protein architectures with α -helices structure for tuning the properties of the protein-hybrid construct for application in different fields.

One of the goals of the development of protein hybrids is producing new therapeutic and detection agents. Proteins can act as stabilizing frameworks, drug storage, and targeting agents, while the nanomaterials possess properties that can be exploited for detection and other therapeutic applications. By combining the two, therapeutic proteins can be merged with custom-designed scaffolds that accommodate a nanomaterial, creating a more versatile platform that enhances existing treatment or detection methods.¹¹⁶ An interesting work was reported by Yang *et al.*, in which they showed that α -lactalbumin can host fluorescent ultras-small gold nanocluster (AuQCs) and keeps its ability to form an anticancer lipoprotein complex for the delivery of its therapeutic effect.¹²⁹ Yang *et al.* aimed to combine a systemic diagnostic with a local therapeutic approach. For this purpose, both whole-body imaging (to locate the tumour) and local imaging abilities with microscopic resolution (to verify drug distribution) were the key aspects. The amino acids tryptophan, lysine, and cysteine, abundant in the α -lactalbumin, were fundamental for the synthesis and the optical properties of the AuNCs (fluorescence emission at 450 nm, 520 nm, and 705 nm). They indeed synthesised three different nanoclusters with fluorescence that covers from the visible to the near-infrared region spectra (AuQC₄₅₀, AuQC₅₂₀, and AuQC₇₀₅), when excited at a single wavelength. Among the three, AuQC₇₀₅ showed a superior *in vivo* imaging signal-to-noise ratio and was selected as molecular imaging probe for their studies. Moreover, Yang *et al.* observed that AuQC₇₀₅ exhibited long circulation times, low accumulation in the reticuloendothelial system, sustained tumour retention, no toxicity effect and renal clearance. Since the large Stokes shift of the AuQCs₇₅₀, due to the combination of the excitation at 500 nm and the emission at 7000 nm, the

autofluorescence was minimised defining an optimal visible–NIR imaging window in which the tissue–light interaction was minimal in the short-wavelength visible and NIR regions. This facilitated the detection and image-guided resection of the breast tumours *in vivo* (xenograft mice bearing MDA-MB-231 tumours). Moreover, the partially unfolded structure of α -lactalbumin in the nanoprobe helped with the formation of an anti-cancer lipoprotein complex with oleic acid that triggers the inhibition of the mitogen-activated protein kinase (MAPK) and PI3K–AKT pathways, immunogenic cell death and the recruitment of infiltrating macrophages. Hence, the main goals reached with this study, were: a whole-body imaging detection of breast cancer with magnetic resonance imaging (MRI) and computed tomography (CT); a local imaging of tumor extent using fluorescence; and a potent local antitumor therapy. Furthermore, thanks to the nanoprobe's safe profile and biodegradability, they are suitable for the systemic detection and localised treatment of cancer.¹²⁹

In 2021, a protein-nanomaterials hybrid was investigated by Cortajarena's and Pereiro's groups using a fluorescent-labelled Hsp90 protein inhibitor with specific Hsp90 binding properties to reduce myocardial pro-fibrotic events *in vitro* and *in vivo*. A cryo 3D imaging approach was used for establishing the intracellular internalisation of the hybrid system.¹³⁰ The proteins employed, were designed in a previously work of Cortajarena *et al.*, with three modified CTPR modules with different affinities for the C-terminal region of Hsp90.¹³¹ Moreover, four cysteines were inserted in the protein sequence for the specific metal coordination and stabilisation of nanoclusters (NC) with different compositions.¹²⁸ Both *in vitro* and *in vivo* experiments demonstrated the potential of these type of multifunctional engineered systems reaching the inhibition of Hsp90 with the use of the engineered protein and allowing the specific detection for the therapeutic molecule, both *in vivo* and *ex-vivo* by tracing the metal nanocluster. Two therapeutic agents were employed, with and without the engineered Hsp90 inhibitory domain, **TPR-Hsp90-AuNC** and **TPR-AuNC**, respectively. Through 3D cryo correlative light and X-ray tomography (CLXT), they observed that the presence of the metal cluster on the protein-nanomaterial hybrid, supported the internalisation and the therapeutic effect of the Hsp90 inhibitory activities of both primary cardiac mouse fibroblasts and NIH-3T3

Chapter 1

cells,¹³⁰ making evident the results obtained in the previous studies.^{128,132,133} Later, soft X-ray tomography (cryo-SXT) experiments showed a distribution of the **TPR-Hsp90-AuNC** system in multivesicular bodies (MVBs) and throughout the cytoplasm. Moreover, the use of cryo-SXT allowed to understand the reaction of the cells due to the treatment by evaluating the morphological changes induced. For example, the NIH-3T3 fibroblasts demonstrated noticeable indications of stress in the form of mitochondria swelling, which was probably caused by the treatment of **TPR-Hsp90-AuNC**. This swelling occurrence was not seen in the case of **TPR-AuNC**, indicating that there was a direct correlation between the molecular effects induced by the binding of the hybrid functional protein to the C-terminal end of Hsp90. Cortajarena's and Pereiro's groups observed that the inhibition of Hsp90 as a key factor involved in the profibrotic signalling cascade, affects the Hsp90-TGF β RI interaction. This promoted the reduction of key myocardial pro-fibrotic events and indicated a new route for the development of antifibrotic and anticancer therapies. In addition, their studies showed how this system could be used as a therapeutic agent for the intracellular localisation for understanding the effect at the cell ultrastructure level, combining the function of the protein with the one of the elements coupled (in this case, fluorescent gold nanocluster).¹³⁰

This study is one of the examples that demonstrate that proteins can be applied for the design of the next generation of pharmaceuticals. Engineered proteins can display therapeutic properties similar to antibodies. However, small protein binders are a better alternative since their reproducibility, stability, biocompatibility and production cost is remarkably better when compared to antibodies. Moreover, modifications of protein binders can be used to enhance their affinity toward target molecules. In particular, repeat proteins can be considered ideal systems, since their modules can be combined with other modules to generate a multifunctional protein, including units that host nanomaterials. Since nanomaterials properties depend on size, shape and structures, the development of protein-based templates that can regulate these characteristics is the key step for the generation of the functional hybrids. In particular, CTPR proteins show good potential for the improvement of protein-hybrid nanomaterials for the biomedical field where the protein is employed as a platform. Furthermore,

the most interesting and promising aspect is not only that they are combine together what the single elements can do separately, but also new properties are showed due to the hybridisation.¹¹⁶ Thus, the capability to develop multifunctional hybrid systems opens the door to realise tailored protein-based systems for more complex applications, such as the one investigated in this thesis, including drug delivery and prodrug photoactivation.

Chapter 2

Bioorthogonal catalysis: the dual role of transition-metal complexes

Chapter 2

2.1. Introduction

Over the years, different approaches have been developed to defeat cancer. With the word cancer, we refer to a group of diseases characterised by uncontrolled cell growth, consequence of a series of disorders. These disorders make cancer a very dynamic condition that is the principal obstacle for reaching an effective cure.^{134,135,136} Chemotherapy, surgery, and radiotherapy are the most common methods, but other approaches such as immunotherapy, gene therapy, and nanomedicine are emerging. Depending on the stage and on the type of cancer and on patient status, a specific treatment is selected. It is possible to receive only one treatment, but for the majority of cases, a combination of more than one approach is adopted. These treatments are built on:

- Chemotherapy: is based on the use of cytotoxic drugs that kill cancer cells.
- Surgery: is a physical procedure to remove the cancerous tissue.
- Radiotherapy: high-powered energy beams, such as X-rays or protons, are adopted to kill cancer cells in a localised tissue area of the body.
- Immunotherapy: is a therapy that employs the body's immune system, helping the body to recognise and destroy cancer cells.
- Gene therapy: is based on using a vector, generally a virus, to deliver specific genetic information into cancer cells changing their native characteristics.¹³⁷

Along the years, many efforts have been spent to try to improve the classical approaches (chemotherapy, surgery and radiotherapy).¹³⁷ Commonly, organic and inorganic compounds, are used in anticancer treatments and many of them have been designed and synthesised. Compounds like doxorubicin (organic)¹³⁸ and cisplatin (inorganic),^{8,9} act by inhibiting cells division and, since cancer cells are characterized by faster growth, they are the predominant target.¹³⁹ However, these drugs are not selective to cancerous cells and can attack the healthy ones as well.

Hence, focusing on the inorganic compounds, the development of metal-based anticancer prodrugs, the inactive form of the drugs, was one way for the resolution of the undesired side effects produced by the drugs. The

Chapter 2

inactive forms indeed are usually less toxic, or almost inert, compared to the drugs and can be activated by enzymatic and/or chemical tools under specific conditions. The use of prodrugs is an encouraging approach to try to raise the therapeutic efficacy and reduce the adverse effects of the pharmacologically active agents by enhancing the stability and the solubility, as well as the biological half-life time, improve the bioavailability and the tissue-target delivery.¹⁴⁰ As reported in Chapter 1, Pt(IV) complexes are good examples of metal prodrugs, extensively studied along the years.

In the development of the use of prodrugs for anticancer treatments, bioorthogonal chemistry recently emerged as an interesting tool for enhancing their selectivity in the activation process.^{141,142} The term bioorthogonal was coined by Bertozzi and co-workers in 2003 to describe the use of Staudinger ligation reactions for the selective modification of glycoproteins with biochemical and biophysical tags.¹⁴³

This reaction refers to chemical modifications that can be performed within living biological systems, such as cultured mammalian cells or even complex organisms like zebrafish or mice, without disrupting their host biochemistry. In the drug development, biorthogonality is primarily concerned about the ability of a catalytic process to occur selectively and trigger a therapeutic response without inducing undesired side reactions. By achieving this selectivity, bioorthogonal reactions offer a powerful tool for studying and manipulating biological systems, with potential applications in drug development, imaging, and diagnostics.¹⁴²

2.1.1. Bioorthogonal chemistry and catalysis reactions combined together

Enzymes are fundamental for the existence of life and its progress. Nature indeed has developed various enzymes for performing biological functions. An enzyme is a protein that acts as a catalyst in living organisms. In some instances, protein alone is inadequate to catalyse a reaction, for this reason such enzymes bring a non-protein component called cofactor to generate a functional catalyst. Generally, metal ions (such as Mn(II) in arginase or Ni(II) in urease) or coenzymes (organic molecules, for example pyridine nucleotides NAD⁺ and NADP⁺, flavin adenine dinucleotide (FAD), biotin, and

heme) are chosen as cofactors.¹⁴⁴ Thanks to their high efficiency in the catalyst tool, enzymes constitute a great reference for researches for the development of synthetic catalysts. In recent years indeed, the synthesis of molecules, that mimic the enzyme behavior, is growing.¹⁴⁵ Moreover, their combination with bioorthogonal chemistry has shown to be a promising approach for the activation of substrates in biological environments.¹⁴² Bioorthogonal reactions are characterized by biocompatibility and selectivity in living system and can be performed in physiological conditions. Thus, biorthogonal catalysis needs to maintain the biocompatibility, as well as selectivity, and not be toxic for the organism at the concentration required for bioorthogonal catalysis.^{146,147}

In the recent years, some studies have reported on the use of metal compounds in complex aqueous buffers or biological environments.^{148,149} Organometallic catalysis in biological systems is emerging as a relatively new field, and it has the potential to unlock opportunities for biological research by enabling non-natural catalytic transformations of exogenous substrates within living organisms. This has significant implications, such as the ability to generate drugs *in situ*, amplify optical signals to enhance the detection of biomarkers, or modify biomolecules using metal-promoted reactions, among other applications.¹⁵⁰ Naturally, obtaining a successful organometallic catalytic reaction in aqueous environment of a living organism is still the biggest challenge. The high concentration of thiols and amine indeed can kill the catalytic activity of the metals. Moreover, confinement in a specific environment of the catalyst, or the target ability of the catalytic complex are points that have to be reached. The improvement in the ligand design indeed might help to find a good balance between reactivity and biological stability of the metal complex.¹⁵⁰

It is important to take into account that in bioorthogonal catalytic reactions, the role of the catalyst is not always attributed to a metal complex. In the last years, our group have started to shift their studies toward the use of organic photocatalyst, such as flavins. Organic photocatalyst can be synthesised from renewable materials, with a good chemical stability due to avoiding metal coordination chemistry.^{151,152} Moreover, for the *in vitro* and

in vivo applications, the use of organic catalysts is more attractive since their great biocompatibility.¹⁵³

This chapter discusses about the combination of bioorthogonal chemistry with catalysis reactions. In particular it will underline the use of a metal complex as catalyst in bioorthogonal catalysis and as substrate for bioorthogonal photocatalysis.

2.2. Bioorthogonal catalysis with metal complex as catalyst

Catalysis is defined as a chemical reaction that occurs in the presence of a catalyst with an increase in the reaction rate without any change in the catalyst amount.¹⁵⁴ The use of metal catalyst has allowed the developed of a huge number of chemical transformations that could not be performed with the classical methodologies.¹⁵⁰ Generally, the majority of these catalytic reactions (for example hydrogenation, Suzuki cross-coupling reactions) take place in organic solvent, in absence of water and under air free condition.^{150,155} However, in the last years, different metal catalysed reactions, that take place in water, have been discovered. This is an interesting result for the implementation of catalytic transformation for the generation of drugs for biological and medical applications since the basic solvent of biological habits is water.¹⁵⁰

In this section, a summary of the most relevant examples of catalysis reactions based on transition-metal complexes is described. One of the first reaction based on the use of transition metal catalyst, reported in 1985, was a ruthenium-catalysed hydrogenation of C-C double bonds in fatty acid inside mesophyll protoplast using hydrogen gas. Unfortunately, the conditions needed for the reaction were too drastic for the cells, and some damage were observed after one hours of reaction.¹⁵⁶ Years later, in 2002, Sharpless and Meldal developed the noteworthy Copper-catalysed Alkyne Azide cycloaddition (CuAAC) reaction (**Figure 2.1a**). This reaction has very good characteristics such as high reaction rate, compatibility with physiological buffer and chemo selectivity. Furthermore, it was classified as bioorthogonal reaction and has been extensively used for biological applications. However, the toxicity of copper and the necessity of reductants

like ascorbate still appeared an obstacle for the living application of the reaction.¹⁵⁷ In 2006, Meggers and co-workers made a breakthrough in this field with a deallylation reaction promote by Ru(II) complex (**Figure 2.1b**). They observed that [Cp**Ru*(cod)Cl] (Cp* = pentamethylcyclopentadienyl, cod = 1,5-cyclooctadiene) was able to liberate amines from their respective allyloxycarbamates in living mammalian cells (HeLa) tolerating the combination of water, air and thiols. The design of catalysts that work under physiological conditions, is usually complicated by the presence of air, water and cellular components (such as thiols) that poison the metallic catalyst. In addition, they observed that by the reaction of bis-allyloxycarbonyl-protected rhodamine 110 with the Ru catalyst, in presence of cell exact and additional glutathione (GSH 3.5 mM), only 6% of yield can be reached. Under the same condition, with an addition of another thiol (thiophenol), the yield of the reaction increased to 80%.¹⁵⁸

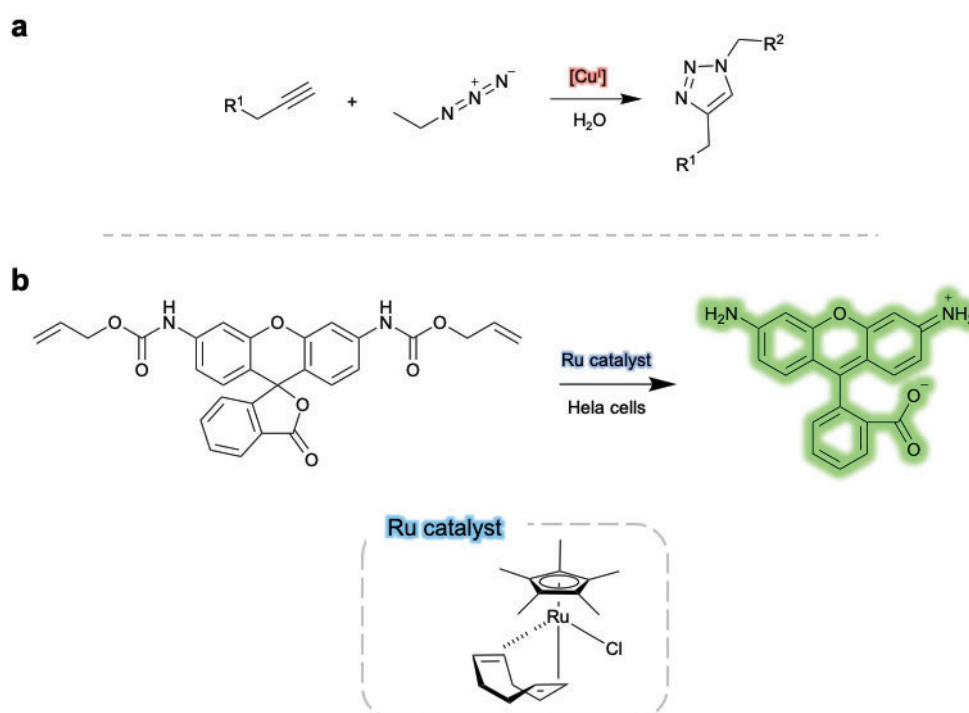


Figure 2.1 (a) Copper-catalysed alkyne azide cycloaddition (CuAAC) from Sharpless and Meldal work. Scheme adapted from ref. 157. (b) Ruthenium-catalysed deallyloxylation from Meggers and collaborators work. Scheme adapted from ref. 158.

Later, in 2014, the same group reported their progress on the catalytic uncaging of allyloxycarbonyl-protected amines, under biologically relevant conditions and within living mammalian cells. They developed new Ru complexes changing their ligands compared to the one employed in their

previous work (**Figure 2.2**). Moreover, the new catalysts did not have the methyl groups since they noticed that they reduce the activity of the catalyst. Hence, the new Ru complexes developed showed the following structures: $\text{CpRu}(\text{QA})(\text{allyl})\text{PF}_6$, $[\text{CpRu}(\text{QA-OMe})(\text{allyl})]\text{PF}_6$ and $[\text{CpRu}(\text{QA-NMe}_2)(\text{allyl})]\text{PF}_6$ (QA = 2-quinolinecarboxylate, A-OMe = 4-methoxy-2-quinolinecarboxylate, QA-NMe₂ = 4-(N,N-dimethylamino)-2-quinolinecarboxylate). The new designed catalysts showed a higher turnover number (TON), reaching for $[\text{CpRu}(\text{QA-NMe}_2)(\text{allyl})]\text{PF}_6$ a value of 270 cycles (60-fold more than the previous work) under biological conditions. They observed that the change in the ligand involved an increase in the stability and reactivity of the catalyst under biological conditions (GSH 5 mM in water/DMSO 200:1) as well as within the cellular cytoplasm. Furthermore, they demonstrated that the stringent requirements of a cellular environment, such as millimolar concentrations of thiols, are not necessarily destructive to a catalyst, but can actually be helpful for a fast reaction. Strong thiol nucleophiles, such as glutathione, indeed actively participate in the catalytic deprotection mechanism investigated by Meggers and co-workers, shifting the rate-determining step from the allylation towards the uncaging step.¹⁵⁹

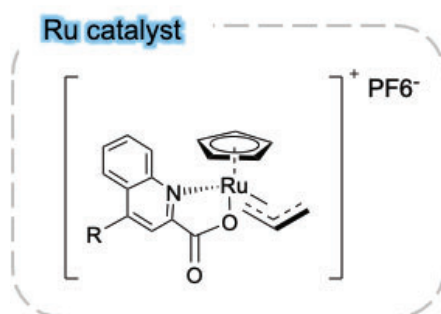


Figure 2.2 Ruthenium catalyst structure employed by Meggers and co-workers; R = H, OMe, NMe₂. Structure adapted from ref. 159.

In the same year, Marscareñas and collaborators reported the first demonstration of the use of metal catalysis to trigger DNA binding events in live cells. They investigated the metal-catalysed uncage reaction of DNA-binding agents, employing alloc-protecting groups, catalysed by Ru complex (**Figure 2.3**). The protecting group reacted with the amidine of fluorogenic DNA-binding bisbenzamidines and with the amino groups of ethidium bromide (chosen as DNA model binder). First, the catalytic uncaging process was investigated in organic solvent and in a biological media. In both the

cases, the reactions were conducted in presence of $\text{RuCp}^*(\text{COD})\text{Cl}$ as catalyst. In the organic solvent, after 20 min, starting material was observed; in the biological media instead a minor amount of the protected product was found after 20 min. Subsequently, Marscareñas' group analysed the deprotection and DNA binding of the DAPI derivative in living cells. They selected chicken embryo fibroblast (CEF) cell, comparing the behavior of DAPI alone to its derivative in the binding with the DNA with fluorescence microscopy. The alloc-protected DAPI, after 30 min of incubation with the cells, showed a distribution all around the cells. After 20 min of the treatment with Ru catalyst, they observed the typical nuclear staining of DAPI. They performed a control experiment, incubating the cell with DAPI alone, in the same work conditions founding that a higher concentration of DAPI was required for seeing a clear staining of the nucleus. This result suggested that the dialloc-derivative of DAPI was internalized very efficiently and converted into DAPI inside the cells, otherwise the staining intensity should have been similar in both cases. Hence, they demonstrated that using allylcarbamate as protecting groups for several DNA binder, not only the interaction with DNA decreased, but also the spectroscopic properties and cellular location changed. In specific, they demonstrated that the bis alloc-protected derivatives of DAPI or ethidium bromide are weaker DNA binders than the non-protected compounds and can be regenerated by reaction with a ruthenium catalytic system.¹⁶⁰

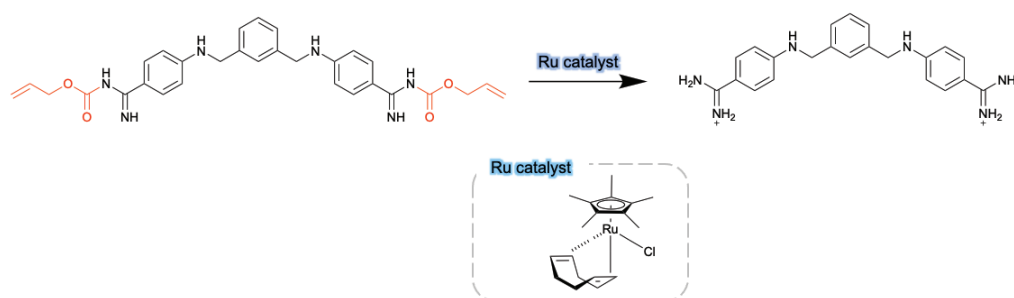


Figure 2.3 Catalytic deprotection of dialloc protected DAPI (in red the Alloc protecting groups) catalysed by $\text{RuCp}^*(\text{COD})\text{Cl}$ complex. Scheme adapted from ref. 160.

Besides ruthenium, other transition metal complexes used in catalysis reactions are palladium (Pd) and gold (Au). The use of Au as catalyst is broadly exploited on carbo and hydrofunctionalisation reactions (like cyclodimerisation) for its carbophilicity. The propensity of gold salts to bind to alkynes has also been used for performing reactions in biological

environment.¹⁶¹ Tanaka and co-workers used gold catalysis for transformation in biological environments. They reported a successfully gold-triggered conversion of 2-alkynylbenzamide (Ayba) protected prodrug into a bioactive anticancer drug (*i.e.* edoxifen, doxorubicin) (**Figure 2.4**).¹⁶² Edoxifen is an active metabolite of tamoxifen, a selective estrogen receptor modulator used in particular for preventing breast cancer in women and treat breast cancer in women and men. Some early phase (1 and 2) studies, have showed that edoxifen exhibited a substantial antitumor activity in tamoxifen-resistant patients, underline the benefit of the use of this active metabolite.¹⁶³ Doxorubicin is a chemotherapy compound, belonging to a class of drugs called anthracyclines. Generally, it is used for treat different types of cancer that affects he breast, bladder, kidneys, ovaries *etc.*¹³⁸ Tanaka and co-workers chose Ayba as protecting group for the study of gold-dependence release of secondary amine under mild and physiological conditions. To investigate the Ayba-based prodrug as anticancer therapeutics, the cytotoxic profile of endoxifen prodrug was tested in ER-positive MCF7 breast cancer cells. They observed, comparing the results of the drug with the ones of the prodrugs, a low difference in the EC₅₀ (55-57 μ M for the Ayba-prodrugs and 25 μ M for the endoxifen). A second anticancer agent, doxorubicin, was then investigated. Tanaka's groups found that under aqueous conditions, the released of primary amine-containing doxorubicin, catalyse by gold compound, was in a range of 60-80%. Based on these results, they moved their studies *in vitro*, exploring different cancer cells lines. An increase in the cytotoxic activity of the Ayba-protected prodrug was found for all the cells lines studied, with a decrease in the EC₅₀ values of: 299 to 52 nM for HeLa, 1420 to 720 nM for A549, and 260 to 50 nM for PC3. The aim of their study was indeed developing an amine releasing reaction that can be compatible in aqueus/physiological environments and can be orthogonally catalysed by gold with no interferences by other transition metals (such as palladium, ruthenium *etc.*). The ability to run multiple designed catalytic transformations without interference between them, could open novel avenues for biological intervention. Indeed, other metals could compete with the catalyst in the reaction, leading to a decrease in the yield of the desired product. In addition, if these metals can catalyse reactions that are not orthogonal to the desired one, they can drive to the formation of unwanted by-products.¹⁶²

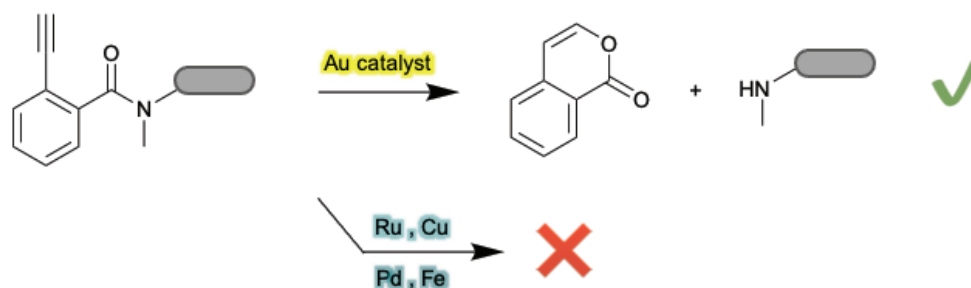


Figure 2.4 Bioorthogonal deprotection of Ayba group via Au-catalysed cyclisation and release of a secondary amine containing a drug (grey cylinder) developed by Tanaka group. Scheme adapted from ref. 162.

Although the direct administration of transition metal catalysts has been thoroughly investigated for therapeutic purposes, its effectiveness is hindered by issues related to solubility, stability, and biocompatibility. However, a possible solution to overcome these limitations is to incorporate transition metal catalysts into artificial nano-scale scaffolds.¹⁶⁴ For example, Rotello and co-workers fabricated a protein-sized bioorthogonal nanozymes, encapsulating hydrophobic transition ruthenium catalyst into the monolayer of water-soluble gold nanoparticles (2 nm gold core) (**Figure 2.5**). The activity of this catalyst can be reversibly controlled by binding a supramolecular cucurbit[7]uril ‘gatekeeper’ (CB[7]) onto the monolayer surface. The gold nanoparticles were decorated by a thiolate hydrophobic alkane chain layer in which the Ru catalyst, [Cp*₂Ru(cod)Cl] (Cp* = pentamethylcyclopentadienyl, cod = 1,5-cyclooctadiene), was encapsulated. The ligands chosen were composed also by a hydrophobic spacer (tetraethylene glycol layer), that provided the biocompatibility, and a dimethylbenzylammonium group as terminal moiety for binding the CB[7] gatekeeper and confer water solubility to the nanozymes. The presence of the CB[7], blocked the accessibility to the catalytic site of the substrate for the metal catalyst, inhibiting its activity. However, the catalytic activity of the nanozymes can be restored by the releasing of the gatekeeper molecules from the AuNPs. They observed indeed that with the addition of a competitive guest molecule, in specific 1-adamantylamine (ADA), the nanozyme activity was completely restored. The efficacy of their nanozyme was demonstrated both in solution and in HeLa cancer cells. Moreover, with this approach, the ruthenium complex was protected from the poisoning of cellular environment and it was possible control the activity of the

Chapter 2

nanozyme. In addition, Rotello and collaborators investigated also the intracellular prodrug activation of the same system, using palladium as catalyst instead of ruthenium to demonstrate the versatility of their catalytic platform. They employed the 1'-bis(diphenylphosphino)ferrocene)palladium(II)dichloride as Pd catalyst, encapsulating it in hydrophobic portion of the AuNP monolayer, and a modified 5-Fluorouracil (5FU) as prodrugs (**Figure 2.5**).¹⁶⁵ 5FU is indeed an antimetabolite drug used for cancer treatments, but shows toxic side effects due to its limited safety profile.¹⁶⁶ They introduced a propargyl moiety at position N1 to convert the 5FU into a prodrug form, blocking in this way its activity. They treated HeLa cells with the nanozyme and the prodrug 5FU, comparing their cell viability in presence and in absence of ADA. Cells that were incubated with also ADA molecule, showed an elevated toxicity at a higher concentration of pro-5FU, while with no ADA, cells retained almost 100% cell viability even at higher concentrations of pro-5FU. Hence, they observed that when the Pd catalyst activated the modified 5FU in the nanozyme platform, in presence of the competitive guest molecule (ADA), a substantial reduction in the cell viability occurred.¹⁶⁵ Despite the interesting results reported by Rotello and co-workers about the mechanism and development of this nanozyme, information about catalytic features of the reaction that they investigated is missing.

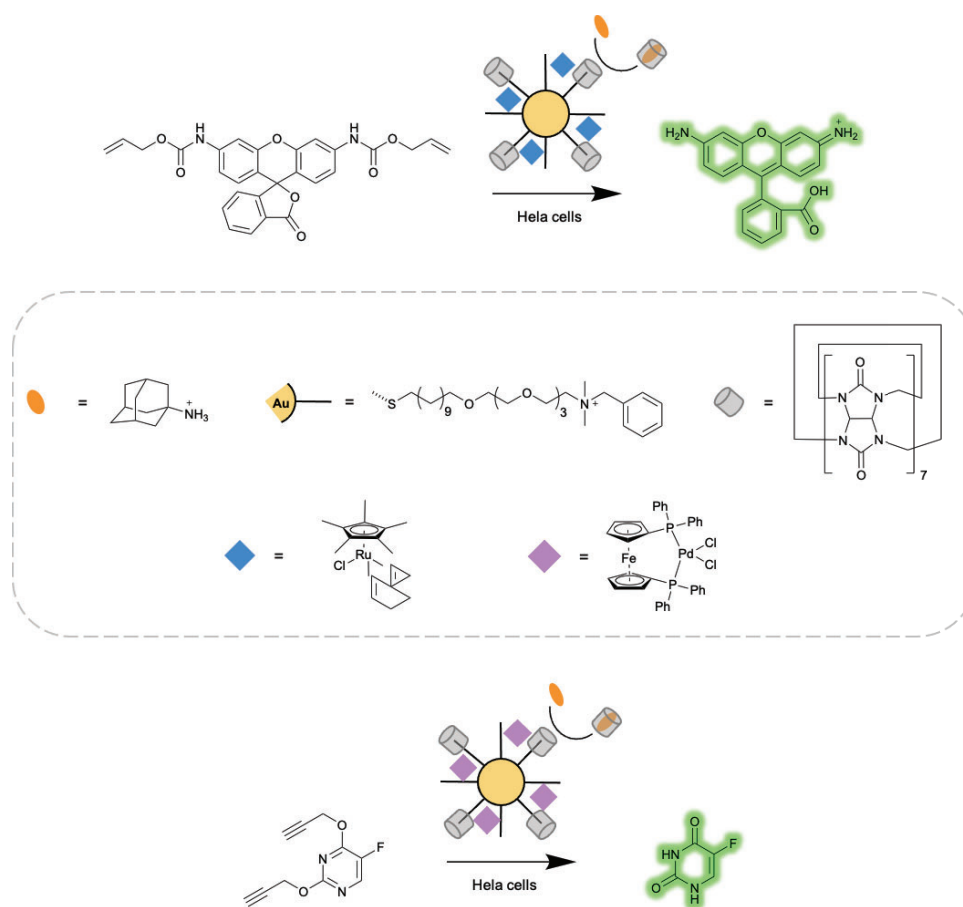


Figure 2.5 Ruthenium-catalysed deallyloxylation reaction (top) and palladium-catalysed prodrug activation (bottom) developed by Rotello's group. The substrate before the reaction (not fluorescent), the nanozyme structure (gold nanoparticle), the catalyst structures (blue rhombus and light purple)), the competitive guest molecule ADA (orange oval), the curcubituril CB[7] (grey cylinder) and the product of the reaction (fluorescent) are reported. Scheme adapted from ref. 165.

In 2018, the same group showed that the modification of the headgroup of the AuNPs coating, could modulate the cellular localisation of the NPs and the catalytic activity of the nanozyme. They synthesised two AuNPs with different monolayer coatings and a 2 nm gold core. A positively charged quaternary ammonium ligands were selected for studying the intracellular localisation (**Pos-NPs**), while zwitterionic sulfobetaine moieties were chosen for the extracellular localisation studies (**Zw-NPs**) (**Figure 2.6**). They generated then the nanozymes encapsulating in both the AuNPs monolayer, **Pos-NPs** and **Zw-NPs**, the ruthenium catalyst $\text{Cp}^*\text{Ru}(\text{cod})\text{Cl}$ (Cp^* = pentamethylcyclopentadienyl, cod =1,5-cyclooctadiene), obtaining respectively cationic **Pos-NZ** and zwitterionic (neutral) **Zw-NZ** nanozymes. First, Rotello and his collaborators investigated the selective cellular uptake

in HeLa and 264.7 macrophage cells observing that the cells treated with **Pos-NZs** showed a higher content of gold compared to the ones treated with **Zw-NZ**. Then, the ability of the two nanozymes to activate profluorophores inside and outside cells were analysed. For the intracellular catalysis experiments, rhodamine derivative **PF1** (green emitter) was selected due to its high permeability through the cell membrane, instead for the extracellular one the resorufin derivative **PF2** (red emitter) was used since its lower cell permeability. They observed that in the absence of the nanozymes, none of **PF1** and **PF2** exhibited fluorescence, instead working with **Pos-NZs** and **Zw-NZs**, the cells exhibited green fluorescence inside the cells and a bright red fluorescence outside the cells. With these results, they demonstrated that their nanozyme-based bioorthogonal systems can activate different profluorophores with a controlled spatial localisation. Later, they explored the ability of **Pos-NZs** and **Zw-NZs** to selectively activate prodrugs inside and outside HeLa cells, using allylcarbamate protected doxorubicin (pro-Dox) as prodrug model. In presence of the nanozymes, the viability of the cells was lower compared to the one of the cells incubate with only the prodrug, indicating the successful catalytic activation of the pro-Dox.¹⁶⁷

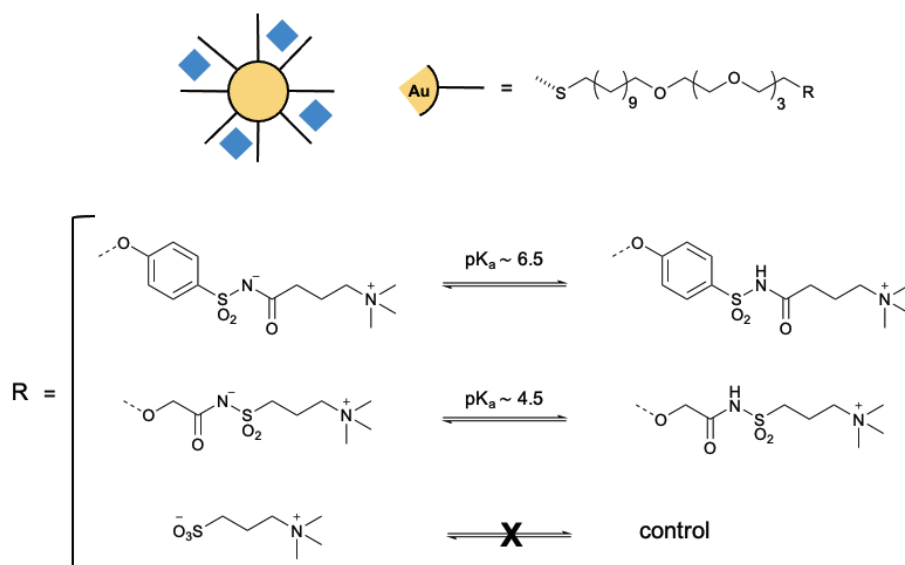


Figure 2.6 Molecular structures of pH switchable and control ligands on gold nanoparticles (AuNPs) for the nanozyme developed by Rotello's group. Scheme adapted from ref. 167.

In 2017, the Weissleder's group showed how nano encapsulated palladium can be used for the delivery and the local activation of prodrugs. They encapsulated the bis[tri(2-furyl)phosphine]palladium(II) dichloride (**PdCl₂(TFP)₂**) catalyst in to poly(lactic-co-glycolic acid)-polyethyleneglycol

(PLGA-PEG) nanoparticles (**Pd-NP**) (diameter 57 ± 2 nm) (**Figure 2.7**). The **PdCl₂(TFP)₂** used was selected after a screening of different Pd compounds in biological conditions, looking at the one with the higher ability in uncage allyloxycarbonyl (alloc)- and propargyloxycarbonyl (poc)-protected amino groups of a model chemotherapeutic prodrug (alloc-doxorubicin (**DOX**)). They examined the ability of the **Pd-NP** to activate the alloc-DOX prodrug in HT1080 cells, after confirming that the nanosystem can mediate the allylcarbamate cleavage on the prodrugs under physiological conditions. The Weissleder's group found that **Pd-NP** could nearly complete the alloc-DOX activation since it showed an IC₅₀ of 26 ± 1 nM, comparable to the one obtained when **Pd-NP** was combined to the uncaged **DOX**. Moreover, the activation of alloc-DOX was tested in mice treated with ES2 OVCA cells. They observed that the nanoparticles can increase the accumulation and the local catalysis in the tumor and that the **Pd-NP** was able to activate the prodrug within the tumor, with a consequence formation of covalent DOX-DNA adducts.¹⁶⁸

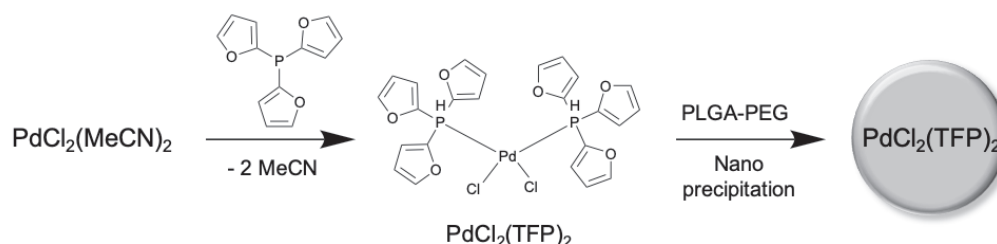


Figure 2.7 Scheme for the synthesis and nanoencapsulation of $\text{PdCl}_2(\text{TFP})_2$ into PLGA-PEG nanoparticles. Scheme adapted from ref. 168.

One year later, the same group proposed the design of a bioorthogonal cleavage strategy based on combining palladium-catalysed deallylation with a self-immolative linker. The linker was functionalized with an aliphatic anchor for encapsulating and blocking the prodrug action. Monomethyl auristatin E (MMAE) and doxorubicin (DOX) were chosen as drugs models and it was modified using a C₁₆ aliphatic anchor for incorporate the Alloc-SIL (self-immolative linker, drugs protective group) for a better nanoencapsulation in a polymeric micellar formulation containing a hydrophobic PLGA-based core (**Alloc-SIL-C₁₆-MMAE / Alloc-SIL-C₁₆-DOX**) (**Figure 2.8**). *In vitro* experiments, conducted in HT1080 fibrosarcoma cancer cells, the C₁₆proMMAE prodrug exhibited a higher cytotoxicity compared to C₁₆proDOX with IC₅₀ values respectively of 15 pM and 50 μM and

comparable to the one of the uncaged parent compound **MMAE**. Moreover, **C₁₆proMMAE** shows >10-fold enhanced cytotoxicity when incubated with sub-micromolar **Pd-NP**. Motivated by the promising results obtained for the *in vitro* studies, they tested the ability of **C₁₆proMMAE** to treat tumours in two complementary mouse models of cancer: subcutaneous HT1080 xenograft tumours in nu/nu mice and MC38 murine colon adenocarcinoma tumours grown intradermally in immunocompetent C57BL/6 mice. The mice were treated with **Pd-NP**, **C₁₆proMMAE NP** and a combination of the two by intravenous injection. They observed that the treatment was not curative for none the tumours models employed, but decreased their growth and after 2 days completely blocked it. From their results, they observed that the C₁₆ nanoencapsulation anchor was important in blocking biological (i.e., cytotoxic) effects of the prodrugs and influenced subcellular distribution. Further optimisation and modification on this anchor are needed for extending it use with other drugs as well.¹⁶⁹

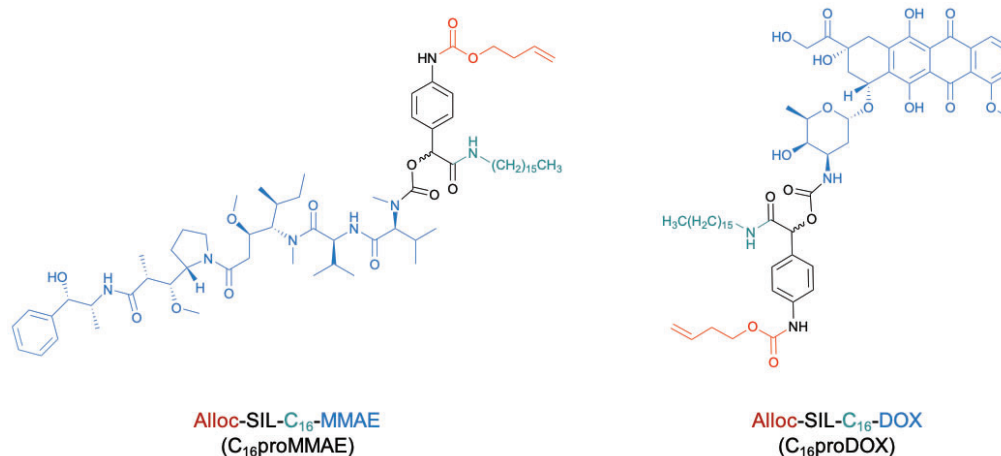


Figure 2.8 Chemical structures of caged MMAE (**Alloc-SIL-C₁₆-MMAE**) and DOX (**Alloc-SIL-C₁₆-DOX**). Colored code for both the structures: bioorthogonally cleavable protecting group (Alloc) in red, self-immolative linker in black, nanoencapsulation anchor in green and drug in blue. Scheme adapted from ref. 169.

The use of palladium catalyst was quite investigated also by Bradley and Unciti-Broceta's groups.^{170,171,172,173} In their works on Pd catalyst, they showed for example the use of heterogeneous polymeric scaffolds, loaded with metallic nanoparticles, for bioorthogonal organometallic reactions. In the first study reported in 2011, they entrapped palladium NPs (Pd NPs) on resin beads for study allylcarbamate cleavage reactions inside HeLa cells. They chose allylcarbamate-protected derivative of amsacrine for

investigating the deprotection reactions studies.¹⁷⁰ Amsacrine is an antineoplastic agent, that intercalates into DNA and inhibits topoisomerase. It is usually employed for the treatment of acute nonlymphocytic leukemia.¹⁷⁴ They observed that alloc protection gave a measurable reduction in the cytotoxic properties of this modified amsacrine derivative. Based on this results, Bradley's group investigated if amsacrine could be released in situ by the catalytic activity of cell-containing Pd⁰ microspheres. Cells incubated with alloc-protected amsacrine showed up an increment of cytotoxicity in cell cultures preloaded with Pd⁰ microspheres. This study was the first work reported on Pd⁰-based heterogeneous catalyst that demonstrated the possibility to intracellular catalytic activity towards exogenous materials. It gives the basis for the customisation of heterogeneous unnatural catalysts for applications in different fields, such as in chemical biology (in situ labelling of cellular structures), pharmacology (*in vitro* prodrug activation of hydrophilic molecules with low cell penetrability) and in medicine (the systemic administration of a prodrug with local activation via implant-captured catalysts).¹⁷⁰

Later, in 2019, Unciti-Broceta and collaborators showed another example of Pd NPs mediated prodrug activation. They developed a bioartificial device composed by cancer-derived exosomes loaded with Pd nanosheets catalyst that showed a preference to target their parental cancer cell line (**Figure 2.9**).¹⁷³ Exosomes are extracellular vesicles that modulate cell-to-cell communication and it has been demonstrated that released exosomes from cancerous cells are involved in cancer progression.¹⁷⁵ The preference of their system, allowed the activation of the protected prodrug in a localized manner. An O-alkyl hydroxamate derivative of panabinstat drug was synthesised. Panabinstat, although its broad activity against many cancer types, dose-limiting systemic toxicities such as diarrhoea, cardiac ischaemic events, arrhythmias and myelosuppression limit, is used against solid tumours.^{173,176} The experiments conducted, revealed that their device can be used as vehicles for targeting A459 cell line and performing the catalytic deprotection of the panobinstat prodrugs in a selective way.¹⁷³

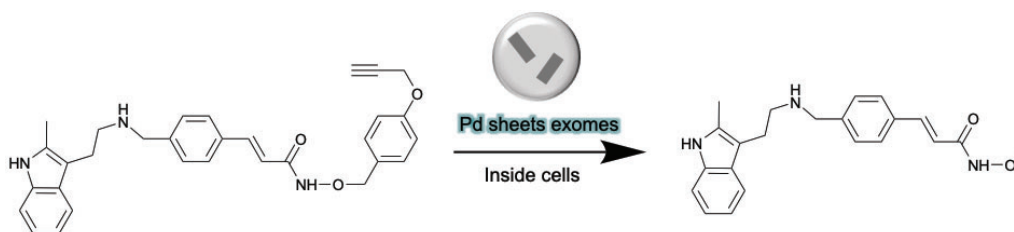


Figure 2.9 Intracellular Pd-exomes-mediated conversion of the prodrug to the clinically approved HDAC inhibitor, panabinstat. Scheme adapted from ref. 173.

Another example of the activation of a prodrug, promoted by palladium catalyst, was reported by the same group recently. They developed an orally 5-Fluorouracil (5-FU) prodrug that was selectively activated by Pd catalysis (**Figure 2.10**). The aim of their work was to try to improve the chemotherapy field, controlling where and when the anticancer drugs were released. To accomplish this, the prodrug developed should be resistant to the first-pass metabolism, unaffected by variations in the enzyme dihydropyrimidine dehydrogenase (DPD) and selectively activated by a bioorthogonal Pd-catalysed reaction.¹⁷⁷ The 5-FU is indeed an antimetabolite drug used to treat colon and pancreatic cancers, but it is quite toxic alone.¹⁶⁶ It is usually detoxified by DPD; however, 3-5% of patients express no or low levels of this enzyme.¹⁷⁸ Unciti-Broceta's group first developed the prodrug and trapped it in its lactim form by alkylating the O atoms of 5-FU, to be unrecognizable by the enzyme and avoid in this way the metabolisation routes of the drug (both anabolic activation and catabolic processing). *In vitro* experiments were then performed in pancreatic cancer BxPC-3 and colorectal cancer HCT116 cells, showing that the trapped lactim prodrug was not anabolically activated in its active form and cytotoxic effect was detected. The activation of the prodrug promoted by the Pd catalyst was subsequently evaluated in cells culture with a significant cytotoxic effect in both the cell lines (BxPC3 and HCT116), while neither the prodrug nor Pd resins individually affected the cell viability. Moreover, their work was the first demonstration that an inactive drug precursor can be administered orally and activated inside a tumor xenograft by intratumorally implanted Pd catalysts. *In vivo* studies indeed showed that the tumours containing Pd devices were characterised by large central necrotic areas close to the resins, indicating that 5-FU had been generated inside the tumour and caused an intratumorally cytotoxic effect.¹⁷⁷

Unciti-Broceta's group also investigate activation of prodrug by gold catalysis. In 2021, they developed a novel bioorthogonal prodrug of the histone deacetylases inhibitors (HDCAi) panobinostat that can be activated by gold catalysis.¹⁷⁹ Histone deacetylases (HDCAs) are a family of enzyme that are involved in the regulation of the gene expression.¹⁸⁰ These enzymes are overexpressed in different human cancers and this leads to the repression of crucial tumor suppressor genes.¹⁸¹ They prepared *O*-propargylated hydroxamate derivative (**Figure 2.10**) as prodrug and ultra-small size AuNPs (2.8 ± 1.2 nm) as catalyst. First, the capacity of Au-catalyst to convert the prodrugs in its active form was tested in physiological conditions, obtaining good response in the ability of cleavage the propargyl group without ant formation of side products. Then, they moved their studies *in vitro*, working with NSCLC A459 cancer cells. Au-catalyst and HDCAs prodrug were incubated with cells separately (as a negative control) and in combination. A great cytotoxic effect was revealed by the treatment with the combinations of both the elements, while no cells death was detected by separately treating. Their study showed how the *O*-propargylation of the hydroxamate group of panobinostat can generate an inactive derivative that is harmless to cells and that can be converted into cytotoxic panobinostat by Au catalysis.¹⁷⁹

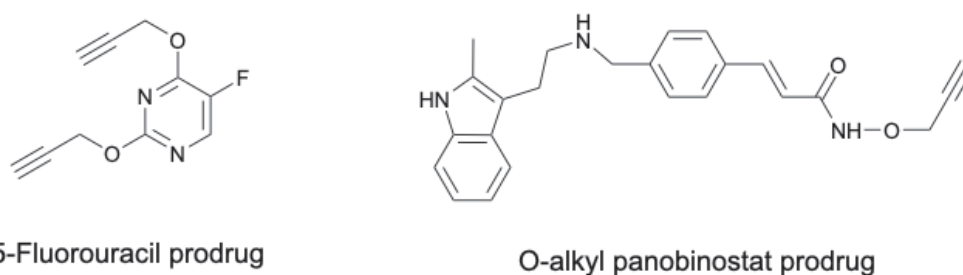


Figure 2.10 5-Fluorouracil and *O*-alkyl panobinostat prodrugs employed in Unciti-Broceta works reported in 2022 and 2021. Structures adapted from ref. 177 for 5-Fluorouracil and from ref. 179 for the *O*-alkyl Panobinostat derivative.

2.3. Bioorthogonal photocatalysis with metal complex as substrate

In chapter 1, the use of Pt(IV) prodrugs as an alternative to the Pt(II) anticancer agents used in the clinics, was reported. Related to the development of the design of new Pt(IV) anticancer complexes, research has been conducted on their photoactivation.¹⁵³ During the last years, different

Chapter 2

studies have been performed about bioorthogonal photoactivation reactions in which the metal complex acts as substrate and the role of catalyst is played by a photoactivable molecule that facilitates the electron transfer. The term bioorthogonal here is related to the ability of these photoactivatable catalysts to make multiple substrate turnovers and to their high selectivity toward the metal substrate conversion in complex biological environments.¹⁸²

Flavins have been shown in these years to be good candidates as catalysts for the photoactivation of Pt(IV) prodrugs reactions. Thanks to their extraordinary redox properties,⁶⁴ they can promote the electron transfer from the reducing agent to Pt(IV) complex. The chemistry behind this reaction, takes place in the presence of an electron donor (such as NADH, amines, ascorbate) and under blue light excitation (460 nm).^{183,184,182,185}

In the first work of the Salassa group on this topic, the platinum prodrug *cis,cis,trans*- [Pt(NH₃)₂(Cl)₂(O₂CCH₂CH₂CO₂H)₂] was photocatalytically converted into the active drug, cisplatin, by riboflavin (Rf) under blue light excitation (460 nm, 2.5 mW/cm²) in a biological environment. In this reaction, 2-morpholinoethanesulfonic acid (MES) was used as electron donor (**Figure 2.11**). Thanks to the particular photoredox properties of Rf, they observed that a sub-stoichiometric concentration of this molecule was enough for photocatalysing the reduction of platinum complex under low doses of blue light (460 nm, 0.75 J/cm²). A turnover frequency (TOF) value of 0.22 s⁻¹ and a total turnover number (TTN) value of 38 under these conditions were obtained. To test the potential of Rf photocatalyst as a bioorthogonal tool for photochemotherapy, the activation of the metal complex was studied in cell culture medium and in prostate cancer cell (PC-3) too. No toxic effects were observed in dark, but under blue light irradiation (1 min, 460 nm, 0.36 J/cm²) a full conversion of the substrate was observed underling the potential of this system.¹⁸³

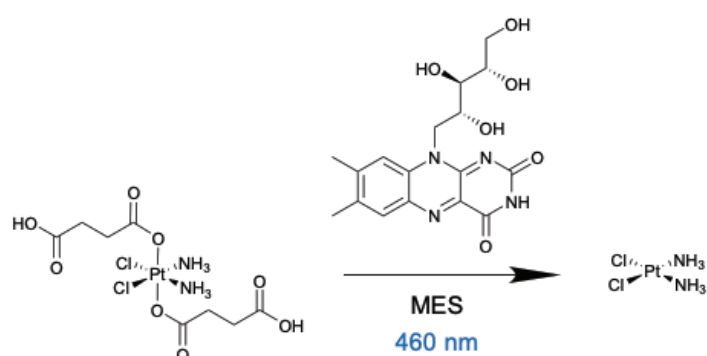


Figure 2.11 Photocatalytic activation of cisplatin from Pt(IV) prodrug under blue light irradiation (460 nm). Riboflavin is the catalyst of the reaction and MES the electron donor. Scheme adapted from ref. 183.

The promising results obtained, encouraged the group to investigate the photoactivation of Pt(IV) prodrugs promoted by two cofactors of **Rf**, flavin adenine dinucleotide (**FAD**) and flavin mononucleotide (**FMN**), and four flavoproteins, **miniSOG** (mini singlet oxygen generator), **NOX** (NADH oxidase from *Thermus thermophilus*), **GOX** (glucose oxidase from *Aspergillus niger*) and **GR** (glutathione reductase from *S. cerevisiae*) (**Figure 2.17**). In presence of NADH and MES and upon irradiation (460 nm), **FAD** was able to completely convert the substrate with a TOF value of 5-9 min⁻¹. On the contrary, in the absence of light, this cofactor did not induce any conversion of the metal complex. The flavoproteins, **GOX** and **GR**, showed a very lower efficiency, instead the behavior of **miniSOG** and **NOX** was comparable to the one of **FAD**. In particular, **NOX**, also in dark condition, was able to instantaneously convert the substrate in presence of NADH (2 mM). **MiniSOG** protein instead needed light activation.¹⁸⁴

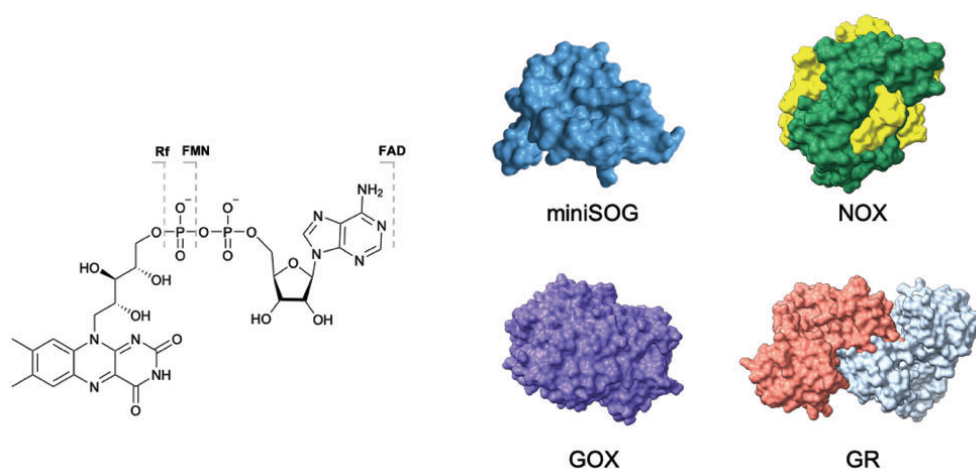


Figure 2.12 Chemical structures of: Rf, FMN, and FAD (on the left). Flavoproteins structures of: miniSOG (PDB ID: 6GPU), NOX (PDB ID: 1NOX), GOX (PDB ID: 1CF3) and GR (PDB ID: 2HQM).

Additional works on flavin derivatives and flavoprotein, have been developed by our group. In 2020, Gurruchaga *et al.* reported the studies on the photocatalytic reactions employing four different free flavins (riboflavin (**Rf**), flavin mono-nucleotide (**FMN**), tetra-O-acetyl riboflavin (**TARF**) and lumiflavin (**Lf**)), the flavoproteins **miniSOG** and four Pt(IV) substrates (*cis,cis,trans*-[Pt(NH₃)₂(Cl)₂(O₂CCH₂CH₂CO₂)₂]²⁻, *cis,cis,trans*-[Pt(NH₃)₂(O₄C₆H₆)(O₂CCH₂CH₂CO₂)₂]²⁻, *cis,cis,trans*-[Pt(NH₃)₂(Cl)₂(O₂CCH₃)₂] and *cis,cis,trans*-[Pt(NH₃)₂(O₄C₆H₆)(O₂CCH₃)₂]) (**Figure 2.13**). The photoactivation reaction was conducted in presence of NADH as electron donor and under blue light irradiation (460 nm, 6 mW/cm²). They founded that the H-bond interactions between the reduced form of flavin (H₂FL or HFL⁻) and the Pt(IV) prodrugs could be fundamental for the conversion of the metal complexes. Moreover, the ribityl chain can stabilized these intermediates, increasing the catalytic efficiency of the reaction. They observed indeed that the lower TOF value was obtained with **Lf** (in 2.6 – 13.3 min⁻¹ range, depend on the substrate analysed). For the flavoprotein, **miniSOG**, the self-quenching of the excited states by protein amino acids reduced its efficiency as catalyst in the reaction (TOF < 5.6 min⁻¹).¹⁸²

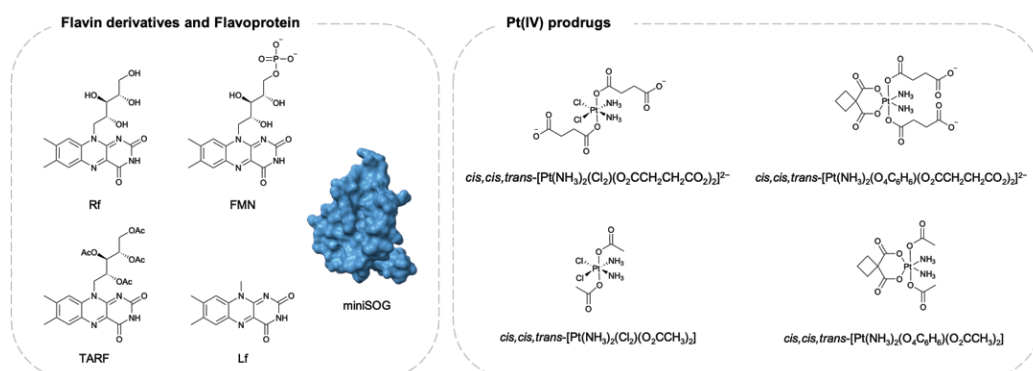


Figure 2.13 Structures of flavin derivatives and flavoprotein (catalysts) and of Pt(IV) prodrugs (substrates) used in Gurruchaga work. Scheme adapted from ref 182.

One year later, Gurruchaga *et al.* investigated site mutagenesis on miniSOG flavoproteins for enhancing their catalytic activity. Three different miniSOG mutants were analysed (Q103V, Q50E and Q50W) for the catalysed conversion of *cis,cis,trans*-[Pt(NH₃)₂(Cl)₂(O₂CCH₂CH₂CO₂H)₂] and *cis,cis,trans*-[Pt(NH₃)₂(Cl)₂(O₂CCH₃)₂] prodrugs, in presence of the electron donor NADH (**Figure 2.14**). Among the mutated flavoproteins, the Q103V one showed the greatest catalytic activity with an 80% of Pt(IV) complex conversion after only 90 sec of blue light irradiation (460 nm, 6 mW/cm²)

and a TOF values 5.6-fold higher compare to the other flavoproteins studied. This enhancement in the catalytic activity was related to the long $^3\text{FMN}^*$ lifetime of Q103V that favoured the NADH-promoted reductive quenching. Moreover, this work was the first demonstration showing that site-directed mutagenesis can be used to change and increase the catalytic activity of flavoproteins in artificial reactions where metals complexes are employed as substrates.¹⁸⁶

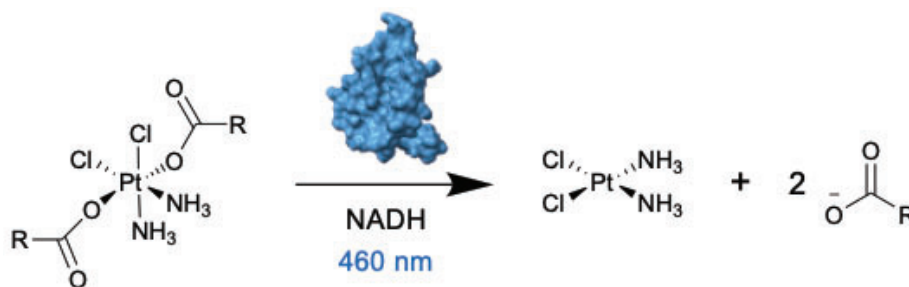


Figure 2.14 Photocatalytic reaction for the Pt(IV) prodrug activation promoted by miniSOG, under blue light irradiation and in presence of NADH as electron donor. Scheme adapted from ref. 186.

Recently Velasco *et al.* showed how a hydrogel matrix could be a valid solution for the catalytic activation and delivery of cisplatin. They employed agarose porous microbeads activated with diethylaminoethyl groups (AGM) as hydrogel matrix for loading the platinum complex *cis,cis,trans*-[Pt(NH₃)₂(Cl)₂(O₂CCH₂CH₂CO₂H)₂] and the catalyst riboflavin-5'-phosphate (**FMN**) through electrostatic interactions. The agarose microstructure participated in the catalytic reaction as electron donor and the release of the drug by light and chemical activation were analysed. After 5 min of low-power blue light irradiation (460 nm, 6 mW/cm²), ¹H-NMR and UPLC experiments showed 100% conversion of the immobilized platinum complexes upon the addition of 1 M NaCl. After 1 min of irradiation, the TOF value achieved was equal to 20.1 ± 0.6 min⁻¹ and no release of cisplatin was observed in the dark. Then, Velasco *et al.* investigated the release of the active platinum species promoted by a chemical stimulation, employing NADH. They incubated their system with 0.5 mM of NADH and observed a 60% release of the immobilized *cis,cis,trans*-[Pt(NH₃)₂(Cl)₂(O₂CCH₂CH₂CO₂H)₂] after 5 min incubation in dark. Hence, they showed how the use of a hydrogel matrix implemented with platinum prodrugs and flavin catalyst can be an efficient system for the generation and release of high concentrations of cisplatin, controlled by very low light

doses or by chemical stimulus such as NADH. They found that fundamental aspect for its efficacy, in both cases, is the microenvironment of the AGM and its functionalisation with the diethylaminoethyl groups. The agarose microstructure provides a high local concentration of reactants, catalyst and substrate molecules increasing the activation rate of Pt(IV) prodrug compared to previous catalytic systems developed for the activation of therapeutic drug.¹⁸⁷

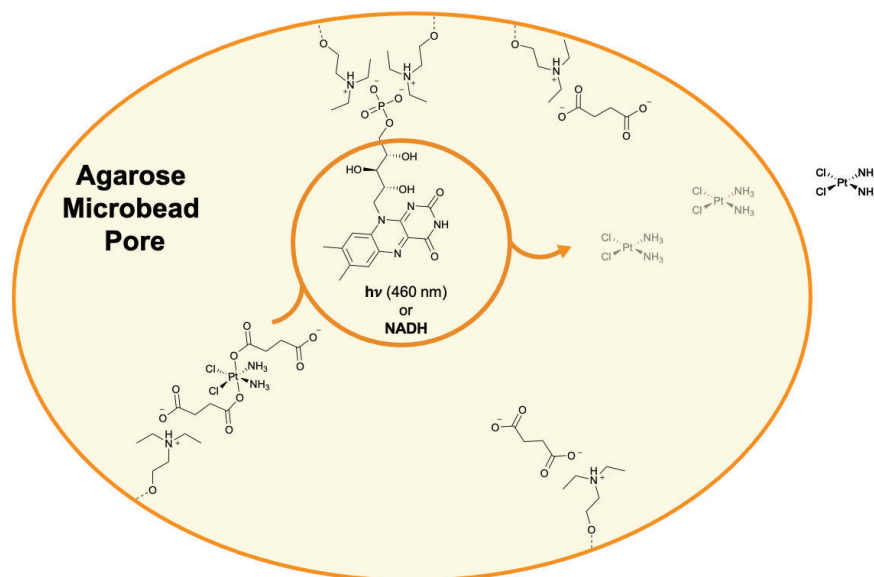


Figure 2.15 Flavin-catalysed generation of cisplatin (Pt(II) complex) from a Pt(IV) prodrug precursor inside diethylaminoethyl agarose microbeads (AGM). Scheme adapted from ref. 187.

Recently, Scoditti *et al.* investigated the key steps of the photocatalytic activation of Pt(IV) complexes by flavins using Density Functional Theory (DFT).¹⁸⁸ The mechanism of the reaction had been previously investigated and reported by Salassa's group, based on experimental studies.^{183,182} In the work of Scoditti *et al.*, *cis,cis,trans*-[Pt(NH₃)₂(Cl₂)(O₂CCH₃)₂] and *cis,cis,trans*-[Pt(NH₃)₂(O₄C₆H₆)(O₂CCH₃)₂] as prodrugs model compound respectively of cisplatin and carboplatin drugs, NADH as electron donor and riboflavin (Rf) as photocatalyst were used. In the first step of the reaction, riboflavin is reduced to its hydroquinone form by the electron donor under light, through an almost barrierless pathway involving the triplet excited state of Rf (³TS). It has been observed indeed that light excitations trigger a faster and favourable reaction compared to the singlet state (dark conditions). The product obtained from this first passage, is the doubly reduced RfH⁻, able to reduce the two Pt(IV) complexes. This reduction happened through a ligand-

bridge-H transfer, where the N(5)-H of the Rf interacts with the oxygens of the acetate ligands of Pt(IV) compounds (**Figure 2.16**). This implies the activation of Pt(IV) complexes through a detachment of the acetate ligands and the formations of the drugs, cisplatin and carboplatin. Moreover, they observed that the free energy barriers for the Pt(IV) reduction promoted by RfH⁻, was lower than in the case of other bioreductants like AsCH⁻ and NADH.¹⁸⁸ Moreover they work confirmed and support the mechanism previously reported by the group of Salassa.^{182,183}

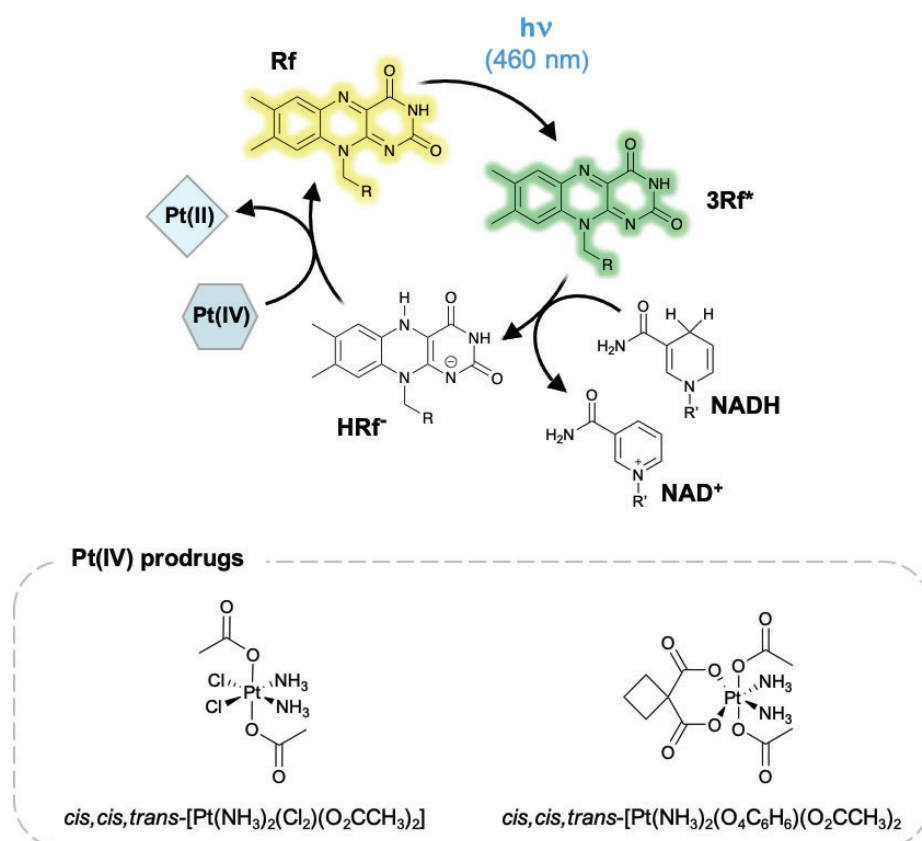


Figure 2.16 Mechanism of the photocatalytic activation of Pt(IV) prodrugs by flavins (R = ribityl; R' = adenine dinucleotide) and the two Pt(IV) prodrug complexes studied. Scheme adapted from ref. 188.

In 2019, the group of Bradley reported the design, the synthesis and the photocatalytic Pt(IV) prodrug activation of a platform able to reduce the metal complex and at the same time generate singlet oxygen using a ruthenium-based photosensitizer (**Figure 2.17**). Platinum complex was activated by Ru upon blue light irradiation (470 nm, 0.58 mW/cm²) showing an 88% conversion after 60 min of illumination. Cell experiments with SKOV-3 and HCT116 cancer cells lines confirmed that the generated toxicity was a

Chapter 2

combination of the effects of oxaliplatin (the active species released by the activation of platinum prodrug) and the reactive oxygen species (ROS) generated by photosensitizer/photocatalyst. Their system indeed showed good cytotoxic capabilities in both the cancer cells lines analysed after illumination. Moreover, they tested the cytotoxicity of Pt(IV) prodrug in oxaliplatin resistant cells, using SKOV-3 allowing to develop resistance to oxaliplatin by sub-culturing in incremental doses of the drug over 3 months. Comparing the IC_{50} values of the prodrug and the drug, respectively $82 \mu\text{M}$ and $25 \mu\text{M}$, the Pt(IV) complex showed a reduced cytotoxicity.¹⁸⁹

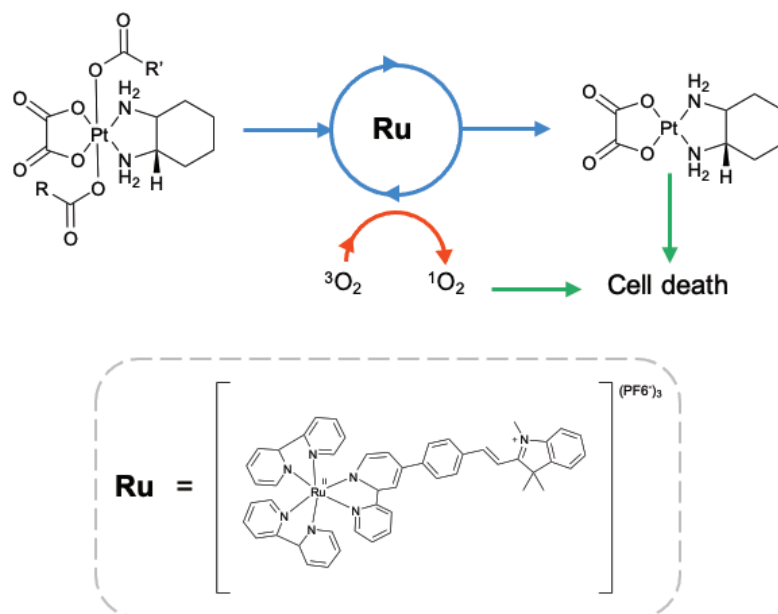


Figure 2.17 Representation of the photocatalytic conversion of Pt(IV) prodrugs to their active Pt(II) drug (oxaliplatin) by a Ru(II) photocatalyst with simultaneous $^1\text{O}_2$ generation. The Ru complex used by Bradley group is reported in the dash grey square. Scheme adapted from ref. 189.

Hence, in this Chapter is reported how bioorthogonal chemistry and catalysis can be combined to activate metal complex in biological environments. Moreover, differently from the traditional concept of catalysis, where the metal complex acts as catalyst for promoting the conversion of organic substrates, few examples of a different approach in which metal is the substrate of the reactions have been reported. This uncommon approach may help in the design of new bioorthogonal metal prodrugs and strategies, for reducing the undesired side effects of their active forms. As shown in this chapter, two strategies have been developed for controlling the activation of metal prodrugs in biological environments through catalytic reactions.

Despite many of them showing good efficiency *in vitro*, improvement in the design of the systems is still needed.

2.4. General objectives

The progress made in biorthogonal catalysis is creating new opportunities to perform chemoselective transformations in complex biological environments, with applications in biomedicine and bioimaging. In recent years, biorthogonal reactions and the use of molecules that mimic the behavior of enzymes have been combined for investigating substrate activation in biological surrounding.¹⁴⁵ Commonly, biorthogonal catalysis transformations are promoted by metal complexes, however new approaches have been developed employing metal-based agents as substrates for these processes. This approach has been applied in the activation of some metal-based prodrugs promoted by organic catalysts or metal ones. Recently, a riboflavin photocatalyst has been used for the activation of Pt(IV) anticancer prodrugs *in vitro* under light irradiation.¹⁸³

The aim of this thesis is to expand this strategy by co-immobilisation of both photocatalysts and prodrugs, on gold nanoparticles as nanozyme scaffold¹⁸⁵ and on engineered repeat proteins as templates¹⁹⁰ (**Figure 2.18**).

Specifically, the thesis chapters focus on:

- Synthesis and characterisation of functionalized riboflavins and platinum complexes (Chapter 3). Commercial riboflavin has been modified implementing a specific functional group for the coupling with the protein. As the two modified riboflavins, also platinum complexes have been activated for the coupling with specific amino acids of the protein. Moreover, depending on the system studied, different platinum complexes have been synthesised. Symmetrical and asymmetrical Pt(IV) prodrugs were developed respectively for the nanozyme and the engineered repeat proteins models.
- Development of a supramolecular nanozyme for the photocatalytic conversion of anticancer platinum prodrugs complexes into cisplatin (drug) under blue light irradiation (Chapter 4). Gold nanoparticles have been employed as scaffolds for interacting with the

photocatalyst (FMN) and the substrate (Pt(IV) complex) thanks to a triazacyclononane functional moiety (TACN) of the thiol ligands.

- Design of a multifunctional hybrid construct for the delivery and activation of a platinum prodrug under blue light *in vitro* (PANC-1 pancreatic cancer cells) (Chapter 5). Engineered consensus tetratricopeptide proteins have been used for loading covalently functional riboflavins and Pt(IV) complexes.

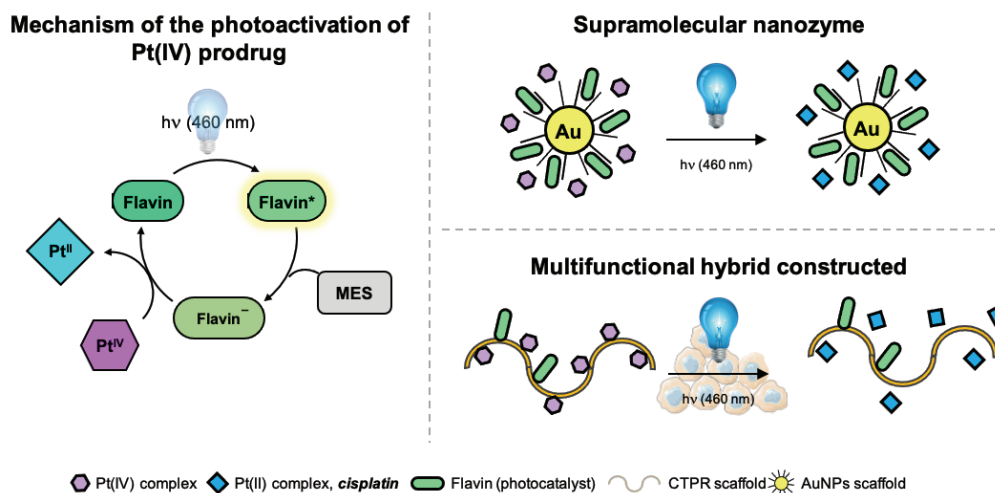


Figure 2.18 Schematic representations of: mechanism of the photoactivation of Pt(IV) prodrug used for the experiments performed in this thesis (on the left); supramolecular nanozyme developed in Chapter 4 (on the right, top) and multifunctional hybrid constructed reported in Chapter 5.

Chapter 3

Synthesis and characterisation of flavins and Pt(IV) complexes

This work can be found published as: L. F. Mazzei, Á. Martínez, L. Trevisan, D. Rosa-Gastaldo, A. L. Cortajarena, F. Mancin, L. Salassa, *Chem Commun.*, 2020, **56**, 10461- 10464.

Chapter 3

3.1. Introduction

3.1.1. Flavins

Flavins are taking more and more relevance for their catalytic activity, in particular flavoenzymes (*i.e.* any enzyme containing a flavin nucleotide, FMN or FAD, as coenzyme) for their participation in many chemical transformations^{191,192} such as catalysis reactions.^{193,194,191} The reactive part of these molecules is the isoalloxazine heterocycle structure that can assume three different oxidation states: quinoid (fully oxidized state), semiquinonid (one-electron reduced state) and hydroquinonid (fully reduced state) (**Figure 3.1**). All of these states are active and own individual reactivity characteristics. For example, quinoid is a strong oxidant which also is its primary reactivity towards substrate molecules.¹⁹² Flavin-containing enzymes have showed a versatile reactivity, participating in oxidations, reductions, and halogenations reactions.¹⁹⁵ Nevertheless, their reactivity, such as their ability of mediating transformations in flavoenzymes, depends on the surroundings. Out of the enzyme environment indeed, the cofactors lose part of their activity showing only a largely reducing capacity. Despite the decrease in the activity, the catalysis application of the isolate cofactor has been highly explored by researchers,^{192,196} for example in the oxygenation reactions with oxygen and hydrogen peroxide as terminal oxidising agents.¹⁹⁶

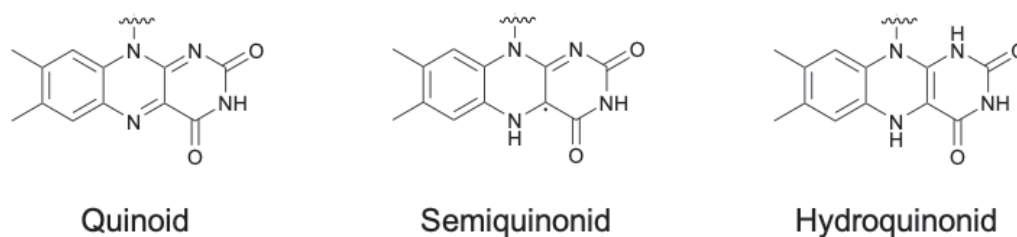


Figure 3.1 The three most common oxidation states of the isoalloxazine heterocycle. Scheme adapted from ref. 192.

Chemical modifications to the isoalloxazine part have been previously investigated since the reactivity of flavins relies on this part and it is known that alterations can enhance the reactivity and the selectivity of transformations.¹⁹² Five different positions for the functionalisation have been identified, N1-, N3-, N5-, C6-C9- and N10- position (**Figure 3.2**).

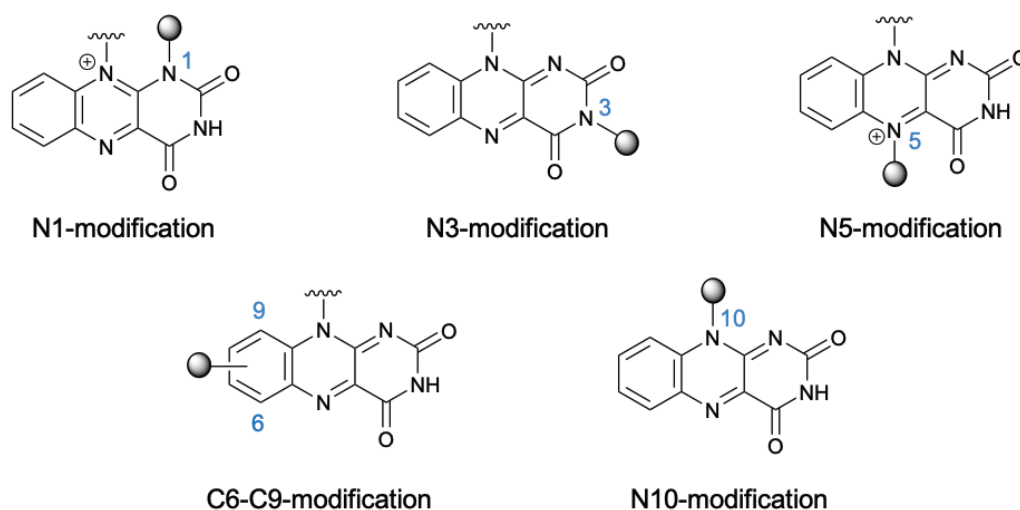


Figure 3.2 Structures of isoalloxazine moiety with the five positions for flavin modifications. Scheme adapted from ref. 192.

In 2001, Sayre group reported a synthesis for a modification between N1 and N10 positions, showing a N1-N10-bridge flavinium salt. They identified that this modified flavin was a stronger oxidant compare to the non-modified molecule.¹⁹⁷ Later, Cibulka's group investigated the behaviour of the N1-N10-bridge flavins under irradiation with visible light. Upon visible light, their redox potential increase from $E = 0.01$ V (ground state) to $E = 2.67$ V (excited state). Thanks to this aspect, Cibulka and co-workers were able to perform also the most challenging oxidations reactions, such as the conversion of *p*-(trifluoromethyl)toluene in the corresponding benzoic acid derivative.⁶⁵

Among the five positions for the functionalisation of the isoalloxazine, N3-modification is one of the most common used. The alteration at this position is very typical for modulating flavins solubility, moreover it does not alter their spectroscopic properties and has been found that increases the photostability.¹⁹² For example, the Zaldo group recently reported a comparison in the photostability between commercial riboflavin and an acetylated analogue, 3-methyl-tetraacetylriboflavin (3MeTARF). Both 3MeTARF and riboflavin revealed similar absorption spectra with the characteristic peaks at 372–374 nm and 446–450 nm respectively. Under blue light irradiation (438 nm), riboflavin underwent rapid photodegradation in contrast to 3MeTARF which remained stable.¹⁹⁸ Depending on the substituents chosen for the modification, different properties of flavins can be tuned. For example, Cibulka, Köning and Vasold

functionalised the N3 position of flavin with a Lewis acid observing an increment in the quantum yields for the photocatalytic oxidation of alcohols with respect to non-modified flavins.¹⁹⁹ Moreover, N3 substitution can be also exploited for immobilising the flavin catalyst on different substrates. An example is given by Gilmour, Ravoo and co-workers who covalently coupled the N3-modified riboflavin on silica nanoparticles. They demonstrated that higher catalytic activity of the flavin in the E to Z isomerization of a benchmark cinnamitrile was reached with this immobilisation.²⁰⁰ Implementation of biomolecules as substituents was showed then by the Imada's group that coupled flavin catalyst to a peptide at the N3-position.²⁰¹ They designed the flavin-peptide catalyst basing first on computational estimation and then screening possible structures by an experimental approach. The conjugate obtained was employed for aerobic sulfoxidations as well as Baeyer-Villiger oxidation, which are both not possible with the riboflavin alone. Furthermore, the system developed by Imada and collaborators was the first flavoenzymes that mimics aerobic oxygenation reactions catalysed by flavins under non-enzymatic conditions. Their studies showed interesting results for flavin-peptide chemistry and computational one, since provide new possibilities for the development of flavin catalysts and highlighted the great potential of computational chemistry for the rational design of peptide-based catalysts.

It was observed in the years that flavins with a modification at N5 position, with a resulting N5-alkylated flavinium salt, can participate in oxidations reactions where molecular oxygen replaces hydrogen peroxide.^{192,202} In 2003 for example, Murahashi, Imada and co-workers showed that these flavinium salts catalysed the oxidation of thioether and amine exploiting molecular oxygen as the terminal oxidant. This reaction was also very efficient and clean.²⁰²

Changes in the aromatic positions, such as at C6 and C9, can modify the reactivity of the flavin catalyst. For example, in 2016, Glusac and co-worker reported the synthesis of a flavin with the incorporation of an iodine at C9 position (**I-FI**). They observed that **I-FI** exhibits a higher intersystem crossing (ISC) to the triplet state after photoexcitation, compared to its non-modified reference compound (**FI**). This increase in the ISC, due to the higher rate of

triplet formation, involved a directly improved on the photocatalytic efficiency of **I-FI**. The introduction of the iodine, indeed, made the flavin a more reactive catalyst in the oxidation of organic substrate, such as benzyl alcohol to benzaldehyde.²⁰³

The last modification is related to the N10 position. Murahashi, Imada and Ono showed in 2002 a chiral N10 flavin modified for enantioselective Baeyer-Villiger oxidations reactions. They demonstrated how to completely regulate the planar chirality of bisflavinium salt (composed by two flavins), using enantiopure trans-diaminocyclohexane (DACH) as a chiral source. Stable stereoisomers were obtained because of the two isoalloxazine cores are stacked and unable to rotate around the N10-CDACH single bond. Moreover, each isoalloxazine acts as a steric barrier for the other, resulting in efficient facial selectivity for the approach of substrates and reagents. They exploited this bisflavinium salt for the oxidation of cyclobutanones, achieving lactone formation with 63% enantiomeric excess. This N10-modified flavin was the first demonstration that organic chiral compounds can catalyse asymmetric Baeyer-Villiger reactions, and that this kind of compound can be a trigger to provide environmentally friendly, clean organocatalytic oxidation reactions.²⁰⁴

3.1.2. Platinum complexes

As reported in Chapter 1 (section 1.1.1), different Pt(IV) prodrugs have been developed in the years aiming at reducing the side effects of Pt(II) anticancer drugs as well as provide to the complex new properties (such as targeting ability).¹¹

One of the most common approach for the oxidation of the Pt centre is working with hydrogen peroxide or chlorine, which comports a two-electron oxidation. This reaction is very rapid and the Pt(IV) complexes obtained are good starting materials for additional derivatisation.⁹ Usually, these reactions are performed in water working with Cl₂ or an excess of H₂O₂, between 50 to 70 °C. Starting from a general Pt(II) precursor with [Pt-L₂X₂] structure (L = leaving ligands, X = non-leaving ligands), after the oxidation of the metal complex, the resulting platinum complexes show respectively

cis,cis,trans-[Pt-(L)₂(X)₂(Cl)₂] and *cis,cis,trans*-[Pt-(L)₂(X)₂(OH)₂] structures (Figure 3.3).⁹

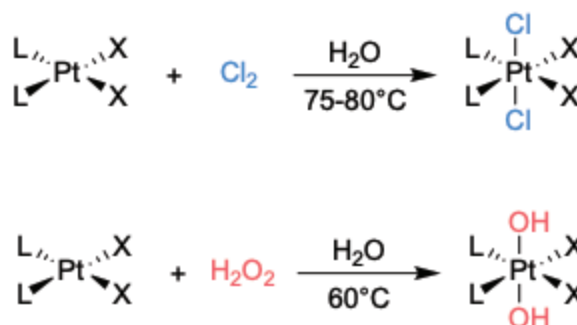


Figure 3.3 Oxidation reactions of Pt(II) complex in presence of chlorine (top) and hydrogen peroxide (bottom) in water. Scheme adapted from ref. 9.

Focusing our attention of the oxidation of Pt(II) complexes by hydrogen peroxide, working in water solvent, both the axial ligands of Pt(IV) compound are hydroxo groups. However, the axial ligands of the product obtained can change depends on the solvent used. For example, the oxidation in alcohols (ROH) with H₂O₂ gives *cis,cis,trans*-[Pt-(L)₂(X)₂(OH)(OR)] as products (Figure 3.4).^{205,206} Optimized protocols have been reported for the synthesis of Pt(IV) anticancer agents starting from cisplatin as the precursor. Cisplatin is one of the most common Pt(II) complex used for anticancer treatments, characterized by two amines (-NH₃) as non-leaving groups and two chloride as leaving ones. In the oxidation reaction, conducted in alcohol as solvent and in presence of H₂O₂, is generally employed 50% of aqueous hydrogen peroxide rather than 30%, like in reactions performed in water. This is due to minimize the amount of water in solution, since it can compete with the alcohol for the coordination to the platinum metal centre.^{206,207} In 1993, Abbott and collaborators, conducted some studies on the mechanisms of Pt(II) complexes oxidation in presence of hydrogen peroxide. They used a ¹⁸O-labeled water solvent and followed the reaction through ¹⁹⁵Pt and ¹³C NMR spectroscopies. It was observed that only one of the hydroxide axial ligands came from the H₂O₂, the other one is from the water solvent.²⁰⁸

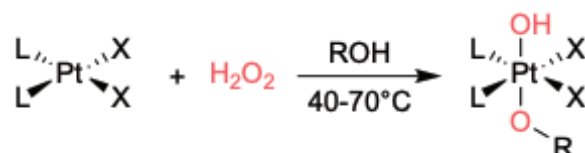


Figure 3.4 Oxidation reaction of Pt(II) complex in presence of hydrogen peroxide in alcohol. Scheme adapted from ref. 205.

The hydrogen peroxide oxidation of platinum (II) complexes has been investigated in the years also in different acidic solvents. Differently for the same reactions performed in water, where there is not preference on the *cis* or *trans* isomers as product, here the researchers observed an isomeric preference. The mechanistic details about the preference towards one of the isomers have not yet been clarified.⁹ For example, Jung's group demonstrated that the oxidation reaction product of [Pt(II)(cbdc)(dpda)] (cbdc=1,1-cyclobutanedicarboxylate, dpda = 2,2-dimethyl-1,3-propanediamine) gives *cis* or *trans* isomer depending on the solvent employed. In acetic acid, with hydrogen peroxide, the results was *cis*-[Pt(IV)(O₂CCH₃)₂(cbdc)(dpda)]; on the contrary the *trans*-[Pt(IV)(O₂CCH₃)₂(cbdc)(dpda)] isomer was obtained working in acetic anhydride in presence of a small amount of acetic acid. Their work was the first demonstration that the difference in using acetic acid or acetic anhydride, critically affects the geometrical isomerism of the product (**Figure 3.5**).²⁰⁹

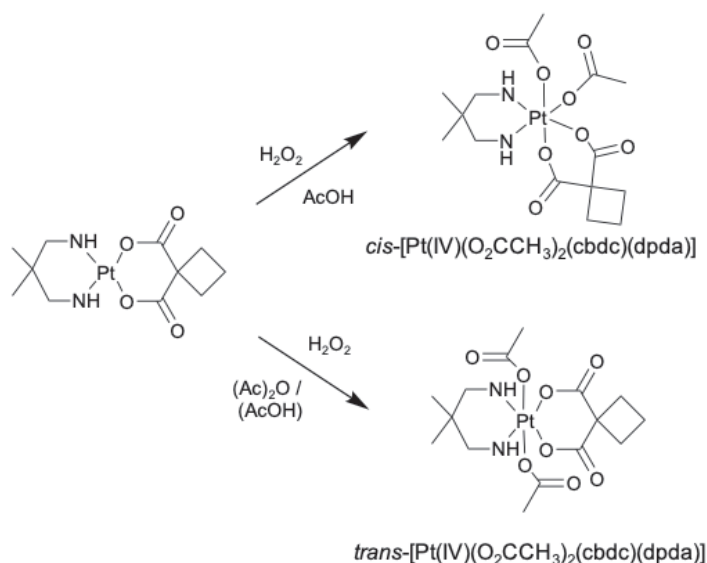


Figure 3.5 Oxidation reactions of Pt(II)(cbdc)(dpda) (cbdc=1,1-cyclobutanedicarboxylate, dpda = 2,2-dimethyl-1,3-propanediamine) in presence of hydrogen peroxide and acetic acid with *cis*-[Pt(IV)(O₂CCH₃)₂(cbdc)(dpda)] as product (top) and in presence of hydron peroxide and acetic anhydride (with a small amount of acetic acid) with *trans*-[Pt(IV)(O₂CCH₃)₂(cbdc)(dpda)] as product (bottom). Scheme adapted from ref. 209.

Pt(IV)-dihydroxo compounds are the starting materials for further derivatized Pt(IV) anticancer complexes. Depending on the mixture reaction, it is possible to obtain a symmetric or an asymmetric Pt(IV) complex with specific functional

groups as axial ligands.⁹ Usually, anhydrides are involved as the most common reagents in these transformations. The first acetylation reaction from a dihydroxo Pt(IV) complex was demonstrated in 1983, using a trifluoro-acetic anhydride.²¹⁰ Later, this chemistry was expanded to include a variety of acid anhydrides, pyrocarbonates and isocyanates.^{9,211} In all the cases reported, the stereochemistry of the dihydroxo Pt(IV) starting complexes is maintained after the reactions.⁹ During the years, a variety of protocols have been reported for obtaining symmetric carboxylate Pt(IV) complexes involving the use of an excess of anhydride in different solvents, such as: acetone,²¹¹ dichloromethane,²¹² acetonitrile^{213,214} and DMSO^{215,216} (**Figure 3.6**). A problem in these reactions is related to the formation of hydrochloric acid (HCl) as byproduct, that can remove the hydroxo ligands of Pt(IV) complex by protonation.⁹ For this reason, optimisations of the condition reaction have been developed such as using refluxing acetone as solvent and an excess of pyridine as base to trap HCl.²¹⁷

In the synthesis of Pt(IV) carboxylates complexes, cyclic anhydrides can also be employed. Among the most common derivatives there are succinic,^{218,219,32} maleic,^{218,220} glutaric,^{218,221} phthalic²²² and naphthalic²²³ anhydrides (**Figure 3.6**). In the first synthetic approaches developed, the reactions were conducted in refluxing dichloromethane for two days.^{9,218,221} Later, the solvent was changed with DMF³² or DMSO²¹⁹ since it gives the possibility to work under softer conditions, 50-80 °C for 6-24 hours.

The synthesis of the asymmetric Pt(IV) complexes follows the same procedure reported for the symmetric ones. The only difference is related to the use of anhydrides, in this case a mixture of different anhydrides or less equivalent of a single one are employed for the reaction (**Figure 3.6**).⁹

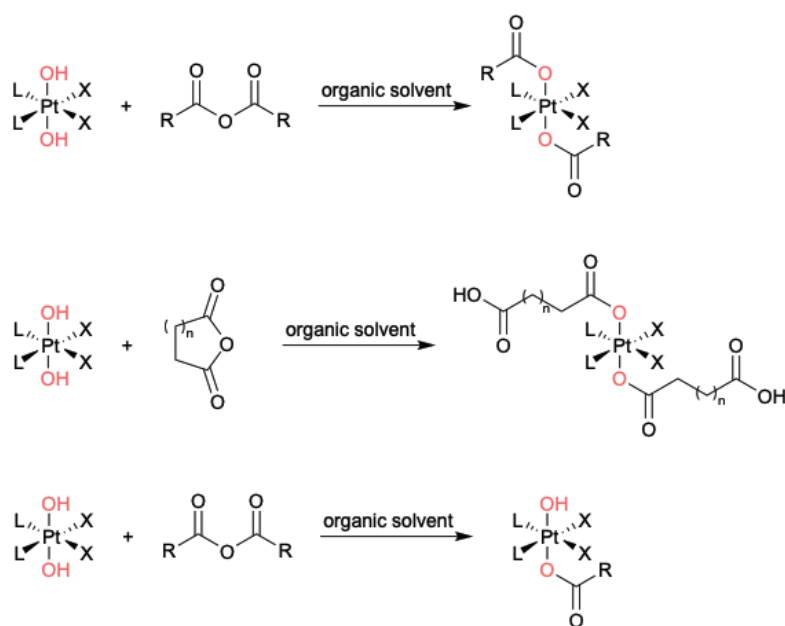


Figure 3.6 Oxidation reactions of Pt(II) complex in presence of anhydrides in organic solvents. (top) symmetric Pt(IV) complex as product of the oxidation of Pt(II) with a linear anhydride; (middle) symmetric Pt(IV) complex as product of the oxidation of Pt(II) with a cyclic anhydride; (bottom) asymmetric Pt(IV) complex as product of the oxidation of Pt(II) with a linear anhydride. Scheme adapted from ref. 9.

3.1.3. Cysteines chemistry of CTPR scaffold functionalisation

Protein modification for incorporating different active elements can be achieved exploiting natural and/or unnatural amino acids. Amongst the natural amino acids, cysteine (Cys) possesses distinctive characteristics that make it suitable for site-specific modification, such as its unique nucleophilicity.^{224,225} To achieve the desired protein modifications, native cysteine can be targeted, or new cysteine residues can be introduced through engineering techniques at the desired site. Two examples of cysteine-based chemistry exploited particularly to develop bio-hybrid structures, and adopted for the studies in this thesis, are alkylation through nucleophilic substitution reaction with haloalkyl reagents and thiol-maleimide chemistry.²²⁵

For accomplishing these two reactions with CTPR proteins, cysteines (Cys) residues are required. In the consensus tetratricopeptide repeat protein sequence (Chapter 1, section 1.3.3), this amino acid is absent.¹¹⁰ Since their high stability, CTPR allows the introduction of a desired number of amino

acids, in a specific location and distance for coordinating different active elements and giving determined properties to the structure.^{115,118} For example, the application of the thiol-maleimide reaction have been employed by the Cortajarena's group in different work using mutated CTPR proteins as scaffold.^{118,120,119} In 2016, Mejías *et al.* designed a modified CTPR protein for assembling a define number of porphyrin chromophores in a defined distance and orientation, using in specific a CTPR protein with four identical repeats where, in each of them, two cysteine mutations were introduced for the immobilisation of the porphyrin derivatives. Two porphyrins were synthesised: free-base and zinc-metalloporphyrin, both decorated with twelve triethylene glycol water-soluble tails and a maleimide reactive group for the conjugation reaction. Their work showed how this scaffold (CTPR), based on a simple unit, can be used for the conjugation with organic molecules by a controlled engineering and introduction of reactive functionalities in desired and defined positions.¹¹⁸ The formation of well-organized and functional CTPR structures based on cys-maleimide chemistry, was highlighted also by another work reported by Mejías *et al.*¹¹⁹ In this latter study, they employed functionalised gold nanoparticles incorporated to the biomolecular templating (CTPR). One of the results to highlight about this study was the demonstration of how the engineered CTPR protein, with specific cysteine mutations, can be used to control the position and the number of AuNPs per protein. Moreover, this was the first work showing AuNPs can be used for enhancing the conductivity of protein-based films composed by engineered proteins.¹¹⁹

3.2. Results and Discussion

In this chapter are reported the synthesis of all the molecules used for this thesis. Two new functionalised riboflavins were synthesized and characterized introducing a modification at N3 position. These two molecules differ for the functional group implemented at the end of the chain: riboflavin with iodoacetamide group (**Rf-IA**) and riboflavin with maleimido group (**Rf-mal**). For the platinum complexes instead, we followed the procedure already describe in literature. We synthesized two platinum complexes that vary for the two axial ligands: a symmetric platinum complex

with two succinate ligands (**Pt1**) and an asymmetric one with a succinate and an acetate ligand (**Pt2**).

We performed the functionalisation of riboflavin to covalently couple it to a protein scaffold (**CTPR** protein) exploiting the functional group introduced and the unique cysteine amino acids within CTPR sequence. We proceeded also with an activation step for **Pt2** complex (**Pt2-NHS**), for the linkage to **CTPR**. The development and the study of the system composed by CTPR, functionalised riboflavin and platinum complex are described in Chapter 5.

3.2.1. Synthesis of iodoacetamide-functionalised riboflavin

In order to conjugate the riboflavin to the CTPR protein scaffold, an iodoacetamide moiety was introduced starting from the commercial riboflavin. The use of iodoacetamide is convenient due to the capability of iodine to undergo nucleophilic substitutions. Moreover, the use of this functional group has been widely employed in bioconjugation chemistries with proteins.^{225,226}

The iodoacetamide-functionalised riboflavin was synthesised through a multi-step reaction reported in **Figure 3.7**. Starting from the commercial riboflavin, the first step is the protection of the hydroxyl groups of ribityl chain by acetonide groups (**I**). Subsequently, a nucleophilic substitution to the isoalloxazine N3 position of protected riboflavin were performed (**II**). All the protected groups were then removed (**III**), and the desired functionalised riboflavin was obtained by reacting with the iodoacetic anhydride (**Rf-IA**).

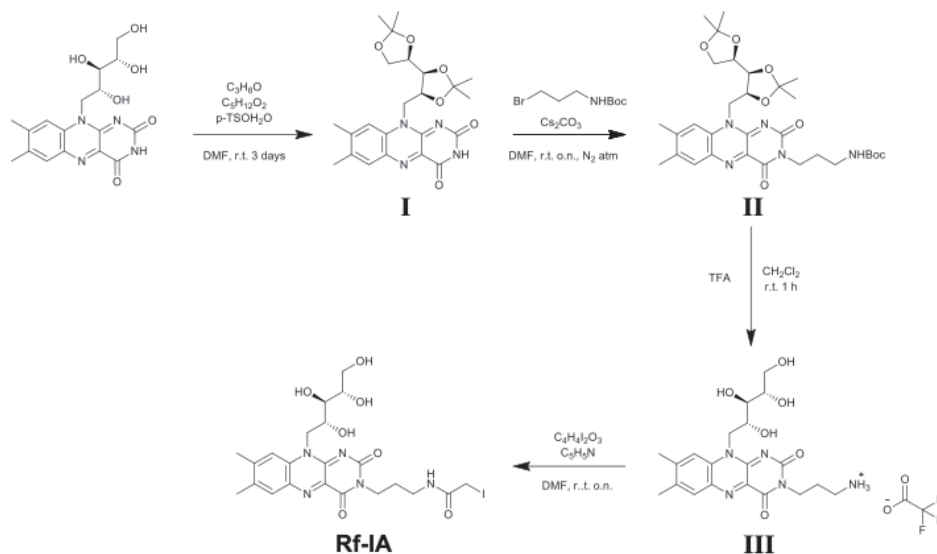


Figure 3.7 Complete synthesis scheme for the iodoacetamide-functionalised riboflavin (**Rf-IA**).

The protection of the hydroxyl groups was required as first step, since the high reactivity of these groups in participating in different type of reactions. They can be deprotonated or protonated making them good nucleophiles and leaving groups for substitution and elimination reactions respectively.²²⁷ Hence, to avoid competition in the nucleophilic substitution between hydroxyl and amine (N3), the functional groups of the ribityl chain were protected. We chose acetonide as protecting groups, because of the adaptability in the deprotection conditions needed for removing both acetonide and tert-butyloxycarbonyl (Boc) groups at the same time. Moreover, in the first synthesis scheme developed, we were using acetate groups for the protection step. This choice was then abandoned, since the deprotection conditions required (HCl as solvent with reflux at 120 °C, for 2 hours) were too harsh for riboflavin since we observed that the ribityl chain was no longer coupled to the isoalloxazine moiety of the molecule at the end of the reaction.

Below is reported the procedure of the four steps for the synthesis of the iodoacetamide-functionalised riboflavin (**Rf-IA**). Each passage, corresponds to a step reported in **Figure 3.7**.

Step 1 (Figure 3.7). 7,8-dimethyl-10-(((4*S*,4'*R*)-2,2,2',2'-tetramethyl-[4,4'-bi(1,3-dioxolan)]-5-yl)methyl)benzo[*g*]pteridine-2,4(3*H*,10*H*)-dione (I)

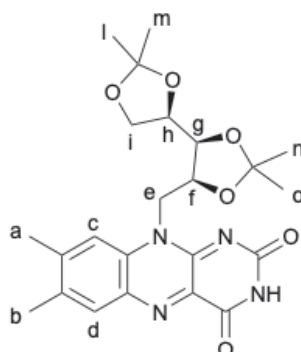


Figure 3.8 Chemical structure of the intermediate **I** for the synthesis of **RF-IA** (step 1), with the letter code used for the assignment in the $^1\text{H-NMR}$.

The first synthesis step was the protection of the hydroxyl group of the ribityl chain by acetonide groups.²⁰⁰ 3.00 g of commercial riboflavin were dissolved in 32 mL of acetone, 40 mL of dimethylformamide and 26 mL of dimethoxypropane. Subsequently, 1.5 g of and p-toluenesulfonic acid monohydrate were added and the reaction mixture was left stirring, at room temperature, covered from light, for 3 days. 80 mL of water were then added and the aqueous phase was extracted with CH_2Cl_2 ; the combined organic phases were dried over MgSO_4 and concentrated under vacuum. The product was then purified by centrifugation at 3500 rpm to remove DMF (after adding 3 mL of diethyl ether to the product) (2.5 g, 70%). It was not possible to purify the final product with column chromatography because of its very low solubility.

$^1\text{H-NMR}$ (300 MHz, CDCl_3), δ (ppm): 8.05 (s, 1H, $\text{H}_{(d)}$), 7.65 (s, 1H, $\text{H}_{(c)}$), 5.23-3.97 (m, 7H, $\text{H}_{(e)}$, $\text{H}_{(f)}$, $\text{H}_{(g)}$, $\text{H}_{(h)}$, $\text{H}_{(i)}$), 2.53 (s, 3H, $\text{H}_{(b)}$), 2.46 (s, 3H, $\text{H}_{(a)}$), 1.52-1.20 (m, 12H, $\text{H}_{(l)}$, $\text{H}_{(m)}$, $\text{H}_{(n)}$, $\text{H}_{(o)}$) (* solvent impurities: 1.60 water) (**Figure 3.9**).

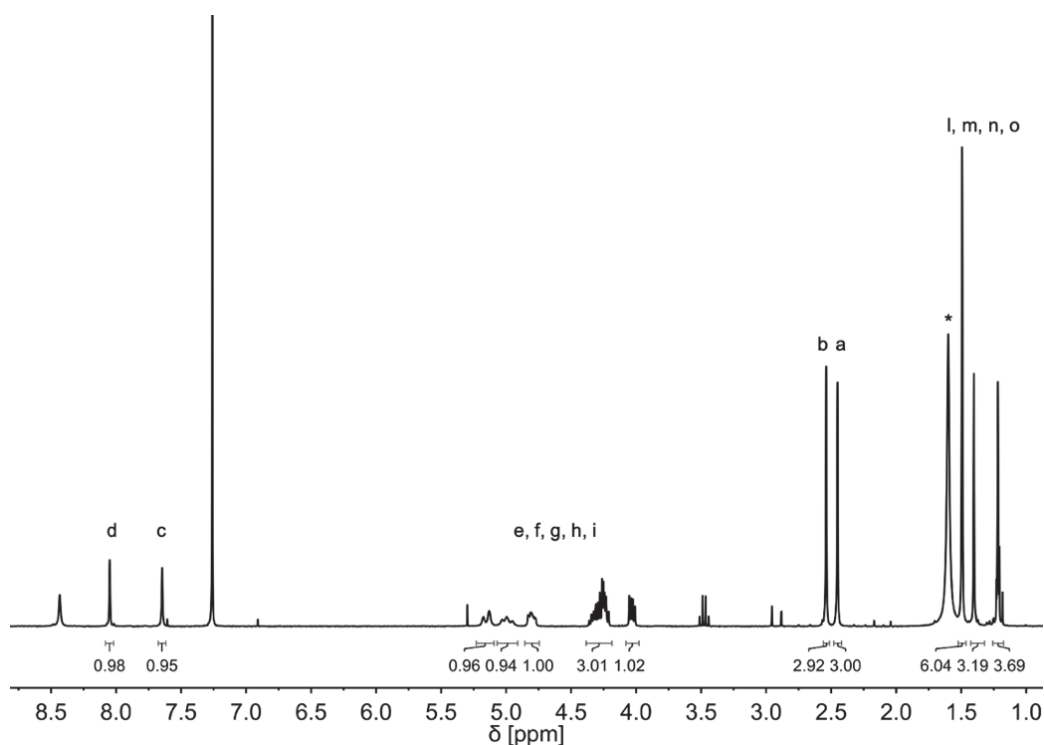


Figure 3.9 $^1\text{H-NMR}$ spectrum of **I** (Figure 3.8) in CDCl_3 .

Step 2 (Figure 3.7). Tert-butyl(3-(7,8-dimethyl-2,4-dioxo-10-(((4*S*,4'*R*,5*S*)-2,2,2',2'-tetramethyl-[4,4'-bi(1,3-dioxolan)]-5-yl)methyl)-4,10-dihydrobenzo[*g*]pteridin-3(2*H*)-yl)propyl)carbamate (II**)**

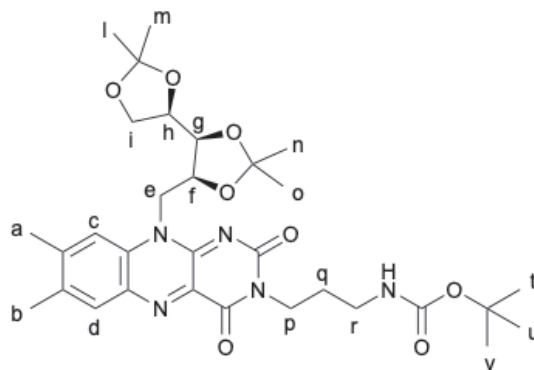


Figure 3.10 Chemical structure of the intermediate **II** for the synthesis of **RF-IA** (step 2), with the letter code used for the assignment in the $^1\text{H-NMR}$.

A nucleophilic substitution to the isoalloxazine N3 was performed as the second reaction step.²²⁸ 0.47 g of the protected riboflavin obtained and 0.51 g of Cs_2CO_3 were suspended in 5 mL of dimethylformamide and left stirring under nitrogen for 30 min. Next, 3-(Boc-amino)propyl bromide was dissolved in 3 mL of dry DMF and added to the reaction mixture, which was stirred

Chapter 3

overnight at room temperature under nitrogen. The reaction mixture was then portioned in CH_2Cl_2 and brine (a saturated solution of NaCl) and the organic phase was washed with brine. The organic phase was kept, dried with MgSO_4 , filtered, and removed under vacuum. The brown oil obtained was purified by column chromatography (eluent CH_2Cl_2 : MeOH 99:1) (0.47 g, 85%).

$^1\text{H-NMR}$ (300 MHz, CDCl_3), δ (ppm): 8.01 (s, H, $\text{H}_{(d)}$), 7.62 (s, 1H, $\text{H}_{(c)}$), 5.20-3.98 (m, 9H, $\text{H}_{(e)}$, $\text{H}_{(f)}$, $\text{H}_{(g)}$, $\text{H}_{(h)}$, $\text{H}_{(i)}$, $\text{H}_{(p)}$), 2.53 (s, 3H, $\text{H}_{(b)}$), 2.45 (s, 3H, $\text{H}_{(a)}$), 1.91 (p, 2H, $J = 6.1$ Hz, $\text{H}_{(q)}$), 1.52-1.17 (m, 21H, $\text{H}_{(l)}$, $\text{H}_{(m)}$, $\text{H}_{(n)}$, $\text{H}_{(o)}$, $\text{H}_{(t)}$, $\text{H}_{(u)}$, $\text{H}_{(v)}$). The $\text{H}_{(r)}$ signal is covered by DMF peaks (* solvents impurities: 8.01, 2.95 and 2.87 dimethylformamide, 5.30 dichloromethane) (**Figure 3.11**).

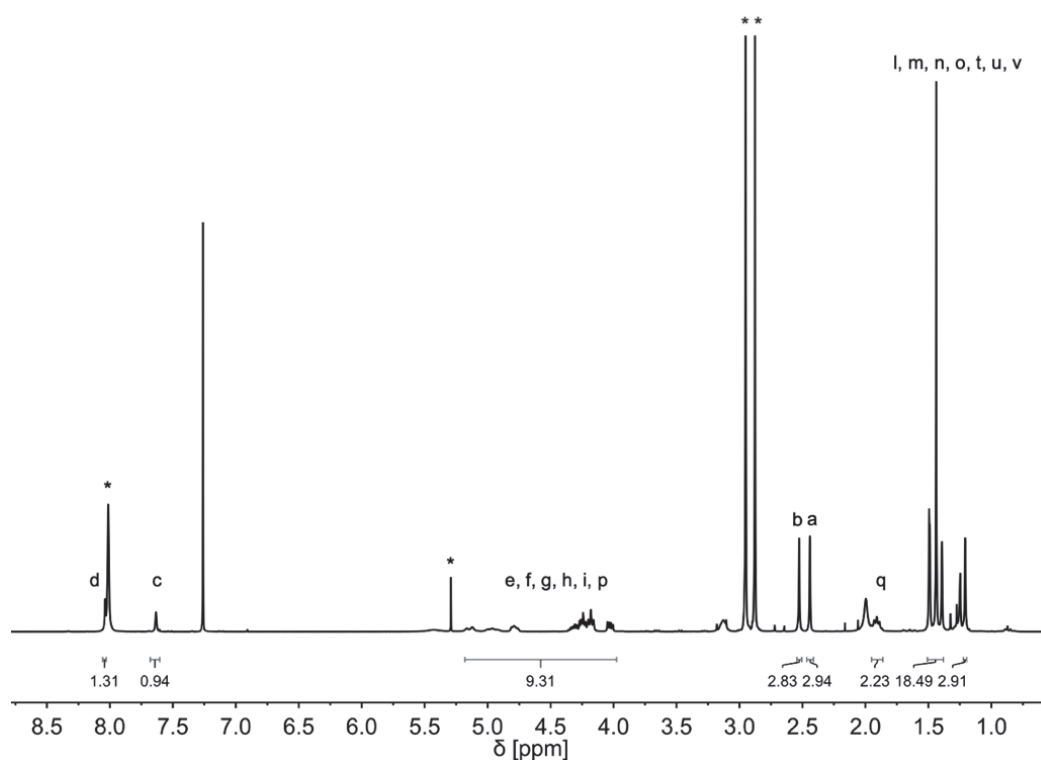


Figure 3.11 $^1\text{H-NMR}$ spectrum of **II** (**Figure 3.10**) in CDCl_3 .

Step 3 (Figure 3.7). 3-(7,8-dimethyl-2,4-dioxo-10-((2R,3R,4S)-2,3,4,5-tetrahydroxypentyl)-4,10-dihydrobenzo[g]pteridin-3(2H)-yl)propan-1-aminium (III)

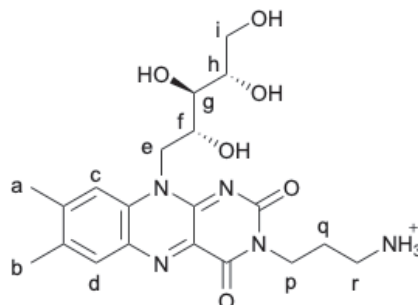


Figure 3.12 Chemical structure of the intermediate **III** for the synthesis of **RF-IA** (step 3), with the letter code used for the assignment in the $^1\text{H-NMR}$.

All the protecting group were removed following a reported procedure.²²⁹ 0.16 g of the protected and functionalised riboflavin were dissolved in 80 mL of CH_2Cl_2 in an ice bath, under stirring; 3 mL of TFA were then added to the mixture and the ice bath was removed. After 1 hour of stirring, at room temperature, the solvent was removed under vacuum and the product obtained was washed four times with CH_2Cl_2 . The final product was purified by column chromatography (eluent $\text{MeOH}:\text{H}_2\text{O}$ 37:63) (0.066 g, 59 %).

$^1\text{H-NMR}$ (300 MHz, CD_3OD), δ (ppm): 8.02 (s, 1H, $\text{H}_{(d)}$), 7.96 (s, 1H, $\text{H}_{(c)}$), 4.18 (t, 2H, $J = 6.6$ Hz, $\text{H}_{(p)}$), 3.91-3.64 (m, 5H, $\text{H}_{(e)}$, $\text{H}_{(f)}$, $\text{H}_{(g)}$, $\text{H}_{(h)}$, $\text{H}_{(i)}$), 3.00 (t, 1H, $J = 7.2$ Hz, $\text{H}_{(r)}$), 2.6 (s, 3H, $\text{H}_{(b)}$), 2.49 (s, 3H, $\text{H}_{(a)}$), 2.08 (p, 2H, $J = 6.9$ Hz, $\text{H}_{(q)}$) (* solvent impurities: 5.49 dichloromethane) (**Figure 3.13**).

ESI-MS, m/z $[\text{M}+\text{H}]^+$ calculated for $\text{C}_{21}\text{H}_{29}\text{N}_4\text{O}_6$: 433.21, found 434.5 (**Figure 3.14**).

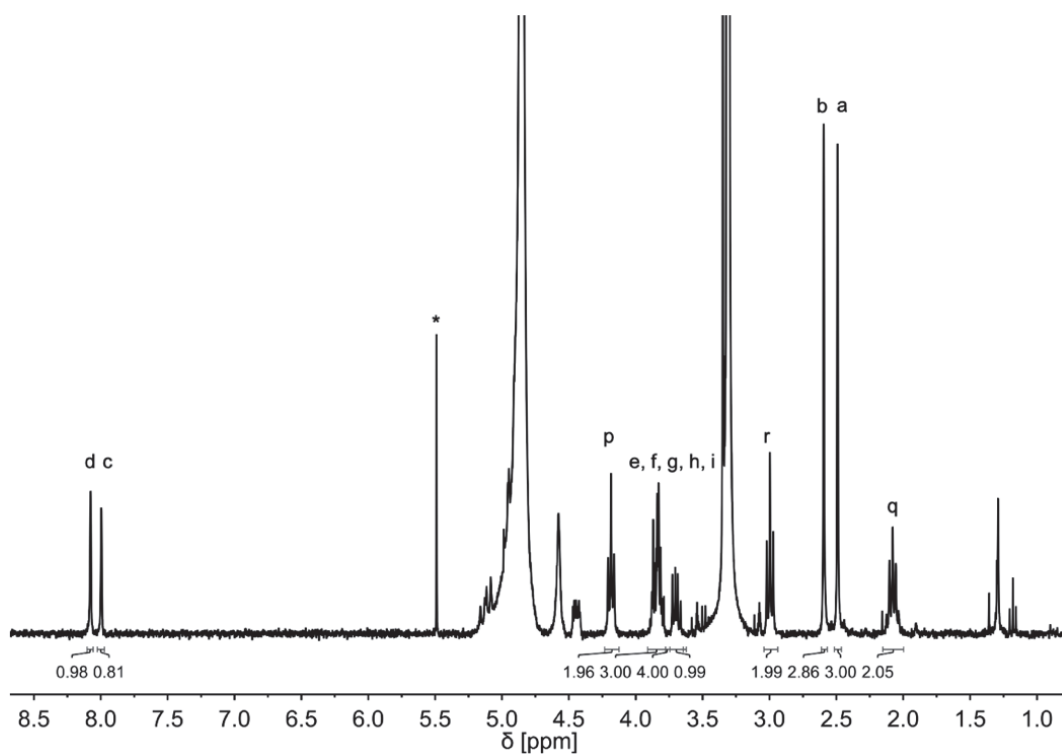


Figure 3.13 $^1\text{H-NMR}$ spectrum of **III** (Figure 3.12) in CD_3OD .

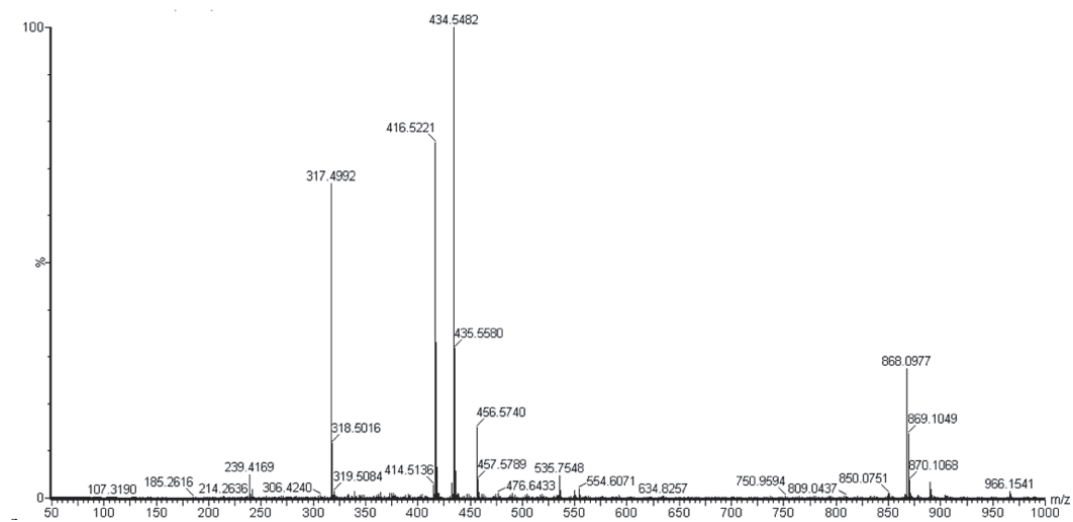


Figure 3.14 ESI-MS spectrum of **III** (Figure 3.12).

Step 4 (Figure 3.7). *N*-(3-(7,8-dimethyl-2,4-dioxo-10-((2*R*,3*R*,4*S*)-2,3,4,5-tetrahydroxypentyl)-4,10-dihydrobenzo[*g*]pteridin-3(2*H*)-yl)propyl)-2-iodoacetamide (Rf-IA)

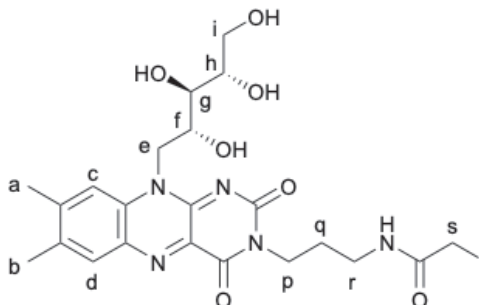


Figure 3.15 Chemical structure of the final product **RF-IA** (step 4), with the letter code used for the assignment in the $^1\text{H-NMR}$ and $^{13}\text{C-NMR}$.

Functionalisation of riboflavin with a terminal iodoacetamide group was achieved by reacting the deprotected riboflavin (**III**, **Figure 3.12**) with iodoacetic anhydride.²³⁰

0.026 g of iodoacetic anhydride, dissolved in 5 mL of dry-DMF, were added dropwise to a 5 mL solution of dry-DMF of the deprotected riboflavin (0.045 g). The addition was performed in an ice bath, removed at the end of this step. The reaction was left stirring at room temperature overnight. The solvent was removed under vacuum and **Rf-IA** was subsequently purified by column chromatography (eluent MeOH:CH₂Cl₂ from 1:5 to MeOH:CH₂Cl₂ 1:3) (6.4 mg, 15%). The final product was characterized by $^1\text{H-NMR}$, $^{13}\text{C-NMR}$ and ESI-MS. The three characteristic absorption peaks of flavin molecules (270 nm, 370 nm, and 445 nm), were observed in **Rf-IA** as well. The modification introduced in the compound did not change its spectroscopy properties (**Figure 3.19**).

$^1\text{H-NMR}$ (300 MHz, CD₃OD), δ (ppm): 8.06 (s, 1H, H_(d)), 4.13 (t, 2H, J = 6.9 Hz, H_(p)), 3.91-3.61 (m, 7H, H_(e), H_(f), H_(g), H_(h), H_(i)), 3.71 (s, 2H, H_(s)), 2.58 (s, 3H, H_(b)), 2.47 (s, 3H, H_(a)), 1.93 (p, 2H, J = 6.9 Hz, H_(q)). The H_(c), H_(r) signals are covered by DMF peaks (* solvent impurities: 8.01 dimethylformamide) (**Figure 3.16**).

^{13}C { ^1H } (125.7 MHz, CD₃OD), δ (ppm): 132.13 (1C, C_(c)), 131.66 (1C, C_(d)), 127.49 (1C, CCN), 124.86 (1C, NCCN), 75.22-71.20 (3C, C_(f), C_(g), C_(h)), 64.79 (1C, C_(i)), 40.60-38.75 (2C, C_(e), C_(p)), 28.48 (1C, C_(q)), 21.40-19.40 (2C, C(CH₃)C, C(CH₃)C), -2.70 (1C, C_(s)) (**Figure 3.17**).

Chapter 3

ESI-MS, m/z $[M+H]^+$ calculated for $C_{22}H_{28}IN_5O_7$: 600.11, found 600 (**Figure 3.15**).

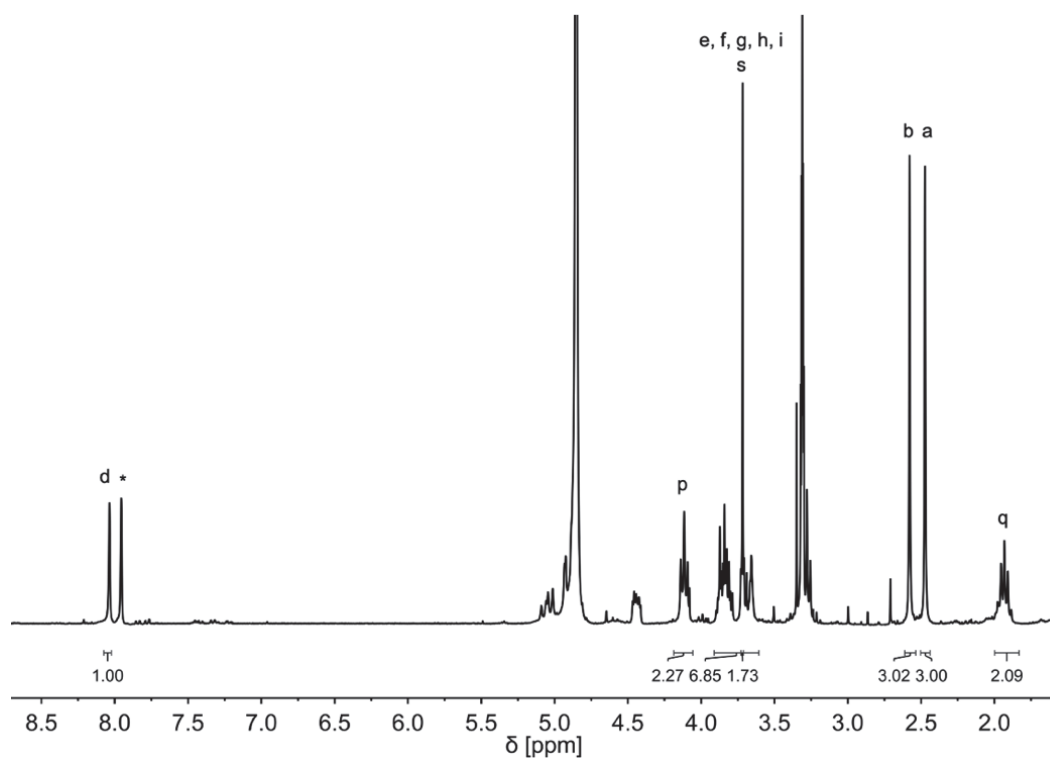


Figure 3.16 1H -NMR spectrum of Rf-IA (**Figure 3.15**) in CD_3OD .

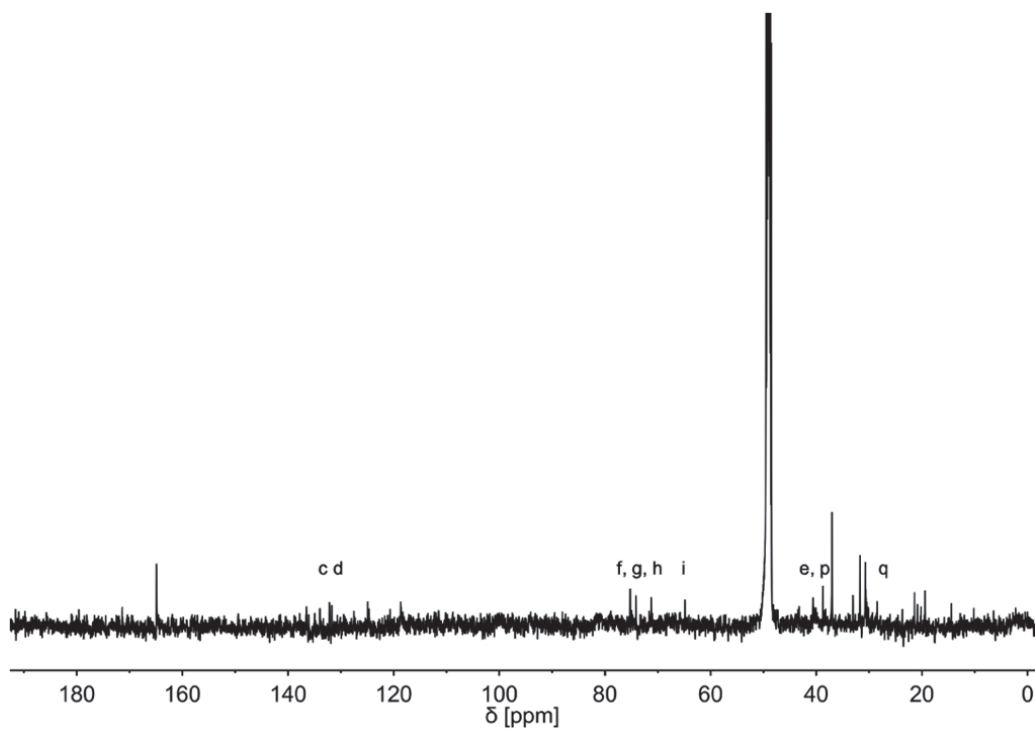


Figure 3.17 ^{13}C -NMR spectrum of Rf-IA (**Figure 3.15**) in CD_3OD .

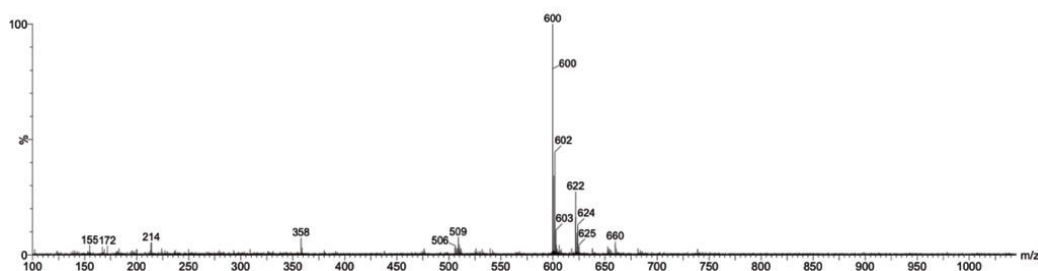


Figure 3.18 ESI-MS spectrum of Rf-IA (Figure 3.15).

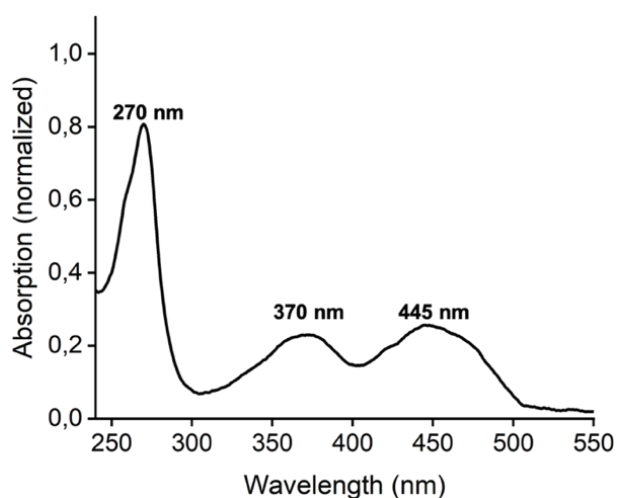


Figure 3.19 UV-Vis of Rf-IA in water.

3.2.2. Synthesis of maleimide-functionalised riboflavin

Another functionalised riboflavin with maleimide moiety was synthesised for the conjugation to CTPR. Thiol-maleimide reaction has been extensively used²²⁵ for conjugating chemical labels, such as small molecules or nanomaterial to biomolecules, in particular to proteins.^{118,120,119,226}

The maleimide-functionalised riboflavin was synthesised through a multi-step reaction reported in **Figure 3.20**. The first three steps are the same reported for the iodoacetamide-functionalised riboflavin (section 3.2.1). In the last one, the deprotected riboflavin reacted with a maleimide ester (**Rf-mal**).

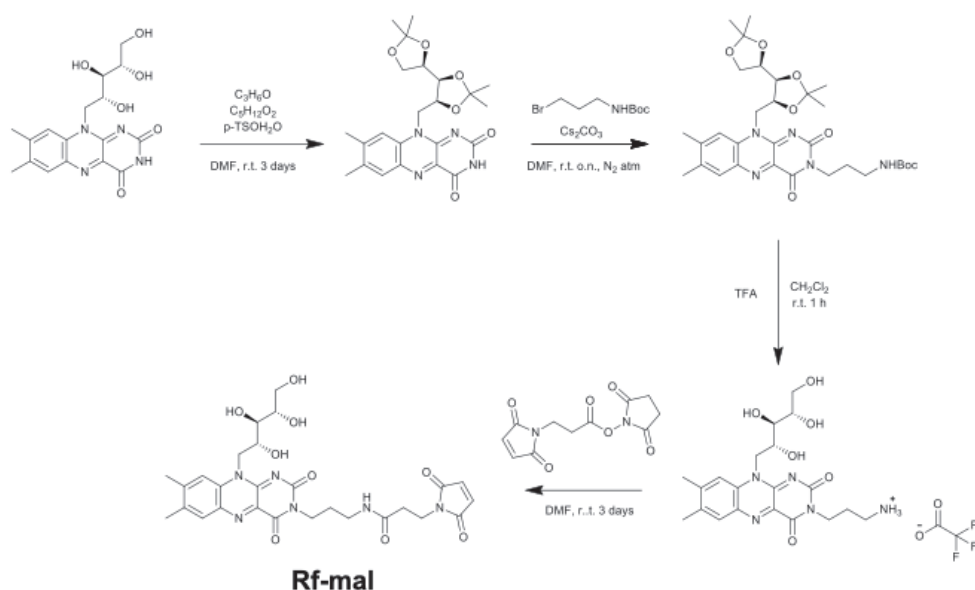


Figure 3.20 Complete synthesis scheme for the maleimide-functionalised riboflavin (**Rf-mal**).

Step 1-3 are identical to the preparation protocol described for **Rf-IA** (*vide supra*), therefore only the last step (step 4) is reported for the **Rf-mal**.

Step 4 (Figure 3.20). *N*-(3-(7,8-dimethyl-2,4-dioxo-10-((2*R*,3*R*,4*S*)-2,3,4,5-tetrahydroxypentyl)benzo[*g*]pteridin-3(2*H*,4*H*,10*H*)-yl)propyl)-3-(2,5-dioxo-2,5-dihydro-1*H*-pyrrol-1-yl)propenamide (**Rf-mal**)

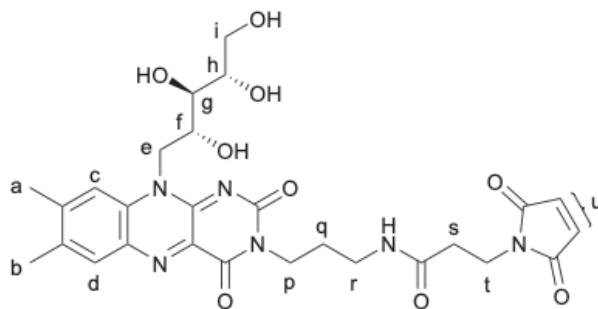


Figure 3.21 Chemical structure of the final product **Rf-mal** (step 4), with the letter code used for the assignment in the $^1\text{H-NMR}$ and $^{13}\text{C-NMR}$.

The maleimide-functionalised riboflavin was obtained by reacting the deprotected functionalised riboflavin with a maleimide ester.²³¹ Before the coupling reaction, deprotected riboflavin was basified with a basic resin, in methanol solvent, overnight. The day after, 48 mg of basified riboflavin and 29 mg of the ester were dissolved in 750 μL of dry-DMF. The reaction was left stirring for 3 days, at room temperature, covered from light. The reaction mixture was then dissolved in 3 mL of methanol and centrifugate for 5 min

at 6500 rpm to remove possible precipitate product. The final functionalised riboflavin was purified by column chromatography (filter column, eluent MeOH) (9.9 mg, 15 %).

$^1\text{H-NMR}$ (300 MHz, CD_3OD), $\delta(\text{ppm})$: 8.05 (s, 1H, $\text{H}_{(d)}$), 7.98 (s, 1H, $\text{H}_{(c)}$), 6.80 (s, 2H, $\text{H}_{(u)}$), 4.19-3.61 (m, 11H, $\text{H}_{(e)}$, $\text{H}_{(f)}$, $\text{H}_{(g)}$, $\text{H}_{(h)}$, $\text{H}_{(i)}$, $\text{H}_{(p)}$, $\text{H}_{(r)}$), 2.60 (s, 3H, $\text{H}_{(s)}$), 2.58 (s, 3H, $\text{H}_{(b)}$), 2.48 (s, 3H, $\text{H}_{(a)}$), 1.93 (p, 2H, $J = 6.9$ Hz, $\text{H}_{(q)}$). The $\text{H}_{(c)}$ signal is covered by DMF peak (* solvent impurities: 8.01, 2.95 and 2.87 dimethylformamide) (**Figure 3.22**).

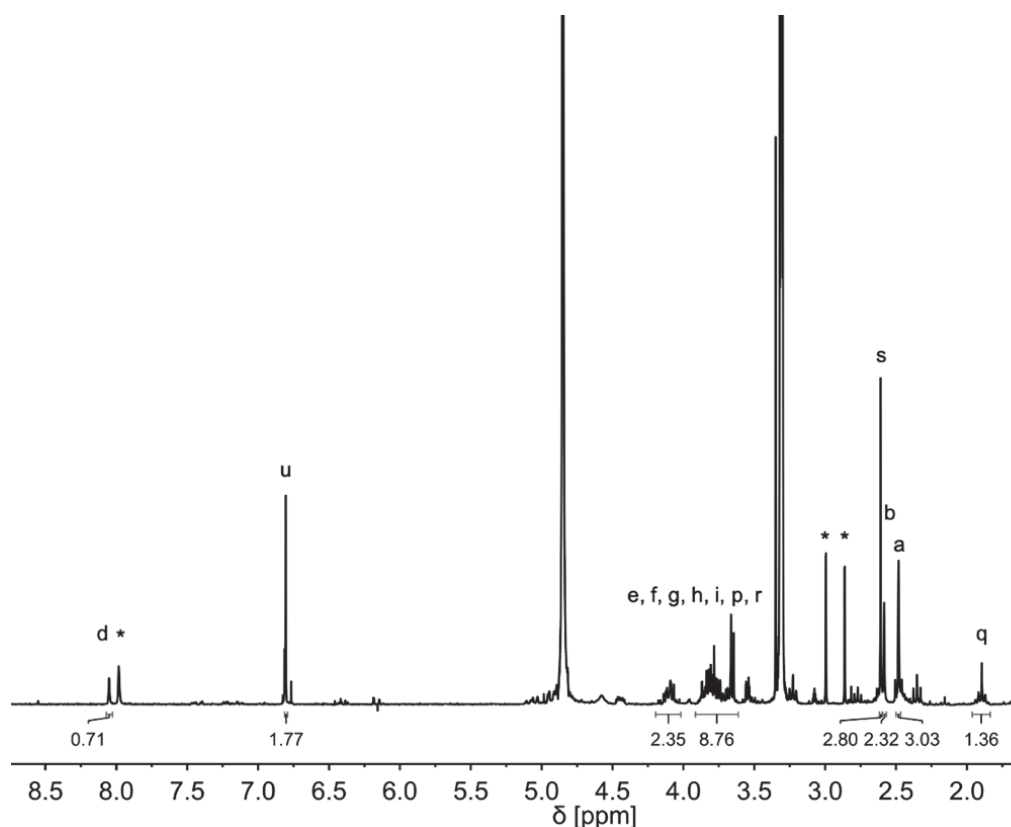


Figure 3.22 $^1\text{H-NMR}$ spectrum of **Rf-mal** (**Figure 3.21**) in CD_3OD .

3.2.3. Synthesis of $\text{cis,cis,trans-[Pt(NH}_3)_2(\text{Cl})_2(\text{O}_2\text{CCH}_2\text{CH}_2\text{CO}_2\text{H})_2]$

$\text{Cis,cis,trans-[Pt(NH}_3)_2(\text{Cl})_2(\text{O}_2\text{CCH}_2\text{CH}_2\text{CO}_2\text{H})_2]$ (**Pt1**) is a prodrug form of cisplatin. Two succinate groups were added to the metal core as axial ligands. We used this complex to analyse its photoactivation under irradiation (460 nm) in presence of gold nanoparticles as inorganic scaffold and riboflavin phosphate (**FMN**) as photocatalyst. Such studies are reported in Chapter 4.

Pt1 was prepared following the procedure described in **Figure 3.23**. Previously reported methods were adopted for the preparation of cisplatin,^{232,233} intermediate **IV**²³⁴ and **Pt1**.

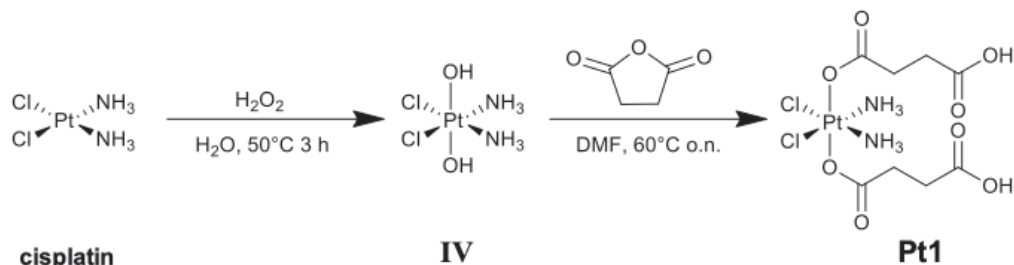


Figure 3.23 Synthetic procedure for the preparation of **Pt1**.

Below is reported the procedure of the two steps for the synthesis of the **Pt1** complex. Each passage corresponds to a step reported in **Figure 3.23**.

Step 1 (Figure 3.23). Cis-diamminedichloroplatinum(II) (*cisplatin*)

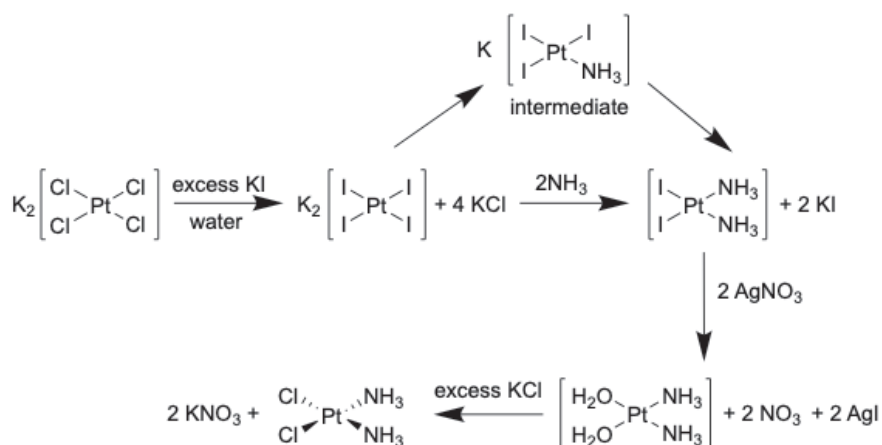


Figure 3.24 Reaction steps of the synthesis of cisplatin for the final product **Pt1** (step 1).

Cisplatin was prepared following the procedure reported by Smith and co-workers (**Figure 3.24**).²³³ 1.65 g of potassium tetrachloroplatinate(II) was dissolved in 15 mL of water and the solution was stirred until its completely dissolution. The reaction mixture was then filtered with porous paper and 2.75 g of KI were then added and the solution was left stirred for another 15 minutes. Afterwards, 1.32 mL of 1:1 NH₃(28-30%):H₂O were added and the solution was stirred for 1 hour, covered from light. A yellow precipitate formed, [Pt(NH₃)₂I₂], that was filtered and dried with cold ethanol and diethyl ether. [Pt(NH₃)₂I₂] was then mixed with AgNO₃ (2 eq) in 48.3 mL of water and

the solution was stirred at 75°C for 90 minutes protected from light. The solid product, AgI, was eliminated by filtering the yellow solution with porous paper and a syringe. 2.2 mmol of KCl for each mmol of $[\text{Pt}(\text{NH}_3)_2\text{I}_2]$ were added to the solution and left stirred for one hour at 70°C. The solution cooled for 2 hours and the final product was obtained filtering and drying with cold acetone and diethyl ether the solution (0.63 g, 53%).

Step 2 (Figure 3.23). *Cis,cis,trans*- $[\text{Pt}(\text{NH}_3)_2(\text{Cl})_2(\text{OH})_2]$ (IV)

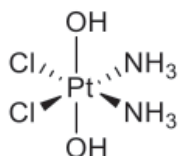


Figure 3.25 Chemical structure of the intermediate **IV** for the synthesis of **Pt1** (step 2).

0.18 g of cisplatin were suspended in 1.5 mL of water and 9 mL of hydrogen peroxide were then added. The mixture was left stirred at 50°C for 3 hours, protected from light, and progressively the solution became clear. After that, the reaction mixture was centrifuged (6500 rpm, 3 min) to remove the unreacted cisplatin and the supernatant was concentrated under reduced pressure. An excess of diethyl ether was added to the residue to favour the precipitation of a yellow solid. The product was collected by centrifugation and washed with acetone (1 mL), dichloromethane (1 mL) and ether (10 mL). The final product, **IV**, was characterized by $^1\text{H-NMR}$, confirming previously reported assignments (0.15 g, 72.5 %).²³⁴

$^1\text{H-NMR}$ (300 MHz, $(\text{CD}_3)_2\text{SO}$), $\delta(\text{ppm})$: 10.2 (s, $\text{H}_{(\text{NH}_3)}$) (**Figure 3.26**).

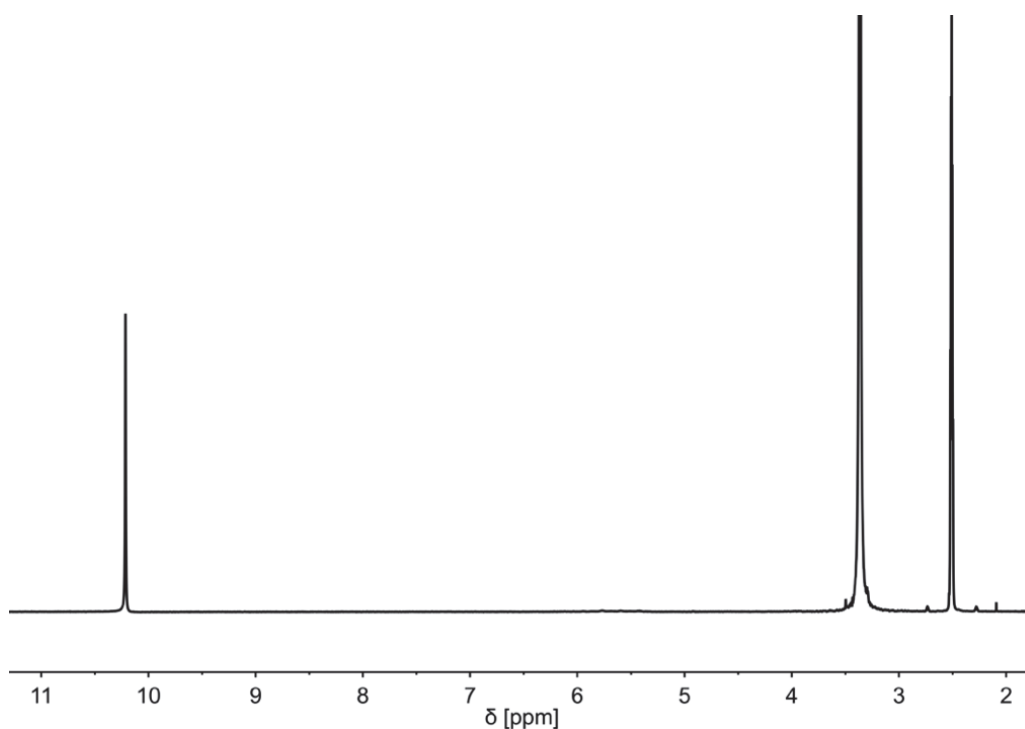


Figure 3.26 $^1\text{H-NMR}$ spectrum of **IV** (Figure 3.25) in $(\text{CD}_3)_2\text{SO}$.

Step 3 (Figure 3.23). *Cis,cis,trans*-[Pt(NH₃)₂(Cl)₂(O₂CCH₂CH₂CO₂H)₂] (Pt1)

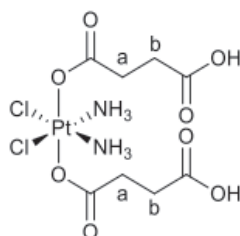


Figure 3.27 Chemical structure of the final product **Pt1** (step 3), with the letter code used for the assignment in the $^1\text{H-NMR}$.

0.14 g of **IV** (Figure 3.25) were suspended in 1 mL of dry DMF; later 0.17 g of succinic anhydride (4 eq.) were added to the solution and the reaction occurred at 60°C overnight, protected from light. The day after, 1.5 mL of CH_2Cl_2 and 45 mL of diethyl ether were added to the reaction mixture to form a yellow solid. The mixture was centrifuged (6500 rpm, 3 min) and the precipitate was dissolved three times with 1 mL of CH_2Cl_2 and 15 mL of diethyl ether. Before the addition of diethyl ether, the product was sonicated until

all the product was in suspension. The final product, **Pt1**, was characterized by NMR and ESI-MS as previously reported (140 mg, 60%).

$^1\text{H-NMR}$ (300 MHz, D_2O), $\delta(\text{ppm})$: 2.56 (t, $J = 6.9$ Hz, $\text{H}_{(b)}$), 2.33 (t, $J = 7.0$ Hz, $\text{H}_{(a)}$) (* solvents impurities: 3.56 diethyl ether, 2.94 and 2.80 dimethylformamide, 2.16 acetone) (**Figure 3.28**).

ESI-MS: m/z $[\text{M}+\text{H}]^+$ calculated for $\text{C}_8\text{H}_{16}\text{Cl}_2\text{N}_2\text{O}_8\text{Pt}$: 534, found 535 (**Figure 3.29**).

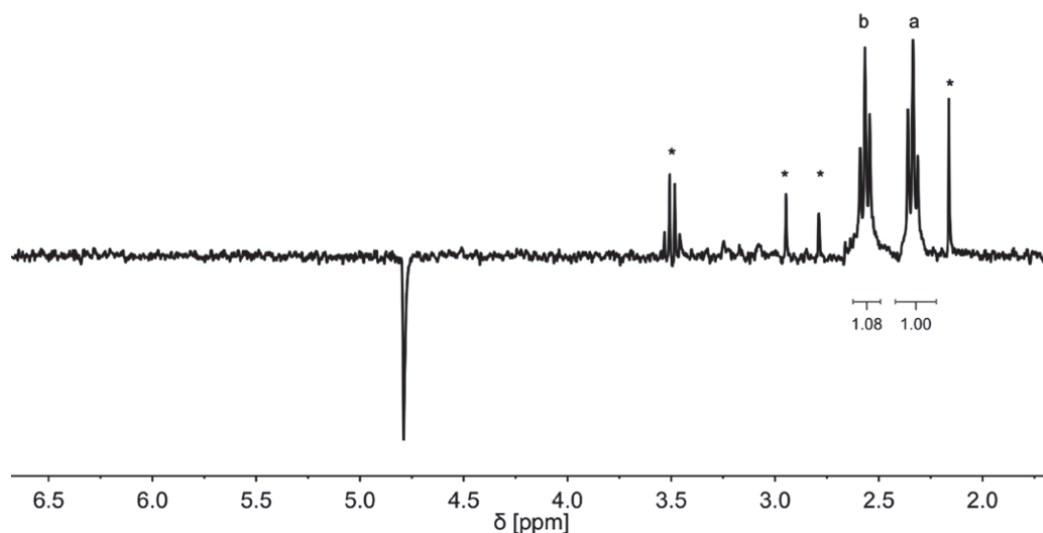


Figure 3.28 $^1\text{H-NMR}$ spectrum of **Pt1** (**Figure 3.27**) in D_2O .

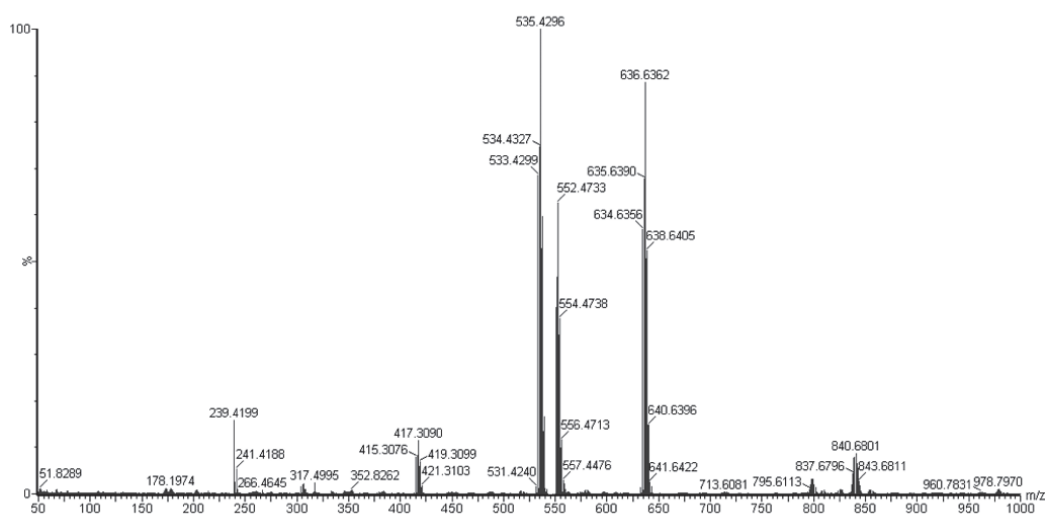


Figure 3.29 ESI-MS spectrum of **Pt1** (**Figure 3.27**).

3.2.4. Synthesis of *cis,cis,trans*- [Pt(NH₃)₂(Cl)₂(OCOCH₃)(O₂CCH₂CH₂CO₂H)] and its NHS- activated derivative

The second platinum complex employed in this work is as well as **Pt1** a prodrug of cisplatin. Differently from **Pt1**, the metal compound reported in this section is asymmetrical. We chose two different axial ligands, succinate and acetate. The selection aimed to avoid secondary reactions, such as protein crosslinking, which could be favoured by the presence of two reactive groups in the symmetric **Pt1**. The asymmetrical platinum complex was implemented in the studies of Pt photoactivation under blue light irradiation (460 nm), covalently bounded to CTPR scaffolds. The results and discussion about this system, are reported in Chapter 5.

The *cis,cis,trans*-[Pt(NH₃)₂(Cl)₂(OCOCH₃)(O₂CCH₂CH₂CO₂H)] complex, **Pt2**, was prepared following the procedure described in **Figure 3.30**. Previously reported methods were adopted for the preparation of cisplatin,^{232,233} **V**,²³⁵ **Pt2**²³⁵ and **Pt2-NHS**.²³⁵

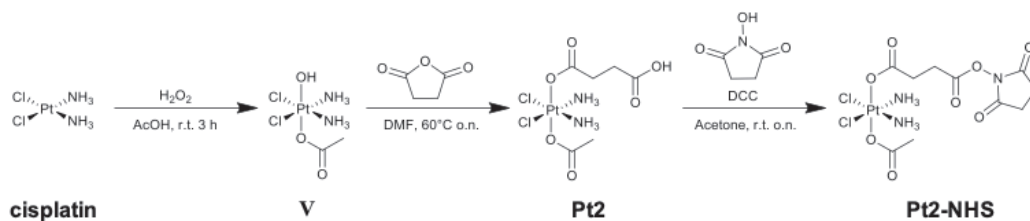


Figure 3.30 Synthetic procedure for the preparation of **Pt2** and **Pt2-NHS**.

Step 1 is identical to the preparation protocol described for **Pt1** (*vide supra*), therefore the step 2-3-4 are reported for the **Pt2**.

Step 2 (Figure 3.30). *Cis,cis,trans*-[Pt(NH₃)₂(Cl)₂(OH)(OCOCH₃)] (**V**)

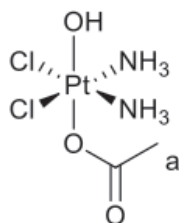


Figure 3.31 Chemical structure of the intermediate **V** (step 2), with the letter code used for the assignment in the ¹H-NMR.

0.20 g of cisplatin were suspended in 97 mL of acetic acid. After the complete dissolution of the complex, 2 mL of hydrogen peroxide were added to the solution. The mixture was reacted for 3 hours, at room temperature and protected from light. Progressively, the solution mixture became clear. Next, it was centrifuged (6000 rpm, 3 min) to remove the unreacted cisplatin and the supernatant was concentrated under reduced pressure. An excess of diethyl ether was added to the residue to favour the precipitation of a yellow solid. The product was collected by centrifugation and washed with acetone, dichloromethane and ether. The final product was characterized by $^1\text{H-NMR}$, confirming previously reported assignments (0.16 g, 64%).²³⁵

$^1\text{H-NMR}$ (300 MHz, $(\text{CD}_3)_2\text{SO}$), $\delta(\text{ppm})$: 6.25-5.70 (m, 6H, 2NH_3), 1.87 (s, 3H, $\text{H}_{(a)}$) (* solvents impurities: 5.75 dichloromethane, 3.33 water, 2.09 acetone, 1.91 acetic acid) (**Figure 3.32**).

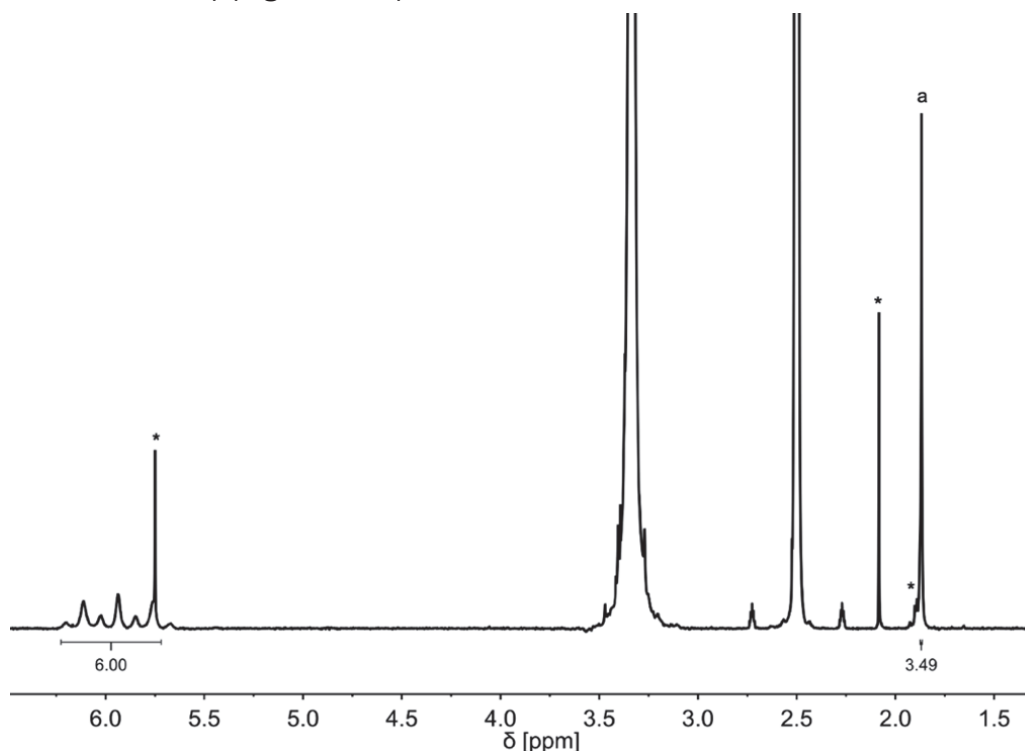


Figure 3.32 $^1\text{H-NMR}$ spectrum of **V** (**Figure 3.31**) in $(\text{CD}_3)_2\text{SO}$.

Step 3 (Figure 3.30). *Cis,cis,trans-*[Pt(NH₃)₂(Cl)₂(OCOCH₃)(O₂CCH₂CH₂CO₂H)] (Pt2)

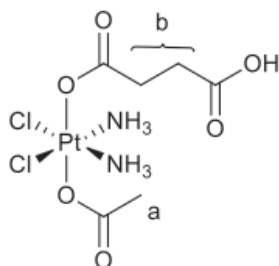


Figure 3.33 Chemical structure of the final product **Pt2** (step 3), with the letter code used for the assignment in the ¹H-NMR.

0.16 g of **V** were suspended in 1 mL of dry-DMF and 0.25 g of succinic anhydride (6 eq.) were then added. The reaction was left stirring at 60°C overnight, protected from light. The day after, 1.5 mL of CH₂Cl₂ and 45 mL of diethyl ether were added to the solution to favour the precipitation of a yellow solid. The mixture was then centrifuged (6500 rpm, 3 min) and the supernatant was discarded. The product was purified by centrifugation (3 times), dissolving first the solid in 1 mL of CH₂Cl₂, sonicating, and then adding 15 mL of diethyl ether to promote the precipitation. The final product, **Pt2**, was characterized by NMR and ESI-MS as previously reported (183 mg, 92%).²³⁵

¹H-NMR (300 MHz, (CD₃)₂SO), δ(ppm): 2.42-2.29 (m, 4H, H_(b)), 1.90 (s, 3H, H_(a)) (* solvents impurities: 2.89 and 2.73 dimethylformamide, 1.91 acetic acid) (**Figure 3.34**).

ESI-MS: m/z [M+H]⁺ calculated for C₆H₁₃Cl₂N₂O₆Pt: 475.98, found 476.99 (**Figure 3.35**).

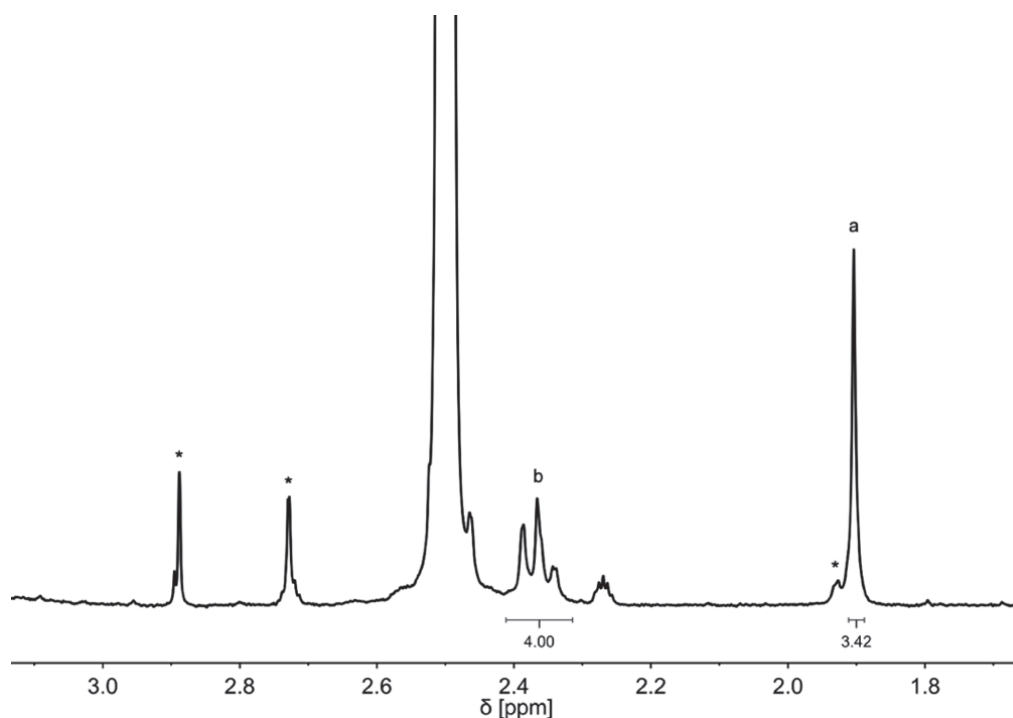


Figure 3.34 ^1H -NMR spectrum of Pt2 (Figure 3.33) in $(\text{CD}_3)_2\text{SO}$.

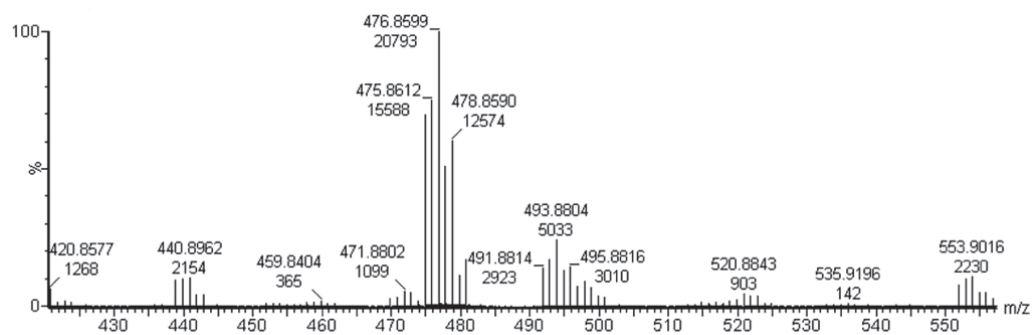


Figure 3.35 ESI-MS spectrum of Pt2 (Figure 3.33).

Step 4 (Figure 3.30). N-Hydroxysuccinimide-Activated *cis,cis,trans*- $[\text{Pt}(\text{NH}_3)_2(\text{Cl})_2(\text{OCOCH}_3)(\text{O}_2\text{CCH}_2\text{CH}_2\text{CO}_2\text{H})]$ (Pt2-NHS)

We needed to activate **Pt2** for the coupling with the lysins residues of the CTPR scaffold. Primary amine ($-\text{NH}_2$) are one of the most common amino acids used for crosslinking or labelling peptides and/or proteins. Different group can be involved in the primary amine reaction, such as the ester NHS used in this thesis.²²⁶ With the reaction between **Pt2** and N-

hydroxysuccinimide (NHS), the activated ester form of the metal compound was obtained (**Pt2-NHS**).

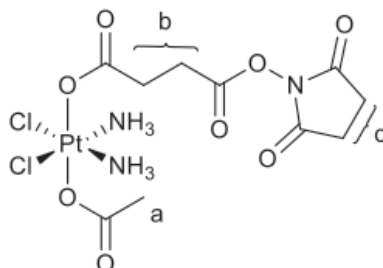


Figure 3.36 Chemical structure of the final activated product **Pt2-NHS** (step 3), with the letter code used for the assignment in the $^1\text{H-NMR}$.

0.13 g of **Pt2** were dissolved in 8 mL of anhydrous acetone and then 0.05 g of N-hydroxysuccinimide (NHS) and 0.070 g of N,N'-dicyclohexylcarbodiimide (DCC) were added to the mixture which was left stirred overnight at room temperature, protected from light. The day after, the reaction was cooled 1 hour in the freezer and the solid precipitate formed was removed by filtration. The product was washed by dissolution in acetone (1 mL), sonicated and precipitated with diethyl ether (10 mL) four times by centrifugation (6500 rpm, 3 min). The final product, **Pt2-NHS**, was characterized by NMR and ESI-MS confirming literature data (93 mg, 58%).²³⁵

$^1\text{H-NMR}$ (300 MHz, $(\text{CD}_3)_2\text{SO}$), δ (ppm): 2.85-2.60 (m, 8H, $\text{H}_{(b)}$, $\text{H}_{(c)}$), 1.90 (s, 3H, $\text{H}_{(a)}$) (**Figure 3.37**).

ESI-MS, m/z $[\text{M}+\text{H}]^+$ calculated for $\text{C}_{10}\text{H}_{17}\text{Cl}_2\text{N}_3\text{O}_8\text{Pt}$: 573.00, found 574.00 (**Figure 3.38**).

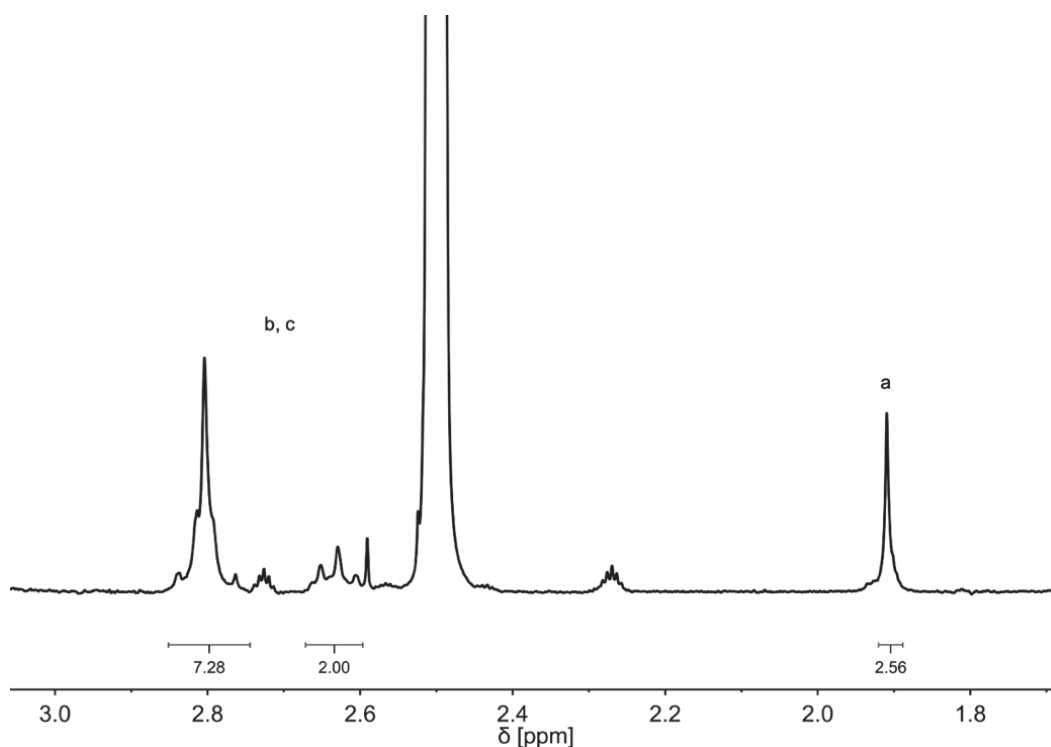


Figure 3.37 $^1\text{H-NMR}$ spectrum of Pt2-NHS (Figure 3.36) in $(\text{CD}_3)_2\text{SO}$.

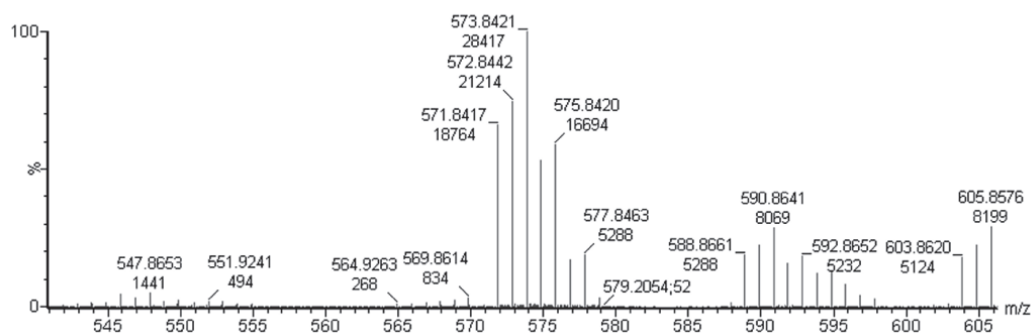


Figure 3.38 ESI-MS spectrum of Pt2-NHS (Figure 3.36).

3.3. Conclusions

In this chapter, we reported the synthesis and characterisation of two functionalised riboflavins and two platinum complexes.

To the best of our knowledge, modified riboflavin with iodoacetamido (**Rf-IA**) and maleimide group (**Rf-mal**) have not been describing before. We added these two functional groups to couple them covalently with CTPR scaffolds. Iodoacetamide moiety was implemented to the commercial

Chapter 3

riboflavin since iodine undergoes nucleophilic substitutions. The choice of maleimide instead was because of thiol-maleimide reactions are commonly exploited to link small molecules to biomolecules taking advantage of the unique thiol reactivity of the natural cysteine amino acid.

The efficiency in the conjugation with CTPR between **Rf-IA** and **Rf-mal** were compared. Maleimide-riboflavin was then discarded for its lower stability, since from the bioconjugation point of view the efficiency of both functionalised riboflavins were comparable. For this reason, the studies reported in chapter 5, concern only to **Rf-IA**.

For the synthesis of platinum complexes, **Pt1**, **Pt2** and **Pt2-NHS**, all the procedure steps are based on already reported procedures. The use of **Pt1** is described in Chapter 3, where its photoactivation in presence of gold nanoparticles is analysed. In chapter 5, the conjugation to the proteins and then the photoactivation of **Pt2** complex, are reported.

3.4. Experimental Section

Materials for synthesis and analysis

Chemicals, solvents and deuterated solvents for NMR were obtained from Merck and used as purchased without further purification. Ultrapure water was deionised and filtered with a Millipore MilliQ system. Thin layer chromatography (TLC) were run on 0.2 mm Macherey-Nagel Alugram Xtra SIL G/UV254 plates and revealed under UV light ($\lambda_{\text{max}} = 254 \text{ nm}$) or with phosphomolybdic acid. Column chromatography was performed with silica gel employing Macherey-Nagel Kieselgel 60 with particles sizes of 0.063–0.2 mm (gravity).

UV-Vis spectroscopy

UV-Vis spectrum was acquired with Biotek Synergy H1 microplate reader. For the measurements, 96 well UV flat bottom MicrotitorPlates (Thermo Fisher) were used.

Nuclear Magnetic Resonance (NMR)

NMR spectra for characterisation work were acquired on a Bruker 500 MHz Ultra Shield spectrometer, operating at 500 MHz for ^1H and 125.7 MHz for ^{13}C , and on a Bruker Fourier 300 MHz, operating at 300 MHz for ^1H and 75.4 MHz for ^{13}C . Spectra were calibrated using residual solvent signals according to previously reported values.²³⁶

Electrospray ionisation mass spectrometry (ESI-MS)

ESI mass spectra were recorded on an Agilent Technologies 1100 Series system equipped with a binary pump (G1312A) and MSD SL Trap mass spectrometer (G2445D SL) with ESI source from solutions in methanol or acetonitrile and 0.1% formic acid.

Chapter 4

Au-based nanozymes for the activation of Pt(IV) anticancer prodrugs

Part of the work presented in this chapter was carried out in collaboration with the group of Prof. Fabrizio Mancin at the Organic Chemistry Department of the University of Padua (UNIPD). They performed DOSY and NOE pumping NMR experiments and TEM measurements. Under their guidance, I have synthesized the Au NP and thiol ligands used herein.

This work can be found published as: L. F. Mazzei, Á. Martínez, L. Trevisan, D. Rosa-Gastaldo, A. L. Cortajarena, F. Mancin, L. Salassa, *Chem Commun.*, **2020**, 56, 10461- 10464.

Chapter 4

4.1. Introduction

Bioorthogonal reactions with the use of transition metal catalysts (TMCs, generally recognized as the group of elements in the middle section of the periodic table (groups 4–11) that behave as catalysts) offer the possibility of realizing transformations in biological system for in situ generation of therapeutic agents.¹⁶⁴ Since the direct use of TMCs in biological system presents limitations due to the biocompatibility, stability and low water solubility, the incorporation of TMCs in engineered nanometric scaffolds has been developed.^{237,164} These systems are also known as nanozymes.¹⁶⁴ Nanozymes can be fabricated by different approaches, such as entrapping metallic nanoparticles (like Pd, Au, Cu) in a polymer matrix,^{238,239} decorating gold nanoscaffolds with catalytic units,²⁴⁰ and encapsulating organometallic catalyst (like Ru or Pd complexes) in a coating ligand shell of a nanometric scaffolds.²⁴¹ Moreover, working on a good model of using nanozymes permits controlling the localisation of the molecular catalyst in specific cellular compartments^{238,242} or tissues¹⁷¹ and triggering their catalytic activity upon external stimuli.²⁴¹ The introduction of transition metal catalysts in nanometric scaffolds, gives also the possibility to increase the water solubility as well as to protect the metal catalysts from biological environments.¹⁶⁴

Rotello and collaborators worked on the encapsulation of TMCs catalysts in nanometric scaffolds, composed by gold nanoparticles (AuNPs). This type of approach needs specific coordination ligands for two reasons: first, for entrapping the metal catalyst in the AuNPs' monolayer with an increase of its stability, and second, for modulating the enzymatic behavior.²⁴³ Lately, Prins and co-workers developed an similar model to the one reported by Rotello, for obtaining a supramolecular systems based on the self-assembly of small molecules on the surface of AuNPs.^{244,245,246} Based on Prins' work, Mancin's group analysed different functional moieties in the AuNPs monolayer for the NMR detection of different analytes. One of the four AuNP investigated was characterised by ligands with neutral charge, while the other three by ligands with positively charges. They found that gold nanoparticles functionalised with a triazacyclononane (TACN) headgroup thiols showed a higher capability in detecting organic anions comparing to the other AuNPs. This results was attributed to the possibility of the

coordination with Zn(II) ions given by TACN groups. Indeed, Zn(II) ions may contribute with additional metal ligand coordination interactions, increasing the sensitivity of TACN AuNPs in detecting organic anions.²⁴⁷

In the past years, an innovative type of bioorthogonal photocatalytic reaction was reported by Salassa group where the metal complexes, in specific platinum complexes, act instead as substrate. In these reactions flavins (like riboflavin and its derivatives) and certain flavoproteins transform Pt(IV) prodrugs into clinically approved anticancer drugs, such as cisplatin and carboplatin, in biological media under blue light irradiation (460 nm). Indeed, mechanistic studies highlighted that light excitation of flavin (FI*) in a presence of an electron donor allows the formation of a double-reduced flavin species (FIH₂/FIH⁻) that is the active catalyst for substrate conversions (**Figure 4.1**).^{183,184,182}

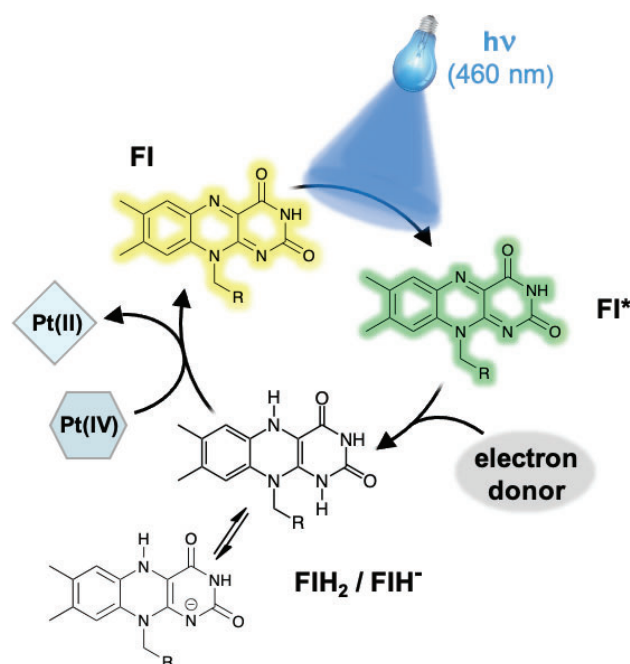


Figure 4.1 Flavin-mediated photocatalytic activation of Pt(IV) prodrugs under blue light irradiation.

4.2. Results and Discussion

In this chapter the first steps in the implementation of photocatalysis towards Pt substrates in nanozymes is reported. To such aim, we selected riboflavin phosphate (**FMN**), 1.9- nm Au nanoparticles decorated with a C11-thiol bearing a 1,4,7-triazacyclononane headgroup (**TACN AuNPs**), and the

complex *cis,cis,trans*-[Pt(NH₃)₂(Cl₂)(O₂CCH₂CH₂COOH)₂] (**Pt1**) as photocatalyst, nanozyme scaffold and substrate, respectively.

4.2.1. Synthesis and characterisation of nanozyme

The implementation of transition metal catalyst into engineered nanometric scaffold (nanozyme), such as gold nanoparticles, provides a protective environment for these metal complexes. Moreover, the surface of these systems can be functionalised introducing specific group for tuning the targeting ability or the catalytic properties.¹⁶⁴

In this chapter, we report on our first approaches in the developed on nanozyme for controlling the photoactivation of Pt(IV) anticancer prodrug. We opted for spherical nanoparticles with a Au core smaller than 2 nm as nanozyme scaffold. Nanoparticles with a small metal core were chosen for minimizing light absorption and scattering by the nanoparticles due to the surface plasmon band, whose intensity depends on the nanoparticle size.²⁴⁸ These nanoparticles were decorated with a C11-thiol bearing a 1,4,7-triazacyclononane headgroup. The complete procedure for the synthesis of this system, is reported below.

The first step to prepare the nanozyme was the synthesis of the thiol ligands (**Figure 4.2**). We performed four reactions for obtaining the final thiol ligands for the functionalisation of AuNPs surface. The first step was the protection of the amine of triazacyclononane moiety (TACN) with tert-butyloxycarbonyl protecting group (Boc). Secondly, an alkyl chain was introduced to the TACN structure by a nucleophilic substitution. This was followed by a thiol-ene reaction to convert the terminal alkene group into a thiol protected as thioacetyl. The final thiol was obtained after a deprotection of Boc and thioacetate groups.

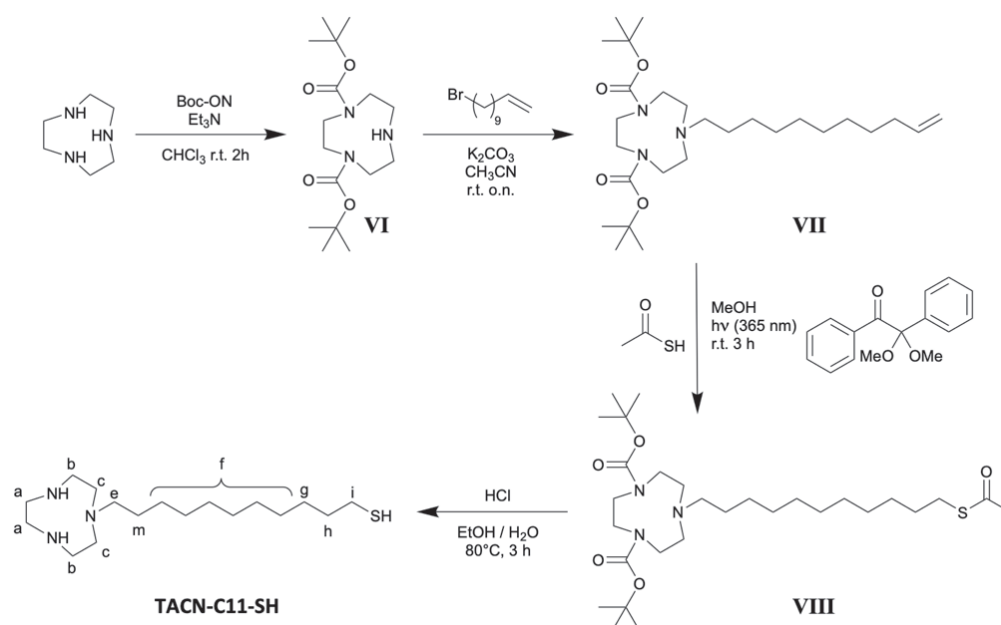


Figure 4.2 Complete synthesis scheme for the thiol ligands, TACN-C11-SH.

Below the procedure of the four steps for the synthesis of the C11-thiol bearing a 1,4,7-triazacyclononane headgroup (TACN-C11-SH) is reported. Each passage corresponds to a step reported in Figure 4.2.

Step 1 (Figure 4.2). Di-tert-butyl 1,4,7-triazonane-1,4-dicarboxylate (VI)

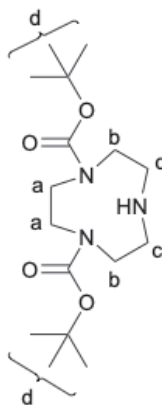


Figure 4.3 Chemical structure of the intermediate VI for the synthesis of TACN-C11-SH (step 1), with the letter code used for the assignment in the ¹H-NMR.

To a solution of 1 g of 1,4,7-triazacyclononane, dissolved in 30 mL of chloroform, 3.2 mL of triethylamine and a solution of 2-(tert-butoxycarbonyloxyimino)-2-phenylacetonitrile (BOC-ON, 3.81 g dissolved in 20 mL of chloroform) were added sequentially dropwise. The reaction was stirred for 2 hours at room temperature. The solvent was evaporated under

reduce pressure and ethyl acetate was added to obtain the residue of the process. The organic phase was then washed with an aqueous solution composed by 4% of NaHCO_3 , brine and 10% of citric acid. The resulting solution was cooled in an ice-bath, then sodium hydroxide was added until reaching a pH of 10 and a turbid solution. The mixture was extracted with CH_2Cl_2 , and the organic phase dried with Na_2SO_4 , filtered and the solvent was removed under vacuum. The final product was characterized by $^1\text{H-NMR}$ (2.12 g, 83%).²⁴⁹

$^1\text{H-NMR}$ (500 MHz, CDCl_3), δ (ppm): 3.45 (m, 4H, $\text{H}_{(a)}$), 3.29 (m, 4H, $\text{H}_{(b)}$), 2.95 (m, 4H, $\text{H}_{(c)}$), 1.48 (s, 18H, $\text{H}_{(d)}$) (* solvent impurities: 2.05 ethyl acetate) (**Figure 4.4**).

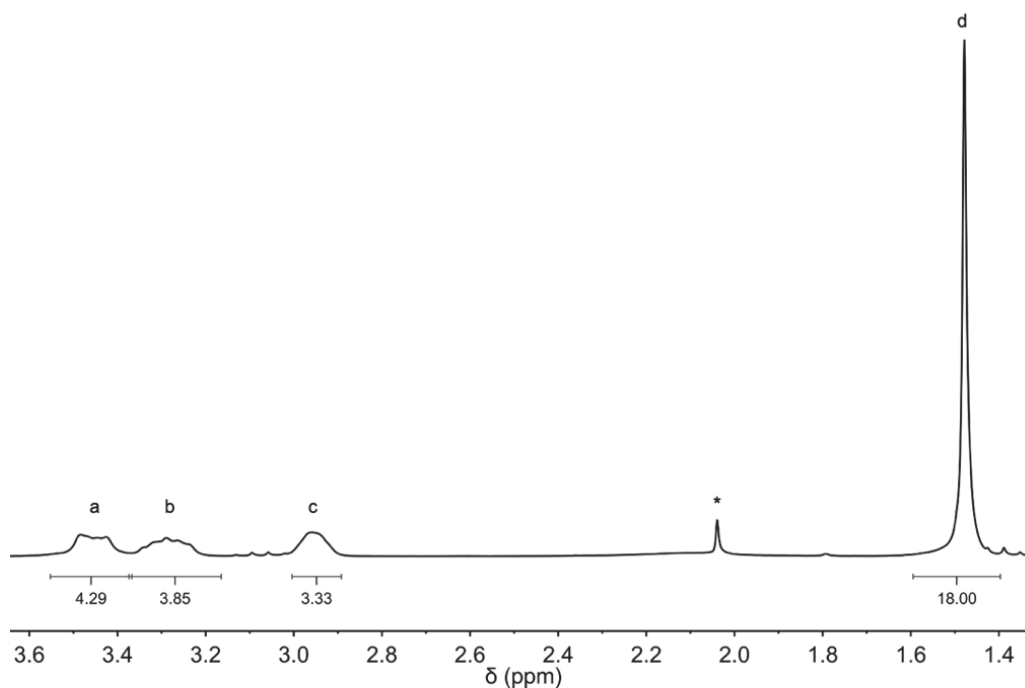


Figure 4.4 $^1\text{H-NMR}$ spectrum of **VI** (**Figure 4.3**) in CDCl_3 .

Step 2 (Figure 4.2). Di-tert-butyl7-(undec-10-en-1-yl)-1,4,7-triazonane-1,4-dicarboxylate (VII)

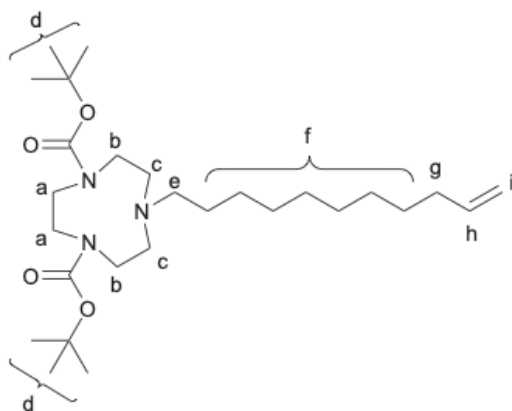


Figure 4.5 Chemical structure of the intermediate **VII** for the synthesis of **TACN-C11-SH** (step 2), with the letter code used for the assignment in the $^1\text{H-NMR}$.

0.4 g of **VI** (**Figure 4.3**) were dissolved in 20 mL of acetonitrile, subsequently 0.20 g of K_2CO_3 and 0.34 g of 11-bromo-1-undecene, dissolved in 5 mL of acetonitrile, were added to the solution. The reaction was left stirred overnight at 30°C . The day after, the solution was filter and the solvent removed under vacuum. The final product was purified by flash chromatography (eluent $\text{CH}_2\text{Cl}_2:\text{MeOH}$ 98:2) and characterized by $^1\text{H-NMR}$ (0.23 g, 40%).²⁴⁴

$^1\text{H-NMR}$ (500 MHz, CD_3OD), δ (ppm): 5.95-5.69 (ddt, $J = 17.0, 10.2, 6.7$ Hz, 1H, - $\text{H}_{(h)}$), 5.05-4.95 (ddt, $J = 1.9, 1.6$ Hz, 1H, $\text{H}_{(i)}$ (- $\text{CH}=\text{CH}_{(1)}\text{H}_{(2)}$)), 4.91 (ddt, $J = 1.2$ Hz, 1H, $\text{H}_{(i)}$ (- $\text{CH}=\text{CH}_{(1)}\text{H}_{(2)}$)), 3.46-3.50 (m, 4H, $\text{H}_{(a)}$), 3.29-3.28 (m, 4H, $\text{H}_{(b)}$), 2.64 (m, 4H, $\text{H}_{(c)}$), 2.59-2.42 (m, 2H, $\text{H}_{(e)}$), 2.05 (q, $J = 6.9$ Hz, 2H, $\text{H}_{(g)}$), 1.48 (s, 18H, $\text{H}_{(d)}$), 1.44-1.24 (m, 14H, $\text{H}_{(f)}$) (**Figure 4.6**).

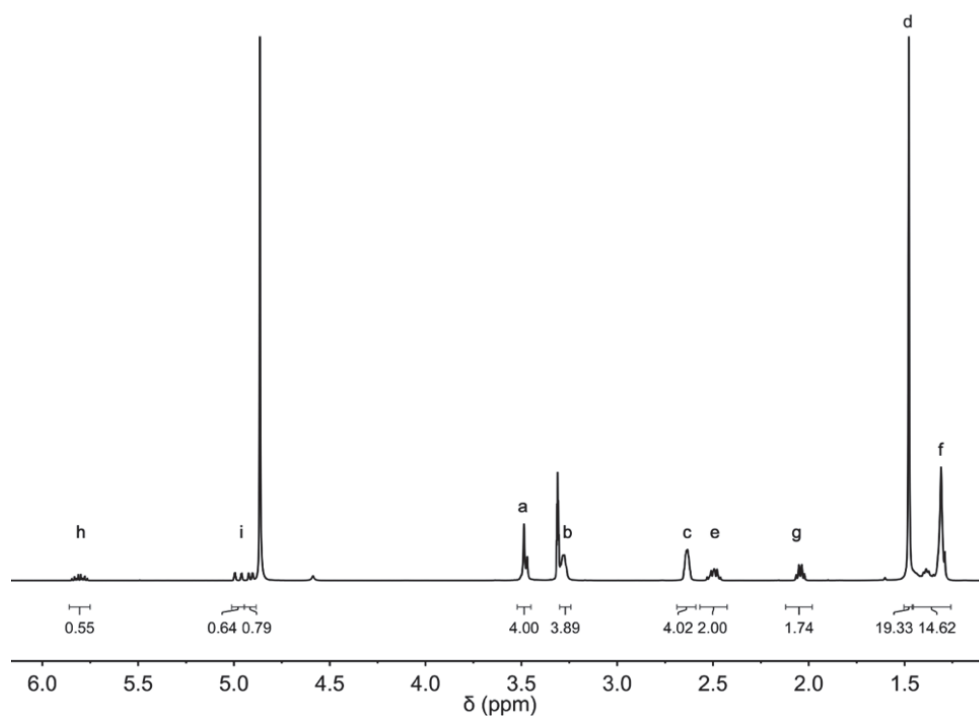


Figure 4.6 $^1\text{H-NMR}$ spectrum of **VII** (Figure 4.5) in CD_3OD .

Step 3 (Figure 4.2). Di-tert-butyl-7-(11-(acetylthio)undecyl)-1,4,7-triazonane-1,4-dicarboxylate (VIII)

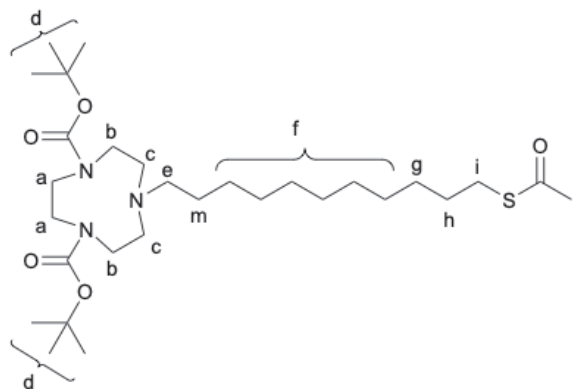


Figure 4.7 Chemical structure of the intermediate **VIII** for the synthesis of **TACN-C11-SH** (step 3), with the letter code used for the assignment in the $^1\text{H-NMR}$.

0.10 g of **VII** (Figure 4.5), 57.2 μL of thioacetic acid and 5.7 mg of 2,2-dimethoxy-1,2-diphenylethanone were dissolved in methanol, previously degassed under nitrogen for 20 min. The reaction was stirred for 3 hours under UV lamp ($\lambda = 365 \text{ nm}$) in a quartz cuvette. The product was then purified by column chromatography (eluent $\text{CH}_2\text{Cl}_2:\text{MeOH}$ 96:4) (0.11 g, 95.9%).²⁵⁰

Chapter 4

$^1\text{H-NMR}$ (500 MHz, CDCl_3), $\delta(\text{ppm})$: 3.54-3.37 (m, 4H, $\text{H}_{(a)}$), 3.32-3.08 (m, 4H, $\text{H}_{(c)}$), 2.85 (t, 2H, $J = 7.4$ Hz, $\text{H}_{(h)}$), 2.67-2.53 (m, 4H, $\text{H}_{(e)}$), 2.49-2.40 (m, 2H, $\text{H}_{(m)}$), 2.32 (s, 3H, $\text{H}_{(l)}$), 1.70-1.06 (m, 36H, $\text{H}_{(d)}$, $\text{H}_{(f)}$, $\text{H}_{(g)}$, $\text{H}_{(h)}$, $\text{H}_{(i)}$) (**Figure 4.8**).

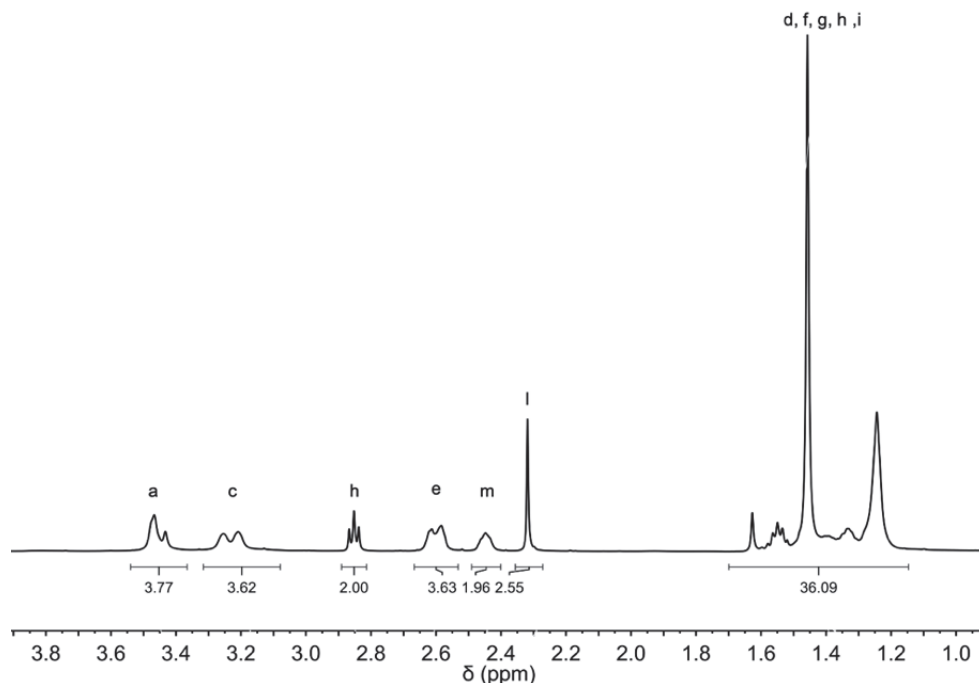


Figure 4.8 $^1\text{H-NMR}$ spectrum of **VIII** (**Figure 4.7**) in CDCl_3 .

Step 4 (**Figure 4.2**). 11-(1,4,7-triazonan-1-yl)undecane-1-thiol (**TACN-C11-SH**)

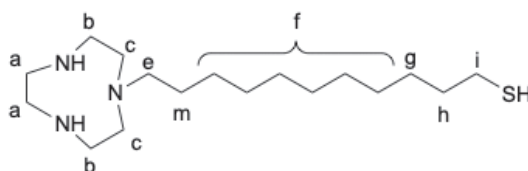


Figure 4.9 Chemical structure of the final product **TACN-C11-SH** (step 4), with the letter code used for the assignment in the $^1\text{H-NMR}$ and $^{13}\text{C-NMR}$.

6 M aqueous HCl (2.5 mL) was added to a solution of **VIII** (104.75 mg, 0.19 mmol) in MeOH (2.5 mL), and the reaction refluxed at 80°C for 3 hours. The solvent was removed under reduced pressure to yield the desired thiol as a white solid (68.9 mg, 65.7% yield). The product was used to functionalize the Au nanoparticles immediately after preparation to avoid its oxidation and the formation of disulphides.²⁴⁴

$^1\text{H-NMR}$ (500 MHz, CD_3OD), $\delta(\text{ppm})$: 3.55 (s, 4H, $\text{H}_{(a)}$), 3.08 (t, 4H, $J=5.8$ Hz, $\text{H}_{(c)}$), 2.88-2.79 (m, 2H, $\text{H}_{(e)}$), 2.49 (t, 2H, $J=7.2$ Hz, $\text{H}_{(i)}$), 1.68-1.53 (m, 4H, $\text{H}_{(h)}$,

$H_{(m)}$), 1.45-1.24 (m, 14H, $H_{(f)}$, $H_{(g)}$). The $H_{(b)}$ signal is covered by the solvent (**Figure 4.10**).

$^{13}C\{^1H\}$ NMR (125.7 MHz, CD_3OD), δ (ppm): 57.23 ($C_{(e)}$), 44.57 ($C_{(b)}$), 43.48 ($C_{(a)}$), 35.22 ($C_{(h)}$), 30.68-28.35 ($C_{(f)}$, $C_{(g)}$), 25.56 ($C_{(m)}$), 24.96 ($C_{(i)}$). The $C_{(c)}$ signal is covered by the solvent (**Figure 4.11**).

ESI-MS, m/z calculated for $C_{17}H_{38}N_3S^+$ $[M+H]^+$ 316, found 315.4.

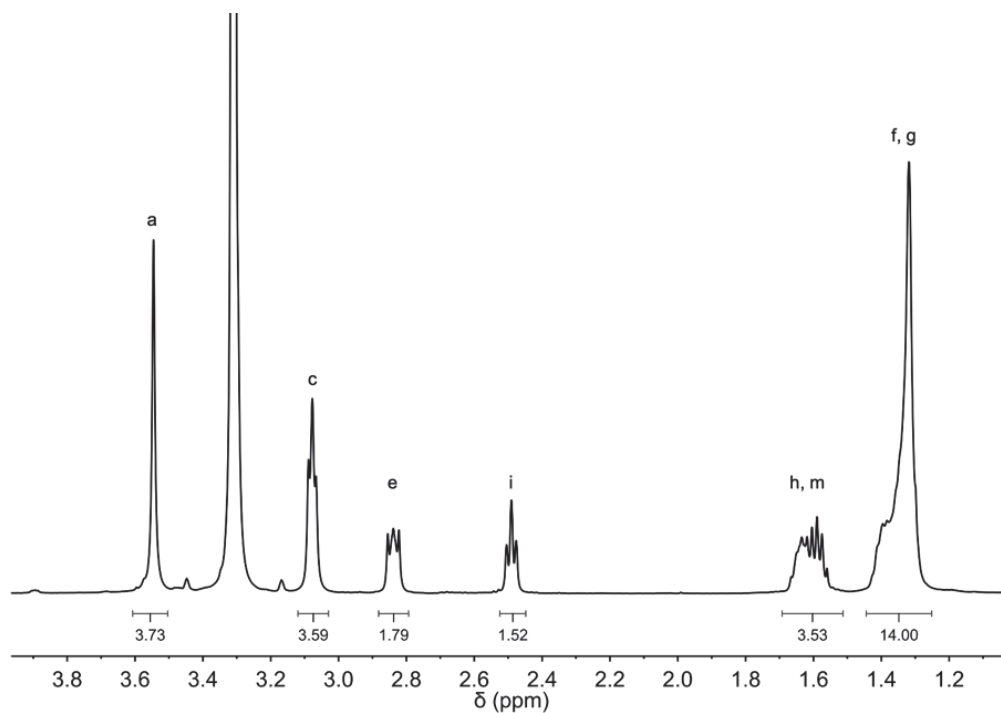


Figure 4.10 1H -NMR spectrum of TACN-C11-SH (**Figure 4.9**) in CD_3OD .

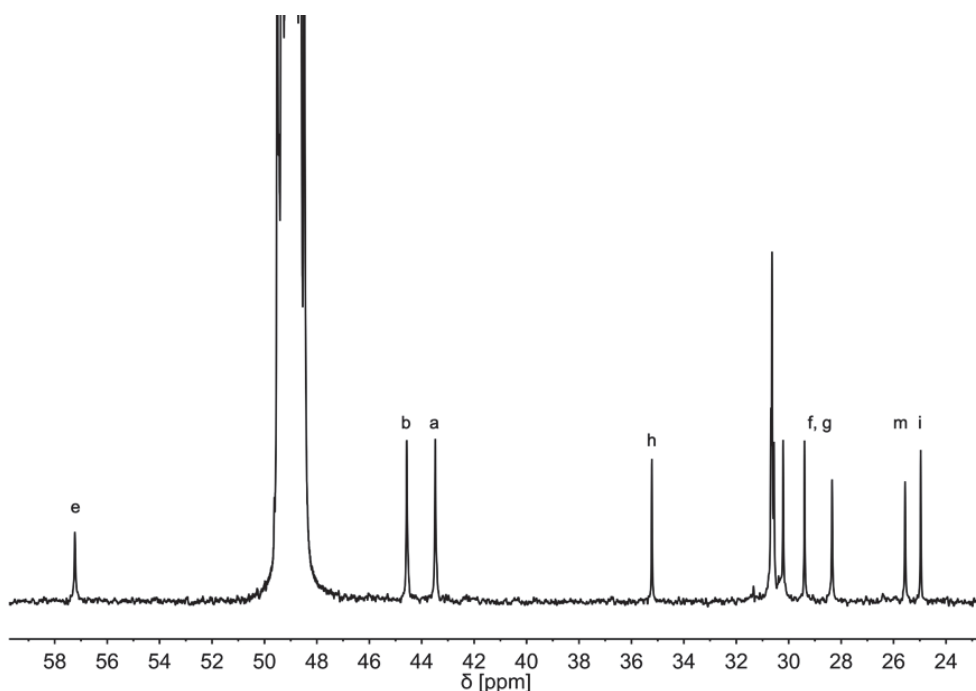


Figure 4.11 ^{13}C -NMR spectrum of TACN-C11-SH (Figure 4.9) in CD_3OD .

Synthesis of gold nanoparticles (TACN AuNPs)

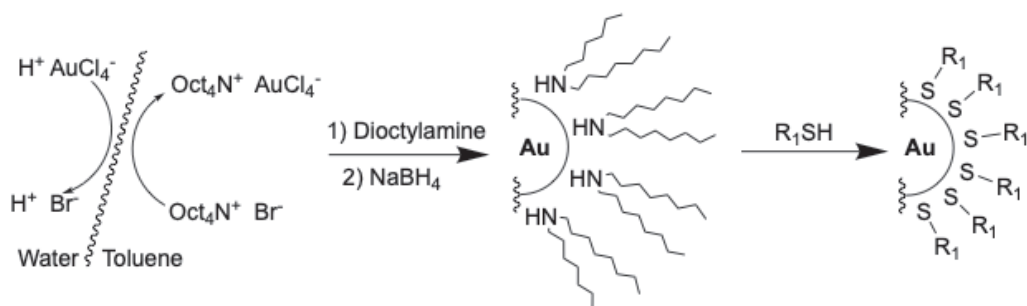


Figure 4.12 Schematic representation of the synthesis procedure for gold nanoparticles.

A modified version of Brust and Schiffrin method was employed for the synthesis of TACN AuNPs (Figure 4.12).²⁵¹ 0.087 g of tetraoctylammonium bromide (TOABr) were dissolved in 65 mL of toluene. This solution was later degassed for 15 minutes with nitrogen and then used to extract an aqueous solution of $\text{HAuCl}_4 \cdot 3\text{H}_2\text{O}$ (9.9 mM). The extract was left stirred for 10 minutes under nitrogen. Subsequently, 380 μL of dioctylamine (DOA) were added in one shot and the solution became dark red, brown, green, light yellow and finally colourless. After 2.5 hours, the solution was put in an ice-bath and 0.024 g of NaBH_4 , dissolved in 150 μl of milliQ water, were added in one shot and the colour of the solution changed to light brown. After 2 hours, the drop

of water from the addition of NaBH_4 was removed from the reaction mixture and 0.022 g of **TACN-C11-SH**, dissolved in 1 mL of methanol, were added in once. 10 minutes later the solution became colourless again and the gold nanoparticles precipitated. TOABr and DOA were removed through 3 triturations with toluene. Each triturations was carried out first sonicating the NPs suspension for 5–10 min and then centrifugating at 5000 rpm for 10 min. The NPs were at the end purified by size-exclusion chromatography twice (stationary phase: SephadexTM LH-20, eluent: methanol) and the solvent was removed under reduced pressure.

Gold nanoparticles were characterized by $^1\text{H-NMR}$, absorbance spectroscopy, transmission electron microscopy (TEM) and thermal gravimetric analysis (TGA) (**Figure 4.13**). $^1\text{H-NMR}$ spectrum corroborated the absence of free ligand molecules in solution, since all the peaks had broad shape. Their intensity and the chemical shift corresponded to the one of **TACN-C11-SH** meaning that the gold core of the nanoparticles had been covered by ligands. The signal corresponding to the methylene group $-\text{SCH}_2$ (2.49 ppm) was not observed in the nanoparticle spectrum due to the large broadening caused by its low mobility (**Figure 4.13a**). The absence of surface plasmon resonance band at about 520 nm in the UV-Vis spectrum, indicate that the size of these NPs was lower than 3 nm (**Figure 4.13b**). This was confirmed by TEM images and size distribution analysis which provided an average diameter of (1.9 ± 0.2) nm (**Figure 4.13c-d**). The molecular formula of AuNPs were given by TGA. The organic phase with respect to the mass of the whole sample was 45.95% (**Figure 4.13e**). Taking in account both TEM and TGA data, the average formula of these gold nanoparticles is $\text{Au}_{212}\text{SR}_{112}$.

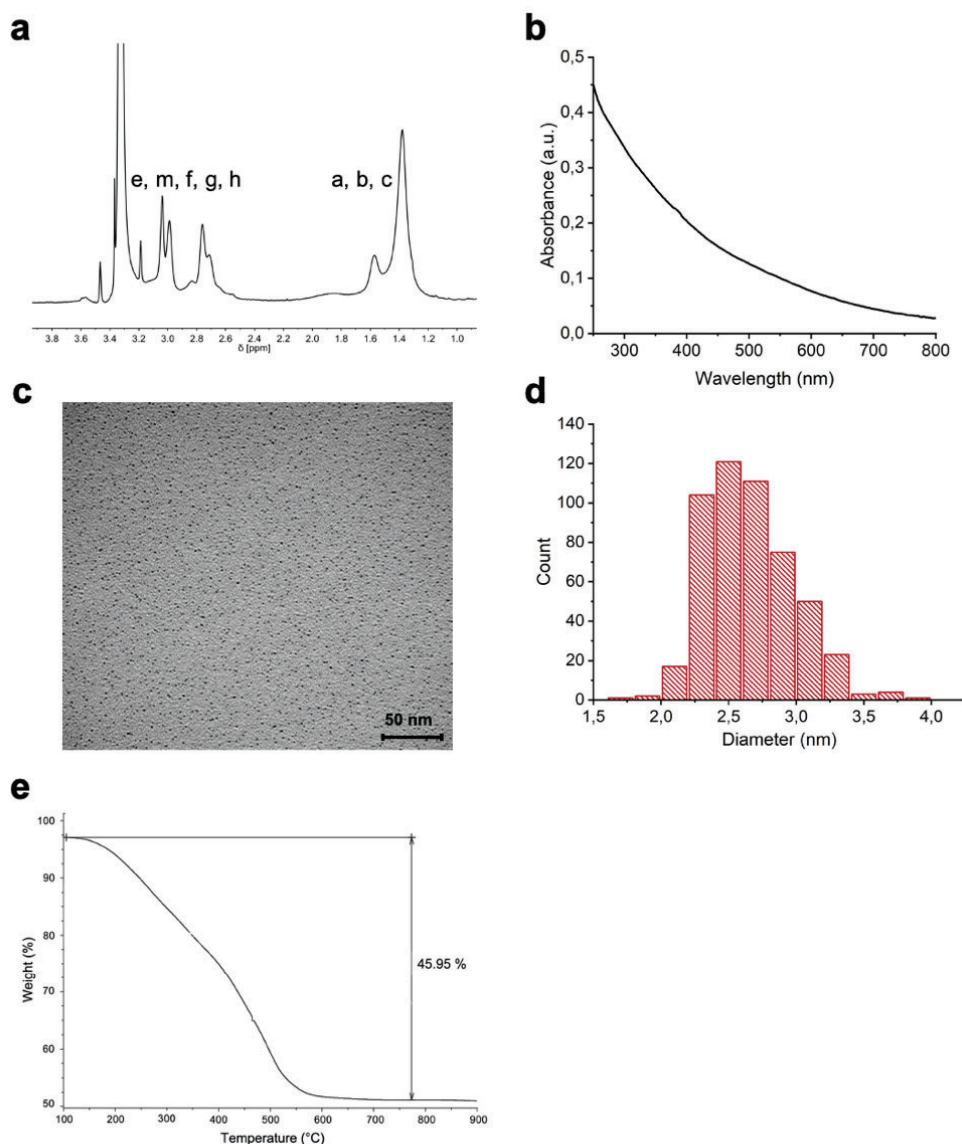


Figure 4.13 Characterisation of TACN AuNPs: (a) ^1H NMR in CD_3OD ; (b) UV-Vis in CH_3OH (0.2 mM); (c) TEM micrograph; (d) Size distribution histogram (number of particles > 250); (e) TGA thermal curve.

4.2.2. Interactions studies of nanozyme scaffolds with Pt complexes and FMN

The choice of TACN as functional moiety group of AuNPs was related to the possibility of making strongly interaction between nanoparticles, platinum complexes and riboflavins phosphate. Moreover, metal ions, such as $\text{Zn}(\text{II})$, can be loaded on TACN groups forming bimetallic binding sites with a good affinity for phosphate. It is known indeed that $\text{Zn}(\text{II})$ complexes are good receptors for phosphate.^{252,253} The ability of Zn -TACN complex to interact

with phosphate groups have been exploited in these years by the groups of Mancin, Scrimin, and Prins. Their studies revealed that this recognition ability is based on two phenomena: the interaction between the negative charge of the phosphate group with the positive one of the metal ions; the hydrophobic interactions between the inner monolayer of nanoparticles ligands with the organic part attached to the phosphate group.^{252,254,246} Furthermore, also the platinum complexes can interact with the functional groups of the AuNPs thanks to their negative charges.

In this chapter, the interactions between **Zn-TACN** moiety with respectively **FMN** and **Pt1** (synthesis and characterisation reported in Chapter 3) are analysed. In the protonated form (**TACN_{NH}** pKa 10.4, 6.8 and 2.4)²⁵⁵ or bounded to Zn(II), the positively charged **TACN** group can indeed interact with the negatively charged phosphate of the **FMN** ribityl sidechain or the one of platinum complexes, since the succinate ligands of the complex are deprotonated at pH above 6.²⁵⁶ The hydrophobic environment, provided by the C11 alkyl spacer of the ligand (AuNPs monolayer) can accommodate the aromatic isoalloxazine ring system of **FMN** (**Figure 4.14**). In specific, the interactions involving **Pt1** were studied by NMR spectroscopy, while in the case of **FMN** fluorescence titrations were performed.

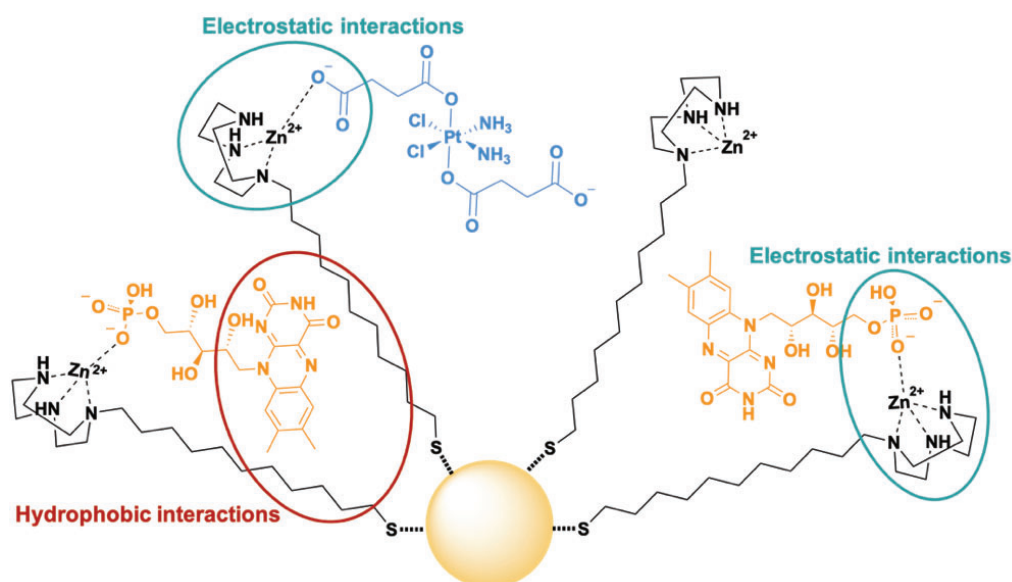


Figure 4.14 Type of interactions between **TACN AuNPs** and **FMN**, and **TACN AuNPs** and **Pt1**. In aqua green the electrostatic interactions between the negative charge of **FMN** and **Pt1** with the positive one of the functional moieties of gold nanoparticles are underlined. In dark red the hydrophobic interaction between the ligand alkyl chain and the aromatic isoalloxazine ring of **FMN** is reported.

NMR interactions studies between Pt complexes and AuNPs ligands

NMR spectroscopy is a technique that could be used for studying the detection of selected compounds. However, the detection of chemical species in complex environments are still complicate due to the overlap of many signals.²⁴⁷ In 2013, Mancin and co-workers, reported a new sensing protocol for overcoming this issue and obtaining the identification and quantification of the analytes also in complex mixture.²⁵⁷ They used gold nanoparticles with a metal core of 2 nm diameter, protected by a ligand monolayer, as matrix. Their approaches is based on the ability to extract the signals of the desired molecules (analyte) recognized by gold nanoparticles through a diffusion-assisted nuclear Overhauser effect experiments (NOE-pumping).^{257,252}

The NOE-pumping method is based on the transfer of the signal from the receptor, in this case nanoparticles, to the bounded molecules. In the first step, diffusion experiment removes all the signal of small molecules, then NOE magnetisation transfer restores only the signals arising from the species recognized by the nanoparticles. Only the signals of the molecules that are interacting with the nanoparticles are visible in the final spectrum.^{258,257,252}

NOE-pumping technique were used in this thesis to determine the interactions between platinum complexes and gold nanoparticles ligands. We combine to the NOE-pumping, another NMR method: diffusion-ordered spectroscopy (DOSY). DOSY experiments are based on the separation of NMR signals of different species according to their diffusion coefficient. Spin echo spectra are measured with a gradient on pulsed field and the signals that decay are analysed to obtain the diffusion coefficients.²⁵⁹

Before performing NOE-pumping and DOSY experiments, we analysed the ¹H-NMR spectra of **Pt1** alone and in presence of **TACN AuNPs** and **FMN**. In the presence of gold nanoparticles, the platinum signals should appear broader, when interacting with NPs, due to the reduction of the tumbling rate.²⁶⁰ The two triplets signals of **Pt1**, corresponding to the protons of the succinate axial ligands, are clearly visible in absence of **TACN AuNPs** and **FMN** (**Figure 4.15a**, top). With the introduction of the nanoparticles, even in the presence of a sub-stoichiometric amount of **TACN AuNPs** (100 μM), compared to 500 μM for **Pt1**, and **FMN** (25 μM), the signals of the complex

appeared broadened (**Figure 4.15a**, bottom). On this basis, we proceeded performing NOE pumping experiments. The results obtained demonstrate that magnetisation was transferred from the **TACN AuNPs** to the metal complex. This effect can be observed only in the case of close (0.4 nm) and sufficiently prolonged contacts. On the top of **Figure 4.15b** the ^1H -NMR spectrum of **Pt1** in presence of **TACN AuNPs** is reported, while on the bottom the NOE-pumping one performed in the same conditions. Comparing the two spectra, the change in the triplets' shape, from sharp to broader, confirming the interaction between **Pt1** and NPs.

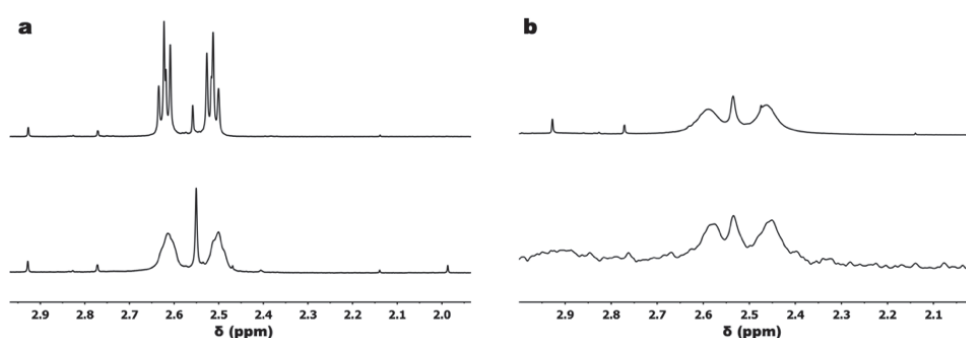


Figure 4.15 (a) Detail of ^1H -NMR spectrum of **Pt1** (500 μM) in the absence (top) and presence (below) of **TACN AuNPs** 100 μM and FMN 25 μM . (b) Detail of ^1H -NMR spectrum (top) of **Pt1** (3 mM) in the presence of **TACN AuNPs** (1 mM) and of NOE pumping spectrum (below) recorded in the same conditions.

The results obtained from NOE pumping experiment, were supported by DOSY as well. The work conditions adopted for this experiment, were the same of the NOE-pumping. DOSY NMR provided a solid evidence of the interaction between **Pt1** and **TACN AuNPs**, looking in the reduction of its diffusion coefficient (**Figure 4.16**).

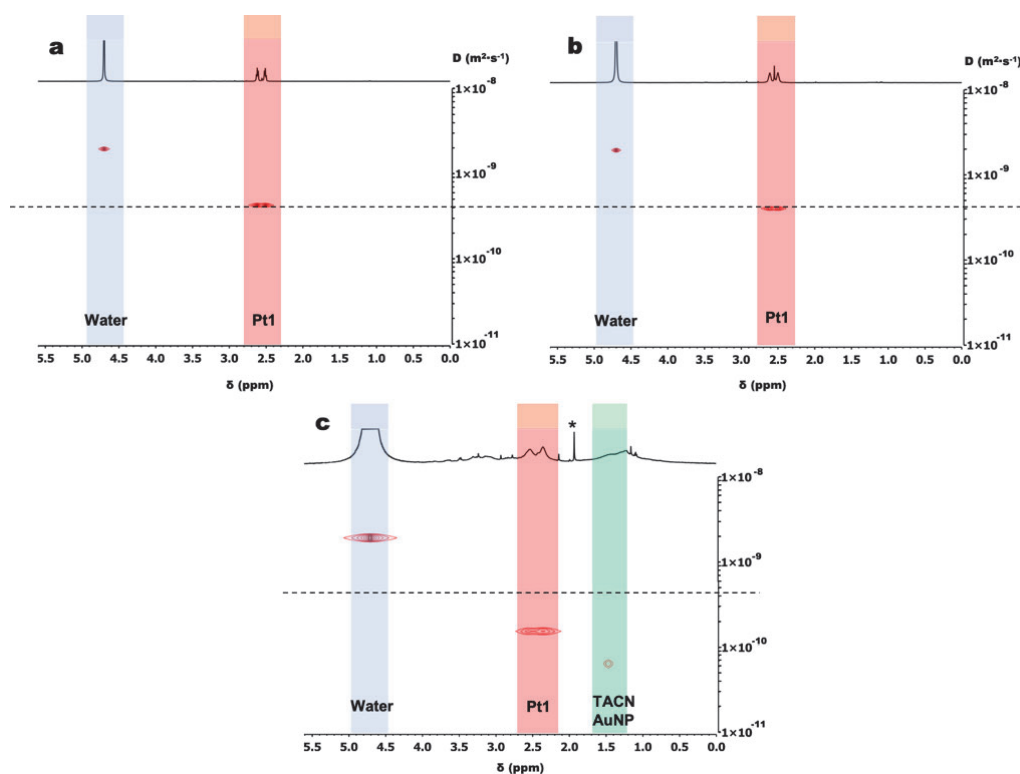


Figure 4.16 DOSY spectra of **Pt1** (500 μM) in D_2O in the absence (a) or in the presence of 100 μM **TACN AuNPs** and 25 μM **FMN** (b) or **AuNPs** 1 mM (c). Asterisks denote impurities. In b, the signals of **TACN AuNPs** are not visible; in c, only selected signals of the **TACN AuNPs** are shown for clarity.

Indeed, the diffusion rate of **Pt1** decreased up to around 4 times in the presence of the nanoparticles with respect to the free complex (1.54×10^{-10} vs. 4.26×10^{-10} m^2/s) as a consequence of the interaction with the monolayer of the NPs (**Table 4.1**).

Table 4.1 Diffusion coefficients D (m^2/s) of water, **Pt1** and **TACN AuNPs** from **Figure 4.16**.

Spectra	Water (error $D / 10^{-10}$ m^2/s)	Pt1 (error $D / 10^{-10}$ m^2/s)	TACN AuNPs (error $D / 10^{-10}$ m^2/s)
a	1.92×10^{-9} (0.001)	4.26×10^{-10} (0.016)	-
b	1.92×10^{-9} (<0.001)	3.97×10^{-10} (0.015)	-
c	1.86×10^{-9} (<0.001)	1.54×10^{-10} (0.19)	6.74×10^{-11} (1.69)

Fluorescence titrations of **FMN** on **AuNPs**

Fluorescence is a common method for the study of different biological elements.^{261,262} Concentrations, structure, function as well as interactions

between biological objects and molecules can be analysed with this technique.²⁶¹

One common problem about fluorescence methods is the non-linearity dependency between fluorescence intensity and fluorescence analyte concentrations. This effect is called inner filter effect. In highly concentrated solutions, there is a decrease of the fluorophore emission intensity due to strong attenuation of the excitation beam along the optical path, so that only molecules at the surface are excited and fluoresce (primary inner filter), and to re-absorption of emitted photons (secondary inner filter).²⁶³ Because of the shorter optical path in the emission direction (4 mm cuvette) and the little overlap between the absorption and emission spectra of the **FMN**, the secondary filter effect can be neglected. Indeed, **FMN** absorption at the emission wavelength (530 nm) is very low due to its relevant Stokes shift (about 70 nm).²⁶¹

To avoid the problem of the inner filter effects in literature it is suggested that fluorescence measurements ought to be performed in solution with a low concentration of fluorescence analyte.^{264,261,262} In this case the fluorescence intensity would be proportional to the concentration of the analyte. Hence, to correct the fluorescence data for the inner filter effect the procedure reported from Roberts and co-workers for the correction of light absorption in fluorescence studies was used.²⁶³ The corrected fluorescence value (F_{corr}) can be extrapolated determining a correction factor (C) that relates it to the fluorescence intensity observed experimentally (F_{obs}) according to the following semiempirical equations:

$$F_{obs} = F_{corr} \cdot C$$

$$C = \frac{(e^{-a \cdot d \cdot [dye]} - e^{-a \cdot [dye]})}{a \cdot [dye](1 - d)} \quad F_{corr} = s \cdot [dye] + F_{blank}$$

$$F_{obs} = (s \cdot [dye] + F_{blank}) \cdot \frac{(e^{-a \cdot d \cdot [dye]} - e^{-a \cdot [dye]})}{a \cdot [dye](1 - d)}$$

where $[dye]$ is the concentration of the fluorophore studied, F_{blank} is the fluorescence intensity at $[dye] = 0$ and a , d and s are parameters to be

determined by fitting the experimental fluorescence intensity (F_{obs}) against [dye].²⁶³

Taking into account this correction, in order to determine the loading of the dye onto **TACN AuNPs**, we exploited the capacity of Au nanoparticle to quench the emission of a fluorophore in its proximity, due to alteration of the fluorescence intensity created by the electric field of the nanoparticle.²⁴⁸ We chose this method to study **FMN** in our system. First, it is a fluoresce molecules, with $\lambda_{ex} = 349$ nm and $\lambda_{em} = 520$ nm (**Figure 4.17**) and a good quantum yield value (0.3 in aqueous solution, 0.46 in acetonitrile);⁵⁹ secondly, thanks to the negatively charge of phosphate group and to the aromatic isoalloxazine rings, **FMN** can interact with both the positively charge of the TACN moiety and the hydrophobic environment of the **TACN AuNPs** monolayer.

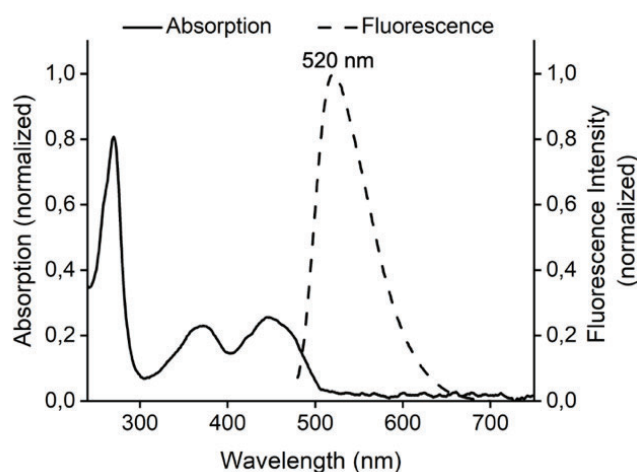


Figure 4.17 Absorption and fluorescence spectra of riboflavin in water.

The incremental addition of **FMN** without any nanoparticles should result in a linear increase of the emission intensity, instead when the nanoparticles are present fluorescence intensity should be reduced while **FMN** is bound to the **TACN AuNPs**. When concentration of **FMN** increases beyond the nanoparticle saturation concentration (concentration at which all the TACN moiety of NPs are interaction with **FMN**), the emission should increase due to free **FMN** in solution.

These titrations were performed working in a 2-(N-morpholino)ethanesulfonic buffer (MES, 5 mM, pH 6), in the absence and

presence of 1 equivalent (respect to the **TACN AuNPs** ligand concentrations, 100 μM) of $\text{Zn}(\text{NO}_3)_2$. The choice of MES was related to the fact that it acts as the electron donor for the conversion of Pt prodrugs; instead $\text{Zn}(\text{NO}_3)_2$ was incorporated to evaluate if the coordination of $\text{Zn}(\text{II})$ ions to TACN could improve the strength of **FMN-TACN AuNPs** interactions.

As a consequence of the interaction with **TACN AuNPs**, **FMN** fluorescence emission was quenched by the gold core of NPs, allowing determination of dye concentration in which all the nanoparticles binding sites are saturated. After the correction for the inner filter effect, a concentration range of 50-60 μM for the **FMN** was found for both the situations, with and without the zinc in the system (**Figure 4.18**). Up to this concentration range FMN is bound to the NPs, while going up to 60 μM is also free in solution because of all the NPs binding sites are already interaction with **FMN** molecules.

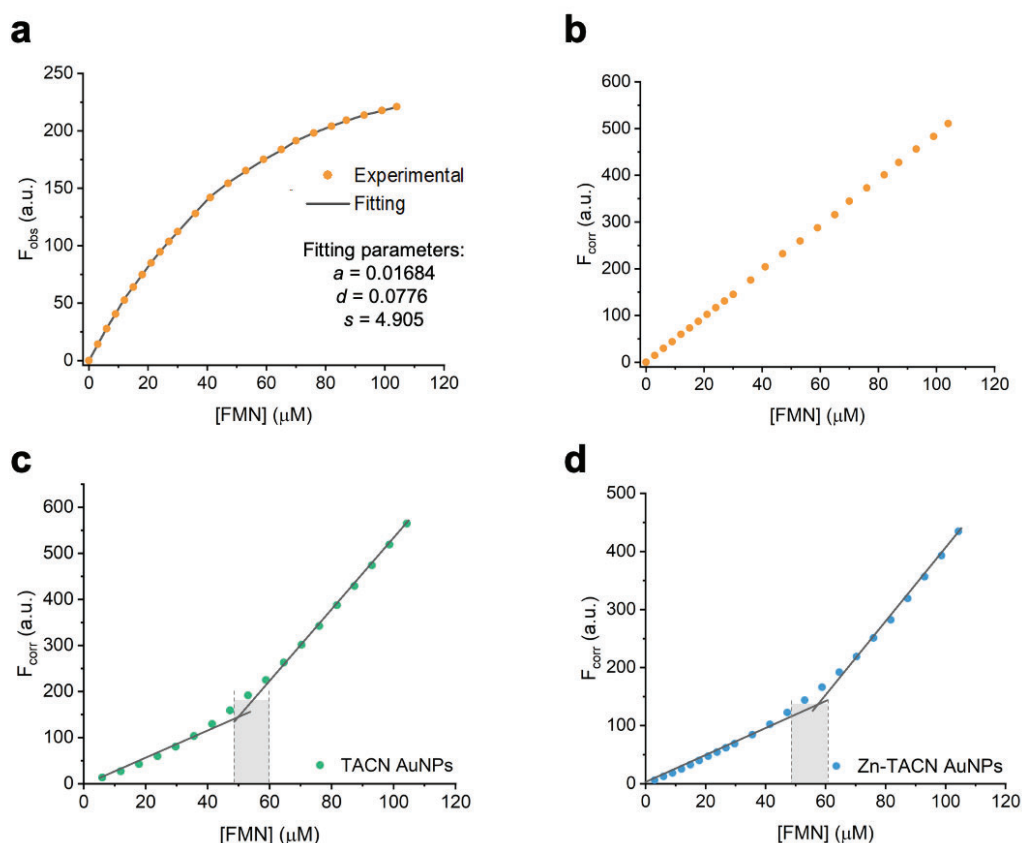


Figure 4.18 FMN fluorescence titrations (a) before and (b-d) after inner filter effect corrections for the **FMN** alone and in the presence of TACN AuNPs (100 μM), with or without addition of 1 equivalent of $\text{Zn}(\text{NO}_3)_2$. The approximate FMN concentration at which the TACN AuNPs binding sites are saturated is obtained at the intersection between the two fitting lines in the graphs c and d (shaded rectangle).

4.2.3. Pt(IV) prodrugs photoactivation studies

As reported in the introduction (section 4.1), we studied the photoactivation of Pt(IV) complex under blue light irradiation. The activation of **Pt1** was mediated by **FMN** that acted as the photocatalyst (**Figure 4.19**).

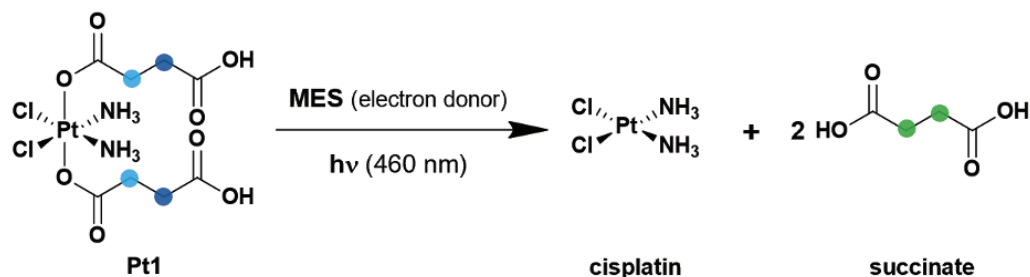


Figure 4.19 Photoreduction scheme under blue light irradiation (460 nm, 5.30 mW/cm²) for **Pt1**. The products of the reaction are cisplatin and two molecules of succinate.²⁶⁵

The conversion of the Pt complex was monitored by quantifying the release of succinate ligand by ¹H-NMR as a function of the irradiation time. Previous work of our group demonstrated that this process corresponded to the generation of the active species, cisplatin.²⁶⁵ The release of succinate ligands is straightforward to identify by ¹H NMR spectroscopy since is associated to the formation of singlet signal around 2.45 ppm and the consequent disappearance of the two triplets corresponding to the succinate ligands coordinated to the Pt centre (around 2.4-2.6 ppm).

Based on fluorescence titrations, we employed 25 μM **FMN**, a value below the saturation limit to avoid the presence of free photocatalyst in solution during the reaction. The concentration of the substrate **Pt1** was fixed at 500 μM to allow monitoring the photocatalysis progression by ¹H-NMR. The reaction was conducted with the presence of MES as electron donor (5 mM, pH 6). The catalytic performance of the nanozyme were analysed for:

- **Pt1** with **FMN**: reference system. Both the metal complex and the catalyst are free in solution (label for the graphs: **FMN**);
- **Pt1** with **FMN** and **TACN AuNPs**: solution containing **Pt1**, **TACN AuNPs**, and **FMN** (label for the graph: **FMN@TACN AuNPs**);
- **Pt1** with **FMN** and **Zn-TACN AuNPs**: solution containing, **Pt1**, **Zn-TACN AuNPs** and **FMN** (label for the graph: **FMN@Zn-TACN AuNPs**);
- **Pt1** with **TACN AuNPs**: solution containing **Pt1**, and the gold nanoparticle (label for the graph: **TACN AuNPs**);

- **Pt1** with **Zn-TACN AuNPs**: the metal complex was free in a solution containing **Zn-TACN AuNPs** (label for the graph: **Zn-TACN AuNPs**).

Under these conditions, we compared the ability and the efficiency of **FMN@TACN AuNPs** to photoactivate **Pt1** under blue light irradiation (460 nm, 5.30 mW/cm²) with the reference system. **FMN@TACN AuNPs** and **FMN** displayed an almost identical behavior, reaching for **FMN@TACN AuNPs** almost an 80% of Pt prodrug conversion already within 7 min and a plateau at 90% conversion after 30 min of light irradiation (460 nm, 5.30 mW/cm²) (**Figure 4.20a**, **Figure 4.21**, **Figure 4.22a**). Moreover, both showed a comparable initial reaction rate indicated by the trend of the first 2 min irradiation points.

As reported before, the functional moiety of these gold nanoparticles can host Zn(II) metal ions. The coordination of Zn(II) to the TACN moiety, implied an increase in the positively charge of the gold nanoparticles. No significant differences were observed after the irradiation (460 nm, 5.30 mW/cm²) for **FMN@TACN AuNPs** and **FMN@Zn-TACN AuNPs**, meaning that the coordination with zinc ions do not influence the activation of the prodrugs (**Figure 4.20a**, **Figure 4.22b**). We investigated also the photoactivation of **Pt1** in the absence of the photocatalyst (**FMN**). After 30 min of blue light irradiation, 62% of Pt(IV) prodrug conversion was observed for **TACN AuNPs** and 50% for **Zn-TACN AuNPs** (**Figure 4.20b**, **Figure 4.23a-b**). Surprisingly, we observed that the AuNPs alone had some catalytic activity. However, the reaction was slower compare to the one in presence of **FMN** in the system. Up to now, we do not have a clearly explanation for this result, but both Salassa's and Mancin's group are investigating on it.

These experiments has allowed us to affirm that the introduction of gold nanoparticles was not affecting the reduction of Pt(IV) complex, since also in the absence of **FMN**, the reaction occurred and that with the implementation of the photocatalyst, the catalytic activity was comparable to the one of the reference system.

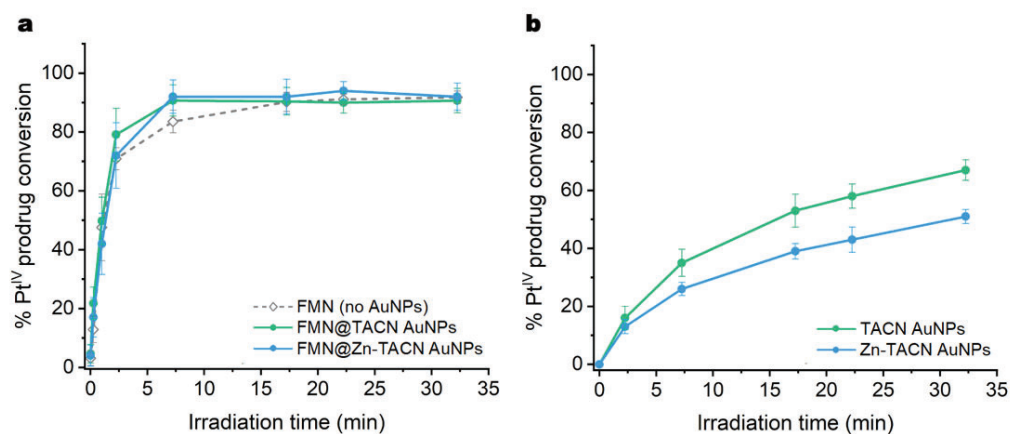


Figure 4.20 (a) Photocatalytic activation of **Pt^{IV}** by **FMN** (grey dashed line), **FMN@TACN AuNPs** (green solid line) and **FMN@Zn-TACN AuNPs** (blue solid line). (b) Photocatalytic activation of **Pt^{IV}** by **TACN AuNPs** (green solid line) and **Zn-TACN AuNPs** (blue solid line). Experimental conditions for both: $[\text{FMN}] = 25 \mu\text{M}$, $[\text{Pt}^{\text{IV}}] = 500 \mu\text{M}$, $[\text{MES}] = 5 \text{ mM}$ (pH 6), $[\text{TACN}]_{\text{AuNPs}} = 0 \mu\text{M}$ or $100 \mu\text{M}$, $[\text{Zn}(\text{NO}_3)_2] = 0 \mu\text{M}$ or $100 \mu\text{M}$, 460 nm (5.30 mW/cm^2). Each point corresponds to an average of a triplicate of triplicate independent measurements.

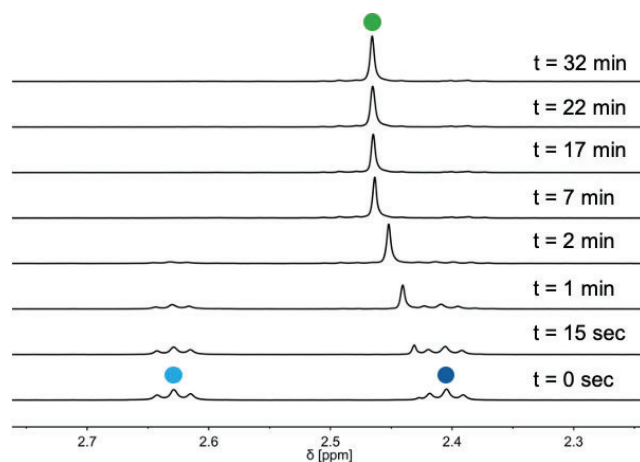


Figure 4.21 Photocatalytic activation of **Pt^{IV}** by free **FMN** in MES buffer (10% D_2O). Experimental conditions: $[\text{FMN}] = 25 \mu\text{M}$, $[\text{Pt}^{\text{IV}}] = 500 \mu\text{M}$, $[\text{MES}] = 5 \text{ mM}$ (pH 6). ¹H-NMR signal labelling: ● $\text{Pt-OCOCH}_2\text{CH}_2\text{CO}_2^-$, ● $\text{Pt-OCOCH}_2\text{CH}_2\text{CO}_2^-$, and ● $\text{free O}_2\text{CCH}_2\text{CH}_2\text{CO}_2^-$.

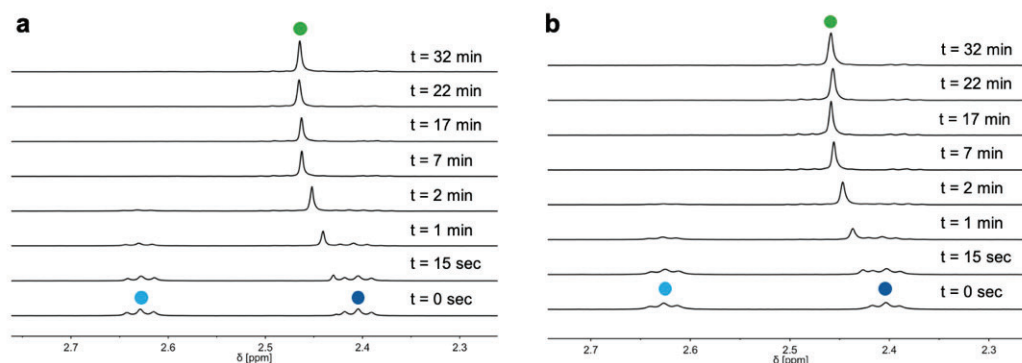


Figure 4.22 Photocatalytic activation of **Pt1** by **FMN@TACN AuNPs** without (a) or with (b) $\text{Zn}(\text{NO}_3)_2$ in MES buffer (10% D_2O). Experimental conditions: $[\text{FMN}] = 25 \mu\text{M}$, $[\text{Pt1}] = 500 \mu\text{M}$, $[\text{MES}] = 5 \text{ mM}$ (pH 6), $[\text{TACN}]_{\text{AuNPs}} = 100 \mu\text{M}$, $[\text{Zn}(\text{NO}_3)_2] = 0 \mu\text{M}$ or $100 \mu\text{M}$, 460 nm (5.30 mW/cm^2). ^1H -NMR signal labelling: ● $\text{Pt-OCOCH}_2\text{CH}_2\text{CO}_2^-$, ● $\text{Pt-OCOCH}_2\text{CH}_2\text{CO}_2^-$, and ● free $\text{O}_2\text{CCH}_2\text{CH}_2\text{CO}_2^-$.

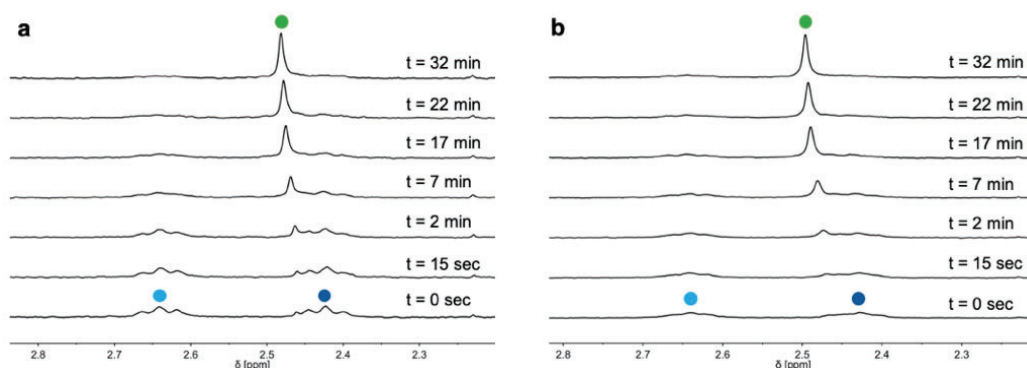


Figure 4.23 Photocatalytic activation of **Pt1** by **TACN AuNPs** without (a) or with (b) $\text{Zn}(\text{NO}_3)_2$ in MES buffer (10% D_2O). Experimental conditions: $[\text{Pt1}] = 500 \mu\text{M}$, $[\text{MES}] = 5 \text{ mM}$ (pH 6), $[\text{TACN}]_{\text{AuNPs}} = 100 \mu\text{M}$, $[\text{Zn}(\text{NO}_3)_2] = 0 \mu\text{M}$ or $100 \mu\text{M}$, 460 nm (5.30 mW/cm^2). ^1H -NMR signal labelling: ● $\text{Pt-OCOCH}_2\text{CH}_2\text{CO}_2^-$, ● $\text{Pt-OCOCH}_2\text{CH}_2\text{CO}_2^-$, and ● free $\text{O}_2\text{CCH}_2\text{CH}_2\text{CO}_2^-$.

Moreover, we investigated the stability of the nanozymes under light irradiation to discard leaking of **FMN** from the AuNPs during catalysis (**Figure 4.24**). In the presence of **TACN AuNPs**, the fluorescence emission of **FMN** remained quenched throughout the whole light-irradiation time, thus demonstrating that the catalyst was associated to the nanozyme scaffold during such period. In addition, the emission intensity of **FMN@TACN AuNPs** underwent a further slight decrease over time due to **FMN** photodegradation,¹⁸³ with almost complete depletion after 10 min. However, the process occurred at a lower rate than for free **FMN**, suggesting a moderate protecting effect of the AuNPs towards **FMN** photobleaching. We hypothesize that such increase in stability positively contributed to the catalytic activity of the system.

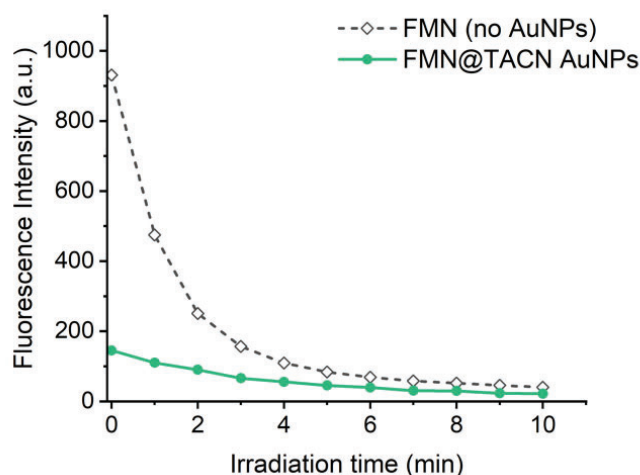


Figure 4.24 Photobleaching of **FMN@TACN AuNPs** and free **FMN**. Experimental conditions: [FMN] = 25 μ M, [Pt2] = 500 μ M, [MES] = 5 mM (pH 6), [TACN]_{AuNPs} = 0 μ M or 100 μ M, 460 nm (5.30 mW/cm²).

Dark controls of **FMN@TACN AuNPs** and **TACN AuNPs**, both with and without the presence of Zn(NO₃)₂, showed that just a 15% of substrate conversion along 48 hours (**Figure 4.25**).

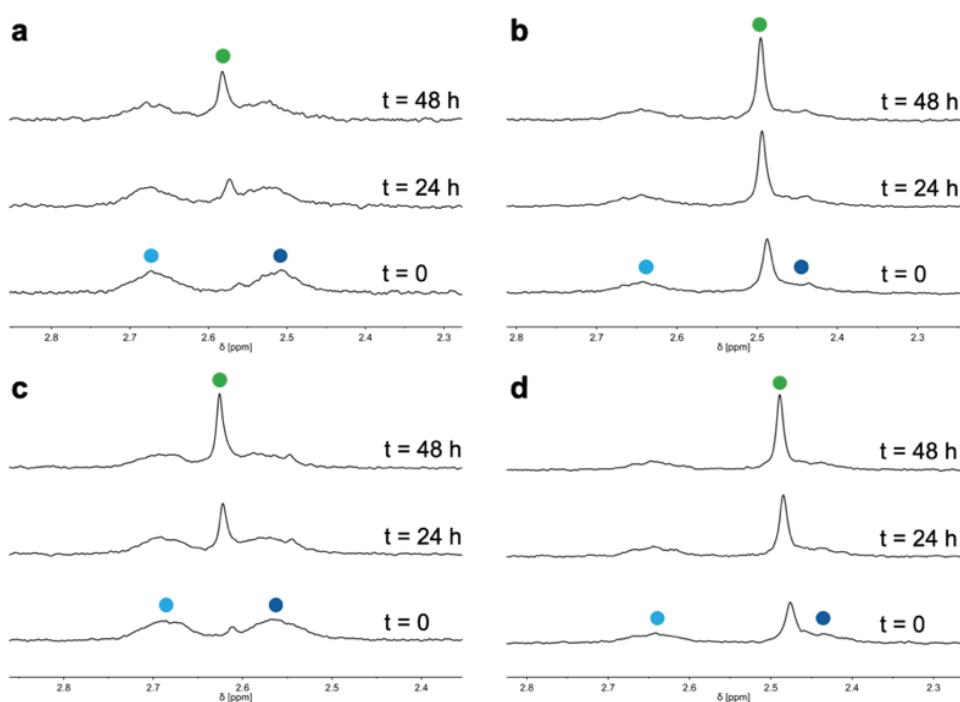


Figure 4.25 Dark stability of **Pt2** in the presence of **FMN@TACN AuNPs** (a) without or (b) with Zn(NO₃)₂, and in presence of **TACN AuNPs** (c) without or (d) with Zn(NO₃)₂ in MES buffer (10% D₂O). Experimental conditions: [FMN] = 25 μ M, [Pt2] = 500 μ M, [MES] = 5 mM (pH 6), [TACN]_{AuNPs} = 100 μ M, [Zn(NO₃)₂] = 0 μ M or 100 μ M, 460 nm (5.30 mW/cm²). ¹H-NMR signal labelling: ● Pt-OCOCH₂CH₂CO₂⁻; ● Pt-OCOCH₂CH₂CO₂⁻; and ● free O₂CCH₂CH₂CO₂⁻.

Turnover frequency (TOF) and turnover number (TON) were calculated for all the systems studied. TOF is the measure of product ratio formed per unit time and the amount of catalyst used, while TON is the absolute number of passes through the catalytic cycle before the catalyst loses its activity.

FMN@TACN AuNPs and **FMN@Zn-TACN AuNPs** showed to be the more efficiently nanozymes, among the studied ones, in the conversion of Pt(IV) prodrug. The TOF values obtained were 7.40 min^{-1} and 7.35 min^{-1} for **FMN@TACN AuNPs** and **FMN@Zn-TACN AuNPs** respectively, corresponding to a TON of 18. In the absence of the photocatalyst the TOF values reached were 8 and 11 times lower, 0.87 min^{-1} for **TACN AuNPs** and 0.65 min^{-1} **Zn-TACN AuNPs**, **FMN** alone showed a TOF of 3.7 min^{-1} , lower than **FMN@TACN AuNPs**, and a TON of 18 (**Figure 4.26**). We conclude that the absence of the photocatalyst (**FMN**) decrease the efficiency of the reaction and that **TACN AuNPs** contribute to an increase in the reaction rate, that could be explained by the proximity of **Pt1** and **FMN** on the NPs surface.

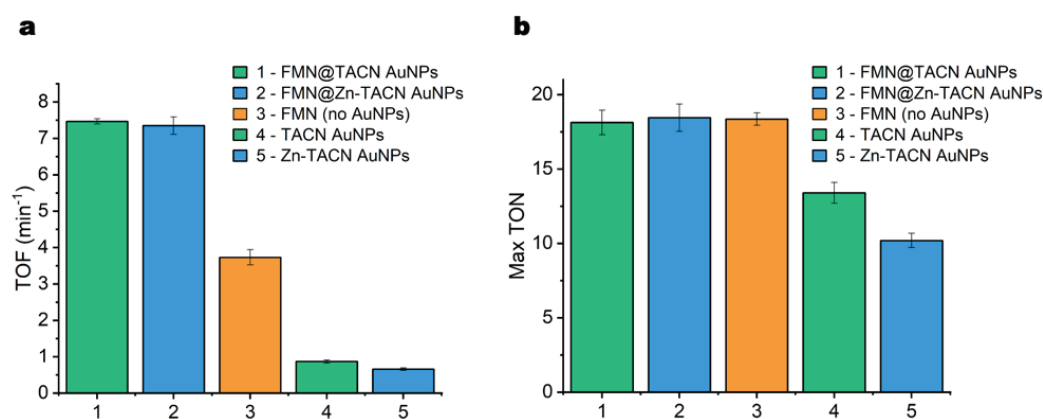


Figure 4.26 (a) TOF values (min^{-1}) and (b) TON values reached after 32 minutes of irradiation for **FMN@TACN AuNPs**, **FMN@Zn-TACN AuNPs**, **FMN**, **TACN AuNPs** and **Zn-TACN AuNPs** in MES buffer (calculated in the range of 15-45% conversion). Experimental conditions: $[\text{FMN}] = 0$ or $25 \mu\text{M}$, $[\text{Pt2}] = 500 \mu\text{M}$, $[\text{MES}] = 5 \text{ mM}$ (pH 6), $[\text{TACN}]_{\text{AuNPs}} = 0 \mu\text{M}$ or $100 \mu\text{M}$, $[\text{Zn}(\text{NO}_3)_2] = 0 \mu\text{M}$ or $100 \mu\text{M}$, 460 nm (5.30 mW/cm^2). Each point corresponds to an average of a triplicate measurement.

4.3. Conclusion

We reported an alternative way of the metal compounds use in the catalysis field, comparing the nanozymes developed by Rotello's group in these years.

In his works, the metal complex plays the common role of the catalyst; in our approach instead, we used platinum complex as substrate and an organic molecule as photocatalyst. The main objective of this work was developing a system for increase the reaction rate of the photoactivation of Pt(IV) prodrugs.

The photoactivation of **Pt1** by the nanozyme was investigated, after confirming by NMR and fluorescence experiments interactions between **TACN AuNPs** with both **Pt1** and **FMN**. We observed that the presence of the gold nanoparticles influences the kinetics of **Pt1** reduction with an increase of the rate of succinate release during photoirradiation. Such a result is quite relevant, since gold nanoparticles may have different and counterbalancing effects on the reaction. First, they can bring in close proximity the Pt(IV) prodrug and FMN increasing the rate of the reaction. Second, they can act as photocatalysis, as demonstrated by the experiments performed without the FMN. Hence, the results described here highlight that **TACN AuNPs** are suitable components to develop supramolecular nanomaterials capable to carry out unconventional flavin-mediated catalytic reactions using Pt(IV) prodrugs as substrates.

Undoubtedly, the catalytic activation of Pt(IV) prodrugs in complex biological environments for our system still needs improvements in the design. The use of this nanozyme *in vitro* and *in vivo* requires that its robustness increases without losing the catalytic activity. For example, the incorporation of PEGylated ligands in the nanoparticle monolayer will likely improve the colloidal stability and biocompatibility of **FMN@TACN AuNPs** and **FMN@Zn-TACN AuNPs**,²⁶⁶ while providing enhanced protection of the **FMN** catalyst from the chemical and biological components present in cells and tissues.

4.4. Experimental section

Materials for synthesis and analysis

Chemicals, solvents and deuterated solvents for NMR were obtained from Merck and used as purchased without further purification. Ultrapure water was deionised and filtered with a Millipore milliQ system. Thin layer chromatography (TLC) were run on 0.2 mm Macherey-Nagel Alugram Xtra

SIL G/UV254 plates and revealed under UV light ($\lambda_{\text{max}} = 254 \text{ nm}$) or with phosphomolybdic acid. Column chromatography was performed with silica gel employing Macherey-Nagel Kieselgel 60 with particles sizes of 0.063–0.2 mm (gravity) or 0.04–0.063 mm (flash). Flash columns were performed by applying a positive nitrogen pressure. Glassware in contact with gold nanoparticles was washed with *aqua regia* before and after its use and rinsed with distilled water.

UV-Vis spectroscopy

UV-Vis spectra were acquired with a Varian Cary 50 UV-Vis spectrophotometer employing 10 mm path length Hellma Suprasil® quartz cuvettes.

Transmission electron microscopy (TEM)

Transmission electron microscopy analysis were run on a FEI Tecnai G12 microscope operating at 100 kV and images registered with an OSIS Veleta 4K camera. TACN AuNPs dissolved in water were deposited on a copper grid and the excess of solvent removed with filtering paper. Size distribution analysis was carried out by modelling nanoparticle intensity profiles employing Gwyddion.²⁶⁷

Thermal gravimetric analysis (TGA)

Thermogravimetric analysis of the thiol-functionalised Au nanoparticles was carried out on *ca.* 1 mg of nanoparticles with a TA Instruments Q5000 IR apparatus. Solvent was removed by heating the sample at 100 °C for 10 minutes and then a 10 °C/min temperature ramp was applied from 100 to 1000 °C.

Fluorescence titrations

Fluorescence spectra were recorded with a Perkin Elmer LS-50B Luminescence Spectrometer. Experiments were conducted at 25°C using a semi-micro fluorescence cuvette with a 10 mm light path. Samples were excited at 460 nm and the emission at 527 nm was used for the titration plots.

100 μM of nanoparticles solution in water was titrated with FMN. The initial fluorescence values obtained were corrected for the inner-filter effect before proceeding with the analysis. The data were then fitted with a *Dynafit* software for performing non-linear least-square regression, using 1:1 binding model.

NMR experiments

DOSY, NOE-PUMPING and NMR spectra. All the spectra for characterisation work were acquired on a Bruker 500 MHz Ultra Shield spectrometer, operating at 500 MHz for ^1H and 125.7 MHz for ^{13}C . Spectra were calibrated using residual solvent signals according to previously reported values.²⁶⁸ Catalysis experiments were performed using a Fourier TM Bruker 300 NMR (300 MHz).

Catalysis. For each experiment concentrations and irradiation time were kept fixed for all the systems analysed. Samples were irradiated for 0 s, 15 s, 1 min, 2 min 15 s, 7 min 15 s, 17 min 15 s, 22 min 15 s and 32 min 15 s working with 500 μM for the substrate and 25 μM for the photocatalyst. Pt(IV) conversion was monitored by quantifying the release of succinate ligands, indicated by the appearance of a singlet signal at around 2.5 ppm and the disappearance of the triplet at (2.6-2.7) ppm. Catalysis experiments were performed by triplicate and the results reported are the mean of the three measurements (\bar{x}). Error bars correspond to the standard errors of each measurement ($\sigma_{\bar{x}}$), calculated as the standard deviation (σ) divided by the square root of the number of measurements (N):

$$\bar{x} = \frac{\sum_{i=1}^N x_i}{N} \quad \sigma = \sqrt{\frac{\sum_{i=1}^N (x_i - \bar{x})^2}{N-1}} \quad \sigma_{\bar{x}} = \frac{\sigma}{\sqrt{N}}$$

Chapter 5

Hybrid protein-based constructs for platinum prodrug photoactivation

This work has been published in: L. F. Mazzei, J. Gurruchaga-Pereda, Á. Martínez, J. Calvo, L. Salassa, A. L. Cortajarena. *Chem Commun.* 2023, **59**, 4754-4757.

Chapter 5

5.1. Introduction

Multifunctional hybrids are constructs composed by biomolecules, such as proteins, and a second component that is usually a synthetic material in the nanoscale dimension.¹ Proteins are known for their remarkable versatility among biomolecules, as they play a crucial role in performing a wide range of functions within cells. These functions include for example transportation, regulation, structural support, and enzymatic activity.² Moreover, proteins are considered optimal candidates for constructing medicines and diagnostic tools.^{2,3} The components of the multifunctional hybrids have to contribute either as structural platform (scaffold material) and/or as functional elements (such as catalytic, optical or conductive properties) in a well define organization structure.^{1,2} The central element of the hybrids is composed by proteins. In recent years, the design and the engineering of proteins have been showed to be outstanding for the development of new functional systems with the application in different fields, such as imaging,⁴ sensing,⁵ conductive materials^{6,7} and catalysis.⁸ Proteins are the most widely used templates and can be employed as a three dimensional scaffold for building the hybrid constructs.¹ In particular repeat proteins, since their repeated modular nature makes them ideal scaffolds for engineering.^{9,10,11} Within this protein family, the consensus tetratricopeptide repeat proteins (CTPRs) are a helix-turn-helix motif of 34 amino acids that has successfully been implemented in the design and fabrication of protein-nanomaterial hybrids for different uses.² Only 8 residues have a key structural role to define the CTPR fold since they are involved in the inter- and intra-repeat packing interactions,^{12,13,14} hence leaving plenty of room for introducing sequence mutations capable of conferring diverse chemical and biological functions.² Moreover, CTPRs have been shown to be robust platforms for the generation of constructs that allow the templating of gold nanoparticles,¹⁵ metallic nanoclusters,¹⁶ redox-active nanoclusters (NCs),¹⁷ carbon nanotubes and porphyrins,¹⁸ among others. These hybrids have so far been studied for applications such as electroconductivity (porphyrins),¹⁹ optics (metallic nanocluster)^{20,21} catalysis (iron-sulfur NCs) and theranostics (redox-active iron-sulfur NCs, gold NCs).^{17,22}

The advantages accomplished in the past decades about the engineering approaches and the computational modelling, have allowed achieving new

protein designs, assemblies and activities. In particular, the control on the protein sequence permits to model the three dimensional structure and the composition of the amino acids that are the main focus for the design of the hybrid constructs.¹ Modifications indeed give the possibility to introduce functional elements on the proteins structure.^{1,23,24} These components can be characterised by biomolecule, such as enzyme, or by synthetic materials, like fluorescent metal nanomaterial, carbon nanomaterials and photo-active elements.¹ Depending on their nature, applications in different fields can be reached, such as: bio-inorganic devices (i) for electricity production with a catalase enzyme entrapped into protein thin films;²⁵ (ii) for *in celulo* imaging and labelling with fluorescent metal NCs incorporated in protein scaffold;¹⁶ (iii) for the stabilization and support of fullerenes²⁶ or carbon nanotubes.¹⁸ The introduction of these elements, can be achieved through bioconjugation process based on non-covalent interactions, covalent bonds mediated by chemical reactions or physical entrapment.^{1,27} Through the use of bioconjugation techniques, functional components can be bound to proteins via reactive amino acids. The hybrid systems can be developed also with an *in situ* synthesis approach in which the functional elements are assembled directly in the presence of the proteins.¹ A classical examples is delineated by the growth of metal nanoparticles on the proteins surface. In the latter case, proteins are used as platform for, first the nucleation of the metal ions and second their growth.^{1,28,29}

The combination of proteins with functional elements opens the possibility to reach additional properties then the proteins alone. Catalysis is one of the fields in which these hybrid systems have been applied. Commonly, enzymes, nanomaterials, such as metal nanoparticles or organometallic complexes are employed as catalytic component in these hybrids. Two approaches can be adopted to develop them: obtaining the protein-based biocatalysts by the coordination between the protein and the catalytic elements; and the use of protein-based catalyst, like enzyme, in bionanomaterials composed of different structural elements.¹ Great examples of bionanohybrid systems developed using the first approach are given by artificial metalloenzymes such as in the work reported by Hayashi and his group.³⁰ They developed an artificial metalloenzyme combining a metal cofactor with an apoprotein after removal the native heme from the

hemoprotein. The apoptroteins indeed give a vacant heme pocket that can be employed as a useful cavity capable of forming an effective coordination sphere of artificially created metalloenzymes.^{30,31,32} Hayashi's group engineered the hemoproteins using a reconstitution method, developing different artificial cofactors. These can be divided in three categories, based on: (i) modification of the heme-propionate side chains; (ii) presence of artificial metalloporphyrinoid with a tetrapyrrole macrocycle ligand; (iii) organometallic species that exhibit activities toward organic reaction not seen in the hemoproteins. They were able to obtain new biocatalysts with a remarkably enhanced activity, the ability to control stereo and regioselectivity and to promote reactions different from those seen in nature, due to the incorporation of metal complex that are not present in nature.³⁰

In light of the versatility and robustness of repeat proteins and the development on the hybrid multifunctional systems, we were intrigued about the prospect of engineering CTPRs as platforms for controlling the activation and delivery of Pt(IV) prodrugs. These are among the most promising anticancer agents and have been extensively investigated, including in clinical trials,^{33,34} as convenient alternatives to clinically approved Pt(II) blockbuster drugs such as cisplatin, carboplatin and oxaliplatin. Working with prodrugs gives the possibility to improve the selectivity of the metal complexes thanks to the addition of tumor-targeting moieties, reduce their side effects and make them more inert compared to the active form of the drugs. These improvements are attributed to the two axial ligands that characterised prodrug complexes (**Figure 5.1**).³³

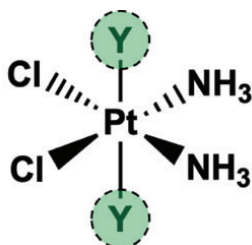


Figure 5.1 Platinum prodrug structure. In green are circled the axial ligands that characterised Pt(IV) complexes.

For example, the functionalization of metal complexes with short peptide sequences and anchoring to whole proteins and antibodies is a well-

established strategy to improve the selectivity and effectiveness of prospective anticancer agents.^{35,36} Kowol, Heffeter, and co-workers recently demonstrated that maleimido-functionalized Pt(IV) prodrugs effectively bind to human serum albumin available in the bloodstream, dramatically improving the pharmacokinetic profile and the antitumoral features of the complexes *in vivo*.^{37,38}

Activation is necessary to convert Pt(IV) prodrugs into their active form, which exhibits therapeutic properties. There are different approaches that can be divided in physiological (e.g. pH) or external activation pathways (e.g. photochemical stimulus or catalysis) (**Figure 5.2**).³⁹

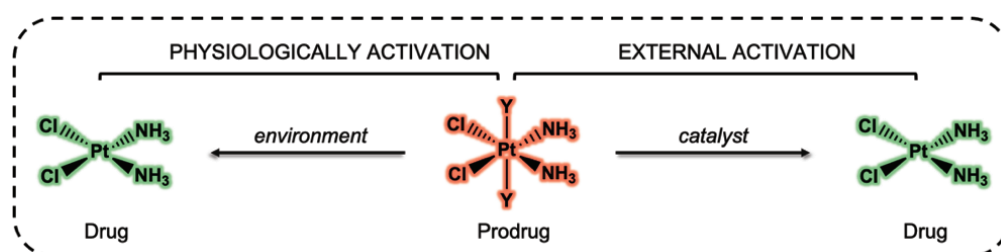


Figure 5.2 Activation pathways from prodrug form, in red (inactive), to the drug one, in green (active). Cisplatin was chosen as reference drug structure.

Some metal prodrugs are designed to release their active form in response to changes in pH or metals redox potential in the target tissue/cells.⁴⁰ In other cases, metal prodrugs can be activated by specific enzymes⁴¹ or proteins present in the body, which can catalyse the cleavage of prodrug ligands and release the drug.⁴² In particular, for platinum anticancer agents (Pt(IV) compounds), glutathione (GSH),⁴³ ascorbate (vitamin C),⁴⁴ NADH, and cysteine-containing proteins⁴⁵ are potential agents for the Pt(IV) complexes activations in cancer cells.⁴⁶ As alternative activation pathway, we recently reported different studies about biorthogonal photocatalytic reactions of a Pt(IV) prodrugs into cisplatin promoted by flavins (as described in Chapter 4). Blue light irradiation (460 nm) is used to excite flavin to its triplet excited state, which oxidizes then an electron donor molecules (such as 2-(N-morpholino)ethane sulfonic acid (MES), NADH or ascorbate). The flavin reduced species obtained interacts with Pt(IV) prodrugs, generating the release of the active Pt(II) complex and the restoration of the photocatalyst (flavin).^{47,48,49,50,51}

In this chapter, bioconjugation procedures to obtain the hybrid protein-based systems are described. Functionalized riboflavin and a platinum prodrug complex were coupled to CTPR scaffolds exploiting the Cys and Lys amino acids within the protein. The motivation of the design of this system was to go a step forward compared to the TACN-AuNPs system described in chapter 4. The improvement here is related to use covalent bonds between the scaffold (CTPR), the photocatalyst (functionalized riboflavin) and the substrates (Pt(IV) complexes) and to incorporate a biological scaffold composed by protein, giving the possibility to have a more stable system and more biocompatible for the *in vitro* studies. The goal of the experiments reported in this chapter is to control the delivery and the photoactivation of platinum prodrugs mediated by riboflavin, both coupled to CTPR scaffolds, in PANC-1 cancer cells line.

5.2. Results and Discussion

5.2.1. Bioconjugation procedure and characterization of hybrid protein-based constructs

In this chapter, we discussed about hybrid protein-based construct for the photoactivation of cisplatin prodrug, mediated by a functionalised riboflavin as photocatalyst. The choice to realize this type of system was: try to increase the photoactivation of platinum prodrug because of the proximity between the metal complexes and the photocatalyst, and have a more controllable internalization of Pt(IV) in cancer cells.

We evaluated three different mutated CTPR proteins as scaffolds in which both prodrug and photocatalyst are covalently bound to the scaffold through lysine (Lys, K) and cysteine (Cys, C) residues respectively. The hybrid protein-based constructs were obtained through two bioconjugation reactions. As photocatalyst we employed the iodoacetamido riboflavin, **Rf-IA**, with an iodine moiety as reactive group (synthesis and characterization reported in chapter 3, section 3.1.1). Instead, as substrate we used a prodrug derivative of cisplatin (Pt(II) complex) with a single active axial ligand, **Pt2** (synthesis and characterization reported in Chapter 3, section 3.2.4). For the scaffold, we employed three CTPR that differed in the total length and number of wild type (WT) modules (**Figure 5.4**). Each CTPR is composed of a **CTPR4** structure that alternates WT and Cys modules, being the second one a mutant module

with a cysteine at position 17 to attach **Rf-IA**. In **Figure 5.3**, the amino acid sequences of the single WT and Cys modules is reported. The difference between these two sequences is based on the amino acid in the position 17: a tyrosine (Y, in green) for the WT (structure with no mutation) and a cysteine (C, in pink) for the Cys module. **CTPR6** and **CTPR8** scaffolds integrate 2 and 4 WT modules in addition to **CTPR4**, respectively. Lysine residues already present in the CTPR(WT) sequence, at position 13 and 26, were exploited for the coupling of **Pt2-NHS** through specific amine chemistry (**Figure 5.4**). Hence, **CTPR4**, **CTPR6**, **CTPR8** can bind only two **Rf-IA** molecules since a single Cys was introduced in the mutated modules. On the other hand, the number of **Pt2-NHS** that can be potentially loaded to the CTPR scaffolds, changes depending on the proteins, in agreement with the number of Lys in both WT and Cys modules. Moreover, we have also to take in consideration the three K residues from the solvating helix of the protein. In the case of **CTPR4**, 11 platinum complexes can be coupled to the protein, for the **CTPR6**, we can reach a maximum of 15 **Pt2** and for the **CTPR8**, 19 metal complexes can be anchored to the scaffold (in the *Experimental Section*, 4.2.5, are reported the complete sequences of the **CTPR4**, **CTPR6** and **CTPR8**).

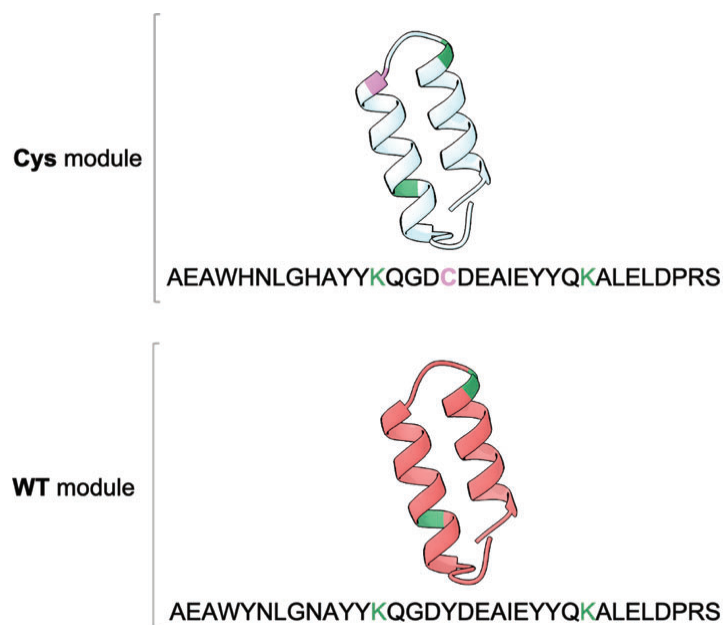


Figure 5.3 Consensus tetratricopeptide repeat (CTPR) protein single modules. On the top, the structural motif of the Cys module, with the amino acids sequences where is underline in pink the mutation introduced, cys (C) and the lys (K) in green already presented in the protein sequence. On the bottom, the structural motif of the WT module, with the amino acids sequences where is underline the lys (K) in green already presented in the protein sequence.

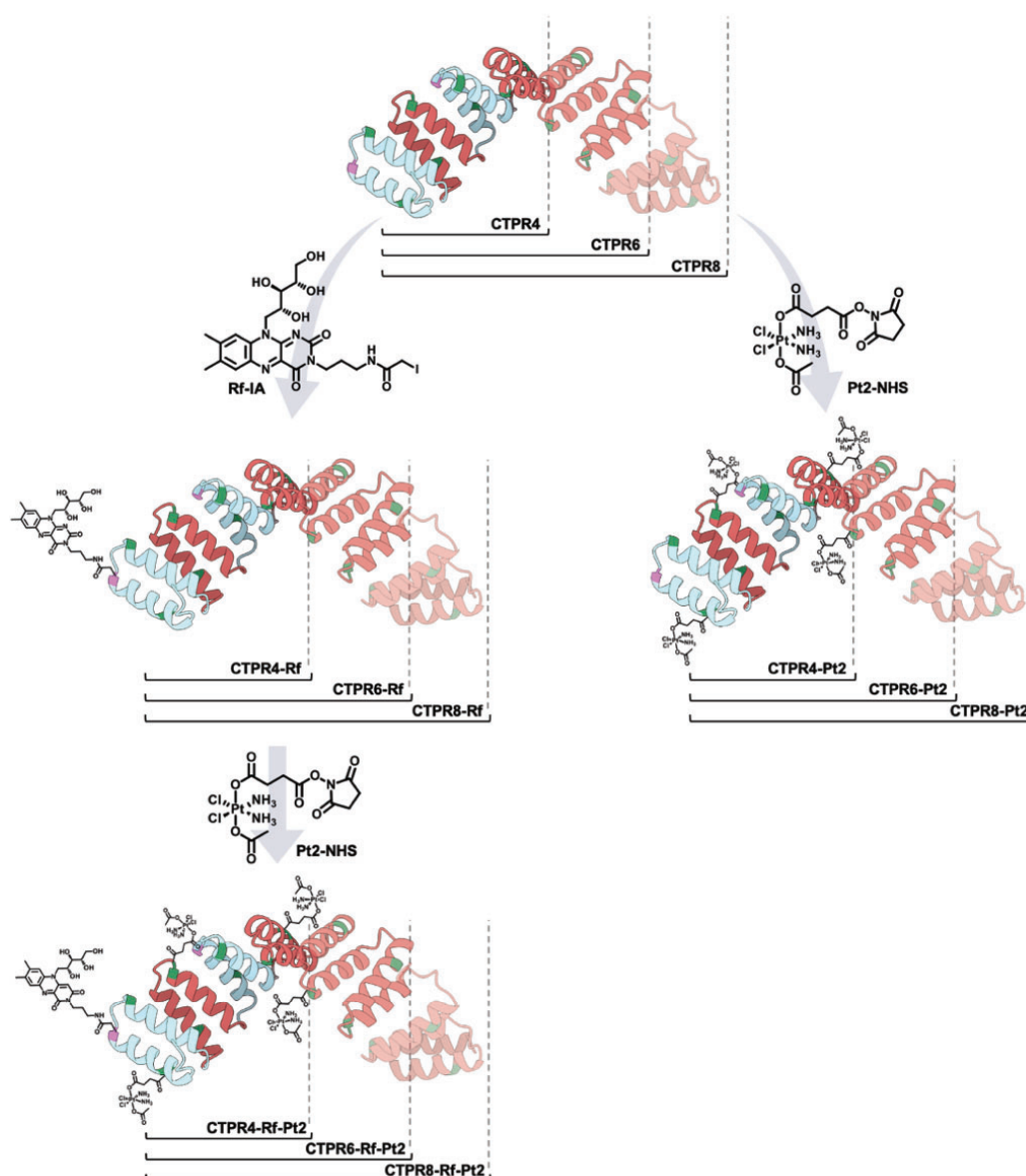


Figure 5.4 Bioconjugation scheme for the hybrids studied in this chapter. CTPR modules with a single cysteine at position 17 and wild-type modules are depicted in light blue and red, respectively. Cysteines used for coupling to **Rf-IA** are highlighted in pink, while lysine sites for coupling to **Pt2-NHS** are colored in green.

After confirming its stability in PBS buffer (**Figure 5.5**), **Rf-IA** was conjugated to the three engineered CTPR scaffolds exploiting iodoacetamide-cysteine chemistry.

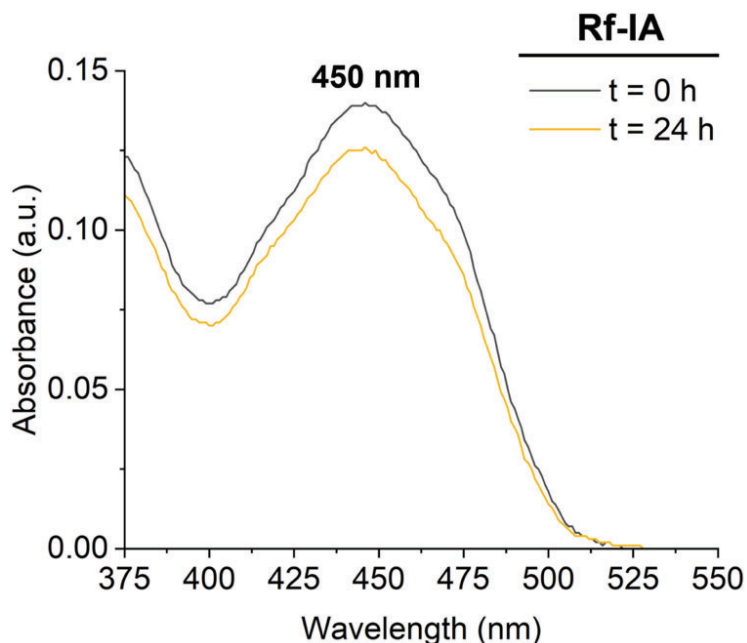


Figure 5.5 UV-Vis spectra of **Rf-IA** molecule in PBS buffer (140 mM NaCl, 50 mM phosphate buffer pH 8.5), over 24 hours.

For the conjugation reaction, a solution of 100 μ M of freshly reduced protein was mixed with **Rf-IA** with a ratio of 1:5.6 cysteine:**Rf-IA** and incubated overnight at room temperature protected from light. Before performing any characterization of the product obtained, **CTPR_n-Rfs** conjugates were first purified to eliminate free **Rf-IA** using a PD-10 desalting column (Experimental section 4.2.5). All the characterizations experiments were performed using the purified system.

The formation of **CTPR_n-Rfs** was first determined by the presence of a band with higher molecular weight compared to CTPR_n in the electrophoresis gel (**Figure 5.6a,d,g**). The gel was imaged firstly monitoring the fluorescence of **Rf-IA** coupled to the protein scaffold and secondly after staining with Coomassie Blue, confirming that the higher molecular weight band is composed of both protein and **Rf-IA**.

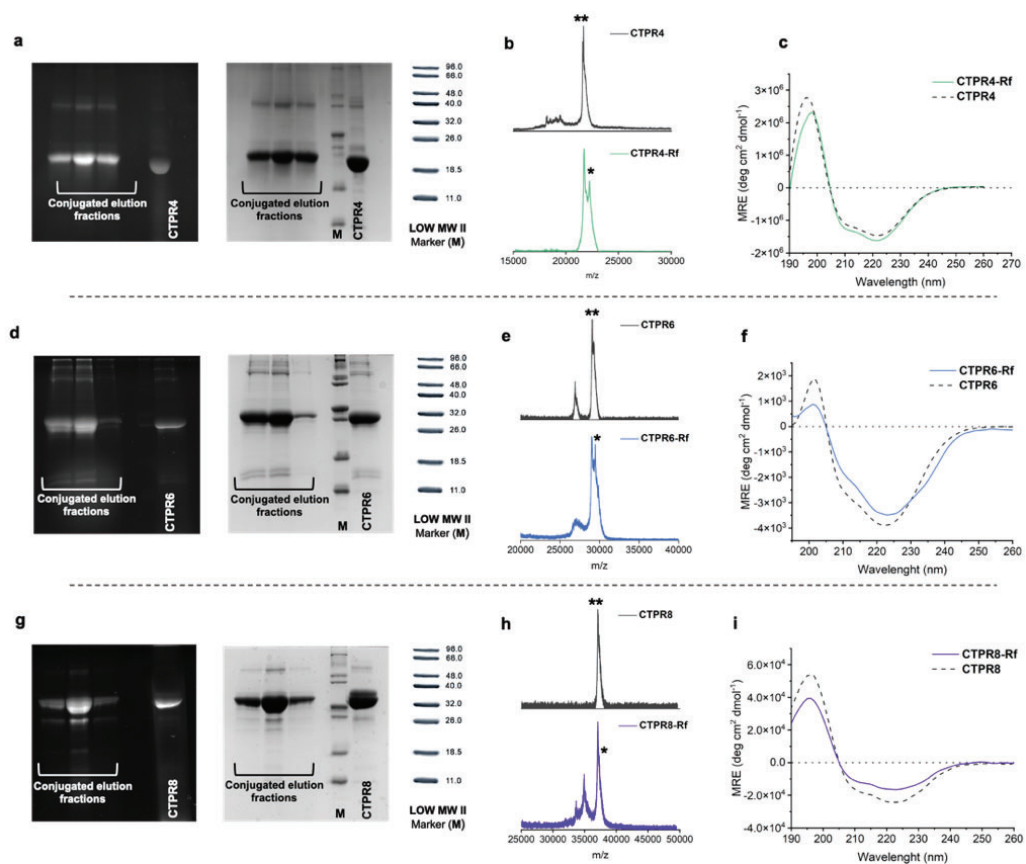


Figure 5.6 Characterization of the **CTPR_n-Rf** conjugate. (a) SDS-PAGE gel electrophoresis of the **CTPR4-Rf** conjugation elution fractions, **CTPR4** control and marker with UV light (left) and after Coomassie Blue staining (right). (b) MALDI-TOF spectra of **CTPR4-Rf** and **CTPR4** control. (c) CD spectra of **CTPR4-Rf** (green solid line) and **CTPR4** (black dashed line) in PB buffer in the spectral region of the protein secondary structure absorption. (d) SDS-PAGE gel electrophoresis of the **CTPR6-Rf** conjugation elution fractions, **CTPR6** control and marker with UV light (left) and after Coomassie Blue staining (right). (e) MALDI-TOF spectra of **CTPR6-Rf** and **CTPR6** control. (f) CD spectra of **CTPR6-Rf** (blue solid line) and **CTPR6** (black dashed line) in PB buffer in the spectral region of the protein secondary structure absorption. (g) SDS-PAGE gel electrophoresis of the **CTPR8-Rf** conjugation elution fractions, **CTPR8** control and marker with UV light (left) and after Coomassie Blue staining (right). (g) SDS-PAGE gels electrophoresis of the **CTPR8-Rf** conjugations elution volumes, **CTPR8** alone and marker. The gel is imaged using UV light to monitor the fluorescence of riboflavin (left) and after Coomassie Blue staining (right). (h) MALDI-TOF spectra of **CTPR8-Rf** and **CTPR8** alone (control). (i) CD spectra of **CTPR8-Rf** conjugate (purple) and **CTPR8** alone (dash) in PB buffer in the spectral region of the protein secondary structure absorption.

MALDI-TOF further confirmed this result proving the number of riboflavin molecules linked to the CTPRs. In the case of **CTPR4-Rf (Figure 5.6b)**, we observed a peak at a higher mass value (22.2 kDa, green plot marked by *) compared to the scaffold alone (21.7 kDa, grey plot marked by **). When the **Rf-IA** is coupled to **CTPR4**, it lost the iodine (leaving group) with the formation of a thiol-carbon bond between the Cys sulfur of CTPR and the carbon from **Rf-IA**. The molecular weight of the functionalized riboflavin without its leaving group is equal to 474 Da. Taking into account the difference in the mass of the peaks found for **CTPR4-Rf** and for the **CTPR4**, we can conclude that this is in agreement with the anchoring of a single riboflavin to **CTPR4**. Linking of a single **Rf** to protein scaffolds was obtained for **CTPR6-Rf** and **CTPR8-Rf** systems as well. The MS spectrum of **CTPR6-Rf** showed indeed a peak at 29.5 kDa (blue plot marked by *), compared to the scaffold alone with a peak at 29.0 kDa (grey plot marked by **) (**Figure 5.6e**). For **CTPR8-Rf**, a peak at 37.4 kDa (purple plot marked by *) were observed, compared to the scaffold alone that showed a peak at 37.0 kDa (grey plot marked by **) (**Figure 5.6h**).

Circular dichroism (CD) measurements for **CTPR_n-Rf** were then performed to study the influence of riboflavin anchoring on the secondary structure of the proteins. CD spectra of CTPRs were compared with the spectra of the **CTPR4-Rf**, **CTPR6-Rf**, and **CTPR8-Rf** in PB buffer. Overall, the CTPR secondary structure was unaltered after the coupling with **Rf-IA**, (**Figure 5.6c,f,i**), confirming, as already reported in literature by our group, the robustness of the protein scaffolds upon functionalization with organic molecules,^{9,18} hence their suitability as platforms for drug delivery.

Once **CTPR_n-Rf** systems were obtained and characterized, we proceeded with the second step, bioconjugating the platinum complexes with CTPR scaffolds. **Pt2-NHS** was selected (synthesis reported in chapter 3, section 3.2.4) for N-hydroxysuccinimide (NHS) ester-lysine coupling. This metal complex presented just one single reactive group (NHS ester) in its axial ligand, useful for avoiding secondary reactions such as protein crosslinking. **CTPR_n-Rf-Pt2** were characterized by ICP-MS and MALDI which indicated that an average of 5 **Pt2** complexes were loaded on the protein platforms for **CTPR6** and 3 for **CTPR4 (Figure 5.7a,c)**. For the **CTPR4-Rf-Pt2** a peak at 23.7 kDa was observed, corresponding to the coupling of a single riboflavin (474

Da) to **CTPR4** (21.7 kDa) and 3 **Pt2** complexes (473 Da). Analogously for **CTPR6-Rf-Pt2**, the peak found, with a molecular weight of 31.8 kDa, corresponded to the **CTPR6** (29.0 kDa) with one **Rf-IA** coupled (474 Da) and 5 **Pt2** complexes (473 Da). The MALDI spectrum of **CTPR8-Rf-Pt2** (not reported) does not provide clear information because of a very low signal-to-noise ratio acquired from the sample. Nevertheless, the presence of **Pt2** coupled to **CTPR8** scaffold was confirmed by ICP mass spectroscopy, obtaining an average of 5 **Pt2** complexes linked to **CTPR8**.

As for **CTPR_n-Rf**, CD studies were performed on **CTPR_n-Rf-Pt2**. We observed that after the coupling with Pt complex a partial loss in the secondary structure of the hybrid was induced (**Figure 5.7b,d,e**). In particular this partial loss was more evident in the case of **CTPR6-Rf-Pt2**. More studies are needed to understand the reasons of such behaviour. Nevertheless, as for **CTPR_n-Rf**, we can consider that the protein structure was mostly preserved, which stressed the robustness of the CTPR protein structure as already reported.⁵²

In addition, we performed the coupling between CTPR scaffolds and Pt complexes (**CTPR_n-Pt2**). The amount of platinum loaded to CTPR scaffolds was quantified with ICP-MS. These **CTPR_n-Pt2** constructs were employed as negative controls for the *in vitro* experiments (section 4.2.3).

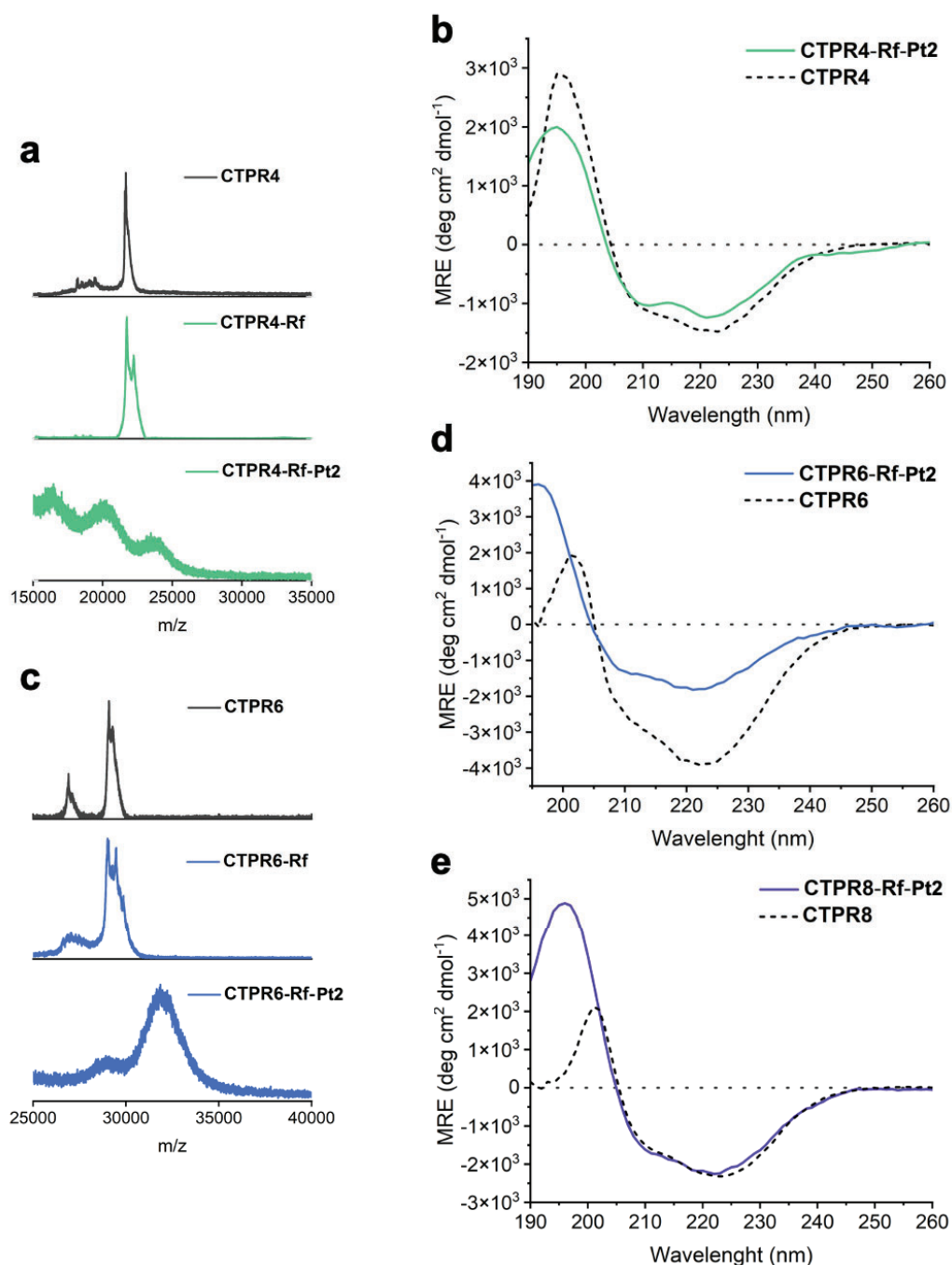


Figure 5.7 Characterization of the CTPR_n-Rf-Pt₂ hybrid. (a) MALDI-TOF spectra of CTPR4-Rf-Pt₂, CTPR4-Rf and CTPR4 (control). (b) CD spectra of CTPR4-Rf (green solid line) and CTPR6 (black dashed line) in PB buffer in the spectral region of the protein secondary structure absorption. (c) MALDI-TOF spectra of CTPR6-Rf-Pt₂, CTPR6-Rf and CTPR6 (control). (d) CD spectra of CTPR6-Rf (blue solid line) and CTPR6 (black dashed line) in PB buffer in the spectral region of the protein secondary structure absorption. (e) CD spectra of CTPR8-Rf (purple solid line) and CTPR8 (black dashed line) in PB buffer in the spectral region of the protein secondary structure absorption.

5.2.2. Photostability and photoactivation studies

Previous studies establish that the stability of flavin can be affected by light.⁵³ On these bases, we evaluated in specific the change on flavins stability covalently bounded to CTPR scaffolds under blue light irradiation. Our prodrug experiments indeed are done with blue light since we irradiate the lowest-energy band at 450 nm of the **Rf-IA**. Moreover, since the photoactivation reactions under investigation require an electron donor, the variation in the stability of flavins in presence of 2-ethanesulfonic acid (MES) was analysed as well.

Therefore, the behavior of **Rf**, **FMN** and **Rf-IA** with respect to **CTPR_n-Rf** under blue light irradiation (460 nm, 3.5 mW/cm²) was investigated. All the samples were irradiated at different time points: 0 sec, 1 min, 5 min, 10 min, 20 min, 30 min and 45 min. We observed a remarkable increase in stability for the functionalized proteins (**CTPR4-Rf**, **CTPR6-Rf** and **CTPR8-Rf**) in the first 20 min of light exposure, comparing to flavins alone where after just 1 min it is possible to observed a decrease in their characteristic 450 nm absorbance band. This effect could be attributed to the ability of the protein scaffold to protect the riboflavin moiety from the photodegradation of its ribityl chain (**Figure 5.8a-f**).⁵⁴ Under blue light irradiation indeed, the degradation of these fluorescence dyes affects the ribityl chains. Then, we investigated also the change in their photostability with the introduction of MES. As previously work demonstrated, flavins photostability can be further enhanced in presence of MES (**Figure 5.8**).^{47,55}

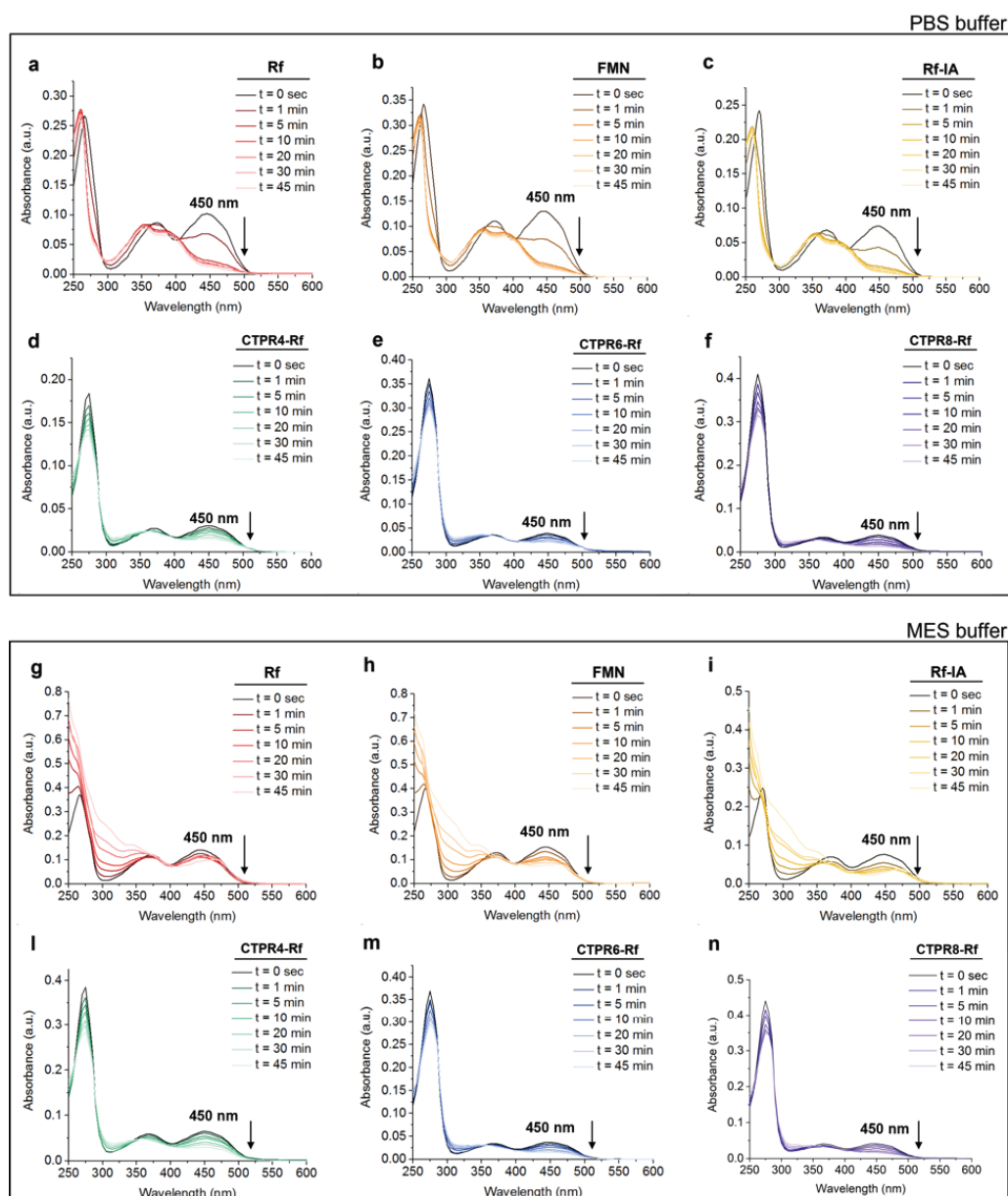


Figure 5.8 Photostability of Rf, FMN, Rf-IA and CTPR_n-Rf in (a-f) PBS (140 mM NaCl, 50 mM phosphate buffer pH 7.4) and (g-n) MES buffer (18 mM, pH 6.4) under blue light irradiation (460 nm, 3.5 mW/cm²).

Based on the results obtained from photostability experiments, catalytic performance of CTPR_n-Rf towards the photoactivation of Pt(IV) prodrugs was assessed. An example of this type of reactions is reported in **Figure 5.9**, using *cis,cis,trans*-[Pt(NH₃)₂(Cl)₂(O₂CCH₂CH₂CO₂H)₂] (**Pt1**) as model substrate and MES as electron donor (18 mM, pH 6.4). **Pt1** has two succinate ligands in the axial position, differing from **Pt2** that coordinates a succinato and an acetato ligand. Our groups extensively employed this symmetric derivative (**Pt1**) as

model substrate for studying flavin-catalyzed activation reactions of Pt anticancer drugs.^{48,49,56} A derivative of riboflavin, **FMN** (riboflavin phosphate), was used as the control catalyst and the flavin/Pt ratio was fixed at 1:100 (5 μM for the catalyst and 500 μM for **Pt1**). Under these conditions, the reaction progression was conveniently monitored by $^1\text{H-NMR}$ following the formation of singlet signal around 2.45 ppm, related to the release of the axial succinate ligands which involved the concomitant generation of cisplatin.⁵⁰

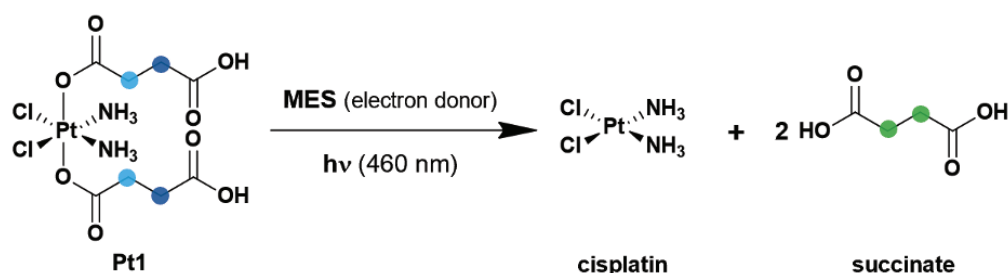


Figure 5.9 Photoreduction scheme under blue light irradiation (460 nm, 3.5 mW/cm²) for **Pt1**. The products of the reaction are cisplatin and two molecules of succinate.

Analysing at the percentage of Pt(IV) conversion, **CTPR6-Rf** was the best catalyst among the protein-linked riboflavins. Although less efficient than **FMN**, which reached almost the total conversion of the substrate in 20 min under the tested conditions, **CTPR6-Rf** presented more than 50% substrate conversion after 20 min of blue light irradiation (460 nm, 3.5 mW/cm²) and a final 85% conversion after 45 min. In particular, the most notable difference between these two models is related to the early light exposure points, where **Pt1** conversion by **FMN** is faster. **CTPR4-Rf** and **CTPR8-Rf** instead, after 45 min of blue light irradiation showed a prodrug conversion equal to 24% and 38% respectively (**Figure 5.10**). All the NMR spectra of the **Pt1** conversion discussed are reported in **Figure 5.11**.

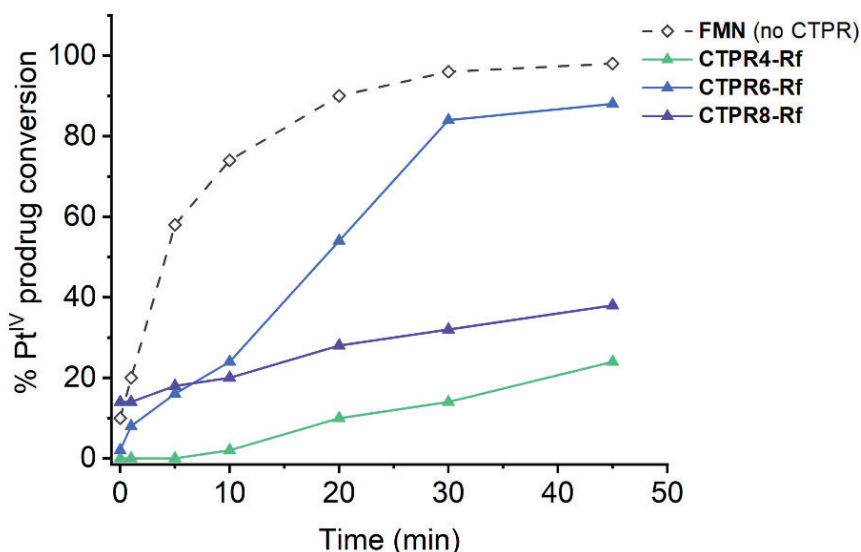


Figure 5.10 Photocatalytic activation of free **Pt1** by **FMN** (grey dashed), **CTPR4-Rf** (green), **CTPR6-Rf** (blue) and **CTPR8-Rf** (purple). Experimental conditions: $[\text{Pt2}] = 500 \mu\text{M}$, $[\text{CTPR}_n\text{-Rf}]_{\text{Rf}} = 5 \mu\text{M}$, $[\text{FMN}] = 5 \mu\text{M}$, $[\text{MES}] = 18 \text{ mM}$ (pH 6.4), $h\nu = 460 \text{ nm}$ (3.5 mW/cm^2).

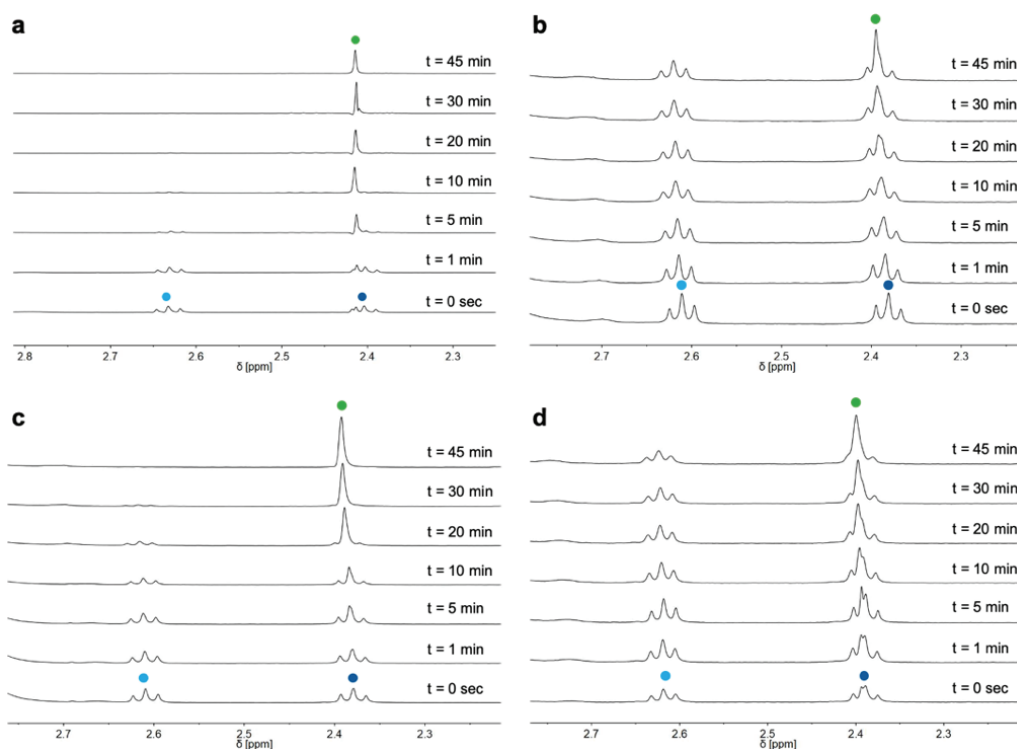


Figure 5.11 Photocatalytic activation under blue light (460 nm) of **Pt1** by (a) free **FMN**, (b) **CTPR4-Rf**, (c) **CTPR6-Rf**, (d) **CTPR8-Rf** in MES buffer (10% D_2O). Experimental conditions: $[\text{Pt1}] = 500 \mu\text{M}$, $[\text{FMN}] = 5 \mu\text{M}$, $[\text{CTPR}_n\text{-Rf}]_{\text{Rf}} = 5 \mu\text{M}$, $[\text{CTPR}_4\text{-Rf}]_{\text{CTPR4}} = 7.6 \mu\text{M}$, $[\text{CTPR}_6\text{-Rf}]_{\text{CTPR6}} = 12 \mu\text{M}$, $[\text{CTPR}_8\text{-Rf}]_{\text{CTPR8}} = 7.7 \mu\text{M}$, $[\text{MES}] = 18 \text{ mM}$ (pH 6.4), $h\nu = 460 \text{ nm}$ (3.5 mW). $^1\text{H-NMR}$ signal labelling: ● $\text{Pt-OCOCH}_2\text{CH}_2\text{CO}_2^-$, ● $\text{Pt-OCOCH}_2\text{CH}_2\text{CO}_2^-$, and ● free $\text{O}_2\text{CCH}_2\text{CH}_2\text{CO}_2^-$.

The catalytic behavior of **FMN** and **CTPR_n-Rf** was investigated also in the dark. We did not observe any conversion of **Pt1** over 48 hours in presence of the photocatalysts alone, **FMN**, or **CTPR_n-Rf** demonstrating the stability of our systems in the absence of light (**Figure 5.12**). Furthermore, no conversion of the Pt(IV) complexes was detected by direct blue light exposure of the substrate alone (**Figure 5.13**).

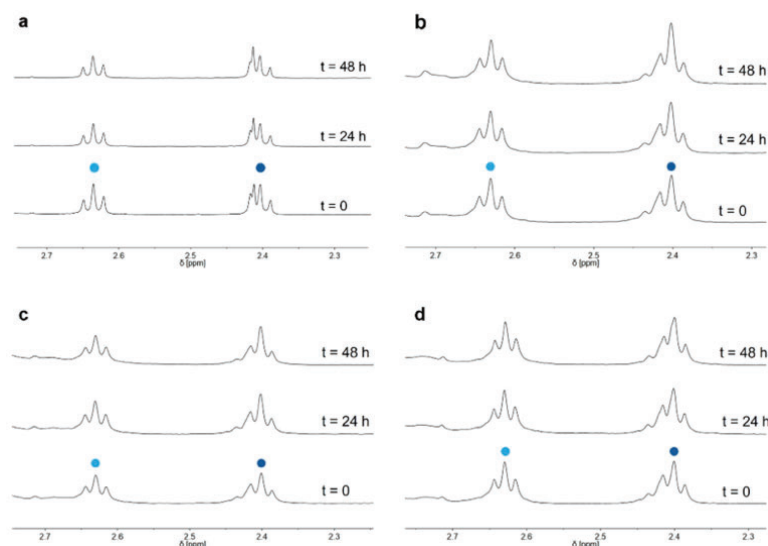


Figure 5.12 Dark stability of **Pt1** in the presence of **FMN** and the protein-catalyst bioconjugate systems in MES buffer (10% D₂O): (a) **FMN**, (b) **CTPR4-Rf**, (c) **CTPR6-Rf**, (d) **CTPR8-Rf**. Experimental conditions: [**Pt1**] = 500 μM, [**FMN**] = 5 μM, [**CTPR_n-Rf**]_{Rf} = 5 μM, [**CTPR4-Rf**]_{CTPR4} = 7.6 μM, [**CTPR6-Rf**]_{CTPR6} = 12 μM, [**CTPR8-Rf**]_{CTPR8} = 7.7 μM, [MES] = 18 mM (pH 6.4), *hν* = 460 nm (3.5 mW). ¹H-NMR signal labeling: ● Pt-OCOCH₂CH₂CO₂H, ● Pt-OCOCH₂CH₂CO₂H, and ● free O₂CCH₂CH₂CO₂H.

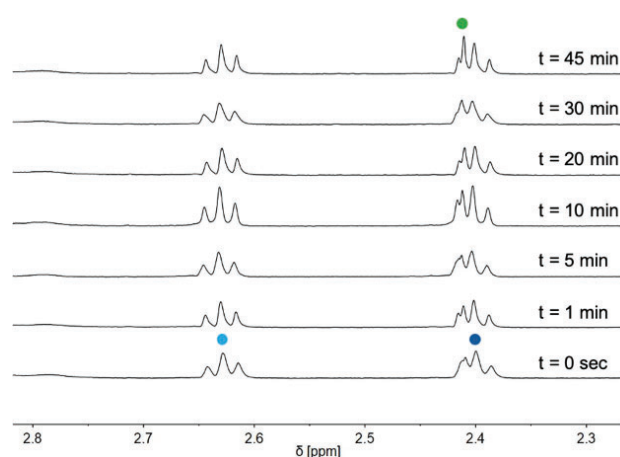


Figure 5.13 Photocatalytic activation under blue light (460 nm) of **Pt1** in MES buffer (10% D₂O). Experimental conditions: [**Pt1**] = 500 μM, [MES] = 18 mM (pH 6.4), *hν* = 460 nm (3.5 mW). ¹H-NMR signal labelling: ● Pt-OCOCH₂CH₂CO₂⁻, ● Pt-OCOCH₂CH₂CO₂⁻, and ● free O₂CCH₂CH₂CO₂⁻.

Since **CTPR6-Rf** showed to be the best performing catalytic among the systems developed, we investigated whether the exposition to blue light could affect the protein secondary structure before moving to the *in vitro* experiments. We studied **CTPR6-Rf-Pt2** with the metal complex couple to the protein scaffold in search of diagnostic spectral changes. MALDI and CD spectra before and after blue light irradiations (460 nm, 3.5 mW/cm²) were compared (**Figure 5.14**). We compared MALDI spectra of **CTPR6-Rf-Pt2** collected at $t = 0$ (no light) and 45 min. For the CD experiment instead, the system was monitored along different irradiation time: 0, 15 min, 30 min and 45 min. In both the cases, MALDI and CD, no changes were observed in the spectra after irradiation (460 nm, 3.5 mW/cm²), indicating that blue light was substantially not affecting proteins structure and the hybrid stability.

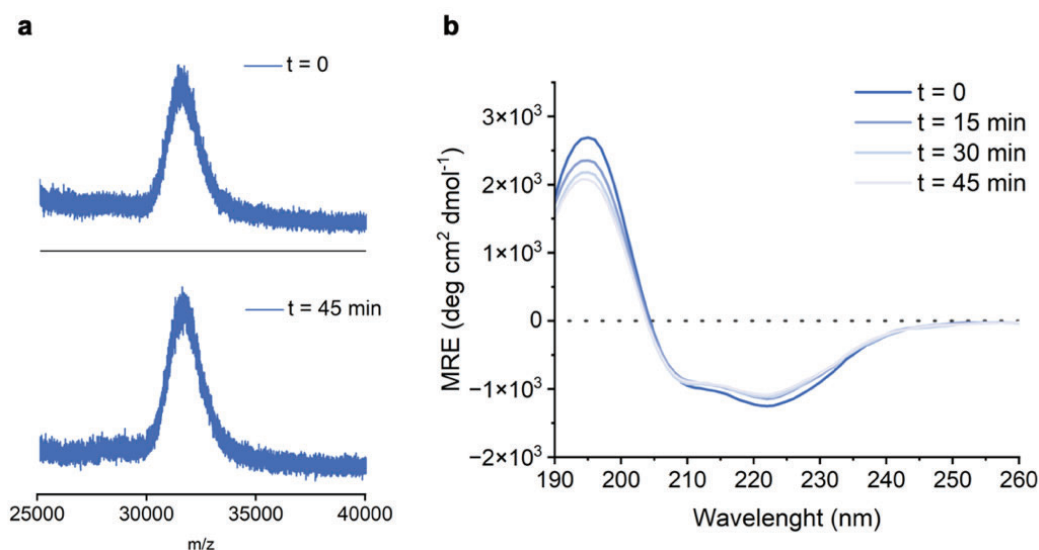


Figure 5.14 Photostability of **CTPR6-Rf-Pt2**. (a) MALDI-TOF spectra of **CTPR6-Rf-Pt2** before ($t = 0$) and after 45 min of light irradiation (460 nm, 3.5 mW/cm²). (b) CD spectra in PB buffer of **CTPR6-Rf-Pt2** at different irradiation times (460 nm, 3.5 mW/cm²) in the spectral region of the protein secondary structure absorption.

5.2.3. Incubation experiments with glutathione (GSH)

Low molecular weight thiol compounds play a crucial role in many biochemical and pharmacological reactions due to the propensity to undergo oxidation reactions, and the velocity with which they can be regenerated.⁵⁷ Glutathione (GSH) is the most abundant intracellular low molecular weight thiol compound synthesised in cells⁵⁸ and its impact on human health is complex.⁵⁹ While GSH can protect cells from oxidative

damage,⁶⁰ metal toxicity,⁶¹ and pathogen invasion,⁶² it also serves as a major deactivator of metallodrugs in vivo, such as platinum drugs.⁵⁹

Since GSH is a reducing agent, it is involved in the inactivation and platinum drugs resistance of tumours.⁶³ GSH is capable of interfering in their interactions with biomolecules,⁶⁴ indeed it binds to platinum drugs forming platinum-glutathione conjugates.⁶³ This effect cause a reduction in the effectiveness of the drug by preventing it from binding to the DNA in cancer cells.^{63,65} Thus, reactions with cysteine-rich proteins, such as glutathione, available at high concentrations in cancer cells, can contribute to the development of platinum drug resistance by sequestering and inactivating them and by promoting their elimination from the cells.⁶⁶ Glutathione conjugates with platinum drugs can be recognized and removed by transporters on the cell surface, allowing them to be excreted from the body more quickly.⁶³

Based on these aspects, we decided to investigate if GSH can influence the reduction of Pt(IV) complexes, releasing Pt(II) species, when they are coupled to **CTPR** proteins. We focused on the **CTPR6** in light of the better catalytic performances showed. **CTPR6-Rf-Pt2**, **Pt2** and cisplatin were co-incubated with an excess of GSH and monitored for 0 h, 6 h and 24 h the appearance or the disappearance of diagnostic Pt species by UPLC-MS. All the samples containing 50 μM Pt were incubated for 24 h with an excess of GSH (1:100) in aqueous solution at room temperature before the measurements.

As expected, cisplatin reacted with GSH, as evidenced by the disappearance of its UPLC peak over time (**Figure 5.15a**). **Pt2** complex instead remained almost intact (**Figure 5.15b**) since the MS peak showed no visible changes. For the protein construct, **CTPR6-Rf-Pt2**, as well we could conclude that is highly stable in the presence of GSH. No considerable peaks could be attributed to free Pt species in the chromatograms collected at different time points, the only exception being a peak in the 24 h time point (4.20 min elution time) where we could detect traces of a high mass species displaying the Pt isotopic pattern (**Figure 5.15c**).

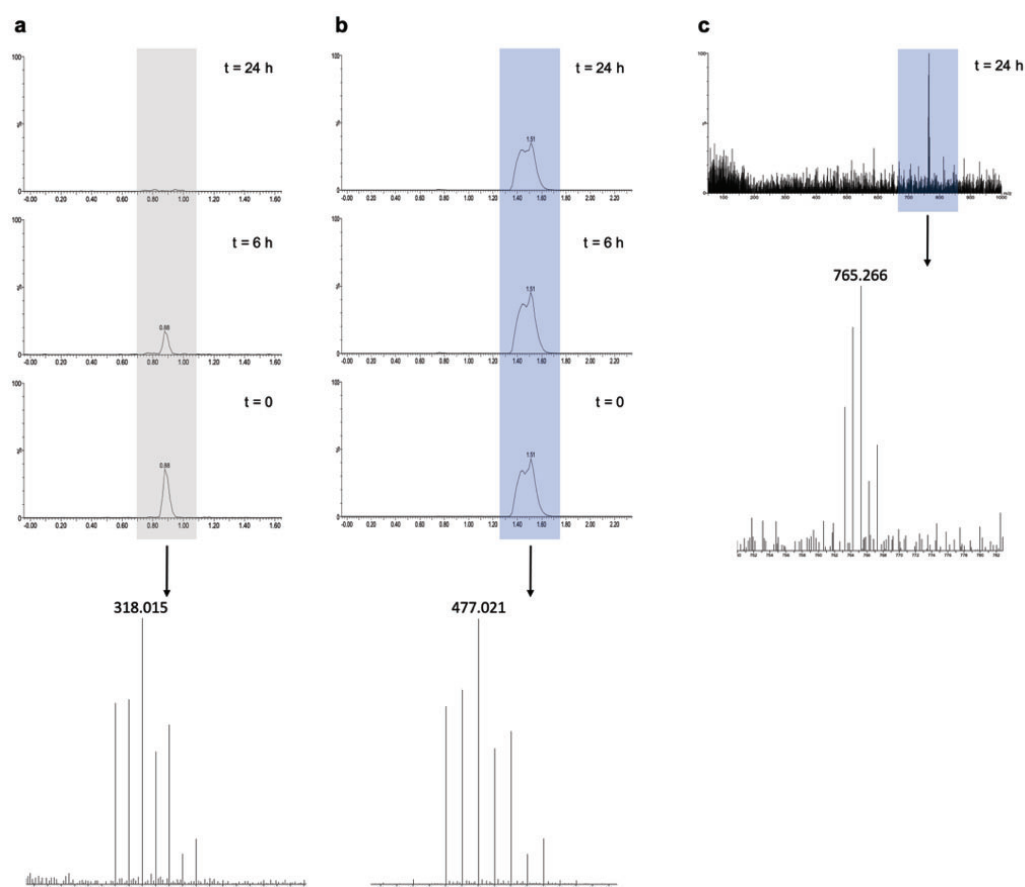


Figure 5.15 (a) Dark stability of cisplatin (50 μM) co-incubated with GSH (500 μM) in water, monitored at 0, 6 h and 24 h: (top) UPLC chromatogram, (bottom) mass spectrum of the elution peak at 0.88 min ($m/z = 318.015$), corresponding to $[\text{Pt}(\text{Cl})_2(\text{NH}_3)_2 + \text{NH}_4^+]$; (b) Dark stability of **Pt2** (50 μM) co-incubated with GSH (500 μM), monitored at 0, 6 h and 24 h: (top) UPLC chromatogram, (bottom) mass spectrum of the elution peak at 1.56 min ($m/z = 477.021$), corresponding to $[\text{Pt2} + \text{H}^+]$; (c) UPLC chromatograms for **CTPR6-Rf-Pt2** (50 μM) co-incubated with GSH (500 μM) at 0, 6 h and 24 h did not show any major MS peak corresponding to free Pt species. We could detect traces of a Pt species ($m/z = 765.266$) only for the 4.2 min elution peak after 24 h of incubation with GSH.

5.2.4. *In vitro* studies

The efficiency of the photoactivation reaction of **Pt2**, for **CTPR-Rf-Pt2**, was then evaluated *in vitro*. PANC-1 cancer cells were selected based on previous studies performed by the group on cell lines derived from pancreas adenocarcinoma,⁶⁷ and because of the relevance of Pt drugs in the treatment of this type of tumors.^{68,69}

For the *in vitro* experiments, we worked with **CTPR6** constructs, for the reason explained in the previous section for the incubation experiments with GSH. Our aim here, was to test the antiproliferative activity of the hybrid **CTPR6-Rf-Pt2** system in comparison to the various components that constitute this construct, *i.e.* **CTPR6-Rf**, free **Pt2**, or **CTPR6-Pt2**.

As a first step, we evaluated the cytotoxicity of **Pt2** compared to cisplatin, chosen as our positive control. Cells were treated with different concentration of these two compounds, 100 μM , 50 μM , 25 μM , 12.5 μM , 6.25 μM and 3.12 μM , for 24 hours. The cell viability was then measured by the resazurin assay after 27 h total. The IC_{50} value for cisplatin was 56.9 μM whereas the **Pt2** prodrug was deemed inactive (**Figure 5.16a**).

Before performing cell viability experiments for the **CTPR6-Rf-Pt2**, the toxicity of **CTPR6** and the direct effect of light on PANC-1 cells line were investigated. We worked with concentrations of **CTPR6** in the 2-63 μM range, to match the doses of **CTPR6-Rf-Pt2** that we can administer to cells considering the maximum Pt loading achieved by the synthesis. **CTPR6** induced a very slight decrease in cell viability, around 10%, as shown in **Figure 5.16b**, also in the case of the higher concentrations. With these results, we can consider that **CTPR6** scaffold is not toxic for PANC-1 cancer cell line.

It is known that light in blue wavelength range is capable of triggering apoptosis in cancer cells.⁷⁰ For this reasons, two different irradiation approaches were analysed. In the first case, an alternation of light on/off periods were performed. Cells were irradiated for 45 min total (460 nm, 3.5 mW/cm^2) with 10 min of irradiation and 10 min of dark (incubator, 37°C) with the last irradiation section of 15 min. In the second case instead, cells were subjected a consecutive 45 min of blue light (460 nm, 3.5 mW/cm^2). As expected, in both the cases cells were stressed by the irradiation, in particular with the second approach (**Figure 5.16c,d**). Based on these data, the on/off light strategy was used for the following experiments.

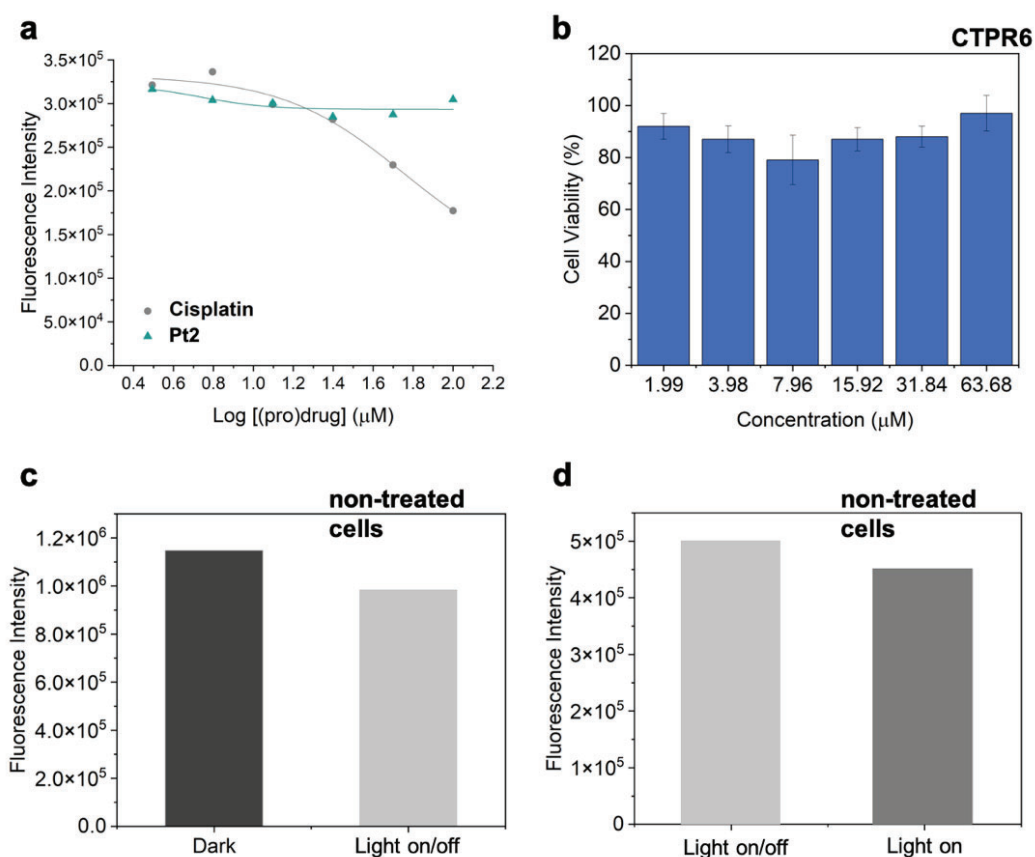


Figure 5.16 (a) Dose response curve of cisplatin and **Pt2** complex in PANC-1 cancer cell line. Experimental conditions for both metals: 3.12 μM , 6.25 μM , 12.5 μM , 25 μM , 50 μM , 100 μM . 24 hours uptake in dark, 37°C. (b) Cell viability percentage in PANC-1 cancer cells following treatment with **CTPR6** in dark condition. Experimental conditions: [**CTPR6**] = 1.99 μM , 3.98 μM , 7.96 μM , 15.92 μM , 31.84 μM , 63.68 μM . 24 hours uptake in dark, 37°C. (c) Fluorescence resorufin (reduced form of resazurin) intensity of non-treated PANC-1 cancer cells in dark condition (dark grey) and under light on/off (light grey). The cells were irradiated for 45 min total, with blue light (3.5 mW/cm²). (d) Fluorescence resorufin (reduced form of resazurin) intensity of non-treated PANC-1 cancer cells with light on/off (light grey) and with light on (medium grey). The cells were irradiated for 45 min total, with blue light (3.5 mW/cm²).

After the first screening on the control systems, the capacity to reduce cancer cell viability was then assessed for **CTPR6-Rf-Pt2** in the dark and under light irradiation. **Figure 5.17** reports the procedure followed for cell viability experiments, starting with the seeding on the first day. After 24 h cells were treated with different Pt concentrations ranging from 73.10 μM to 2.28 μM . Samples were dissolved in cell culture medium (DMEM/F-12 medium without phenol red and supplemented with 10% fetal bovine serum FBS and 1% penicillin/streptomycin) to reach the desired concentrations and cells were incubated for another 24 hours. The third day, cells were washed

with PBS and after that irradiated for 45 min with 460 nm light (3.5 mW/cm^2 , alternating light on/off time periods). The last day, cell viability was measured by resazurin assay.

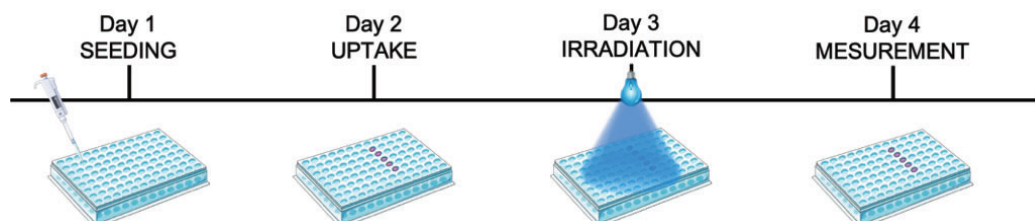


Figure 5.17 Procedure scheme for cell viability experiments.

According to the data obtained, the **CTPR6-Rf-Pt2** provided nearly the same killing ability as cisplatin upon light activation (**Figure 5.18a**). Our hybrid system achieved almost a 40% reduction in cell viability at $73.10 \mu\text{M}$, compared to cisplatin that, at the same concentration, decreased to 60%. On the contrary, no toxic effects were observed in the dark for the protein conjugate whereas cisplatin showed a decrease in the cell viability approximately of 30% (**Figure 5.18b**). These results were compared to the ones of free **Pt2** (**CTPR6-Rf + free Pt2**, ratio 1:28 Rf:Pt2). A very low decrease in the cell viability was observed under blue light irradiation, reaching only 10% with the higher concentration. Otherwise, no changes in cell viability were detected in dark.

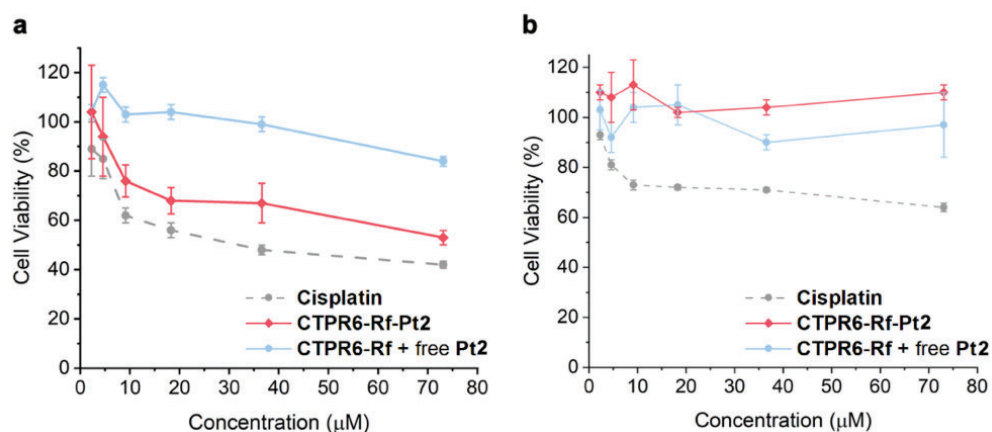


Figure 5.18 (a) Percentage cell viability in PANC-1 cancer cells following treatment with cisplatin (grey dashed line), **CTPR6-Rf-Pt2** (solid red line) and **CTPR6-Rf + free Pt2** (solid light blue line) under light irradiation (45 min, light on/off regime, 460 nm, 3.5 mW/cm^2). (b) Percentage cell viability in PANC-1 cancer cells following treatment with cisplatin (grey dashed line), **CTPR6-Rf-Pt2** (solid red line) and **CTPR6-Rf + free Pt2** (solid light blue line) in the dark.

In addition to **CTPR6-Rf-Pt2** and **CTPR6-Rf** + free **Pt2**, we performed irradiation/dark experiments using single components and their combinations: **CTPR6-Pt2** and **CTPR6-Rf**. These two constructs were selected as negative controls to check, for the first one, if the photoreduction can undergo also in the absence of the photocatalyst (**Rf**) and, for the second one, if **CTPR6-Rf** could exert any photodynamic therapy (PDT) action. The concentrations adopted in previous experiments were maintained and in the case of **CTPR6-Rf** the concentration of **Rf** was the same used in **CTPR6-Rf-Pt2** construct. We found that both **CTPR6-Pt2** and **CTPR6-Rf** reduced cell viability to a lower extent than the multicomponent hybrid, that is only 10% under irradiation and 5% in the dark (**Figure 5.19a,b**).

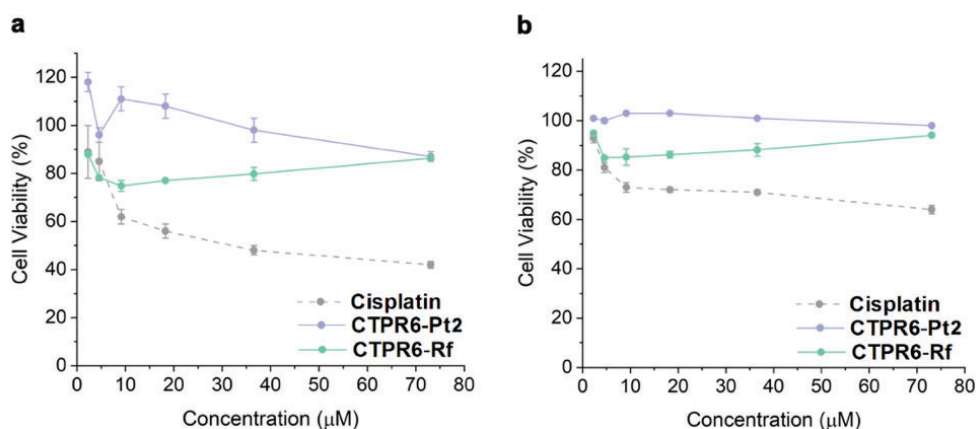


Figure 5.19 (a) Percentage cell viability in PANC-1 cancer cells following treatment with cisplatin (dashed line), **CTPR6-Pt2** (violet) and **CTPR6-Rf** (green) systems under light irradiation (45 min, on/off regime 460 nm, 3.5 mW/cm²). (b) Percentage cell viability in PANC-1 cancer cells following treatment with cisplatin (dashed line), **CTPR6-Pt2** (violet) and **CTPR6-Rf** (green) systems in dark conditions. The concentrations reported refer to drug/prodrug.

These results suggest that the flavin moiety plays a key role as phototrigger for the Pt(IV) reduction and that co-localization of **Rf** and **Pt2** within the cell was beneficial to improve the effectiveness of our flavin-mediated activation strategy. Moreover, the transformation of the Pt prodrug into cisplatin in **CTPR6-Rf-Pt2** was likely to occur due to endogenous electron donors present in the cell, since no external reductants (e.g. MES) were employed in these experiments and light was administered only after cells were washed from the (pro)drugs and the medium replaced.

5.3. Conclusions

CTPRs covalently functionalized with riboflavin allowed artificial flavoproteins capable of triggering the photocatalytic activation of a Pt(IV) anticancer complex. The versatility of these proteins supported further derivatization by co-loading of metal-based prodrugs directly onto the protein scaffold, ultimately providing hybrid systems for the controlled delivery of Pt anticancer agents. Compared to supramolecular nanozymes based on Au nanoparticles⁵⁰ discussed in chapter 4, where we exploited electrostatic and hydrophobic interactions, the covalent anchoring of **Rf** and **Pt2** adopted here represent a step forward in terms of biocompatibility and robustness. A single cysteine modification was introduced in two CTPR modules for the coupling with riboflavin, while the metal complexes were loaded using lysine residues present in the CTPR sequence. In addition, CTPRs are viable alternatives to other metallodrug protein-based carriers such as antibodies (Abs). Abs are protein complexes naturally synthesized to interact with specific molecule and nowadays are taken as reference system for the coupling design.² The use of antibody, however, presents some disadvantage. Their large size (>150 kDa), their complex quaternary structure and the post-translational modifications, required to become fully functional, cause issues related to limited stability, low reproducibility and high production and storage costs.⁷¹ Hence, working with CTPRs can be a valuable alternative approach to avoid this type of problems.

The increase in the robustness constructs connected with the presence of CTPR was observed on the riboflavin photostability when free and coupled to protein scaffold. Under blue light irradiation, indeed, riboflavin and its derivatives alone displayed a decrease in their characteristic 450 nm absorbance band after 1 min of blue light irradiation. On the contrary, their stability was enhanced to 20 min upon irradiation when coupled to **CTPR_n**. We concluded that the protective ability of the protein scaffold could be the reason behind the slow degradation of the riboflavin and its derivatives from the ribityl chain. The increment in the stability has been further enhanced by the introduction of an electron donor, as previously reported.^{47,49,55}

From a catalytic point of view, hybrid construct based on **CTPR6** were the best ones in terms of platinum prodrug activation under blue light

irradiation, reaching 85% of Pt(IV) conversion after 45 min. Based on these results, **CTPR6-Rf-Pt2** was tested *in vitro* showing efficiency in cell killing ability almost comparable to cisplatin. The results obtained from *in vitro* studies indicated the first step toward the design of a biocompatible platform for the controlled delivery of a clinically-approved Pt drug.

The aim of this work was designing a hybrid model that could improve the pharmacokinetics of the drugs and potentially reduce their side effects. Further optimization in the design and synthesis of these hybrid protein-based systems is fundamental try to obtain a system that could enhance the platinum complexes uptake. This will be potentially useful to push **CTPR_n-Rf-Pt** assemblies toward *in vivo* studies, where their potential benefits in terms of drug pharmacokinetics and selective accumulation into tumours can be truly assessed.

5.4. Experimental section

Materials

Chemicals, solvents and deuterated solvents for NMR were obtained from Merck and used as purchased without further purification. Ultrapure water was deionised and filtered with a Millipore milliQ system.

UV-Vis spectroscopy

UV-Vis spectra were acquired with Biotek Synergy H1 microplate reader, NanoDrop Spectrophotometer ND-1000 and NanoDrop One^c Spectrophotometer. For the microplate reader measurements, 96 well UV flat bottom MicrotiterPlates (Thermo Fisher) were used. For both NanoDrop instruments, the measurements were performed loading 3.5 µl of sample.

Circular dichroism (CD)

CD was used to determine the secondary structure of the CTPR units. CD was performed using a Jasco J-1500 spectropolarimeter. A quartz cuvette (0.1 mm path length) was used. The CD spectra were acquired at 1 nm increments and 2 seconds average time over a wavelength range of 190 to 260 nm.

Electrospray ionization mass spectrometry (ESI-MS)

ESI mass spectra were recorded on an Agilent Technologies 1100 Series system equipped with a binary pump (G1312A) and MSD SL Trap mass spectrometer (G2445D SL) with ESI source from solutions in methanol or acetonitrile and 0.1% formic acid.

MALDI-TOF MS

The proteins and the riboflavin derivative were analysed using MALDI-TOF MS UltrafleXtreme III (Bruker) mass spectrometer. 3-(4-hydroxy-3,5-dimethoxyphenyl)prop-2-enoic acid was used as matrix at 10 mg/ml dissolved in a 70% acetonitrile and 0.1% TFA solution for proteins samples, 2,5-dihydroxybenzoic acid was used as matrix at 20 mg/ml dissolved in 70% acetonitrile and 0.1% TFA for organic compound. The samples were prepared at a sample to matrix solution ratio of 1:4 (v/v) and 5 μ l of the mixture deposited on the sample plate.

Inductively coupled plasma mass spectrometry (ICP-MS)

The amount of platinum in conjugated samples was determined by ICP-MS iCAP-Q (ThermoFisher) spectrometer. The samples were digested with aqua regia (overnight) and diluted with water before the measurements.

Liquid chromatography mass spectrometry (LC-MS)

LC-MS experiment was carried out using a UHPLC chromatography system (Acquity UPLC, Waters, Milford, USA) coupled with an ESI-TOF mass spectrometer (LCT Premier XE, Waters, Milford, USA). The chromatographic separation was performed on an Acquity BEH reversed phase C18 column, using a mobile phase consisting of 100 mM ammonium formate in water (A) and acetonitrile (B). The gradient method was as follows: 0-1.5 min at 99% A, 1.5-6 min to 1% A, 6-8 min at 1% A, 8-8.5 min to 99% A, 8.5-10 min to 99%. The mass spectrometry detection was accomplished working in positive / W mode. The MS range acquired was between m/z 100-1000. The capillary and cone voltages were set at 1500 and 100V, respectively. Masslynx v4.1 software was used to analyze chromatograms and spectra (Waters, Milford, MA, USA). The use of ammonium formate as a buffer in the aqueous mobile

phase enables the detection of platinum complexes as ammonium adducts. Similarly, the presence of platinum can be confirmed by comparing experimental isotopic distributions with calculated ones.

Gel electrophoresis

15% SDS-PAGE electrophoresis gels were used to monitor the conjugation reaction. Low range protein was used as molecular weight marker (LMW II) (nzytech) and the conjugated fractions were mixed with SDS loading buffer. The gel was first imaged using UV-light to monitor the fluorescence of the functionalized riboflavin and then stained with Coomassie Blue.

NMR experiments

All NMR spectra were acquired on a Bruker 500 MHz Ultra Shield spectrometer, operating at 500 MHz for ^1H . Spectra were calibrated using residual solvent signals according to previously reported values.⁷² For each experiment concentrations and irradiation time were kept fixed for all the system analysed. Samples were irradiated with a custom-made array of blue light emitting diodes (460 nm, 3.5 mW/cm²) for 0 s, 1 min, 5 min, 10 min, 20 min, 30 min and 45 min. Photocatalysis experiments were carried in a NMR tube with a total volume of 500 μL with the following composition: 500 μM platinum prodrug, 5 μM flavin catalyst, 7 μM and 12 μM substrate, 18 mM MES (pH 6.4) in 10% D₂O - 90% H₂O. Pt(IV) conversion was monitored by quantifying the release of succinate ligands, indicated by the appearance of a singlet signal at around 2.5 ppm and the disappearance of the triplet at (2.6-2.7) ppm.

Cell culture experiments (resazurin assay)

PANC-1 pancreatic cancer cell line was obtained from the American Type Tissue Collection (ATCC) and cultured in DMEM/F-12 medium (without phenol red) supplemented with 10% fetal bovine serum (FBS) and 1% penicillin/streptomycin at 37 °C under 5% CO₂. Cells were passed at 70% of confluence.

Cell viability was measured using resazurin assay. For the measurements, PANC-1 were seeded in 96-well plates with a density of 7500 cells per well and allowed to adhere overnight. The medium was then substituted with

fresh complete medium containing the samples at the desired concentration and cells were incubated for another 24 hours. The medium was replaced by a solution mixture of DMEM/F-12 medium and resazurin, after a wash with 200 μ l of DPBS, and the cells incubated at 37 °C for 3 hours. Viability measurements were then conducted at 37 °C. The samples were excited at 560 nm and the fluorescence collected at 590 nm. Fluorescence spectra were recorded with Biotek Synergy H1 microplate reader using sterilized Nuclon Delta Surface 96 well (Thermo Fisher Scientific). Cell viability was expressed as percent value calculated as:

$$\text{Cell viability (\%)} = 100 - (\text{F.I.}_T / \text{F.I.}_C * 100)$$

Where F.I._T is the fluorescence of treated cells and F.I._C is the fluorescence of the untreated cells.

For the cell irradiation experiments, blue light (460 nm, 3.5 mW/cm²) was used. Cells were seeded, incubated for 24 hours with samples and washed with 200 μ l of DPBS before being irradiated for 45 min. It was alternated a time period of 10 min light on/off, 15 min for the last irradiation section. Cell viability was then measured with resazurin assay, as described before.

CTPR proteins design and purification

Based on a consensus CTPR4 protein cloned into pPro-EXHTa, two cysteine residues were introduced at positions 17 in the first and third CTPR repeat. The CTPR4 obtained is composed by alternating modules without any mutation, called wild type module (WT, (A E A W Y N L G N A Y Y K Q G D Y D E A I E Y Y Q K A L E L D P R S), as second and fourth ones, and with two cysteine modules, as first and third ones. The expressed proteins present some additional residues at the N-terminus derived from the cloning strategy and a solvating helix at the C-terminus. The sequence of the amino acids for **CTPR4** is reported below. The two cysteines mutation positions are underlined in pink, the His-tag in green and the solvating helix in light blue:

CTPR4

MSYYHHHHHDYDIPTTENLYFQGAMGS

A E A W H N L G H A Y Y K Q G D C D E A I E Y Y Q K A L E L D P R S

AEAWYNLGNAYYKQGDYDEAIEYYQKALELDPRS
AEAWHNLGHAYYKQGDCDEAIEYYQKALELDPRS
AEAWYNLGNAYYKQGDYDEAIEYYQKALELDPRS
AEAKQNLGNAKQKQG

Based on the mutated **CTPR4**, previously reported, two and four CTPR(WT) repeats were added to obtain **CTPR6** and **CTPR8**, respectively. The sequences of the amino acids are reported below respectively for **CTPR6** and **CTPR8**. The two cysteines mutation positions are underlined in pink, the His-tag in green and the solvating helix in light blue:

CTPR6

MSYYHHHHHDYDIPTTENLYFQGAMGS
AEAWHNLGHAYYKQGDCDEAIEYYQKALELDPRS
AEAWYNLGNAYYKQGDYDEAIEYYQKALELDPRS
AEAWHNLGHAYYKQGDCDEAIEYYQKALELDPRS
AEAWYNLGNAYYKQGDYDEAIEYYQKALELDPRS
AEAWYNLGNAYYKQGDYDEAIEYYQKALELDPRS
AEAWYNLGNAYYKQGDYDEAIEYYQKALELDPRS
AEAKQNLGNAKQKQG

CTPR8

MSYYHHHHHDYDIPTTENLYFQGAMGS
AEAWHNLGHAYYKQGDCDEAIEYYQKALELDPRS
AEAWYNLGNAYYKQGDYDEAIEYYQKALELDPRS
AEAWHNLGHAYYKQGDCDEAIEYYQKALELDPRS
AEAWYNLGNAYYKQGDYDEAIEYYQKALELDPRS
AEAWYNLGNAYYKQGDYDEAIEYYQKALELDPRS

A E A W Y N L G N A Y Y K Q G D Y D E A I E Y Y Q K A L E L D P R S

A E A W Y N L G N A Y Y K Q G D Y D E A I E Y Y Q K A L E L D P R S

A E A W Y N L G N A Y Y K Q G D Y D E A I E Y Y Q K A L E L D P R S

A E A K Q N L G N A K Q K Q G

All the proteins were expressed as His-tagged fusion and purified first using standard affinity chromatography methods based on previously published protocols¹⁴ for His-tagged CTPR proteins using 0.5% deoxycholic acid in the lysis buffer and secondly by size exclusion chromatography through a HiLoad 16/600 Superdex 75 pg (for CTPR4 and CTPR6) and HiLoad 16/600 Superdex 200 pg (for CTPR8) column using FPLC. The proteins were then stored in PBS buffer (140 mM NaCl, 50 mM phosphate buffer pH 7.4) with β -mercaptoethanol frozen at -20°C . The protein concentration was determined by UV-absorbance at 280 nm using the extinction coefficient calculated from the amino acid composition ($\epsilon_{\text{CTPR4}} = 54905 \text{ M}^{-1} \text{ cm}^{-1}$, $\epsilon_{\text{CTPR6}} = 83660 \text{ M}^{-1} \text{ cm}^{-1}$, $\epsilon_{\text{CTPR8}} = 114030 \text{ M}^{-1} \text{ cm}^{-1}$).

Synthesis and characterization of hybrid protein-based systems

CTPR_n-Rf bioconjugation

We adopted the same procedure for the riboflavin bioconjugation of the three protein scaffolds, namely **CTPR4**, **CTPR6**, and **CTPR8**.¹⁹ Prior to any conjugation, purified CTPR at a protein concentration of about 100 μM was freshly reduced with 1 mM 1,4-dithio-DL-threitol (DTT) for 20 minutes to ensure full reduction of the cysteine residues. DTT was removed by buffer exchange over a Nap-5 column (GE Healthcare Life Science, prepacked with Sephadex G-25) in PBS buffer (140 mM NaCl, 50 mM phosphate buffer, pH 8.5). Protein fractions without DTT were eluted directly in the **Rf-IA** solution giving a ratio of 1:5.6 cysteine:**Rf-IA**. The coupling reaction occurred overnight, at room temperature and covered from light. The reaction mixture was then passed through a PD-10 desalting column (GE Healthcare Life Science, prepacked with Sephadex G-25) to eliminate the free dye. The final concentration of CTPR and functionalized riboflavin coupled to the protein scaffold was calculated from the absorption spectra taking in account the absorbance correction for the protein's peak at 274 nm. The correction was calculated employing the following equation:

$$A_{274}(\text{corr}) = A_{274} - [A_{450}(\text{dye}) * CF_{274}(\text{dye})]$$

$$CF_{274}(\text{dye}) = A_{274} / A_{450}$$

where A_{274} is the absorbance of the sample at 274 nm, $A_{450}(\text{dye})$ is the absorbance at 450 nm of the functionalized riboflavin, $CF_{274}(\text{dye})$ is the correction factor for the dye at 274 nm (Figure 5.20).⁷³

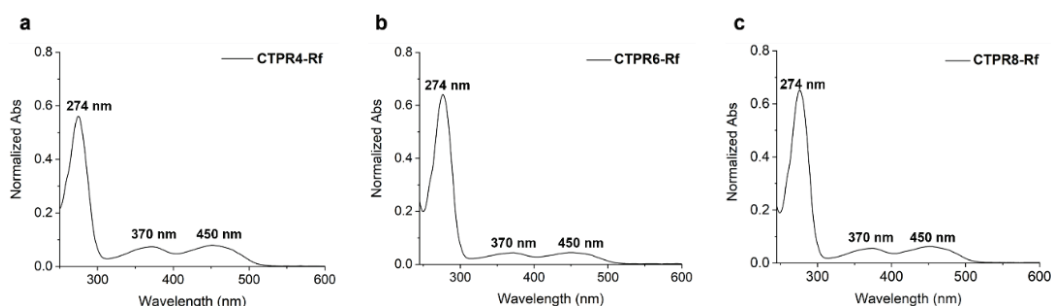


Figure 5.20 UV-Vis spectra of conjugated systems: (a) **CTPR4-Rf**, (b) **CTPR6-Rf** and (c) **CTPR8-Rf** in PBS buffer (140 mM NaCl, 50 mM phosphate buffer pH 8.5) after the elimination of free functionalized riboflavin.

CTPR_n-Rf-Pt2 bioconjugation

CTPR_n-Rf conjugated samples were reacted with the NHS-activated Pt complex (**Pt2-NHS**). To a 25 μM CTPR_n, 10 eq of **Pt2-NHS** (stock solution: 4.6 mM in PBS buffer 140 mM NaCl, 50 mM phosphate buffer, pH 7.4) were added using a lysine:Pt ratio of 1:10. The reaction was carried out overnight, at room temperature and covered from light. The reaction mixture was passed through a PD-10 desalting column (GE Healthcare Life Science, prepacked with Sephadex G-25) to eliminate unreacted **Pt2-NHS** complex. The final concentration of metal complex linked to CTPR_n scaffold was calculated with ICP-MS resulting in a ratio of 1:5 CTPR:Pt for **CTPR6** and **CTPR8** and 1:3 for **CTPR4**.

Note: conjugation reaction of 2 h should be optimal based on tests performed at a later stage monitoring the stability of **Pt2-NHS** in PBS buffer (pH 7.4) overtime.

CTPR_n-Pt2 bioconjugation

To a 25 μM CTPR_n, 10 eq of **Pt2-NHS** (stock solution: 4.6 mM in PBS buffer, 140 mM NaCl, 50 mM phosphate buffer, pH 7.4) were added using a lysine:Pt ratio of 1:10. The reaction occurred overnight, at room temperature and covered by light. The reaction mixture was passed through a PD-10 desalting

column (GE Healthcare Life Science, prepacked with Sephadex G-25) to eliminate free **Pt2-NHS** complex. The final concentration of metal complex linked to the CTPR_n scaffold was calculated by ICP-MS mass spectrometry measurements resulting in a ratio of 1:5 CTPR:Pt.

Note: conjugation reaction of 2 h should be optimal based on tests performed at a later stage monitoring the stability of **Pt2-NHS** in PBS buffer (pH 7.4) overtime.

Chapter 6

General conclusions and future perspective

Chapter 6

This thesis has focused on the design of supramolecular and protein-based constructs for the photocatalytic activation of platinum anticancer agents. In particular, the reaction studied here employed the metal complex as substrate rather than catalyst, with flavin derivatives serving as photocatalysts. The initial hypothesis of this thesis was to investigate the platinum prodrugs photoactivation reaction by the co-immobilization of both the photocatalyst (flavin) and the substrate (platinum anticancer prodrugs) on a gold nanozyme, as well as on engineered repeat proteins as templates. Both nanozymes and protein-based hybrid constructs, have been demonstrated to assist the catalyst in the selective and efficient conversion of the inactive Pt(IV) prodrugs into the active Pt(II) complex (cisplatin) after blue light exposure, in an aqueous environment and *in vitro*.

In detail, the first step of the thesis involved performing organic and inorganic chemistry to functionalize the individual elements of these constructs to promote electrostatic interactions or covalent bonds with the scaffolds. Then, the Pt(IV) prodrugs conversion was studied initially for the supramolecular Au nanozyme model in a PBS buffer and later for the protein hybrid *in vitro* (PANC1-1 cancer cells). In both cases, the activation of platinum complexes was conducted under blue light irradiation (460 nm), and only for the studies conducted in PBS buffer, in presence of an electron donor (MES). In this sense, the initial assumption made in this thesis, has been demonstrated in aqueous buffer and in cancer cells.

The main achievements of this thesis can be summarised as follows:

- **Synthesis and characterization of functionalised riboflavins.** Two functionalised riboflavins and two platinum complexes were synthesised. Starting from the commercial vitamin riboflavin (**Rf**), through multi-step reactions, the iodoacetamide- and the maleimide-functionalised riboflavin were obtained (**Rf-IA** and **Rf-mal** respectively). A single difference in the synthesis process was related to the last step of the reactions, in which the two functional moieties were introduced to the **Rf**. The modification of the vitamin was needed for its covalent coupling to the protein scaffolds (CTPR) through a nucleophilic substitution for the **Rf-IA** and to a maleimide-thiol reaction for the **Rf-mal**. The characterization performed ($^1\text{H-NMR}$, $^{13}\text{C-NMR}$, and ESI-MS), confirmed

the successful synthesis of both molecules, which, to the best of our knowledge, are the first riboflavins reported with these functional moieties.

- **Use of nanozyme scaffold for the activation of Pt(IV) prodrugs.** Here, the study of the activation of Pt(IV) prodrug, in its active form (cisplatin), was conducted in the nanozyme. Gold nanoparticles decorated with a triazacyclononane functional group (**TACN AuNPs**), riboflavin phosphate (**FMN**), and the platinum complex were selected respectively as an inorganic scaffold, photocatalyst, and substrate for the photoactivation studies. After investigating the interaction between **TACN AuNPs** with **FMN** and Pt complex, the study moved to the photocatalytic performances of the nanozyme. The prodrug conversion was monitored in presence of MES as electron donor and under blue light (460 nm). The results obtained showed that the presence of TACN gold nanoparticles influenced the kinetics of Pt(IV) compounds conversion with an increase in the reaction rate of cisplatin release. Further improvements in the nanozyme design are needed for moving their study *in vitro* and *in vivo*.
- **Design of multifunctional hybrid constructed for the delivery and activation of Pt(IV) prodrug *in vitro*.** The work developed in this chapter showed that CTPR proteins can be functionalised with riboflavin molecules and platinum compounds for the delivery and activation of the metal complexes. Unlike the study developed with the nanozyme, here covalent bonds were exploited between the CTPR scaffold with modified riboflavin and Pt(VI) prodrugs, representing a step forward in terms of biocompatibility and robustness. Photostability experiments revealed that CTPR proteins contribute to the enhancement of the robustness of the construct. Under blue light irradiation, the photostability of riboflavin coupled to CTPR increased from 1 min (free) to 20 min (coupled). From a catalytic point of view, the photoconversion of the platinum complexes was studied first in PBS buffer for all CTPR scaffolds analysed (**CTPR4**, **CTPR6**, and **CTPR8**). The **CTPR6** system showed to be most efficient one in terms of prodrug activation. *In vitro* studies in a pancreatic cancer cell line (PANC-1 cancer cells) were conducted for the **CTPR6** construct. The cell viability experiments indicated an efficiency in cell-killing ability almost comparable to the one of cisplatin (drug, positive control). The

photostability of the catalyst was improved due to the presence of the protein scaffold. Moreover, colocalization of both the catalyst and the substrate on CTPR was achieved, obtaining a higher control on the system and closer interacting elements. For the *in vitro* experiments, the colocalization of riboflavin and Pt compounds allowed activation of the metal complex after washing the cells.

In summary, the studies developed in this thesis demonstrate that gold nanoparticles and engineered repeat proteins are promising scaffolds for the co-immobilization of the photocatalyst and the prodrugs, enabling better control over the localization and activation of the prodrugs. However, these results are a first step, and both systems need optimization in the design for moving into *in vivo* experiments. In the case of the nanozyme, the incorporation of PEGylated ligands in the nanoparticle monolayer could potentially improve their colloidal stability and biocompatibility, while providing enhanced protection of the catalyst from the chemical and biological components present in cells and tissues. Another possible improvement could be using the idea applied for the protein constructs in the nanoparticles model, where a covalent bond between the NPs thiols with the catalyst and the prodrugs could be a promising approach to avoid interference by the environment. For the protein-based platform, we obtained promising results with the multifunctional engineered systems. However, we encountered limitations in achieving high modification yields when loading the modified riboflavin onto the protein scaffolds. This effect could be due to a potential steric hindrance between the riboflavins, which may prevent subsequent molecules from reaching the coordination sites. To improve the system, larger spacing between the coordination site within the scaffold could be encoded due to the repeated nature of the system, which would allow for the generation of larger arrays. The photoconversion efficacy of the Pt prodrugs could also be improved by the specific coordination of the Pt at defined positions within the CTPR scaffold, which could be achieved by knocking down the other lysines and encoding only one lysine per repeat for Pt coordination. This would allow for precise location and control of the spacing between the two functional elements within the scaffold. Computational simulations exploring the orientation of the attached molecules with respect to the protein scaffold may facilitate the

Chapter 6

design of improved systems. Finally, the capability of the protein scaffold to genetically encode other biological functionalities, such as specific targeting peptides, will allow for the generation of targeted multifunctional therapeutic systems for future in vivo applications.

References

- 1 S. N. P. Kruse and E. K. H. Permin, *Medicin*, 2008, **36**, 21–40.
- 2 U. Ndagi, N. Mhlongo and M. Soliman, *Drug Des. Devel. Ther.*, 2017, **11**, 599–616.
- 3 B. R. T. Krigas and Loreta Van Camp, *Nature*, 1965, **205**, 698–699.
- 4 M. Hyeraci, V. Scalcon, A. Folda, L. Labella, F. Marchetti, S. Samaritani, M. P. Rigobello and L. Dalla Via, *ChemMedChem*, 2021, **16**, 1956–1966.
- 5 E. Cvitkovic, *Semin Oncol*, 1998, **25**, 1.
- 6 M. A. Fuertes, C. Alonso and José. M. Pérez, *Chem. Rev.*, 2003, **103**, 645–662.
- 7 V. Cepeda, M. A. Fuertes, J. Castilla, C. Alonso, C. Quevedo and J. M. Perez, *Anticancer Agents Med. Chem.*, 2007, **7**, 3–18.
- 8 P. B. Tchounwou, S. Dasari, F. K. Noubissi, P. Ray and S. Kumar, *J. Exp. Pharmacol.*, 2021, **13**, 303–328.
- 9 J. J. Wilson and S. J. Lippard, *Chem. Rev.*, 2014, **114**, 4470–4495.
- 10 I. Amador-Martínez, E. Y. Hernández-Cruz, A. P. Jiménez-Urbe, L. G. Sánchez-Lozada, O. E. Aparicio-Trejo, E. Tapia, J. Barrera-Chimal and J. Pedraza-Chaverri, *Future Pharmacol.*, 2021, **1**, 3–26.
- 11 E. Wexselblatt and D. Gibson, *J. Inorg. Biochem.*, 2012, **117**, 220–229.
- 12 E. Cvitkovic, *Cancer Treat. Rev.*, 1998, **24**, 265–281.
- 13 T. C. Johnstone, K. Suntharalingam and S. J. Lippard, *Chem. Rev.*, 2016, **116**, 3436–3486.
- 14 H. Reiber, M. Ruff and M. Uhr, *Clin. Chim. Acta*, 1993, **217**, 163–173.
- 15 K. Lemma, D. A. House, N. Retta and L. I. Elding, *Inorganica Chim. Acta*, 2002, **331**, 98–108.
- 16 E. Wexselblatt and D. Gibson, *J. Inorg. Biochem.*, 2012, **117**, 220–229.
- 17 F. Michelet, R. Gueguen, P. Leroy, M. Wellman, A. Nicolas and G. Siest, *Clin. Chem.*, 1995, **41**, 1509–1517.
- 18 L. Drougge and L. I. Elding, *Inorganica Chim. Acta*, 1986, **121**, 175–183.
- 19 K. Lemma, T. Shi and L. I. Elding, *Inorg. Chem.*, 2000, **39**, 1728–1734.
- 20 Y. Zhang, C. Xu, X. Yang and K. Pu, *Adv. Mater.*, 2020, **32**, 2002661.
- 21 K. D. Tutsch, R. Z. Arzoomanian, D. Alberti, M. B. Tombes, H. I. Robins, D. R. Spriggs and G. Wilding, *Invest. New Drugs*, 1999, **17**, 63–72.
- 22 C. Sessa, J. Vermorken, J. Renard, S. Kaye, D. Smith, W. ten Bokkel Huinink, F. Cavalli and H. Pinedo, *J. Clin. Oncol.*, 1988, **6**, 98–105.

- 23 M. Clavel, S. Monfardini, S. Gundersen, S. Kaye and I. J. Renard, *Eur. J. Cancer Clin. Oncol.*, 1988, **24**, 1345–1348.
- 24 Nicholas J. Petrelli, Patrick J. Creaven, L. Herrera and A. Mittelman, *Cancer Chemother. Pharmacol.*, 1989, **23**, 61–62.
- 25 D. J. M. Bernard Poiesz, A. D. Sandra Ginsberg, N. N. Arthur Louise and Robert Comis, *Am J Clin Oncol*, 1989, **12**, 129–131.
- 26 R. de Wit, M. Tesselaar, T. C. Kok, C. Seynaeve, C. J. Rodenburg, J. Verweij, P. A. Helle and G. Stoter, *Eur. J. Cancer Clin. Oncol.*, 1991, **27**, 1383–1385.
- 27 H. Anderson, J. Wagstaff, D. Crowther, R. Swindell, M. J. Lind, J. McGregor, M. S. Timms, D. Brown and P. Palmer, *Eur. J. Cancer Clin. Oncol.*, 1988, **24**, 1471–1479.
- 28 D. Tsvetkova and S. Ivanova, *Molecules*, 2022, **27**, 2466.
- 29 D. P. P. C. A. Stenberg, F. W. O. Sartor, W. R. Berry J. Ferrero, A. Koletsky, S. Falcon, F. E. Nathan, and M. E. Petrone, *Proc Am Soc Clin Oncol*, 2007, 145.
- 30 K. A. Lyseng-Williamson and C. Fenton, *Drugs*, 2005, **65**, 2513–2531.
- 31 L. R. Kelland, B. A. Murrer, G. Abel, C. M. Giandomenico, P. Mistry and K. R. Harrap, *Cancer Res.*, 1992, **52**, 822–828.
- 32 M. Reithofer, M. Galanski, A. Roller and B. K. Keppler, *Eur. J. Inorg. Chem.*, 2006, **2006**, 2612–2617.
- 33 H. Varbanov, S. M. Valiahdi, A. A. Legin, M. A. Jakupec, A. Roller, M. S. Galanski and B. K. Keppler, *Eur. J. Med. Chem.*, 2011, **46**, 5456–5464.
- 34 S. Dhar and S. J. Lippard, *Proc. Natl. Acad. Sci.*, 2009, **106**, 22199–22204.
- 35 K. J. Cullen, Z. Yang, L. Schumaker and Z. Guo, *J. Bioenerg. Biomembr.*, 2007, **39**, 43–50.
- 36 M. Harper, A. Antoniou, E. Villalobos-Menuey, A. Russo, R. Trauger, M. Vendemelio, A. George, R. Bartholomew, D. Carlo, A. Shaikh, J. Kupperman, E. W. Newell, I. A. Bepalov, S. S. Wallace, Y. Liu, J. R. Rogers, G. L. Gibbs, J. L. Leahy, R. E. Camley, R. Melamede and M. K. Newell, *FASEB J.*, 2002, **16**, 1550–1557.
- 37 N. J. Farrer, L. Salassa and P. J. Sadler, *Dalton Trans.*, 2009, 10690.
- 38 K. Li, G. S. Ming Tong, Q. Wan, G. Cheng, W.-Y. Tong, W.-H. Ang, W.-L. Kwong and C.-M. Che, *Chem. Sci.*, 2016, **7**, 1653–1673.
- 39 B. Rosenberg, L. Van Camp, E. B. Grimley and A. J. Thomson, *J. Biol. Chem.*, 1967, **242**, 1347–1352.

- 40 N. A. K. J. K. Nagle, H. M. P. J. Bednarski and A. Vogler, *Anticancer Drug Des*, 1996, **11**, 155–71.
- 41 N. A. Kratochwil, M. Zabel, K.-J. Range and P. J. Bednarski, *J. Med. Chem.*, 1996, **39**, 2499–2507.
- 42 P. J. Bednarski, F. S. Mackay and P. J. Sadler, *Anticancer Agents Med. Chem.*, 2007, **7**, 75–93.
- 43 A. F. Westendorf, J. A. Woods, K. Korpis, N. J. Farrer, L. Salassa, K. Robinson, V. Appleyard, K. Murray, R. Grünert, A. M. Thompson, P. J. Sadler and P. J. Bednarski, *Mol. Cancer Ther.*, 2012, **11**, 1894–1904.
- 44 N. J. Farrer, J. A. Woods, L. Salassa, Y. Zhao, K. S. Robinson, G. Clarkson, F. S. Mackay and P. J. Sadler, *Angew. Chem. Int. Ed.*, 2010, **49**, 8905–8908.
- 45 A. Gandioso, E. Shaili, A. Massaguer, G. Artigas, A. González-Cantó, J. A. Woods, P. J. Sadler and V. Marchán, *Chem. Commun.*, 2015, **51**, 9169–9172.
- 46 E. Shaili, M. Fernández-Giménez, S. Rodríguez-Astor, A. Gandioso, L. Sandín, C. García-Vélez, A. Massaguer, G. J. Clarkson, J. A. Woods, P. J. Sadler and V. Marchán, *Chem. Eur. J.*, 2015, **21**, 18474–18486.
- 47 V. Venkatesh, N. K. Mishra, I. Romero-Canelón, R. R. Vernooij, H. Shi, J. P. C. Coverdale, A. Habtemariam, S. Verma and P. J. Sadler, *J. Am. Chem. Soc.*, 2017, **139**, 5656–5659.
- 48 N. G. Blanco, C. R. Maldonado and J. C. Mareque-Rivas, *Chem. Commun.*, 2009, 5257.
- 49 C. R. Maldonado, N. Gómez-Blanco, M. Jauregui-Osoro, V. G. Brunton, L. Yate and J. C. Mareque-Rivas, *Chem. Commun.*, 2013, **49**, 3985.
- 50 P. Thanasekaran, H.-D. Gao and H.-M. Lee, in *Phosphors, Up Conversion Nano Particles, Quantum Dots and Their Applications*, ed. R.-S. Liu, Springer Singapore, Singapore, 2016, pp. 391–418.
- 51 G. Chen, H. Qiu, P. N. Prasad and X. Chen, *Chem. Rev.*, 2014, **114**, 5161–5214.
- 52 E. Ruggiero, J. Hernández-Gil, J. C. Mareque-Rivas and L. Salassa, *Chem. Commun.*, 2015, **51**, 2091–2094.
- 53 S. Perfahl, M. M. Natile, H. S. Mohamad, C. A. Helm, C. Schulzke, G. Natile and P. J. Bednarski, *Mol. Pharm.*, 2016, **13**, 2346–2362.
- 54 A. M. Edwards, in *Flavins and Flavoproteins*, eds. S. Weber and E. Schleicher, Springer New York, New York, NY, 2014, vol. 1146, pp. 3–13.

- 55 B. König, S. Kümmel, E. Svobodová and R. Cibulka, *Phys. Sci. Rev.*, 2018, **3**, 20170168.
- 56 A. Wynter Blyth, *J Chem Soc Trans*, 1879, **35**, 530–539.
- 57 C. A. Northrop-Clewes and D. I. Thurnham, *Ann. Nutr. Metab.*, 2012, **61**, 224–230.
- 58 J. D. Walsh and A.-F. Miller, *J. Mol. Struct.*, 2003, **623**, 185–195.
- 59 P. F. Heelis, *Chem. Soc. Rev.*, 1982, **11**, 15.
- 60 M. A. Sheraz, S. H. Kazi, S. Ahmed, Z. Anwar and I. Ahmad, *Beilstein J. Org. Chem.*, 2014, **10**, 1999–2012.
- 61 L. M. Bouchet, A. A. Heredia, J. E. Argüello and L. C. Schmidt, *Org. Lett.*, 2020, **22**, 610–614.
- 62 T. Morack, J. B. Metternich and R. Gilmour, *Org. Lett.*, 2018, **20**, 1316–1319.
- 63 N. P. Ramirez, B. König and J. C. Gonzalez-Gomez, *Org. Lett.*, 2019, **21**, 1368–1373.
- 64 V. Srivastava, P. K. Singh, A. Srivastava and P. P. Singh, *RSC Adv.*, 2021, **11**, 14251–14259.
- 65 J. Zelenka, E. Svobodová, J. Tarábek, I. Hoskovcová, V. Boguschová, S. Bailly, M. Sikorski, J. Roithová and R. Cibulka, *Org. Lett.*, 2019, **21**, 114–119.
- 66 M. Hall, in *The Enzymes*, Elsevier, 2020, vol. 47, pp. 37–62.
- 67 D. Grosheva and T. K. Hyster, in *Flavin-Based Catalysis*, eds. R. Cibulka and M. Fraaije, Wiley, 1st edn., 2021, pp. 291–313.
- 68 K. F. Biegasiewicz, S. J. Cooper, X. Gao, D. G. Oblinsky, J. H. Kim, S. E. Garfinkle, L. A. Joyce, B. A. Sandoval, G. D. Scholes and T. K. Hyster, *Science*, 2019, **364**, 1166–1169.
- 69 C. Buzea, I. I. Pacheco and K. Robbie, *Biointerphases*, 2007, **2**, MR17–MR71.
- 70 V. Harish, D. Tewari, M. Gaur, A. B. Yadav, S. Swaroop, M. Bechelany and A. Barhoum, *Nanomaterials*, 2022, **12**, 457.
- 71 F. Silva, C. Mendes, A. D’Onofrio, M. P. C. Campello, F. Marques, T. Pinheiro, K. Gonçalves, S. Figueiredo, L. Gano, M. Ravera, E. Gabano and A. Paulo, *Nanotheranostics*, 2023, **7**, 22–40.
- 72 C. Bao, N. Beziere, P. del Pino, B. Pelaz, G. Estrada, F. Tian, V. Ntziachristos, J. M. de la Fuente and D. Cui, *Small*, 2013, **9**, 68–74.

- 73 P. Tan, H. Li, J. Wang and S. C. B. Gopinath, *Biotechnol. Appl. Biochem.*, 2020, bab.2045.
- 74 M. J. Hostetler, J. E. Wingate, C.-J. Zhong, J. E. Harris, R. W. Vachet, M. R. Clark, J. D. Londono, S. J. Green, J. J. Stokes, G. D. Wignall, G. L. Glish, M. D. Porter, N. D. Evans and R. W. Murray, *Langmuir*, 1998, **14**, 17–30.
- 75 S. Siddique and J. C. L. Chow, *Appl. Sci.*, 2020, **10**, 3824.
- 76 P. Ghosh, G. Han, M. De, C. Kim and V. Rotello, *Adv. Drug Deliv. Rev.*, 2008, **60**, 1307–1315.
- 77 G. Han, P. Ghosh and V. M. Rotello, *Nanomed.*, 2007, **2**, 113–123.
- 78 D. A. Giljohann, D. S. Seferos, W. L. Daniel, M. D. Massich, P. C. Patel and C. A. Mirkin, *Angew. Chem. Int. Ed.*, 2010, **49**, 3280–3294.
- 79 P. Baptista, A. Fernandes, S. Figueiredo, R. Vinhas, M. Cordeiro, F. Carlos and S. Mendo, *Nanobiosens. Dis. Diagn.*, 2015, 11.
- 80 M.-C. Daniel and D. Astruc, *Chem Rev*, 2004, 293–346.
- 81 D. A. Giljohann, D. S. Seferos, W. L. Daniel, M. D. Massich, P. C. Patel and C. A. Mirkin, *Angew. Chem. Int. Ed.*, 2010, **49**, 3280–3294.
- 82 L. A. Austin, M. A. Mackey, E. C. Dreaden and M. A. El-Sayed, *Arch. Toxicol.*, 2014, **88**, 1391–1417.
- 83 Faraday M, *Philos. Trans. R. Soc. Lond.*, 1857, **147**, 145–181.
- 84 J. Turkevich, P. C. Stevenson and J. Hillier, *J. Phys. Chem.*, 1953, **57**, 670–673.
- 85 S. Kumar, K. S. Gandhi and R. Kumar, *Ind. Eng. Chem. Res.*, 2007, **46**, 3128–3136.
- 86 C. Carnovale, G. Bryant, R. Shukla and V. Bansal, *Prog. Mater. Sci.*, 2016, **83**, 152–190.
- 87 M. Brust, M. Walker, D. Bethell, D. J. Schiffrin and R. Whyman, *J. Chem. Soc. Chem. Commun.*, 1994, **0**, 801–802.
- 88 F. Manea, C. Bindoli, S. Polizzi, L. Lay and P. Scrimin, *Langmuir*, 2008, **24**, 4120–4124.
- 89 D. Pissuwan, T. Niidome and M. B. Cortie, *J. Control. Release*, 2011, **149**, 65–71.
- 90 S. Dhar, W. L. Daniel, D. A. Giljohann, C. A. Mirkin and S. J. Lippard, *J. Am. Chem. Soc.*, 2009, **131**, 14652–14653.
- 91 S. D. Brown, P. Nativo, J.-A. Smith, D. Stirling, P. R. Edwards, B. Venugopal, D. J. Flint, J. A. Plumb, D. Graham and N. J. Wheate, *J. Am. Chem. Soc.*, 2010, **132**, 4678–4684.

- 92 N. Wheate and J. Collins, *Anticancer Agents Med. Chem.*, 2005, **5**, 267–279.
- 93 F. Silva, A. Paulo, A. Pallier, S. Môme, É. Tóth, L. Gano, F. Marques, C. F. G. C. Geraldés, M. M. C. A. Castro, A. M. Cardoso, A. S. Jurado, P. López-Larrubia, S. Lacerda and M. P. Cabral Campello, *Materials*, 2020, **13**, 513.
- 94 F. Silva, M. P. Cabral Campello and A. Paulo, *Materials*, 2020, **14**, 4.
- 95 H. Mendoza-Nava, G. Ferro-Flores, F. de M. Ramírez, B. Ocampo-García, C. Santos-Cuevas, L. Aranda-Lara, E. Azorín-Vega, E. Morales-Avila and K. Isaac-Olivé, *J. Nanomater.*, 2016, **2016**, 1–11.
- 96 N. Chanda, V. Kattumuri, R. Shukla, A. Zambre, K. Katti, A. Upendran, R. R. Kulkarni, P. Kan, G. M. Fent, S. W. Casteel, C. J. Smith, E. Boote, J. D. Robertson, C. Cutler, J. R. Lever, K. V. Katti and R. Kannan, *Proc. Natl. Acad. Sci.*, 2010, **107**, 8760–8765.
- 97 S. Cuesta-Lopez and R. Serrano-Lopez, 2013, 22–23.
- 98 A. Breda, N. F. Valadares, O. N. de Souza and R. C. Garratt, *Protein Struct.*
- 99 O. Botta, Ed., *Strategies of life detection*, Springer, Dordrecht ; Boston, 2008.
- 100 A. L. Cortajarena and L. Regan, in *Comprehensive Biophysics*, Elsevier, 2012, pp. 267–289.
- 101 F. Parmeggiani and P.-S. Huang, *Curr. Opin. Struct. Biol.*, 2017, **45**, 116–123.
- 102 M. Hatzfeld, in *International Review of Cytology*, Elsevier, 1998, vol. 186, pp. 179–224.
- 103 F. Parmeggiani, R. Pellarin, A. P. Larsen, G. Varadamsetty, M. T. Stumpp, O. Zerbe, A. Caflisch and A. Plückthun, *J. Mol. Biol.*, 2008, **376**, 1282–1304.
- 104 P. Enkhbayar, M. Kamiya, M. Osaki, T. Matsumoto and N. Matsushima, *Proteins Struct. Funct. Bioinforma.*, 2003, **54**, 394–403.
- 105 A. V. Kajava, G. Vassart and S. J. Wodak, *Structure*, 1995, **3**, 867–877.
- 106 A. V. Kajava, *J. Mol. Bio.*, 1998, **277**, 519–527.
- 107 H. K. Binz, M. T. Stumpp, P. Forrer, P. Amstutz and A. Plückthun, *J. Mol. Biol.*, 2003, **332**, 489–503.
- 108 L. K. Mosavi, D. L. Minor and Z. Peng, *Proc. Natl. Acad. Sci.*, 2002, **99**, 16029–16034.
- 109 T. Hirano, N. Kinoshita, K. Morikawa and M. Yanagida, *Cell*, 1990, **60**, 319–328.

- 110 E. R. G. Main, Y. Xiong, M. J. Cocco, L. D'Andrea and L. Regan, *Structure*, 2003, **11**, 497–508.
- 111 T. Kajander, A. L. Cortajarena, E. R. G. Main, S. G. J. Mochrie and L. Regan, *J. Am. Chem. Soc.*, 2005, **127**, 10188–10190.
- 112 L. D'Andrea and L. Regan, *Trends Biochem. Sci.*, 2003, **28**, 655–662.
- 113 A. L. Cortajarena and L. Regan, *Protein Sci.*, 2011, **20**, 336–340.
- 114 A. L. Cortajarena, S. G. J. Mochrie and L. Regan, *Protein Sci.*, 2011, **20**, 1042–1047.
- 115 E. R. G. Main, K. Stott, S. E. Jackson and L. Regan, *Proc. Natl. Acad. Sci.*, 2005, **102**, 5721–5726.
- 116 K. B. Uribe, E. Guisasola, A. Aires, E. López-Martínez, G. Guedes, I. R. Sasselli and A. L. Cortajarena, *Acc. Chem. Res.*, 2021, **54**, 4166–4177.
- 117 M. H. Ahmed, M. S. Ghatge and M. K. Safo, in *Vertebrate and Invertebrate Respiratory Proteins, Lipoproteins and other Body Fluid Proteins*, eds. U. Hoeger and J. R. Harris, Springer International Publishing, Cham, 2020, vol. 94, pp. 345–382.
- 118 S. H. Mejías, J. López-Andarias, T. Sakurai, S. Yoneda, K. P. Erazo, S. Seki, C. Atienza, N. Martín and A. L. Cortajarena, *Chem. Sci.*, 2016, **7**, 4842–4847.
- 119 S. H. Mejias, E. López-Martínez, M. Fernandez, P. Couleaud, A. Martin-Lasanta, D. Romera, A. Sanchez-Iglesias, S. Casado, M. R. Osorio, J. M. Abad, M. T. González and A. L. Cortajarena, *Nanoscale*, 2021, **13**, 6772–6779.
- 120 J. López-Andarias, S. H. Mejías, T. Sakurai, W. Matsuda, S. Seki, F. Feixas, S. Osuna, C. Atienza, N. Martín and A. L. Cortajarena, *Adv. Funct. Mater.*, 2018, **28**, 1704031.
- 121 Y. L. Boersma and A. Plückthun, *Curr. Opin. Biotechnol.*, 2011, **22**, 849–857.
- 122 A. Aires, M. Möller and A. L. Cortajarena, *Chem. Mater.*, 2020, **32**, 5729–5738.
- 123 T. Douglas, E. Strable, D. Willits, A. Aitouchen, M. Libera and M. Young, *Adv. Mater.*, 2002, **14**, 415–418.
- 124 X. Gao, Y. Cui, R. M. Levenson, L. W. K. Chung and S. Nie, *Nat. Biotechnol.*, 2004, **22**, 969–976.

- 125 X. Michalet, F. F. Pinaud, L. A. Bentolila, J. M. Tsay, S. Doose, J. J. Li, G. Sundaresan, A. M. Wu, S. S. Gambhir and S. Weiss, *Science*, 2005, **307**, 538–544.
- 126 E. D. Spoeerke and J. A. Voigt, *Adv. Funct. Mater.*, 2007, **17**, 2031–2037.
- 127 U. Resch-Genger, M. Grabolle, S. Cavaliere-Jaricot, R. Nitschke and T. Nann, *Nat. Methods*, 2008, **5**, 763–775.
- 128 A. Aires, I. Llarena, M. Moller, J. Castro-Smirnov, J. Cabanillas-Gonzalez and A. L. Cortajarena, *Angew. Chem. Int. Ed.*, 2019, **58**, 6214–6219.
- 129 J. Yang, T. Wang, L. Zhao, V. K. Rajasekhar, S. Joshi, C. Andreou, S. Pal, H. Hsu, H. Zhang, I. J. Cohen, R. Huang, R. C. Hendrickson, M. M. Miele, W. Pei, M. B. Brendel, J. H. Healey, G. Chiosis and M. F. Kircher, *Nat. Biomed. Eng.*, 2020, **4**, 686–703.
- 130 J. Groen, A. Palanca, A. Aires, J. J. Conesa, D. Maestro, S. Rehbein, M. Harkiolaki, A. V. Villar, A. L. Cortajarena and E. Pereiro, *Chem. Sci.*, 2021, **12**, 15090–15103.
- 131 A. L. Cortajarena, F. Yi and L. Regan, *ACS Chem. Biol.*, 2008, **3**, 161–166.
- 132 R. A. Cáceres, T. Chavez, D. Maestro, A. R. Palanca, P. Bolado, F. Madrazo, A. Aires, A. L. Cortajarena and A. V. Villar, *J. Mol. Cell. Cardiol.*, 2018, **123**, 75–87.
- 133 A. Aires, D. Maestro, J. Ruiz del Rio, A. R. Palanca, E. Lopez-Martinez, I. Llarena, K. Geraki, C. Sanchez-Cano, A. V. Villar and A. L. Cortajarena, *Chem. Sci.*, 2021, **12**, 2480–2487.
- 134 Z. Qiu, H. Li, Z. Zhang, Z. Zhu, S. He, X. Wang, P. Wang, J. Qin, L. Zhuang, W. Wang, F. Xie, Y. Gu, K. Zou, C. Li, C. Li, C. Wang, J. Cen, X. Chen, Y. Shu, Z. Zhang, L. Sun, L. Min, Y. Fu, X. Huang, H. Lv, H. Zhou, Y. Ji, Z. Zhang, Z. Meng, X. Shi, H. Zhang, Y. Li and L. Hui, *Cancer Cell*, 2019, **36**, 179–193.e11.
- 135 Z.-F. Lim and P. C. Ma, *J. Hematol. Oncol.*, 2019, **12**, 134.
- 136 A. R. Parikh, I. Leshchiner, L. Elagina, L. Goyal, C. Levovitz, G. Siravegna, D. Livitz, K. Rhrissorrakrai, E. E. Martin, E. E. Van Seventer, M. Hanna, K. Slowik, F. Utro, C. J. Pinto, A. Wong, B. P. Danysh, F. F. de la Cruz, I. J. Fetter, B. Nadres, H. A. Shahzade, J. N. Allen, L. S. Blaszkowsky, J. W. Clark, B. Giantonio, J. E. Murphy, R. D. Nipp, E. Roeland, D. P. Ryan, C. D. Weekes, E. L. Kwak, J. E. Faris, J. Y. Wo, F. Aguet, I. Dey-Guha, M. Hazar-Rethinam, D. Dias-Santagata, D. T. Ting, A. X. Zhu, T. S. Hong, T. R. Golub,

- A. J. Iafrate, V. A. Adalsteinsson, A. Bardelli, L. Parida, D. Juric, G. Getz and R. B. Corcoran, *Nat. Med.*, 2019, **25**, 1415–1421.
- 137 M. Arruebo, N. Vilaboa, B. Sáez-Gutierrez, J. Lambea, A. Tres, M. Valladares and Á. González-Fernández, *Cancers*, 2011, **3**, 3279–3330.
- 138 A. G. Patel and S. H. Kaufmann, *eLife*, 2012, **1**, e00387.
- 139 P. Freres, G. Jerusalem and M. Moonen, in *Anti-Cancer Treatments and Cardiotoxicity*, Elsevier, 2017, pp. 7–11.
- 140 J. B. Zawilska, J. Wojcieszak and A. B. Olejniczak, *Pharmacol. Rep.*, 2013, **65**, 1–14.
- 141 X. Ji, Z. Pan, B. Yu, L. K. De La Cruz, Y. Zheng, B. Ke and B. Wang, *Chem. Soc. Rev.*, 2019, **48**, 1077–1094.
- 142 S. Alonso-de Castro, A. Terenzi, J. Gurruchaga-Pereda and L. Salassa, *Chem. Eur. J.*, 2019, **25**, 6651–6660.
- 143 H. C. Hang, C. Yu, D. L. Kato and C. R. Bertozzi, *Proc. Natl. Acad. Sci.*, 2003, **100**, 14846–14851.
- 144 N. S. Punekar, in *ENZYMES: Catalysis, Kinetics and Mechanisms*, Springer Singapore, Singapore, 2018.
- 145 Y. Lyu and P. Scrimin, *ACS Catal.*, 2021, **11**, 11501–11509.
- 146 E. M. Sletten and C. R. Bertozzi, *Acc. Chem. Res.*, 2011, **44**, 666–676.
- 147 R. K. V. Lim and Q. Lin, *Sci. China Chem.*, 2010, **53**, 61–70.
- 148 M. Patra and G. Gasser, *ChemBioChem*, 2012, **13**, 1232–1252.
- 149 T. W. Hambley, *Dalton Trans.*, 2007, 4929.
- 150 M. Martínez-Calvo and J. L. Mascareñas, *Coord. Chem. Rev.*, 2018, **359**, 57–79.
- 151 M. V. Bobo, J. J. Kuchta and A. K. Vannucci, *Org. Biomol. Chem.*, 2021, **19**, 4816–4834.
- 152 M. Neumann, S. Földner, B. König and K. Zeitler, *Angew. Chem. Int. Ed.*, 2011, **50**, 951–954.
- 153 X. Yang, L. Ma, H. Shao, X. Ling, M. Yao, G. Luo, E. Sicilia, G. Mazzone, M. Gao and B. Z. Tang.
- 154 P. Muller, *Pure Appl. Chem.*, 1994, **66**, 1077–1184.
- 155 P. J. Dyson and P. G. Jessop, *Catal. Sci. Technol.*, 2016, **6**, 3302–3316.
- 156 L. Vigh, F. Joo and A. Cseplo, *Eur. J. Biochem.*, 1985, **146**, 241–244.
- 157 V. V. Rostovtsev, L. G. Green, V. V. Fokin and K. B. Sharpless, *Angew. Chem.*, 2002, **114**, 2708–2711.
- 158 C. Streu and E. Meggers, *Angew. Chem.*, 2006, **118**, 5773–5776.

- 159 T. Völker, F. Dempwolff, P. L. Graumann and E. Meggers, *Angew. Chem. Int. Ed.*, 2014, **53**, 10536–10540.
- 160 M. I. Sánchez, C. Penas, M. E. Vázquez and J. L. Mascareñas, *Chem Sci*, 2014, **5**, 1901–1907.
- 161 A. Seoane and J. L. Mascareñas, *Eur. J. Org. Chem.*, 2022, e202200118.
- 162 K. Vong, T. Yamamoto, T. Chang and K. Tanaka, *Chem. Sci.*, 2020, **11**, 10928–10933.
- 163 S. J. M. P. Goetz, J. M. Reid, and J. R. Hawse, *Endocrinol. J*, 2021, **162**.
- 164 X. Zhang, R. Huang, S. Gopalakrishnan, R. Cao-Milán and V. M. Rotello, *Trends Chem.*, 2019, **1**, 90–98.
- 165 G. Y. Tonga, Y. Jeong, B. Duncan, T. Mizuhara, R. Mout, R. Das, S. T. Kim, Y.-C. Yeh, B. Yan, S. Hou and V. M. Rotello, *Nat. Chem.*, 2015, **7**, 597–603.
- 166 J. D. Sara, J. Kaur, R. Khodadadi, M. Rehman, R. Lobo, S. Chakrabarti, J. Herrmann, A. Lerman and A. Grothey, *Ther. Adv. Med. Oncol.*, 2018, **10**, 1-18.
- 167 R. Das, R. F. Landis, G. Y. Tonga, R. Cao-Milán, D. C. Luther and V. M. Rotello, *ACS Nano*, 2019, **13**, 229–235.
- 168 M. A. Miller, B. Askevold, H. Mikula, R. H. Kohler, D. Pirovich and R. Weissleder, *Nat. Commun.*, 2017, **8**, 15906.
- 169 M. A. Miller, H. Mikula, G. Luthria, R. Li, S. Kronister, M. Prytyskach, R. H. Kohler, T. Mitchison and R. Weissleder, *ACS Nano*, 2018, **12**, 12814–12826.
- 170 R. M. Yusop, A. Unciti-Broceta, E. M. V. Johansson, R. M. Sánchez-Martín and M. Bradley, *Nat. Chem.*, 2011, **3**, 239–243.
- 171 J. T. Weiss, J. C. Dawson, K. G. Macleod, W. Rybski, C. Fraser, C. Torres-Sánchez, E. E. Patton, M. Bradley, N. O. Carragher and A. Unciti-Broceta, *Nat. Commun.*, 2014, **5**, 3277.
- 172 J. Clavadetscher, E. Indrigo, S. V. Chankeshwara, A. Lilienkampf and M. Bradley, *Angew. Chem. Int. Ed.*, 2017, **56**, 6864–6868.
- 173 M. Sancho-Albero, B. Rubio-Ruiz, A. M. Pérez-López, V. Sebastián, P. Martín-Duque, M. Arruebo, J. Santamaría and A. Unciti-Broceta, *Nat. Catal.*, 2019, **2**, 864–872.
- 174 L. Gate, *Amsacrine*, Elsevier, 2008.
- 175 M. Osaki and F. Okada, *Yonago Acta Med.*, 2019, **62**, 182–190.

- 176 A. M. Rajan, F. K. Buadi and V. Rajkumar, *Am. J. Hematol.*, 2016, **91**, E5–E6.
- 177 C. Adam, T. L. Bray, A. M. Pérez-López, E. H. Tan, B. Rubio-Ruiz, D. J. Baillache, D. R. Houston, M. J. Salji, H. Y. Leung and A. Unciti-Broceta, *J. Med. Chem.*, 2022, **65**, 552–561.
- 178 C. A. T. C. Lunenburg, L. M. Henricks, H.-J. Guchelaar, J. J. Swen, M. J. Deenen, J. H. M. Schellens and H. Gelderblom, *Eur. J. Cancer*, 2016, **54**, 40–48.
- 179 B. Rubio-Ruiz, A. M. Pérez-López, V. Sebastián and A. Unciti-Broceta, *Bioorg. Med. Chem.*, 2021, **41**, 116217.
- 180 Y. Cheng, C. He, M. Wang, X. Ma, F. Mo, S. Yang, J. Han and X. Wei, *Signal Transduct. Target. Ther.*, 2019, **4**, 62.
- 181 M. A. Glozak and E. Seto, *Oncogene*, 2007, **26**, 5420–5432.
- 182 J. Gurruchaga-Pereda, V. Martínez-Martínez, E. Rezabal, X. Lopez, C. Garino, F. Mancin, A. L. Cortajarena and L. Salassa, *ACS Catal.*, 2020, **10**, 187–196.
- 183 S. Alonso-de Castro, E. Ruggiero, A. Ruiz-de-Angulo, E. Rezabal, J. C. Mareque-Rivas, X. Lopez, F. López-Gallego and L. Salassa, *Chem. Sci.*, 2017, **8**, 4619–4625.
- 184 S. Alonso-de Castro, A. L. Cortajarena, F. López-Gallego and L. Salassa, *Angew. Chem. Int. Ed.*, 2018, **57**, 3143–3147.
- 185 L. F. Mazzei, Á. Martínez, L. Trevisan, D. Rosa-Gastaldo, A. L. Cortajarena, F. Mancin and L. Salassa, *Chem. Commun.*, 2020, **56**, 10461–10464.
- 186 J. Gurruchaga-Pereda, V. Martínez-Martínez, E. Formoso, O. Azpitarte, E. Rezabal, X. Lopez, A. L. Cortajarena and L. Salassa, *J. Phys. Chem. Lett.*, 2021, **12**, 4504–4508.
- 187 S. Velasco-Lozano, S. A. Castro, C. Sanchez-Cano, A. I. Benítez-Mateos, F. López-Gallego and L. Salassa, *Chem. Sci.*, 2022, **13**, 59–67.
- 188 S. Scoditti, E. Dabbish, G. E. Pieslinger, E. Rezabal, X. Lopez, E. Sicilia and L. Salassa, *Phys. Chem. Chem. Phys.*, 2022, **24**, 5323–5329.
- 189 D. J. Norman, A. Gambardella, A. R. Mount, A. F. Murray and M. Bradley, *Angew. Chem. Int. Ed.*, 2019, **58**, 14189–14192.
- 190 S. H. Mejias, A. Aires, P. Couleaud and A. L. Cortajarena, in *Protein-based Engineered Nanostructures*, eds. A. L. Cortajarena and T. Z. Grove, Springer International Publishing, Cham, 2016, vol. 940, pp. 61–81.
- 191 C. T. Walsh and T. A. Wencewicz, *Nat Prod Rep*, 2013, **30**, 175–200.

- 192 A. Rehpenn, A. Walter and G. Storch, *Synthesis*, 2021, **53**, 2583–2593.
- 193 J. Rocha-Martín, D. Vega, J. M. Bolivar, C. A. Godoy, A. Hidalgo, J. Berenguer, J. M. Guisán and F. López-Gallego, *BMC Biotechnol.*, 2011, **11**, 101.
- 194 M. W. Fraaije and A. Mattevi, *Trends Biochem. Sci.*, 2000, **25**, 126–132.
- 195 G. de Gonzalo and M. W. Fraaije, *ChemCatChem*, 2013, **5**, 403–415.
- 196 R. Cibulka, *Eur. J. Org. Chem.*, 2015, **2015**, 915–932.
- 197 W.-S. Li, N. Zhang and L. M. Sayre, *Tetrahedron*, 2001, **57**, 4507–4522.
- 198 A. Wolnicka-Glubisz, A. Pawlak, M. Insinska-Rak and A. Zadlo, *J. Photochem. Photobiol. B*, 2020, **205**, 111820.
- 199 R. Cibulka, R. Vasold and B. König, *Chem. Eur. J.*, 2004, **10**, 6223–6231.
- 200 J. B. Metternich, S. Sagebiel, A. Lückener, S. Lamping, B. J. Ravoo and R. Gilmour, *Chem. Eur. J.*, 2018, **24**, 4228–4233.
- 201 Y. Arakawa, K. Yamanomoto, H. Kita, K. Minagawa, M. Tanaka, N. Haraguchi, S. Itsuno and Y. Imada, *Chem. Sci.*, 2017, **8**, 5468–5475.
- 202 Y. Imada, H. Iida, S. Ono and S.-I. Murahashi, *J. Am. Chem. Soc.*, 2003, **125**, 2868–2869.
- 203 K. A. Korvinson, G. N. Hargenrader, J. Stevanovic, Y. Xie, J. Joseph, V. Maslak, C. M. Hadad and K. D. Glusac, *J. Phys. Chem. A*, 2016, **120**, 7294–7300.
- 204 S.-I. Murahashi, S. Ono and Y. Imada, *Angew. Chem. Int. Ed.*, 2002, **41**, 2366–2368.
- 205 T. S. Chung, Y. M. Na, S. W. Kang, O.-S. Jung and Y.-A. Lee, *Transit. Met. Chem.*, 2005, **30**, 541–545.
- 206 R. P. Feazell, N. Nakayama-Ratchford, H. Dai and S. J. Lippard, *J. Am. Chem. Soc.*, 2007, **129**, 8438–8439.
- 207 V. Pichler, P. Heffeter, S. M. Valiahdi, C. R. Kowol, A. Egger, W. Berger, M. A. Jakupec, M. S. Galanski and B. K. Keppler, *J. Med. Chem.*, 2012, **55**, 11052–11061.
- 208 R. D. Larsen and E. H. Abbott, *Inorg Chem*, 1993, **32**, 2049–2055.
- 209 Y.-A. Lee O.-S. Jung and K. H. Yoo, *Bull. Chem. Soc. Jpn.*, 2003, 107–110.
- 210 P.J. Creaven, J.W. Cowens, F.A. Stevie, J.L. Alderfer, G.E. Hansen, and L. Pendyala, *Int. J. Mass. Spectrom.*, 1983, 177–180.
- 211 C. M. Giandomenico, M. I. Rheinheimer, S. B. Wyer, G. E. BossardJ and J. D. Higgins, *Inorg. Chem.*, 1995, **34**, 1015–1021.

- 212 M. S. Davies, M. D. Hall, S. J. Berners-Price and T. W. Hambley, *Inorg. Chem.*, 2008, **47**, 7673–7680.
- 213 S. Shamsuddin, C. C. Santillan, J. L. Stark, K. H. Whitmire, Z. H. Siddik and A. R. Khokhar, *J. Inorg. Biochem.*, 1998, **71**, 29–35.
- 214 S. R. Ali Khan, S. Huang, S. Shamsuddin, S. Inutsuka, K. H. Whitmire, Z. H. Siddik and A. R. Khokhar, *Bioorg. Med. Chem.*, 2000, **8**, 515–521.
- 215 S. Dhar, F. X. Gu, R. Langer, O. C. Farokhzad and S. J. Lippard, *Proc. Natl. Acad. Sci. U.S.A*, 2008, **105**, 17356–17361.
- 216 H. Xiao, L. Yan, Y. Zhang, R. Qi, W. Li, R. Wang, S. Liu, Y. Huang, Y. Li and X. Jing, *Chem. Commun.*, 2012, **48**, 10730.
- 217 M. S. Galanski and B. K. Keppler, *Inorg. Chem.*, 1996, **35**, 1709–1711.
- 218 A. Alvarez-Valdés, J. M. Pérez, I. López-Solera, R. Lannegrand, J. M. Contiente, P. Amo-Ochoa, M. J. Camazón, X. Solans, M. Font-Bardía and C. Navarro-Ranninger, *J. Med. Chem.*, 2002, **45**, 1835–1844.
- 219 K. R. Barnes, A. Kutikov and S. J. Lippard, *Chem. Biol.*, 2004, **11**, 557–564.
- 220 M. R. Reithofer, M. S. Galanski, V. B. Arion and B. K. Keppler, *Chem. Commun.*, 2008, 1091–1093.
- 221 J. M. Perez, M. Camazón, A. Alvarez-Valdes, A. G. Quiroga, L. R. Kelland, C. Alonso and M. C. Navarro-Ranninger, *Chem. Biol. Interact.*, 1999, **117**, 99–115.
- 222 W. H. Ang, S. Pilet, R. Scopelliti, F. Bussy, L. Juillerat-Jeanneret and P. J. Dyson, *J. Med. Chem.*, 2005, **48**, 8060–8069.
- 223 C. F. Chin, Q. Tian, M. I. Setyawati, W. Fang, E. S. Q. Tan, D. T. Leong and W. H. Ang, *J. Med. Chem.*, 2012, **55**, 7571–7582.
- 224 N. M. Giles, A. B. Watts, G. I. Giles, F. H. Fry, J. A. Littlechild and C. Jacob, *Chem. Biol.*, 2003, **10**, 677–693.
- 225 S. B. Gunnoo and A. Madder, *ChemBioChem*, 2016, **17**, 529–553.
- 226 G. T. Hermanson, Ed., in *Bioconjugate Techniques*, Academic Press, Boston, Third Edition., 2013.
- 227 J. Ashenhurst, *Master Org. Chem*, 2022.
- 228 A. Y.-T. Huang, C.-H. Tsai, H.-Y. Chen, H.-T. Chen, C.-Y. Lu, Y.-T. Lin and C.-L. Kao, *Chem. Commun.*, 2013, **49**, 5784.
- 229 J. Alguacil, S. Defaus, A. Claudio, A. Trapote, M. Masides and J. Robles, *Eur. J. Org. Chem.*, 2010, **2010**, 3102–3109.

- 230 C. Garino, S. Ghiani, R. Gobetto, C. Nervi, L. Salassa, V. Ancarani, P. Neyroz, L. Franklin, J. B. Alexander Ross and E. Seibert, *Inorg. Chem.*, 2005, **44**, 3875–3879.
- 231 B. Frisch, C. Boeckler and F. Schuber, *Bioconjug. Chem.*, 1996, **7**, 180–186.
- 232 R. A. Alderden, M. D. Hall and T. W. Hambley, *J. Chem. Educ.*, 2006, **83**, 728.
- 233 K. M. Brière, R. Goel, F. H. Shirazi, D. J. Stewart and I. C. P. Smith, *Cancer Chemother. Pharmacol.*, 1996, **37**, 518–524.
- 234 M. Ravera, E. Perin, E. Gabano, I. Zanellato, G. Panzarasa, K. Sparnacci, M. Laus and D. Osella, *J. Inorg. Biochem.*, 2015, **151**, 132–142.
- 235 H. Yao, Z. Xu, C. Li, M.-K. Tse, Z. Tong and G. Zhu, *Inorg. Chem.*, 2019, **58**, 11076–11084.
- 236 H. E. Gottlieb, V. Kotlyar and A. Nudelman, *J. Org. Chem.*, 1997, **62**, 7512–7515.
- 237 A. Unciti-Broceta, E. M. V. Johansson, R. M. Yusop, R. M. Sánchez-Martín and M. Bradley, *Nat. Protoc.*, 2012, **7**, 1207–1218.
- 238 A. M. Pérez-López, B. Rubio-Ruiz, V. Sebastián, L. Hamilton, C. Adam, T. L. Bray, S. Irusta, P. M. Brennan, G. C. Lloyd-Jones, D. Sieger, J. Santamaría and A. Unciti-Broceta, *Angew. Chem. Int. Ed.*, 2017, **56**, 12548–12552.
- 239 J. Clavadetscher, S. Hoffmann, A. Lilienkampf, L. Mackay, R. M. Yusop, S. A. Rider, J. J. Mullins and M. Bradley, *Angew. Chem. Int. Ed.*, 2016, **55**, 15662–15666.
- 240 F. Mancin, L. Prins, P. Pengo, L. Pasquato, P. Tecilla and P. Scrimin, *Molecules*, 2016, **21**, 1014.
- 241 G. Y. Tonga, Y. Jeong, B. Duncan, T. Mizuhara, R. Mout, R. Das, S. T. Kim, Y.-C. Yeh, B. Yan, S. Hou and V. M. Rotello, *Nat. Chem.*, 2015, **7**, 597–603.
- 242 A. Gupta, R. Das, G. Yesilbag Tonga, T. Mizuhara and V. M. Rotello, *ACS Nano*, 2018, **12**, 89–94.
- 243 R. Cao-Milán, L. D. He, S. Shorkey, G. Y. Tonga, L.-S. Wang, X. Zhang, I. Uddin, R. Das, M. Sulak and V. M. Rotello, *Mol. Syst. Des. Eng.*, 2017, **2**, 624–628.
- 244 G. Pieters, A. Cazzolaro, R. Bonomi and L. J. Prins, *Chem. Commun.*, 2012, **48**, 1916.

- 245 D. Zaramella, P. Scrimin and L. J. Prins, *J. Am. Chem. Soc.*, 2012, **134**, 8396–8399.
- 246 G. Pieters, C. Pezzato and L. J. Prins, *Langmuir*, 2013, **29**, 7180–7185.
- 247 M.-V. Salvia, F. Ramadori, S. Springhetti, M. Diez-Castellnou, B. Perrone, F. Rastrelli and F. Mancin, *J. Am. Chem. Soc.*, 2015, **137**, 886–892.
- 248 X. Liu, M. Atwater, J. Wang and Q. Huo, *Colloids Surf. B Biointerfaces*, 2007, **58**, 3–7.
- 249 S. Kimura, E. Bill, E. Bothe, T. Weyhermüller and K. Wieghardt, *J. Am. Chem. Soc.*, 2001, **123**, 6025–6039.
- 250 A. K. Tucker-Schwartz, R. A. Farrell and R. L. Garrell, *J. Am. Chem. Soc.*, 2011, **133**, 11026–11029.
- 251 P. Pengo, S. Polizzi, L. Pasquato and P. Scrimin, *J. Am. Chem. Soc.*, 2005, **127**, 1616–1617.
- 252 M. Diez-Castellnou, M.-V. Salvia, S. Springhetti, F. Rastrelli and F. Mancin, *Chem. - Eur. J.*, 2016, **22**, 16957–16963.
- 253 H. T. N. K. A. Jolliffe and X. Liu, *Chem. Soc. Rev.*, 2012, **41**, 4928–4965.
- 254 R. Bonomi, F. Selvestrel, V. Lombardo, C. Sissi, S. Polizzi, F. Mancin, U. Tonellato and P. Scrimin, *J. Am. Chem. Soc.*, 2008, **130**, 15744–15745.
- 255 X. Y. Yu, J. Z. Zhang, in *Macrocyclic Polyamines*, Wiley-VCH Verlag GmbH & Co. KGaA, Weinheim, Germany, 2017, pp. 45–81.
- 256 A. Garaikoetxea Arguinoniz, N. Gómez Blanco, P. Ansorena Legarra and J. C. Mareque-Rivas, *Dalton Trans.*, 2015, **44**, 7135–7138.
- 257 B. Perrone, S. Springhetti, F. Ramadori, F. Rastrelli and F. Mancin, *J. Am. Chem. Soc.*, 2013, **135**, 11768–11771.
- 258 A. Chen and M. J. Shapiro, *J. Am. Chem. Soc.*, 1998, **120**, 10258–10259.
- 259 G. A. Morris, in *Encyclopedia of Magnetic Resonance*, ed. R. K. Harris, John Wiley & Sons, Ltd, Chichester, UK, 2009.
- 260 F. Rastrelli, S. Jha and F. Mancin, *J. Am. Chem. Soc.*, 2009, **131**, 14222–14224.
- 261 A. V. Fonin, A. I. Sulatskaya, I. M. Kuznetsova and K. K. Turoverov, *PLoS ONE*, 2014, **9**, e103878.
- 262 T. Weitner, T. Friganović and D. Šakić, *Anal. Chem.*, 2022, **94**, 7107–7114.
- 263 B. Birdsall, R. W. King, M. R. Wheeler, C. A. Lewis, S. R. Goode, R. B. Dunlap and G. C. K. Roberts, *Anal. Biochem.*, 1983, **132**, 353–361.
- 264 J. R. Lakowicz and B. R. Masters, *J. Biomed. Opt.*, 2008, **13**, 029901.

- 265 S. Alonso-de Castro, A. Terenzi, S. Hager, B. Englinger, A. Faraone, J. C. Martínez, M. S. Galanski, B. K. Keppler, W. Berger and L. Salassa, *Sci. Rep.*, 2018, **8**, 17198.
- 266 R. Tavano, D. Segat, E. Reddi, J. Kos, M. Rojnik, P. Kocbek, S. Iratni, D. Scheglmann, M. Colucci, I. M. R. Echevarria, F. Selvestrel, F. Mancin and E. Papini, *Nanomed.*, 2010, **5**, 881–896.
- 267 D. Nečas and P. Klapetek, *Open Phys.*, 2012, **10**, 181–188.
- 268 G. R. Fulmer, A. J. M. Miller, N. H. Sherden, H. E. Gottlieb, A. Nudelman, B. M. Stoltz, J. E. Bercaw and K. I. Goldberg, *Organometallics*, 2010, **29**, 2176–2179.
- 269 A. Beloqui and A. L. Cortajarena, *Curr. Opin. Struct. Biol.*, 2020, **63**, 74–81.
- 270 A. Farhadi, F. Sigmund, G. G. Westmeyer and M. G. Shapiro, *Nat. Mater.*, 2021, **20**, 585–592.
- 271 M. R. Berwick, L. N. Slope, C. F. Smith, S. M. King, S. L. Newton, R. B. Gillis, G. G. Adams, A. J. Rowe, S. E. Harding, M. M. Britton and A. F. A. Peacock, *Chem. Sci.*, 2016, **7**, 2207–2216.
- 272 P. Couleaud, S. Adan-Bermudez, A. Aires, S. H. Mejías, B. Sot, A. Somoza and A. L. Cortajarena, *Biomacromolecules*, 2015, **16**, 3836–3844.
- 273 L. Altamura, C. Horvath, S. Rengaraj, A. Rongier, K. Elouarzaki, C. Gondran, A. L. B. Maçon, C. Vendrely, V. Bouchiat, M. Fontecave, D. Mariolle, P. Rannou, A. Le Goff, N. Duraffourg, M. Holzinger and V. Forge, *Nat. Chem.*, 2017, **9**, 157–163.
- 274 N. Gogurla, A. K. Sinha, D. Naskar, S. C. Kundu and S. K. Ray, *Nanoscale*, 2016, **8**, 7695–7703.
- 275 I. Medalsy, M. Klein, A. Heyman, O. Shoseyov, F. Remacle, R. D. Levine and D. Porath, *Nat. Nanotechnol.*, 2010, **5**, 451–457.
- 276 E. R. G. Main, J. J. Phillips and C. Millership, *Biochem. Soc. Trans.*, 2013, **41**, 1152–1158.
- 277 T. Kajander, A. L. Cortajarena and L. Regan, in *Protein Design*, Humana Press, New Jersey, 2006, vol. 340, pp. 151–170.
- 278 S. H. Mejias, Z. Bahrami-Dizicheh, M. Liutkus, D. J. Sommer, A. Astashkin, G. Kodis, G. Ghirlanda and A. L. Cortajarena, *Chem. Commun.*, 2019, **55**, 3319–3322.
- 279 X. Wu, X. He, K. Wang, C. Xie, B. Zhou and Z. Qing, *Nanoscale*, 2010, **2**, 2244.

- 280 H. Hu, P. Huang, O. J. Weiss, X. Yan, X. Yue, M. G. Zhang, Y. Tang, L. Nie, Y. Ma, G. Niu, K. Wu and X. Chen, *Biomaterials*, 2014, **35**, 9868–9876.
- 281 J. F. Ross, A. Bridges, J. M. Fletcher, D. Shoemark, D. Alibhai, H. E. V. Bray, J. L. Beesley, W. M. Dawson, L. R. Hodgson, J. Mantell, P. Verkade, C. M. Edge, R. B. Sessions, D. Tew and D. N. Woolfson, *ACS Nano*, 2017, **11**, 7901–7914.
- 282 V. Liljeström, A. Ora, J. Hassinen, H. T. Rekola, Nonappa, M. Heilala, V. Hynninen, J. J. Joensuu, R. H. A. Ras, P. Törmä, O. Ikkala and M. A. Kostianen, *Nat. Commun.*, 2017, **8**, 671.
- 283 D. Sánchez-deAlcázar, S. Velasco-Lozano, N. Zeballos, F. López-Gallego and A. L. Cortajarena, *ChemBioChem*, 2019, **20**, 1977–1985.
- 284 M. Liutkus, A. López-Andarias, S. H. Mejías, J. López-Andarias, D. Gil-Carton, F. Feixas, S. Osuna, W. Matsuda, T. Sakurai, S. Seki, C. Atienza, N. Martín and A. L. Cortajarena, *Nanoscale*, 2020, **12**, 3614–3622.
- 285 V. Biju, *Chem Soc Rev*, 2014, **43**, 744–764.
- 286 Z. Wang, H. Gao, Y. Zhang, G. Liu, G. Niu and X. Chen, *Front. Chem. Sci. Eng.*, 2017, **11**, 633–646.
- 287 M. Roucan, M. Kielmann, S. J. Connon, S. S. R. Bernhard and M. O. Senge, *Chem. Commun.*, 2018, **54**, 26–29.
- 288 K. Oohora, A. Onoda and T. Hayashi, *Acc. Chem. Res.*, 2019, **52**, 945–954.
- 289 F. Schwizer, Y. Okamoto, T. Heinisch, Y. Gu, M. M. Pellizzoni, V. Lebrun, R. Reuter, V. Köhler, J. C. Lewis and T. R. Ward, *Chem. Rev.*, 2018, **118**, 142–231.
- 290 Y.-W. Lin, *Coord. Chem. Rev.*, 2017, **336**, 1–27.
- 291 S. M. Meier-Menches and A. Casini, *Bioconjug. Chem.*, 2020, **31**, 1279–1288.
- 292 V. del Solar and M. Contel, *J. Inorg. Biochem.*, 2019, **199**, 110780.
- 293 J. Mayr, P. Heffeter, D. Groza, L. Galvez, G. Koellensperger, A. Roller, B. Alte, M. Haider, W. Berger, C. R. Kowol and B. K. Keppler, *Chem. Sci.*, 2017, **8**, 2241–2250.
- 294 H. Schueffl, S. Theiner, G. Hermann, J. Mayr, P. Fronik, D. Groza, S. van Schonhooven, L. Galvez, N. S. Sommerfeld, A. Schintlmeister, S. Reipert, M. Wagner, R. M. Mader, G. Koellensperger, B. K. Keppler, W. Berger, C. R. Kowol, A. Legin and P. Heffeter, *Chem. Sci.*, 2021, **12**, 12587–12599.
- 295 I. Nasibullin, I. Smirnov, P. Ahmadi, K. Vong, A. Kurbangalieva and K. Tanaka, *Nat. Commun.*, 2022, **13**, 39.

- 296 N. Graf and S. J. Lippard, *Adv. Drug Deliv. Rev.*, 2012, **64**, 993–1004.
- 297 B. Du, D. Li, J. Wang and E. Wang, *Adv. Drug Deliv. Rev.*, 2017, **118**, 78–93.
- 298 M. Markovic, S. Ben-Shabat and A. Dahan, *Pharmaceutics*, 2020, **12**, 1031.
- 299 G. R. Gibbons, S. Wyrick and S. G. Chaney, *Cancer Res.*, 1898, **49**, 1402–1407.
- 300 Y. Fu, K. E. Bruce, H. Wu and D. P. Giedroc, *Metallomics*, 2016, **8**, 61–70.
- 301 M. Sinisi, F. P. Intini and G. Natile, *Inorg. Chem.*, 2012, **51**, 9694–9704.
- 302 P. Zhang and P. J. Sadler, *Eur. J. Inorg. Chem.*, 2017, **2017**, 1541–1548.
- 303 T. Kajander, A. L. Cortajarena, S. Mochrie and L. Regan, *Acta Crystallogr. D Biol. Crystallogr.*, 2007, **63**, 800–811.
- 304 F. Müller, Ed., in *Chemistry and biochemistry of flavoenzymes*, CRC Press, Boca Raton, 1991.
- 305 J. Ribes, P. Cossard, K. Al Yaman, I. Bestel and E. Badarau, *RSC Adv.*, 2023, **13**, 2355–2364.
- 306 L. C. P. Gonçalves, H. R. Mansouri, S. PourMehdi, M. Abdellah, B. S. Fadiga, E. L. Bastos, J. Sá, M. D. Mihovilovic and F. Rudroff, *Catal. Sci. Technol.*, 2019, **9**, 2682–2688.
- 307 J. Gurruchaga-Pereda, V. Martínez-Martínez, E. Formoso, O. Azpitarte, E. Rezabal, X. Lopez, A. L. Cortajarena and L. Salassa, *J. Phys. Chem. Lett.*, 2021, **12**, 4504–4508.
- 308 D. A. Dickinson and H. J. Forman, *Biochem. Pharmacol.*, 2002, **64**, 1019–1026.
- 309 H. J. Forman, H. Zhang and A. Rinna, *Mol. Aspects Med.*, 2009, **30**, 1–12.
- 310 H. D. Nguyen and L. H. Do, *Curr. Opin. Chem. Biol.*, 2022, **71**, 102213.
- 311 G. Asantewaa and I. S. Harris, *Curr. Opin. Biotechnol.*, 2021, **68**, 292–299.
- 312 M. Valko, H. Morris and M. Cronin, *Curr. Med. Chem.*, 2005, **12**, 1161–1208.
- 313 A. Fraternali, S. Brundu and M. Magnani, *Biol. Chem.*, 2017, **398**, 261–275.
- 314 L. Amable, *Pharmacol. Res.*, 2016, **106**, 27–36.
- 315 D. Wang and S. J. Lippard, *Nat. Rev. Drug Discov.*, 2005, **4**, 307–320.
- 316 A. Krezel and W. Bal, *Acta Biochim. Pol.*, 1999, **46**, 567–580.
- 317 B. A. J. Jansen, J. Brouwer and J. Reedijk, *J. Inorg. Biochem.*, 2002, **89**, 197–202.

- 318 M. T. Saung and L. Zheng, *Clin. Ther.*, 2017, **39**, 2125–2134.
- 319 G. K. Gresham, G. A. Wells, S. Gill, C. Cameron and D. J. Jonker, *BMC Cancer*, 2014, **14**, 471.
- 320 G. Yan, L. Zhang, C. Feng, R. Gong, E. Idiiatullina, Q. Huang, M. He, S. Guo, F. Yang, Y. Li, F. Ding, W. Ma, V. Pavlov, Z. Han, Z. Wang, C. Xu, B. Cai, Y. Yuan and L. Yang, *Int. J. Biochem. Cell Biol.*, 2018, **103**, 81–88.
- 321 H. K. Binz, P. Amstutz and A. Plückthun, *Nat. Biotechnol.*, 2005, **23**, 1257–1268.
- 322 L. De Rosa, A. L. Cortajarena, A. Romanelli, L. Regan and L. D. D’Andrea, *Org Biomol Chem*, 2012, **10**, 273–280.

Acknowledgments

First, I would like to thank both of my supervisors Prof. Aitziber L. Cortajarena and Prof. Luca Salassa for their support and their advice. I am grateful for the opportunity that you gave me to work on a multidisciplinary PhD project, and for leading me from the first day to the last one. Thanks also for your patience with the thesis writing part of this journey.

Second, I am grateful to all the people working at the Biomolecular Nanotechnology Lab and the Inorganic Photochemistry Lab. A special thanks go to *Las Lokis*, Laura-Idoia-Elena, for their working support and not only and to be always there for helping me or take a beer! Thanks also to Liher, to be patient with all my *agobios* moments and to be a reference. I want to thanks also Max, Paolo, Kepa, Aitor, Gunnar, and Antonio! A big thanks is also for Álvaro, for being an amazing teacher in the chemistry lab.

I would like to thank also other three people that I met here during my PhD: Eli T., Eli L., and Ceci. Eli and Eli took the good decision to leave Donostia before I started to write my thesis (very good choice), but also from far away they were and are fundamental for all the paths that I did. Ceci was not so lucky, and she live this period close to me. Sorry Ceci! Thanks to all of them to be good friends.

I am also thankful to all the people working in CICbiomaGUNE and in the DIPC, from the platform managers, technicians, maintenance, o admin employers.

Last, but not least, I would like to thank my family and my friend to be always there for me. I am especially thankful to my parents for never having doubted about my capability and to Stefano, for everything.

Thanks to all of you, also the people that are not directly mentioned here!

List of publications

1) Toward supramolecular nanozymes for the photocatalytic activation of Pt(IV) anticancer prodrugs. **Laura F. Mazzei**, Álvaro Martínez, Lucia Trevisan, Daniele Rosa-Gastaldo, Aitziber L. Cortajarena, Fabrizio Mancin and Luca Salassa. *Chem. Commun.*, 2020,**56**, 10461-10464.

2) Engineered flavoproteins as bioorthogonal photo-triggers for the activation of metal-based anticancer prodrugs. **Laura F. Mazzei**, Juan Gurruchaga-Pereda, Álvaro Martínez, Javier Calvo Martínez, Luca Salassa and Aitziber L. Cortajarena. *Chem. Commun.*, 2023,**59**, 4754-4757.

**AUTHORISATION OF THE THESIS SUPERVISOR
FOR ITS PRESENTATION**

Mr/Ms. Dr. Aitziber López Cortajarena with National ID Card num. 20221068C

In his/her capacity as Supervisor of the Doctoral Thesis:

Engineering hybrid nanostructures for the photocatalytic activation of Pt(IV) prodrugs completed within the Doctoral Programme Química Aplicada y de los Materiales Poliméricos

by the PhD student Mr/Ms Laura Filomena Mazzei,

having reviewed the SIMILARITY REPORT issued by the tool provided for this purpose by the university, hereby authorises the presentation of the aforementioned Doctoral Thesis, given that it fulfils the conditions necessary for its viva.

In San Sebastian on 20th of April , 2023

THE THESIS SUPERVISOR



Signed: Aitziber López Cortajarena

**AUTHORISATION OF THE THESIS SUPERVISOR
FOR ITS PRESENTATION**

Mr/Ms. Luca Salassa_with National ID Card num. Y2262902S

In his/her capacity as Supervisor of the Doctoral Thesis:

Engineering hybrid nanostructures for the photocatalytic activation of Pt(IV) prodrugs completed within the Doctoral Programme Química Aplicada y de los Materiales Poliméricos

by the PhD student Mr/Ms Laura Filomena Mazzei,

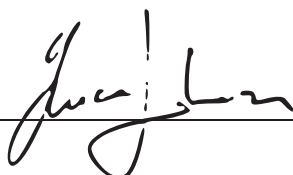
having reviewed the SIMILARITY REPORT issued by the tool provided for this purpose by the university, hereby authorises the presentation of the aforementioned Doctoral Thesis, given that it fulfils the conditions necessary for its viva.

In Donostia-San Sebastián on the 20th of April, 2023

THE THESIS SUPERVISOR

Luca Salassa

Signed: _____



Firmado por SALASSA LUCA - Y2262902S
el día 20/04/2023 con un certificado emitido
por AC FNMT Usuarios

**AUTHORISATION OF THE THESIS TUTOR
FOR ITS PRESENTATION**

Mr/Ms. Miren Ostra

In his/her capacity as Tutor of the Doctoral Thesis:

Engineering hybrid nanostructures for the photocatalytic activation of Pt(IV) prodrugs completed within the Doctoral Programme Química Aplicada y de los Materiales Poliméricos

by the PhD student Mr/Ms. Laura Filomena Mazzei

and supervised by Dr. Aitziber López Cortajarena and Dr. Luca Salassa

hereby authorises the presentation of the aforementioned Doctoral Thesis, given that it fulfils the conditions necessary for its viva.

In Donostia, on 21st of April 2023

THE THESIS TUTOR

Signed: MIREN OSTRA BELDARRAIN

AUTHORISATION OF THE DOCTORAL PROGRAMME'S ACADEMIC COMMISSION

The Academic Commission of the Doctoral Programme in Applied Chemistry and Polymeric Materials during its meeting held on 21ST of April, 2023, agreed to authorise the presentation of the Doctoral Thesis entitled: Engineering hybrid nanostructures for the photocatalytic activation of Pt(IV) prodrugs, supervised by Dr. Aitziber López Cortajarena and Dr. Luca Salassa and presented by Mr/Ms. Laura Filomena Mazzei and registered with the Department of Applied Chemistry.

In Donostia on 21st of April 2023.

THE COORDINATOR OF THE DOCTORAL PROGRAMME

Signed: MIREN OSTRA BELDARRAIN

DEPARTMENT AUTHORISATION

The Board of the Department QUIMICA APLICADA during its meeting held on 26 of april, 2023 agreed to authorise the processing of the Doctoral Thesis entitled:

“Engineering hybrid nanostructures for the photocatalytic activation of Pt(IV) prodrugs”

supervised by Dra. Aitziber López Cortajarena and Dr. Luca Salassa and presented by Ms. Laura Filomena Mazzei to this Department.

In Donostia, on 26 of april, 2023

APPROVED BY THE DEPARTMENT DIRECTOR AND DEPARTMENT SECRETARY



**ROSA
MARIA
GARCIA
ARRONA -
72435622C**

Firmado digitalmente por ROSA MARIA GARCIA ARRONA - 72435622C
Fecha: 2023.04.26 11:40:30 +02'00'

Signed: JOSE MANUEL SECO BOTANA
DEPARTMENT DIRECTOR

Signed: ROSA GARCIA ARRONA
DEPARTMENT SECRETARY

ACTA DE GRADO DE DOCTOR O DOCTORA
ACTA DE DEFENSA DE TESIS DOCTORAL

DOCTORANDO/A DON/DÑA. Laura Filomena Mazzei

TITULO DE LA TESIS: Engineering hybrid nanostructures for the photocatalytic activation of Pt(IV) prodrugs.

El Tribunal designado por la Comisión de Postgrado de la UPV/EHU para calificar la Tesis Doctoral arriba indicada y reunido en el día de la fecha, una vez efectuada la defensa por el/la doctorando/a y contestadas las objeciones y/o sugerencias que se le han formulado, ha otorgado por _____ la calificación de:
unanimidad ó mayoría

SOBRESALIENTE / NOTABLE / APROBADO / NO APTO

Idioma/s de defensa (en caso de más de un idioma, especificar porcentaje defendido en cada idioma):

Castellano _____

Euskera _____

Otros Idiomas (especificar cuál/cuales y porcentaje) _____

En _____ a _____ de _____ de _____

EL/LA PRESIDENTE/A,

EL/LA SECRETARIO/A,

Fdo.:

Fdo.:

Dr/a: _____

Dr/a: _____

VOCAL 1º,

VOCAL 2º,

VOCAL 3º,

Fdo.:

Fdo.:

Fdo.:

Dr/a: _____ Dr/a: _____ Dr/a: _____

EL/LA DOCTORANDO/A,

Fdo.: _____